THE UNIVERSITY
of EDINBURGH

Understanding the role of UBA1 in the pathogenesis of spinal muscular atrophy

Hannah Karen Shorrock

A thesis submitted for the degree of Doctor of Philosophy

The University of Edinburgh

2017

Declaration

I declare that this thesis was composed entirely by myself and is based on my own work, unless clearly stated in the text. The work in this thesis has not been submitted for any other degree or professional qualification.

Hannah Karen Shorrock

Acknowledgements

First of all, I would like to thank my supervisor Prof Tom Gillingwater. Tom, thank you being so incredibly supportive throughout my PhD. Thank you for your optimism and positivity, even when there were many tears, I always came out of progress meeting feeling better than when I went in. Thank you for putting up with me, for telling me to take breaks and for letting me have my big holidays. Thank you for making time to discuss my project, to keep me on track and for always being kind and patient. I cannot say thank you enough.

I would also like to thank my second supervisor Dr Ewout Groen. Thank you for teaching me how to do everything and for always making time to teach me. Thank you for the long chats about my project, about everything science and about everything not science. Thank you for the laughs, the brews, the jelly babies and the figure making tutorials. Thank you for being honest but not too harsh, for telling me when I was wrong and when I did good. Thank you Ewout.

I would also like to thank Prof Dies Meijer for being my thesis committee chair, Dr Thomas Wishart for the advice and help throughout my PhD and Dr Heidi Fuller for the interesting collaboration on oesophagi. I would like to thank Douglas Lamont and the FingerPrints proteomics facility for performing the label-free proteomic screen in this thesis and Maica Llavero Hurtado for all of the help and advice with analysing the proteomics dataset. I would also like to thank Dr James Sleigh and Prof Giampietro Schiavo for their advice and guidance on the role of GARS in sensory neuron pathology in CMT2D. I would like to thank Prof Mike Cousin and Dr Anthony Antonellis for the gifts of constructs used in this project. I would like to thank Prof Richard Ribchester and Prof Simon Parson for the interesting and illuminating discussions and Dr Gillian Hunter for her support and advice. I would also like to thank all the staff in the HRB BRR, in particular Alan Kirkwood and Peter Rutherford, for going above and beyond with the animal husbandry of the Taiwanese mouse colony.

I would like to thank the Euan MacDonald Centre for funding my PhD, and for the opportunities to present at postgraduate symposia and public events.

I would also like to thank the students that have worked on and helped out with my project. Firstly, I would like to thank my Masters student Dinja, who has been amazing at everything; thank you for being so independent and technically capable, thank you for all your hard work on tRNA synthetases. I would like to thank my Masters student Amr, for his help with IHCs and for his hard work performing distribution analysis. I would like to thank Elena for helping to optimise the ubiquitylation assay and Ines B for looking after the cells and for all the Unicorns.

To Fiona, thank you for the hugs and the chats. Thank you for insisting on morning brew time and lab lunch time. Thank you for your help and support and kindness and fighting for me to learn neuron culture. Thank you for inviting me to yours for tea and distracting me with Esme; thank you for looking after me. To Penelope, thank you for the crash course in restriction cloning, for all the fish, for all the hugs and all the wine. Thank you for all of your help and support during your time in the lab and beyond. To Ines, thank you for being a voice of reason, for being a sensible influence, for being kind, for drinking in the park, for all the Thai and that time I got chips on a burger. Thank you for letting me come and distract you when I needed distracting.

I would like to thank Natalie for always making sure I was alright, for letting my cry and chat, and for always being kind. I would like to thank all of the 'Murray girls' for their kindness, entertainment and the knowledge that if I go into your office there will most definitely be laughter. To Nikky, thank you for taking over the management of the mouse colony so I could focus on my thesis, I feel happy leaving the mice in your capable hands. I would like to thank Ross for the anatomy lessons and the interesting discussions. I would also like to thank Kiterie and Heidi for being brave enough and kind enough to provide feedback on my thesis. To everyone who has been part of the Gillingwater lab during my PhD, thank you for being so nice to work with.

I would like to thank everyone who has made my PhD experience what it has been. I have really enjoyed my PhD, but it wouldn't be the same without the people I met during my time at Edinburgh. Whether you were a friendly face in the corridor, gave kind words of support while I was writing my thesis or kept me amused along the way, I would like to say thank you for all the little things and the small moments that made this experience what it has been.

Finally, I would like to thank my family for keeping me smiling, even when I was too tired to do anything else. To Mum and Dad, thank you for the phone calls, for the visits, for the 'writing retreats', for the food and the washing and looking after me. I would like to thank you both for your never-ending supply of positivity and motivational support.

To all of the above, you are brilliant and I would not have gotten through this without your support. Thank you.

Abstract

Spinal muscular atrophy (SMA) is an autosomal recessive neuromuscular disorder characterized by widespread loss of lower motor neurons from the spinal cord. Lower motor neuron degeneration leads to a progressive decline in motor development, manifesting as muscle atrophy and weakness. It is now well characterised that ubiquitin homeostasis is altered in SMA and that reduction of the ubiquitin-like modifier-activating enzyme 1 (UBA1) is central to this disruption. UBA1 is responsible for activating ubiquitin as the first step in the ubiquitin conjugation process, marking unwanted proteins for degradation by the proteasome. While it is known that therapies targeting UBA1 rescue neuromuscular phenotypes in SMA models, the mechanism by which UBA1 mediates neurodegeneration is unclear. In fact, very little is known about the function of UBA1 beyond its canonical role in the ubiquitin proteasome system. To better understand the role of UBA1 in motor neuron degeneration, a robust set of antibodies for both in vivo and in vitro work to study UBA1 have been identified. This enabled a novel characterisation of UBA1 distribution throughout disease progression in SMA spinal motor neurons to be performed, revealing that UBA1 reduction is an important pre-symptomatic molecular feature of SMA. To identify downstream targets of UBA1 critical for UBA1-mediated degeneration in SMA, label-free proteomics was performed on HEK293 cells after overexpression or knockdown of UBA1. The proteomics data was analysed across multiple platforms, including Biolayout, IPA and DAVID to identify UBA1-dependent pathways and demonstrated that modulation of UBA1 levels lead to disruption of key cellular pathways including translation elongation, nuclear transport, and tRNA synthetases. Validation of target proteins from these UBA1-dependent pathways identified that the tRNA synthetase GARS behaves in a UBA1-dependent manner across a range of model systems *in vitro* and *in vivo*. It was then identified that GARS expression is significantly dysregulated across a range of neuronal tissues in a mouse model of SMA. Interestingly, mutations in GARS cause Charcot-Marie-Tooth disease type 2D (CMT2D), an axonal neuropathy, in which a disruption to sensory neuron fate in dorsal root ganglia has recently been identified. In a mouse model of SMA we identified a phenotype consistent with that in the CMT2D mouse model and showed that disruption to sensory neuron fate is

reversible and dependent on changes in UBA1 and GARS expression in SMA. In conclusion, modulation of UBA1 levels leads to disruption of key cellular pathways, with dysregulation of tRNA synthetases a prominent feature that is likely to play a role in the pathogenesis of SMA.

Lay Summary

The most common inherited form of death during childhood is a motor neuron disease called spinal muscular atrophy (SMA). In SMA, motor nerves in the spinal cord degenerate and die meaning that they can no longer pass signals from the brain to the muscle. This means that the child has weak muscles and does not develop normal motor skills. One of the molecular pathways that is changed in SMA is the system responsible for recycling unwanted proteins by breaking them down so that the building blocks of the proteins can be used elsewhere. In SMA, the key disruption to this protein recycling pathway is a reduction in the levels of a particular protein, called ubiquitin-like modifier-activating enzyme 1 (UBA1). Therapies that increase UBA1 protein levels reverse muscle weakness and motor nerve degeneration in mice that have SMA. However, it is still unknown how low levels of UBA1 causes motor nerve degeneration in SMA. To try and understand how UBA1 is involved in degeneration, tools and techniques to study UBA1 in cells and mice were developed. This meant that a study to look at the amount of UBA1 protein through disease progression could be performed. In this study, I found that reduction of UBA1 levels occurs very early on in the disease, before motor nerves die and before muscle become weak. This suggests that low levels of UBA1 has a key role in causing motor nerve degeneration in SMA. To see how UBA1 might be causing or contributing to motor nerve degeneration in SMA, a study was performed to identify proteins that are changed due to the reduction in UBA1 levels. This showed that changes in UBA1 levels leads to changes in key pathways within cells, including a disruption of transport within the cell, and disruption to the process of making proteins. One of the proteins identified in this study that is involved in making other proteins is called GARS. We found that there are changes in the levels of GARS in mice that have SMA. Genetic changes in GARS causes another hereditary disease called Charcot-Marie-Tooth disease type 2D (CMT2D). This disease is similar to SMA as it also causes motor nerve death and muscle weakness. CMT2D patients also have degeneration of sensory nerves. Mice that have CMT2D have different amounts of the types of sensory nerves. To see if GARS could be causing degeneration in SMA, we looked at types of sensory nerves present in SMA mice. The SMA mice have the same disruption to sensory nerves that occurs in mouse

models of CMT2D. This disruption to sensory nerves is caused by changes in protein levels of GARS and UBA1. By increasing UBA1 protein levels, GARS protein levels were restored and the change to sensory nerve types was reversed. In conclusion, changes to UBA1 levels disrupts important pathways within cells, which is likely to play a role in causing the degeneration seen in SMA.

Contents

List of Figures

List of Tables

List of Appendices

List of Abbreviations

α-Tub	α-Tubulin
AARS	Alanyl-tRNA synthetase
AAV9	Adeno-associated virus serotype 9
AD	Alzheimer's disease
AIMP1, 2, 3	Aminoacyl tRNA synthetase complex-interacting multifunctional protein 1, 2 and 3
ALS	Amyotrophic lateral sclerosis
AMP	Adenosine monophosphate
ASO	Antisense oligonucleotide
Atg3	Ubiquitin-like-conjugating enzyme Atg3
Atg7	Ubiquitin-like modifier-activating enzyme Atg7
Atg8	Autophagy-related protein 8
ATP	Adenosine triphosphate
BAG6	Large proline-rich protein BAG6
BCA	Bicinchoninic acid (assay)
BSA	Bovine serum albumin
Cdk1	Cyclin-dependent kinase 1
ChAT	Choline Acetyltransferase
CMT	Charcot-Marie-Tooth disease
CMT2D	Charcot-Marie-Tooth disease type 2D
COPS3	COP9 signalosome complex subunit 3
CTNNB1	beta-catenin
Ctrl	Control
DAPI	4',6-diamidino-2-phenylindole
DAVID	Database for Annotation, Visualization and Integrated Discovery
DCAF7	DDB1- and CUL4-associated factor 7
DI-CMTC	Dominant intermediate Charcot-Marie-Tooth disease type C
DIV	Days *in vitro*
DMEM	Dulbecco's Modified Eagle's medium

DNA	Deoxyribonucleic acid
dNTPs	Deoxynucleotide triphosphate
DRG	Dorsal root ganglia
DTT	Dithiothreitol
DUB	Deubiquitylating enzyme
E	Embryonic day
EDTA	Ethylenediaminetetraacetic acid
EEF1A, A1, A2	Elongation factor 1-alpha, 1-alpha 1 and 1-alpha 2
EEF1B2, 1D, 1G	Elongation factor 1-beta, 1-delta and 1-gamma
EEF2	Elongation factor 2
EIF4A1, EIF4G	Eukaryotic initiation factor 4A-I and 4 gamma
ES	Enrichment score
Exp	Experiment
FASP	Filter-aided sample preparation
FAT10	Ubiquitin D
FL-SMN	Full length survival motor neuron protein
FUS	Fused in sarcoma
FVB	Friend leukemia virus B strain
G1, G2, S	Gap 1, Gap 2 and synthesis phase of cell cycle
GAPDH	Glyceraldehyde-3-phosphate dehydrogenase
GARS	Glycyl-tRNA synthetase
GFP	Green fluorescent protein
GO	Gene ontology
H3	Histone H3
HARS	Histidyl-tRNA synthetase
HD	Huntington's disease
HECT domain	Homologous to the E6-AP Carboxyl Terminus domain
HEK293	Human embryonic kidney cells 293
hpf	hours post fertilisation
HPRT	Hypoxanthine-guanine phosphoribosyltransferase
HSP90AA1	Heat shock protein HSP 90-alpha
IB	Immunoblot

ICC	Immunocytochemistry
IGF-1	Insulin like growth factor 1
IGHMBP2	DNA-binding protein SMUBP-2
IHC	Immunohistochemistry
IPA	Ingenuity pathway analysis
IPO4, IPO9	Importin-4, Importin-9
iPSC	Induced pluripotent stem cell
iTRAQ	isobaric Tags for relative and absolute quantitation
KARS	Lysyl-tRNA synthetase
KD	Knockdown
KPNA3, KPNB1	Importin subunit alpha-4, beta-1
KPNB2	Transportin-1
LALr	rostral Levator auris longus
LC-MS	Liquid chromatograph-mass spectrometry
LRSAM1	E3 ubiquitin-protein ligase LRSAM1
LTQ	Linear ion trap
MARS	Methionyl-tRNA synthetase
MO	Morpholino
MORC2	MORC family CW-type zinc finger protein 2
MPLA	Multiplex ligation-dependent probe amplification
mRNA	Messenger ribonucleic acid
NCALD	Neurocalcin Delta
NCR	Nuclear to cytoplasmic ratio
NEDD4L	E3 ubiquitin-protein ligase NEDD4-like
NEDD8	Neural Precursor Cell Expressed, Developmentally Down-Regulated 8
NF200	Neurofilament Protein 200 (heavy neurofilament)
NLS	Nuclear localisation sequence
NMJ	Neuromuscular junction
OCT	Optimal cutting temperature compound
OE	Overexpression
P	Postnatal day

PARP1	Poly [ADP-ribose] polymerase 1
PBS, PBST	Phosphate buffered saline, PBS Triton X-100
PCNA	Proliferating cell nuclear antigen
PCR	Polymerase chain reaction
PD	Parkinson's disease
PDCD4	Programmed cell death protein 4
PFA	Paraformaldehyde
PFN1	Profilin-1
PGAM1	Phosphoglycerate mutase 1
PGK1	Phosphoglycerate kinase 1
PIEZO2	Piezo-type mechanosensitive ion channel component 2
PLS3	Plastin 3
PMP22	Peripheral myelin protein 22
PVDF	Polyvinylidene difluoride
RAN	GTP-binding nuclear protein Ran
RanBP1	Ran-specific GTPase-activating protein
RanBP2	E3 SUMO-protein ligase RanBP2
RanGAP	Ran GTPase-activating protein 1
RING-finger	Really Interesting New Gene - finger
RIPA	Radioimmunoprecipitation assay buffer
Rho A	Transforming protein RhoA
RNP	Ribonuclear protein
ROCK	Rho-associated protein kinase
RT	Room temperature
siRNA	Small interfering ribonucleic acid
SMA	Spinal muscular atrophy
SMARD1	Spinal muscular atrophy with respiratory distress type 1
SMN	Survival motor neuron protein
SMN1, SMN2	*Survival motor neuron 1 and 2 genes*
snoRNP	Small nucleolar ribonucleoprotein
snRNP	Small nuclear ribonuclear protein
SOD1	Cu/Zn superoxide dismutase 1

SUMO	Small ubiquitin-related modifier 1
TNFRSF21	Tumor necrosis factor receptor superfamily member 21
tRNA	transfer ribonucleic acid
tSMN	tagged survival motor neuron protein
Ub	Ubiquitin
UBA1	Ubiquitin-like modifier activating enzyme 1
UBA1a, UBA1b	UBA1 isoform a and isoform b
UBA6	Ubiquitin-like modifier-activating enzyme 6
UBL	Ubiquitin-like protein
UCHL1	Ubiquitin carboxyl-terminal hydrolase isozyme L1
UPS	Ubiquitin proteasome system
Usp9x	Ubiquitin carboxyl-terminal hydrolase FAF-X
WARS	Tryptophanyl-tRNA synthetase
XL-SMA	X-linked spinal muscular atrophy
YARS	Tyrosyl-tRNA synthetase

Chapter 1 Introduction

1.1 Spinal muscular atrophy

Spinal muscular atrophy (SMA) is a hereditary form of motor neuron disease, characterized by degeneration of motor neurons in the anterior horn of the spinal cord (Kolb and Kissel, 2011). This leads to progressive proximal muscle weakness and atrophy and, in severe cases, paralysis and death. The prevalence of SMA is approximately 1-2 per 100,000 persons, and with an incidence of 1 in ~10,000 live births this autosomal recessive disease is the most common genetic cause of infant mortality (Lunn and Wang, 2008; Sugarman et al., 2012; Verhaart et al., 2017). The monogenetic cause of SMA has been long known (Lefebvre et al., 1995) and as such there has been considerable drive within the research community to understand SMA and develop promising therapeutic strategies to treat this lethal disease. This section (1.1) of the introduction contains text adapted from my published review (Shorrock and Gillingwater, 2016).

1.1.1 The history of SMA

Spinal muscular atrophy was first described by Guido Werdnig in 1891 where he presented the case of two infant brothers with proximal muscle weakness and atrophy (Dubowitz, 2009; Werdnig, 1891). This was supplemented by seven additional cases from three separate families described by Johan Hoffmann from 1893 to 1900 (Dubowitz, 2009; Hoffmann, 1893, 1897, 1900). Interestingly, the first description of what is now known as severe SMA was not until 1903 when Beevor described the fourth affected child in one family; the previous three cases had died by 6 months, and this case showed degeneration of anterior horn cells of the spinal cord (Beevor, 1902; Dubowitz, 2009). During the 1950s a milder form of SMA was described by Kugelberg and Welander. The report described patients who were ambulant and presented with muscular dystrophy; however, the disease was shown to be neurogenic based on electromyography (Dubowitz, 2009; Kugelberg and Welander, 1956). Similarly, in the 1960s an intermediate form of SMA was described in a review of 12 cases by Victor Dubowitz (Dubowitz, 1964). During

characterisation of the wide range of cases of SMA, anterior horn cell degeneration and proximal weakness were identified along with weakness affecting axial, intercostal and bulbar musculature; it therefore became understood that these are the hallmarks of SMA. Throughout the rest of the 20th century the variability in severity of SMA was further characterised and defined (Dubowitz, 2009).

1.1.2 Clinical manifestations

The degeneration of lower motor neurons that occurs in SMA leads to a progressive decline in motor development, manifesting as muscle atrophy and weakness, primarily affecting proximal muscle groups (Harding et al., 2015). The profile of disease progression can vary substantially between patients with some phases of plateau in the decline of motor development (Mercuri et al., 2016). Based on the age of onset, motor function achieved, and typical age of death, SMA can be classified into as many as five distinct clinical subgroups with varying severity (Mercuri et al., 2012).

Type 0 SMA is the most severe form of the disease, with onset occurring *in utero* with reduced fetal movements. Life does not normally extend beyond the first few weeks after birth and patients present with joint contractures and a failure to swallow and breathe (Kolb and Kissel, 2011). Type 1 SMA, otherwise known as Werdnig-Hoffman disease, is the most common type of SMA (Hoffmann, 1893; Mercuri et al., 2012; Werdnig, 1891). Disease onset occurs by six months and patients are unable to sit without support and cannot control head movement (Lunn and Wang, 2008). Patients with SMA type 1 show generalized muscle weakness with severe hypotonia and often a bell-shape-like conformation of the thorax due to impaired ribcage expansion. Poor bulbar function and weak intercostal muscles lead to difficulties feeding and breathing, resulting in death within the first two years of life in the absence of palliative care (Faravelli et al., 2015).

Patients with type 2 SMA (Dubowitz disease) have an intermediate phenotype and are able to maintain a sitting position unaided; some patients may be able to stand but do not develop the ability to walk independently (Dubowitz, 1964; Faravelli et al., 2015). Onset occurs between 7 and 18 months of age where the

patients show a delay in the development of gross motor skills; death frequently occurs during adolescence due to respiratory problems (Dubowitz, 2009; Lunn and Wang, 2008). Type 3 SMA (Kugelbery-Welander disease) shows marked symptom heterogeneity: some patients are able to walk independently and have some muscle weakness, while others begin to walk but require wheelchair assistance in childhood. Patients show wasting of proximal muscle groups and varying degrees of muscle hypotonia while bulbar involvement is less frequent than in the more-severe forms of SMA (Dubowitz, 2009; Kugelberg and Welander, 1956; Lunn and Wang, 2008). Type 4 SMA disease onset typically occurs in the second or third decade of life, with patients suffering from muscular weakness, atrophy and fasciculations without respiratory problems (Faravelli et al., 2015). The disease course is usually stable and mild. For both SMA type 3 and type 4, life expectancy is often comparable to that of the general population (Mercuri et al., 2012). In all subtypes, molecular genetic analysis is now the gold standard for diagnosis. Several rare forms of SMA also exist, including X-linked SMA, SMA with respiratory distress, and spinal and bulbar muscular atrophy (Kennedy's disease) (Faravelli et al., 2015).

1.1.3 Genetics of SMA

By performing linkage analysis, several groups identified that the disease-causing gene for SMA resided on the long arm of chromosome 5, location 5q11.2 – 13.3 (Brzustowicz et al., 1990; Lefebvre et al., 1995; Melki et al., 1990) (Figure 1-1A). Lefebvre et al. (1995) identified that this genomic region contains a large inverted duplication and narrowed the critical region to a 140kb segment within the telomeric section of this duplication. They were then able to identify that the survival motor neuron 1 (*SMN1*) gene was either absent or interrupted in 226 of 229 SMA patients investigated. The three remaining patients had either a point mutation or a short deletion at consensus splice sites of introns 6 and 7 (Lefebvre et al., 1995).

It is now understood that in ~95% of cases SMA is caused by homozygous deletion or mutation of *SMN1* (Lefebvre et al., 1995). A mutation for which 1 in ~50 people are carriers (Lunn and Wang, 2008; Sugarman et al., 2012). *SMN1* is a 20kb gene comprised of 9 exons interrupted by 8 introns, encoding the survival motor

neuron protein (SMN), which is comprised of 294 amino acids (Figure 1-1B). Humans are unique as they have two *SMN* genes, a telomeric *SMN1* copy and an almost identical, centromeric *SMN2* copy (Lefebvre et al., 1995) (Figure 1-1A). The *SMN2* gene has a C to T substitution that leads to alternative splicing, resulting in the exclusion of exon 7 from mRNA which therefore encodes an unstable, truncated protein product (Lorson et al., 1999; Monani et al., 1999). This unstable protein product is then rapidly degraded (Han et al., 2012; Lefebvre et al., 1995) (Figure 1-1B). However, exclusion of exon 7 is incomplete and a small amount of *SMN2* pre-mRNA transcripts retain exon 7 during splicing. This results in the production of full length SMN protein; it is estimated that approximately 10-15% of the protein produced from *SMN2* is full length SMN (Lefebvre et al., 1997; Monani et al., 1999) (Figure 1-1B). As complete loss of SMN protein is embryonic lethal (Monani et al., 2000), SMA patients are dependent on SMN protein produced by the *SMN2* gene (Hamilton and Gillingwater, 2013).

SMN1 and *SMN2* are located in an unstable genomic region, meaning that there is variability in the number of copies of *SMN2* between individuals (Schmutz et al., 2004). These differences in *SMN2* copy number cause variability in the SMA phenotype: individuals with a higher *SMN2* copy number have a less severe disease phenotype (Harding et al., 2015). Thus, *SMN2* copy number represents the primary determinant of disease severity in SMA (Kolb and Kissel, 2011). Interestingly, however, SMN protein levels do not always correlate with *SMN2* copy number (Crawford et al., 2012; Wadman et al., 2016) and the number of *SMN2* copies does not always correlate directly with disease severity in patients (Wadman et al., 2017). Indeed, twins with the same *SMN1* genotype and *SMN2* copy number have been shown to present with different severities of SMA; in one instance one twin was diagnosed with SMA type 1 while the other had SMA type 2 (Pane et al., 2017). Characterisation of discordant families such as this lead to the identification of other genetic modifiers, such as *PLS3* and *NCALD,* that influence the clinical phenotype of SMA (Hosseinibarkooie et al., 2016; Oprea et al., 2008; Riessland et al., 2017).

Following the identification of the disease-causing gene, it has become possible to model SMA in various animal systems (McWhorter et al., 2003; Sleigh et

al., 2011). Animal models of SMA focus on reducing the amount of full length SMN protein and exist for *Caenorhabditis elegans*, *Drosophila melanogaster*, *Danio rerio* (zebrafish) and *Mus musculus* (mouse) (Jablonka and Sendtner, 2017; Sleigh et al., 2011). There is also now a large animal model of SMA in pigs (Duque et al., 2015). Of these, mouse and zebrafish models are the most widely used with several mouse models of SMA being available, most of which are based on deleting the endogenous mouse *Smn* gene and inserting an *SMN2*-like transgene. Studies in these animal models have led to an increased understanding of the molecular pathogenesis of SMA (Jablonka and Sendtner, 2017; Sleigh et al., 2011).

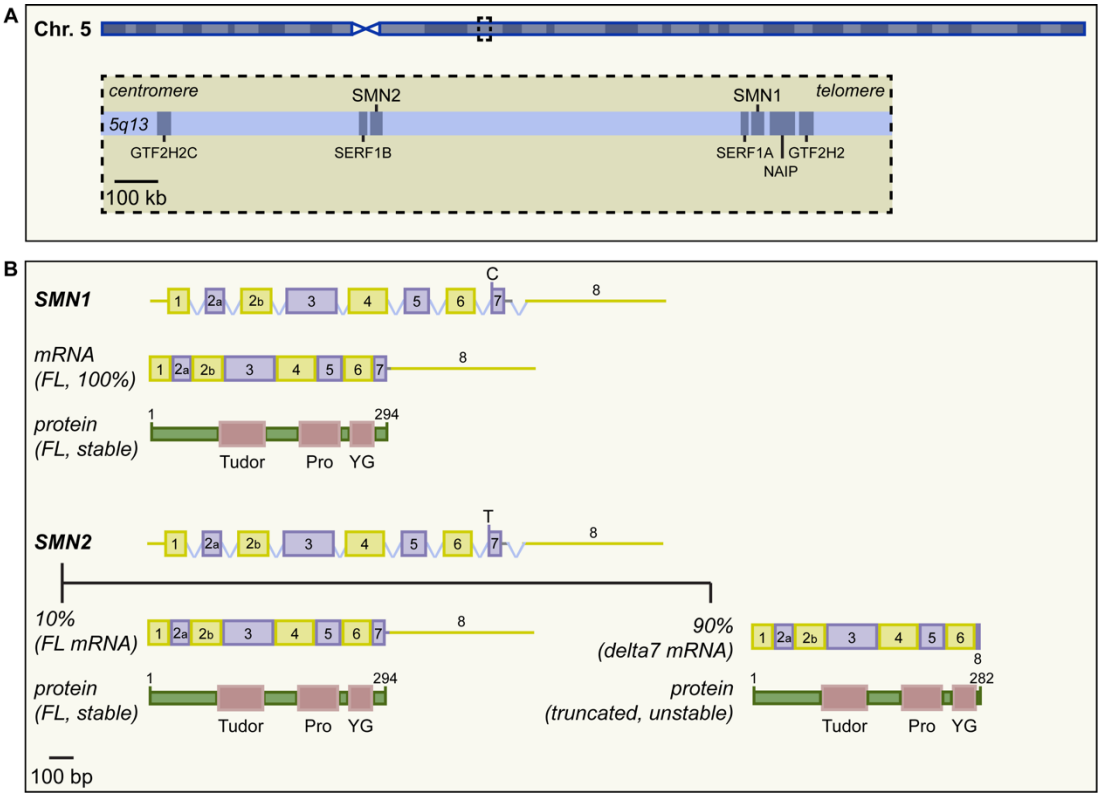

Figure 1-1 Genetics of SMA

A Overview of the human chromosome 5q13 locus containing the telomeric *SMN1* and the centromeric *SMN2* genes. **B** Structure, splicing and protein production from *SMN1* and *SMN2*. Full length SMN protein contains multiple functional domains: tudor domain (Tudor) which regulates the interaction with Sm proteins and other RGG-domain containing proteins; a proline-rich region (Pro) which is known to regulate the interaction of SMN and profilin; and a YG-box domain (YG) which regulates the self-oligomerization SMN. Adapted from (Groen et al., *in preparation*).

1.1.4 The survival motor neuron protein

In order to successfully target the survival motor neuron protein (SMN) as a therapeutic approach for SMA, it is necessary to understand the functions of the SMN protein, the downstream effects of the reduction in SMN and the widespread cellular and molecular pathways subsequently disrupted in this disease.

1.1.4.a Biogenesis of snRNPs

Survival motor neuron protein is a ubiquitously expressed, multifunctional protein that forms a macromolecular complex essential for the splicing of pre-mRNAs (Fischer et al., 1997; Liu et al., 1997; Massenet et al., 2002). SMN associates with Gemins 2-8 and unrip to form a complex that then facilitates the formation, transport and maturation of small nuclear ribonuclear proteins (snRNPs). snRNPs consist of 7 Sm core proteins and uridine-rich small nuclear RNAs (Fischer et al., 1997; Liu et al., 1997; Pellizzoni et al., 2002). Once formed the partially mature snRNPs are imported into the nucleus where they mature in Cajal bodies. The snRNPs then localise to nuclear speckles from where they can be recruited to active spliceosomes in the nucleus when required (Jady et al., 2003; Sleeman and Lamond, 1999; Spector and Lamond, 2011).

During pre-mRNA splicing, snRNPs are essential for the excision of introns from mRNA precursors in the nucleus (Massenet et al., 2002). Reduced SMN levels lead to a tissue specific decrease in snRNP assembly that correlates with phenotypic severity in mouse models of SMA (Gabanella et al., 2007). Interestingly, SMN depletion increases the mobility of snRNPs as a direct effect of the impaired snRNP maturation, meaning that the snRNPs spend relatively less time within the spliceosome and more time in nuclear speckles (Clelland et al., 2012). Moreover, widespread splicing defects have been found in SMA tissues with a wide diversity of genes being affected (Zhang et al., 2008), including genes encoding splicing regulators and proteins required for motor circuit function (Huo et al., 2014; Lotti et al., 2012). However, it has also been suggested that splicing defects may represent a late feature of SMA indicating that alternative splicing events could represent a

consequence of disease progression in SMA, rather than the primary cause (Baumer et al., 2009).

Further studies have suggested a broader role of SMN in RNP formation. It has been identified that SMN is involved in the formation, regulation and function of snoRNPs (small nucleolar RNPs), involved in post-translational modification of noncoding RNAs (Pellizzoni et al., 2001), and signal recognition particles, required to transport newly synthesized proteins, amongst other RNP complexes (Piazzon et al., 2013; Tisdale and Pellizzoni, 2015). Furthermore, SMN has been shown to influence a range of other RNA-related processes such as directly influencing pre-mRNA splicing, along with roles in the transport and translation of mRNAs (Fallini et al., 2012; Makarov et al., 2012; Prescott et al., 2014; Rossoll et al., 2003); functions that lead to clear phenotypes in SMA model systems (see 1.1.4.b).

1.1.4.b Axonal and synaptic functions of SMN

Aside from its housekeeping function in snRNP assembly, SMN has been shown to have additional roles that may contribute to disease pathogenesis in SMA. For example, during axonogenesis and axonal sprouting there is a progressive shift of SMN towards an axonal localisation in human spinal cord, suggesting an axonal function of SMN (Giavazzi et al., 2006). Indeed, SMN is essential for RNA transport within the axonal compartment and is also involved in axonal elongation, with loss of SMN leading to defects in axon outgrowth (Groen et al., 2013; McWhorter et al., 2003; Rossoll et al., 2003).

SMN localises to granules associated with cytoskeletal micro- and macro-filament systems in neurons along which the SMN granules show rapid bidirectional movement (Bechade et al., 1999; Pagliardini et al., 2000; Zhang et al., 2003). These SMN granules are involved in axonal transport to deliver mRNAs to the synapse, where local translation can occur (Fallini et al., 2012). For example, through interaction with mRNA binding proteins, SMN is involved in the localisation of beta-actin and beta-actin mRNA to growth cones of developing motor neurons, which leads to axonal elongation and growth cone size regulation (Rossoll et al., 2003). Interestingly, while SMN deficient motor neurons have reduced growth cone size

(Groen et al., 2013; Rossoll et al., 2003), mice that lack beta-actin in motor neurons do not (Cheever et al., 2011), indicating that other pathways contribute to the defective axonal elongation phenotype in SMA. Indeed, in SMA decreased interaction of SMN and profilin has been shown to lead to an increase in the formation of profilin/ROCK complexes which in turn activates Rho A. As a negative regulator of axon outgrowth, this inappropriate activation of Rho A has been shown to lead to defects in neuritogenesis in SMA (Bowerman et al., 2009; Nolle et al., 2011). Moreover, it has been demonstrated that Insulin like growth factor 1 (IGF-1) is essential for enhancing axonal outgrowth of motor neurons. Intriguingly, circulating IGF-1 levels are also reduced as a consequence of the SMN reduction in SMA (Hua et al., 2011; Tsai et al., 2014).

Furthermore, defects in endocytosis have also been implicated in SMA pathogenesis. Endocytosis is essential for synaptic function and signal transduction at the neuromuscular junction (NMJ), one of the primary sites of pathology in SMA (Hosseinibarkooie et al., 2017). In SMA both misregulation of calcium dynamics and alterations to F-actin dynamics cause defects in endocytosis (Hosseinibarkooie et al., 2016; Riessland et al., 2017). Overexpression of one of the primary genetic modifiers of SMA, Plastin 3 (PLS3), rescues defects in endocytosis in several models of SMA. This likely occurs through the interaction of PLS3 with coronin 1C which then restores the amount of F-actin in SMA (Hosseinibarkooie et al., 2016). Moreover, another genetic modifier of SMA, neurocalcin delta (NCALD), is a neuronal calcium sensor protein that regulates the activity of clathrin (a calcium-sensitive regulator of endocytosis) in a calcium dependent manner (Hosseinibarkooie et al., 2017). Reduction in the amount of NCALD increases the presynaptic function of clathrin which reverses the reduction of the pool of synaptic vesicles that occurs in SMA (Riessland et al., 2017). Together these insights suggest that reduction of SMN leads to multiple defects in the growth, development and maintenance of synaptic and axonal functions that are more widespread than the specific role of SMN in RNA related processes.

1.1.4.c The ubiquitin proteasome system and energy homeostasis in SMA

Several other cellular and molecular pathways are also dysregulated in SMA due to reduced SMN levels. For example, ubiquitin homeostasis is altered in SMA whereby SMN depletion in mouse models of SMA leads to down-regulation of ubiquitin-like modifier-activating enzyme 1 (UBA1) and accumulation of its downstream targets, including beta-catenin (CTNNB1) (Fuller et al., 2015; Wishart et al., 2014). Indeed, in zebrafish, knockdown of UBA1 is sufficient to induce an SMA-like phenotype (Wishart et al., 2014). The proteasome is also of interest for SMA as SMN degradation is mediated by the ubiquitin proteasome system (UPS) (Chang et al., 2004) and inhibiting proteasome function has been shown to increase SMN levels, rendering this a potential therapeutic target (Kwon et al., 2011). Furthermore, the deubiquitylase Usp9x associates with and stabilises the SMN complex through interaction with SMN, which it deubiquitylates. Usp9x does not, however, deubiquitylate and stabilise the truncated SMN protein produced by *SMN2*, which is therefore rapidly degraded (Han et al., 2012).

Disrupted energy homeostasis and alterations of mitochondrial function have also been implicated in SMA. For example, SMN reduction in NSC34 cells and motor neurons leads to depletion of ATP levels (Acsadi et al., 2009; Miller et al., 2016). Mitochondrial trafficking and morphology are also altered in iPSC-derived motor neurons from SMA patient fibroblasts (Xu et al., 2016). Importantly, impaired mitochondrial biogenesis has also been seen in skeletal muscle biopsies from SMA patients (Ripolone et al., 2015). Moreover, motor neuron vulnerability in SMA correlates with the bioenergetic profile of the motor neurons. More vulnerable motor neuron pools have reduced transcript levels of *Pgk1* which encodes the glycolytic enzyme phosphoglycerate kinase 1 (PGK1). Interestingly, knockdown of *pgk1* is sufficient to mimic the SMA phenotype in wild-type zebrafish (Boyd et al., 2017). Overall, this indicates that reduced SMN leads to disruption of multiple cellular pathways beyond RNP formation and RNA processing.

The identification of these novel cellular and molecular functions of SMN indicates the broad role for SMN in the pathogenesis of SMA and in motor neuron biology. Clearly, these studies show that the cellular and molecular pathways disrupted on SMN depletion extend beyond the canonical role of SMN in snRNP formation. These insights also open-up the possibility of developing SMN-independent therapies for the treatment of SMA.

1.1.5 SMA is a multisystem disorder

Regardless of whether therapies being developed for SMA are SMN-dependent or SMN-independent, one key element of any successful therapy is the ability to deliver it to the cells, tissues and organs that are most affected in the disease. In the case of SMA, the main pathological target is alpha motor neurons (Powis and Gillingwater, 2015): ~25-30% of lower motor neuron cell bodies are lost from the spinal cord of late symptomatic SMA mice (Monani et al., 2000). This selective loss of lower motor neurons is present in all human patients (Dubowitz, 2009). However, neuromuscular pathology is apparent before the overt loss of motor neuron cell bodies occurs in SMA models (McWhorter et al., 2003; Murray et al., 2008) and importantly, NMJ defects are present in SMA patients (Hamilton and Gillingwater, 2013; Wadman et al., 2012). The neuromuscular system appears to develop relatively normally in SMA mice, but early in the disease, structural and functional defects are seen in both nerve and muscle (McGovern et al., 2008; Murray et al., 2010). These include early pathological changes at the NMJ, such as nerve terminal loss, synaptic accumulation of neurofilament proteins, and defective maturation of acetylcholine receptor clusters (Cifuentes-Diaz et al., 2002; McGovern et al., 2008; Murray et al., 2010). Alongside these early changes in distal extremities of motor neurons, intrinsic defects have been reported in skeletal muscle, including smaller myotubes as well as reduced proliferation, fusion defects of myoblasts and increased cell death (Martinez-Hernandez et al., 2009; Shafey et al., 2005). These pathological changes in muscle occur independently of neuron degeneration and correlate with SMN reduction in model systems (Boyer et al., 2013; Martinez-Hernandez et al., 2009; Murray et al., 2008; Shafey et al., 2005).

Aside from lower motor neurons, low SMN levels also affect other cell types that reside within the nervous system. For example, a defective myelination phenotype has been observed in the peripheral nervous system where the maturation of axo-glial interactions at paranodes was disrupted in SMA mice; the myelin sheaths were also thinner and there was an increase in the number of large diameter unmyelinated axons. These phenotypes were due to intrinsic defects in Schwann cells in mouse models of SMA (Aghamaleky Sarvestany et al., 2014; Hunter et al., 2014; Hunter et al., 2016). Altered function of astrocytes has also been implicated in SMA pathogenesis whereby defects in contact interactions between motor neurons and astrocytes leads to impaired synaptogenesis (Rindt et al., 2015; Zhou et al., 2016). SMA astrocytes also showed increased production and secretion of microRNAs (Sison et al., 2017) suggesting that the defects in astrocytes, like those in Schwann cells, are cell autonomous and not a result of motor neuron pathology in SMA. Furthermore, pathological changes have been reported in the thalamus, cerebral cortex, brainstem and dorsal root ganglia in severe cases of SMA (Harding et al., 2015). In severe mouse models of SMA, the low levels of SMN have also been shown to impair neurogenesis and disrupt cell proliferation leading to abnormal hippocampal development (Wishart et al., 2010).

Alongside pathological changes in the nervous system and skeletal muscle, defects in peripheral tissues and organs including the heart, pancreas and blood vessels have also been reported in SMA patients (Hamilton and Gillingwater, 2013; Harding et al., 2015; Sintusek et al., 2016; Somers et al., 2015). For example, in SMA type 1 patients, septal defects and structural abnormalities of the cardiac outflow tract are relatively common, while cardiac rhythm disorders are more common in patients with milder SMA (Wijngaarde et al., 2017). Vascular defects have also been reported in severe SMA patients including distal digital necrosis and vascular depletion in skeletal muscle (Hamilton and Gillingwater, 2013; Somers et al., 2015). Interestingly, the extent of vasculature in mid-symptomatic SMA mice was reduced by 50% compared to control mice leading to significant functional hypoxia of the spinal cord in SMA (Somers et al., 2015).

There have also been several recent studies implicating defects of the immune system in SMA. These phenotypes include impaired T-cell development in the thymus and an almost complete absence of B-cells in the spleen; both organs also show structural differences and increased cell death in mouse models of SMA (Deguise and Kothary, 2017; Thomson et al., 2017). Studying mouse models of SMA has also revealed developmental failure of the liver in SMA mice (Szunyogova et al., 2016). Along with the reported defects in bone and the identification of clot-like accumulations in hearts from SMA mice (Hamilton and Gillingwater, 2013; Szunyogova et al., 2016), this suggests that disruption to normal hematopoiesis may also occur in SMA. Abnormalities in the intestine and lungs have also been reported in mouse models of SMA (Hamilton and Gillingwater, 2013). Taken together these findings demonstrate that low levels of SMN in SMA lead to multisystem phenotypes with organ systems, tissues and specific cell types showing a broad spectrum of vulnerability.

One working hypothesis to explain the presence of extra-neuronal pathology in SMA is the 'threshold hypothesis' where differential thresholds for low SMN levels exist in different cell types, with motor neurons being most vulnerable in SMA due to their exceptional sensitivity to low levels of SMN (Hamilton and Gillingwater, 2013; Sleigh et al., 2011). Although extra-neural phenotypes may often manifest at the subclinical level in SMA patients, they are becoming of increasing importance as therapies prolonging a patient's survival run the risk of unmasking disorders of other organ systems. Moreover, several studies have shown that restoring SMN in motor neurons or skeletal muscle alone is insufficient to correct disease pathology in SMA mice and that peripheral SMN restoration is likely to be essential for long-term rescue of SMA (Hua et al., 2015; Hua et al., 2011). Overall, these findings suggest that any successful therapy for SMA will need to target not only motor neurons and skeletal muscle, but also more widespread, systemic pathology.

1.1.6 Therapeutic advances for SMA

Due to the clear monogenic cause of ~95% of cases of SMA and the robust animal models available to study the disease, therapy development has been at the forefront

of SMA research. Until recently, palliative care options to assist with management of symptoms and prevention of complications were the only option for patients with SMA. Excitingly, however, the first therapy for SMA has recently been approved. There are also several other therapies at advanced stages of clinical trials and in pre-clinical development. Given the central role that SMN plays in the disease, it is not surprising that the most clinically advanced therapies for SMA are targeted at increasing SMN protein levels. However, there are also SMN-independent therapies currently in clinical trials - mainly neuroprotective factors or muscle strength-enhancing compounds - and several therapies currently in development in animal models of SMA targeting pathways affected downstream of SMN.

1.1.6.a SMN-targeted therapies

The recently approved treatment for SMA, Spinraza, is an antisense oligonucleotide (ASO). Several ASOs have been developed that are directed against sequences that inhibit the inclusion of *SMN2* exon 7 (Singh et al., 2017). The binding of ASOs to this regulatory motif prevents the binding of repressor factors which in turn promotes the inclusion of exon 7, thereby increasing the amount of full-length SMN protein produced by *SMN2* (Keil et al., 2014; Singh et al., 2006). Spinraza is at the forefront of these ASO-based therapies and has been approved for treatment of all types of SMA in Europe and the USA. A subgroup of type 1 SMA patients show substantial improvements in motor function following treatment with Spinraza; however not all patients respond in the same manner with more modest effects reported for other type 1 SMA patients (Chiriboga et al., 2016; Finkel et al., 2016). Currently, treatment with Spinraza requires repeated administration via intrathecal injection which is expensive and adds considerable burden for patients. A second generation of ASOs for treatment of SMA are currently under development which might overcome the current disadvantages by allowing less invasive delivery routes and improving efficacy (Hammond et al., 2016).

There are other strategies, several of which are currently in clinical trials, aimed at increasing SMN protein levels. One of these is based around small molecules that modify *SMN2* splicing and increase SMN levels. After promising

results from screens in rodent and cell models of SMA, studies taking this more traditional pharmacological approach (including RG7916 and branaplam [formerly LMI070]) are currently in clinical trials (Naryshkin et al., 2014), with initial reports suggesting some benefit (Chamas., 2017; Mercuri, 2017). Other small molecule strategies to increase the levels of SMN protein include the use of histone-deacetylase inhibitors such as Valporic acid, however, clinical trials for this approach have been disappointing (Kissel et al., 2014; Krosschell et al., 2017).

Another strategy aimed at increasing SMN protein levels currently in clinical trials, is gene therapy to replace the faulty *SMN1* gene. Promising pre-clinical data from animal models showed that adeno-associated virus (AAV) mediated *Smn* gene replacement resulted in widespread expression of SMN in the spinal cord and significantly increased survival of SMA model mice (Dominguez et al., 2011; Foust et al., 2010; Passini et al., 2010; Valori et al., 2010). In the ongoing phase 1 gene therapy clinical trial, *SMN1* within a self-complimentary adeno-associated virus serotype 9 (scAAV9) vector is being delivered intravenously to type 1 SMA patients. This initial clinical trial is evaluating both the safety and efficacy of the treatment in the small group of infants enrolled in the study (Mendell, 2017). Although a detailed report of this study has yet to be released, initial results from this trial are so far very promising (Mendell, 2017). The one dose administration method for this therapy also makes it an attractive therapeutic approach, however, as viral gene therapy is not commonly used in clinical practice there are logistical problems to overcome if the therapy were to become widely available and there would need to be long-term health monitoring to check the safety of the treatment.

Regardless of the technological approach used to increase SMN levels, the ‘therapeutic time-window’ within which therapy must be delivered to have a maximal effect needs to be considered. Several studies have indicated that SMN is required at early stages of development and that sufficient SMN levels are essential for NMJ maturation during the early post-natal period (Chang et al., 2015; Iyer et al., 2015; Kariya et al., 2014). It has also been demonstrated that late stage *Smn* gene replacement using scAAV9 failed to ameliorate NMJ defects, while pre-symptomatic delivery of scAAV9-Smn resulted in near complete rescue of the SMA phenotype in

mouse models (Robbins et al., 2014). Together, these studies indicate that treatment using SMN-enhancing therapies will need to occur before overt symptoms are apparent for a full restoration of the SMA phenotype.

Indeed, there is now a move towards pre-symptomatic diagnosis of SMA by inclusion of real-time PCR genotyping assay for *SMN1* on routine newborn screening panels of dried blood spot. By confirming this initial assay with a multiplex ligation-dependent probe amplification (MPLA) assay, a study identified 7 asymptomatic SMA patients over a two-year period (Chien et al., 2017). Thus, this strategy would enable genetic diagnosis of SMA and therapy administration before the onset of overt symptoms, when the treatment is most likely to give the greatest benefit to the patient.

1.1.6.b SMN-independent therapies

While the first-generation of SMN-dependent therapies progress through the clinical trial process there are several second-generation SMN-independent therapies currently in pre-clinical and clinical development. The most clinically-advanced of these are centred around administering neuroprotective factors, or enhancing muscle strength. Olesoxime is one potential neuroprotective factor which exerts its neuroprotective effects by binding to components of the mitochondrial permeability pore (Sunyach et al., 2012). Phase 2 clinical trials for type 2 and non-ambulatory type 3 SMA patients indicated that olesoxime is safe and leads to a maintenance of motor function (Bertini et al., 2017).

Several drugs in trials to improve muscle strength in SMA have previously been approved for other disorders involving weakness of the neuromuscular system. These include pyridostigmine which is in clinical trials for SMA types 2, 3 and 4, and 4-Aminopyridine, in trials in ambulatory SMA patients. Both these therapies are being assessed for their endurance-enhancing properties and their effect on reducing fatigability in SMA patients. Novel compounds to treat neuromuscular dysfunction, muscular weakness and muscle fatigue are also in development for SMA. For example, CK-2127107, a fast skeletal muscle troponin complex activator, is currently in Phase 2 clinical trials following safe pharmacokinetic and pharmacodynamics

findings in Phase 1 trials (Hwee et al., 2015). Similarly, SRK-015 is an inhibitor of myostatin that has been shown to improve muscle function in SMA mice and is due to enter clinical trials for SMA in 2018 (ScholarRock, 2017).

1.1.6.c Targeting pathways affected in SMA

Other SMN-independent therapies at early stages of development follow on from recent advances in the understanding of cellular and molecular pathways dysregulated downstream of SMN reduction in SMA (see 1.1.4.b and 1.1.4.c) and aim to target these pathways. For example, members of the Rho-kinase (ROCK) pathway have become attractive therapeutic targets due to their known potential to modulate axon outgrowth and growth cone motility. Although targeting downstream effectors of ROCK did not rescue phenotypes in mouse models of SMA (Bowerman et al., 2009), inhibiting ROCK did lead to positive outcomes (Bowerman et al., 2010; Bowerman et al., 2012). Both Fasudil and Y-27632 inhibit ROCK and resulted in an increase in the survival of SMA mice and improved NMJ maturation and muscle fibre size (Bowerman et al., 2010; Bowerman et al., 2012). Although toxicity was associated with Fausidil at high doses and motor neuron cell death was not reduced, the increase in survival points towards the importance of targeting muscle in SMA treatment strategies (Bowerman et al., 2010; Bowerman et al., 2012).

The ubiquitin-proteasome system has also been highlighted as a potentially attractive therapeutic target for SMA. For example, inhibiting the chymotrypsin-like activity of the 26S proteasome using bortezomib increased SMN levels in peripheral tissues of SMA mice, improved motor function and increased survival (Kwon et al., 2011). When SMA mice were treated with a combinatorial therapy of bortezomib and trichostatin A, a histone deacetylase inhibitor that increases SMN protein levels, the improvements observed across all aspects of the SMA phenotype were greater than when mice were treated with only one therapy (Kwon et al., 2011). This study therefore provides a proof-of-principle that combinatorial therapies targeting SMN and SMN-independent pathways in SMA may represent a viable therapeutic approach. However, due to toxicity issues associated with using available proteasome inhibitors, including bortezomib, specifically targeting the ubiquitylation

of SMN may be a more suitable therapeutic approach and may lead to a reduction in the non-specific effects associated with targeting the proteasome (Groen and Gillingwater, 2015). Indeed, it has recently been identified that the compound ML372 selectively inhibits the ubiquitylation of SMN and has no effect on the 20S catalytic activity of the proteasome. Administration of this compound to SMA mice increased SMN protein levels in muscle, brain and spinal cord, and improved motor function and survival of SMA mice (Abera et al., 2016).

Alongside evidence suggesting that targeting SMN protein stability via the UPS may be an attractive therapeutic approach for SMA, recent experiments have demonstrated that UBA1, a key E1 ubiquitin-activating enzyme required for UPS function, is a major downstream target of SMN (Fuller et al., 2015; Wishart et al., 2014). SMN-induced reduction of UBA1 levels in SMA leads to disruption of UBA1-dependent targets, such as an accumulation of beta-catenin (Wishart et al., 2014). Experiments in SMA animal models targeting these UBA1-dependent pathways have demonstrated improvements in neuromuscular phenotypes, suggesting that these pathways are amenable to therapeutic intervention (Powis et al., 2016; Wishart et al., 2014).

1.1.6.d Combinatorial therapies

It is possible that combinatorial therapies - treating SMA patients with more than one therapy, each from different strategies - will have the greatest potential to ameliorate the full spectrum of SMA disease phenotypes. Combining SMN enhancement therapies with muscle strength enhancing drugs or neuroprotective factors may help to preserve and strengthen the connections between neurons and muscles. This approach may result in effective treatment of SMA symptoms beyond the therapeutic time-window in which SMN-dependent therapies alone will be effective. It is likely that the first combinatorial therapies to enter the clinic for SMA will be a combination of SMN-dependent therapies and muscle strength enhancing compounds. Indeed, Scholar Rock has announced that they intend to develop SRK-015 in combination with therapies targeting the genetic cause of SMA for clinical trials in SMA patients (ScholarRock, 2017).

While combinatorial therapies may appear attractive from both clinical and scientific perspectives, it may become necessary from a logistical aspect of therapy development for clinical trials to be combinatorial. As more patients are being treated with Spinraza, or are enrolled on clinical trials for other SMN-targeted therapies, the pool of SMA patients with no prior treatment for enrolment on clinical trials will become reduced; thus, rendering combinatorial approaches for second generation therapies necessary at the clinical trial level, at least for more severe forms of SMA.

Alternative combinatorial therapeutic approaches include combining therapies to enhance *SMN* gene transcription with treatments to reduce SMN degradation (see 1.1.6.c). Or alternatively, combining therapies that target genetic modifiers or downstream pathways in SMA with SMN-dependent therapies. These approaches have the benefit of a possible dose reduction of the SMN enhancing agent, which may help to reduce toxicity and increase efficacy (Kwon et al., 2011). To study such combinations of therapies, intermediate mouse models of SMA have been generated by administering suboptimal doses of SMN-targeted ASOs, thereby recapitulating the situation in SMA patients for which SMN-targeted therapies do not completely rescue their symptoms (Zhou et al., 2015). Early pre-clinical, combinatorial therapy experiments using such mouse models have shown promising results. For example, by increasing PLS3 expression there was a significant improvement in survival and improvement of motor function compared to treatment with the SMN-targeted ASO alone (Hosseinibarkooie et al., 2016; Kaifer et al., 2017). Interestingly, this therapy also restored defects in endocytosis seen in SMA (Hosseinibarkooie et al., 2016). Similarly, combination of suboptimal SMN-targeted ASOs and down-regulation of NCALD improved a range of neuromuscular phenotypes in the SMA mice (Riessland et al., 2017).

Importantly, the studies described here provide a proof-of-concept that combinatorial therapies are a promising therapeutic approach for the next generation of SMA therapies. While it is likely that the first clinical combinatorial therapies will be a combination of SMN-targeted therapies and muscle strength enhancing drugs, due to the multisystem defects in SMA and the range of pathways disrupted in this disease, it may prove more beneficial to target SMN and correct downstream

pathways that are disrupted in SMA. This may be of particular importance in severe SMA patients and may be especially beneficial when targeting pathways known to be disrupted pre-symptomatically in SMA models and patients. One such candidate that would merit being tested in a combinatorial approach is UBA1. While it is known that UBA1 is a key downstream target of SMN and that therapies targeting UBA1 rescue neuromuscular phenotypes across a range of SMA models (Powis et al., 2016; Wishart et al., 2014), the mechanism by which UBA1 mediates degeneration in SMA is unknown.

1.2 Ubiquitin-like modifier activating enzyme 1

The ubiquitin-like modifier activating enzyme 1 (UBA1) is a promising therapeutic target for combinatorial therapy of SMA. UBA1 is the ubiquitin activating enzyme at the apex of the ubiquitin conjugation process and its role in this process is well characterised. Interestingly, UBA1 has also been shown to be important for neuronal homeostasis and has been implicated in a wide range of neurodegenerative conditions.

1.2.1 UBA1 and the ubiquitin proteasome system

As previously mentioned, UBA1 is responsible for activating ubiquitin in the ubiquitin proteasome system (UPS). In this process, the active adenylation domain of UBA1 binds Mg^{2+} and ATP to catalyse the binding with ubiquitin (Figure 1-2). This complex is then stabilised by the inactive adenylation domain of UBA1 (for domain organisation of UBA1 see Figure 1-3) (Lee and Schindelin, 2008). AMP is then released allowing the formation of a high-energy thioester bond between the carboxyl terminus of ubiquitin and the reactive cysteine (C632) of UBA1 (Figure 1-2). In another Mg^{2+} and ATP dependent reaction a ternary complex is formed, consisting of the UBA1-ubiquitin thioester with another molecule of ubiquitin-AMP bound (Bedford et al., 2011; Haas et al., 1982). This favourable conformation of the UBA1-ubiquitin complex enables a transthiolation reaction to occur, resulting in the thioester bound ubiquitin being transferred to an E2 conjugating enzyme, again forming a thioester bond (Schulman and Harper, 2009). UBA1 then forms a thioester bond with the second ubiquitin, again releasing AMP, thus activating this ubiquitin molecule (Figure 1-2). Formation of a ternary complex again allows the transfer of the activated ubiquitin to an E2 enzyme and in this manner the ubiquitin activation cycle continues (Bedford et al., 2011).

Once the activated ubiquitin is bound to an E2 conjugating enzyme, the E2 can then bind an E3 ligase enzyme which is typically already bound to a protein substrate; therefore, allowing the transfer of ubiquitin to an acceptor lysine residue on the substrate (Figure 1-2) (Bedford et al., 2011). This process may continue

leading to the formation of polyubiquitin chains on the protein substrate (Ye and Rape, 2009). In some situations, an E4 enzyme may also be involved in the elongation of ubiquitin chains (Ciechanover and Brundin, 2003). If the polyubiquitin chain is formed by linking ubiquitin molecules at K48, on release from the E3 ligase enzyme the proteasome recognises the substrate for degradation. If the substrate is monoubiquitylated or polyubiquitylated using different ubiquitin lysine sites, on release from the E3 ligase the ubiquitylation on the protein substrate will signal for different functions of the substrate such as enzyme activation, signalling and protein trafficking (Figure 1-2) (Kulathu and Komander, 2012; Ye and Rape, 2009). Finally, deubiquitylating enzymes remove ubiquitin moieties from protein substrates (Figure 1-2) (Ciechanover and Brundin, 2003) and so may alter the function of the substrate or prevent its degradation by regulation of the ubiquitin modifications. Therefore, through activation of ubiquitin at the outset of this conjugation process, UBA1 can influence a range of downstream pathways through its canonical function.

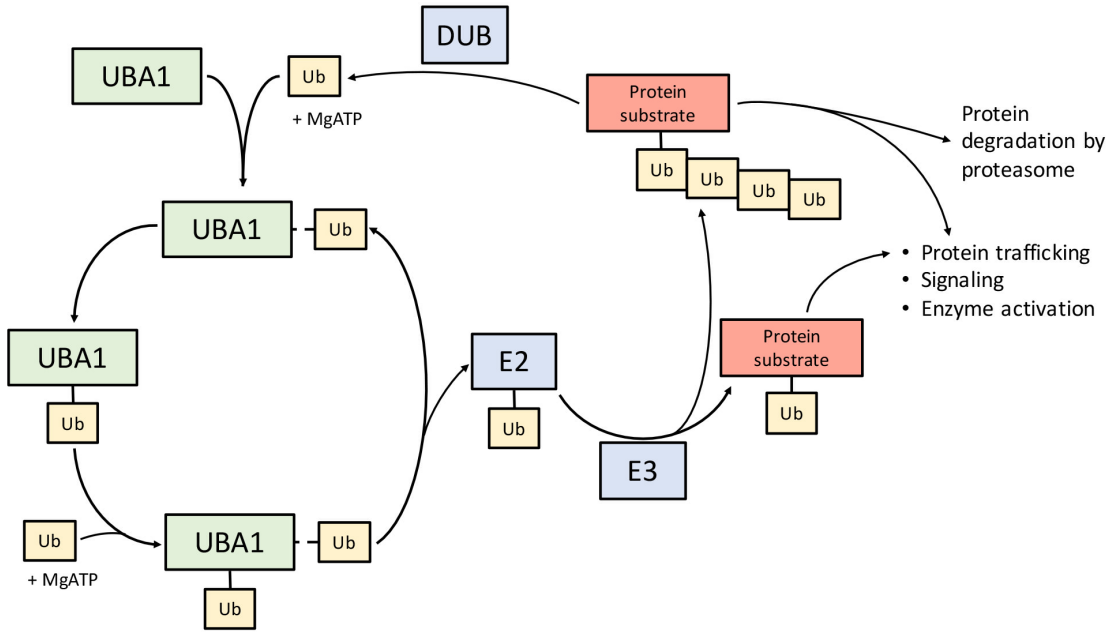

Figure 1-2 The ubiquitin conjugation pathway

Overview of the ubiquitin conjugation pathway leading to protein degradation or altered function of the substrate protein. Ub: ubiquitin; UBA1: Ubiquitin-like modifier activating enzyme 1; E2: E2 ubiquitin conjugating enzymes; E3: E3 ubiquitin ligase enzymes; DUB: deubiquitylating enzymes. E2, E3 and DUB enzymes have different specificities for the

enzymes in the pathway and the protein substrates. Solid lines represent thioester bonds, dashed lines represent ubiquitin-AMP bound to UBA1.

1.2.2 UBA1 and neuronal homeostasis

Neurons are very specialised cells with specific needs for local translation and degradation to maintain cellular homeostasis and normal functioning. With the UPS having key roles in these processes, it is unsurprising that the UPS is required for many different aspects of pre-and postsynaptic development and function (Deglincerti et al., 2015; Jiang et al., 2010). For example, inhibition of the proteasome prevents a reduction in the number of readily releasable vesicles at active synapses. This in turn prevents the induction of persistent presynaptic silencing and so inhibition of the proteasome interferes with adaptive plasticity of hippocampal neurons (Jiang et al., 2010). The UPS was also shown to be important for the response of growth cones to axonal guidance cues. RhoA is one example of a transcript that is locally translated in response to axon guidance cues. In growth cones there are high levels of ubiquitylation of RhoA which lead to its degradation (Deglincerti et al., 2015). Similarly, the main targets of ubiquitylation in the growth cone are newly synthesised, locally translated proteins, suggesting that UPS activity is required for efficient responses to both attractive and repulsive axon guidance cues during neuronal development (Deglincerti et al., 2015).

Not surprisingly, as UBA1 is a key component of the UPS, specific requirement of UBA1 itself has been shown to be necessary for development and maintenance of neuronal function. For instance, inhibition of UBA1 causes an increase in miniature and spontaneous synaptic currents in cultured hippocampal neurons. This occurs at both excitatory and inhibitory synapses indicating that UBA1 may be necessary to regulate the activity state of presynaptic proteins (Rinetti and Schweizer, 2010). Similarly, loss of UBA1 blocks axon pruning during development in *Drosophila*, a process that is mediated by local degeneration (Watts et al., 2003), suggesting that UBA1 is required for normal axonal pruning. Furthermore, UBA1 has also been implicated in the slow Wallerian degeneration (Wld^{s}) phenotype, a mouse model in which axons and synapses are protected from degeneration. One of

the pathways through which this neuroprotection is thought to occur is increased levels of UBA1 with specific changes in the synaptic expression of UBA1 (Wishart et al., 2007; Wishart et al., 2008). Together, these findings reveal an important role for the UPS and, more specifically, for UBA1 in the regulation of a range of cellular and molecular pathways necessary for the maintenance and function of neurons.

1.2.3 Protein homeostasis and UBA1 in neurodegeneration

Given the importance of UBA1 and the UPS in neuron development and function it is not surprising that disruption to protein homeostasis and UBA1 have been identified in a range of neurodegenerative conditions. Many neurodegenerative diseases display a common molecular signature of disruption to protein homeostasis through accumulation of ubiquitylated proteins in aggregates (Rubinsztein, 2006). In several diseases, such as Parkinson's disease (PD), Alzheimer's disease (AD), Huntington's disease (HD) and amyotrophic lateral sclerosis (ALS), there is evidence that these protein aggregates contribute to disease pathogenesis (Arrasate and Finkbeiner, 2012; Blokhuis et al., 2013; Ittner and Gotz, 2011; Lashuel et al., 2013). Disruption of protein homeostasis has also been evidenced in neurodegenerative diseases in the absence of ubiquitylated protein aggregates, for example in SMA (Fuller et al., 2015; Wishart et al., 2014).

Interestingly, mutations in components of the UPS machinery lead to several of these conditions. Mutations in the E3 ligase *PARKIN*, the E3 ligase component *FBXO7* and the deubiquitylating enzyme *UCHL1* are associated with PD (Leroy et al., 1998; Lohmann et al., 2015; Ryan et al., 2015). Similarly, mutations in *UBQLN2* which encodes a protein that targets polyubiquitylated proteins to the proteasome, cause ALS (Deng et al., 2011). Interestingly, motor neuron specific knockout of the proteasome subunit Rpt3 lead to ALS like phenotypes in mice, including aggregation of proteins (Tashiro et al., 2012). It has also been shown that mutations in *Drosophila Uba1* lead to reduced survival and motor impairment, implicating specific dysfunction of UBA1 in neurodegeneration (Liu and Pfleger, 2013).

Indeed, disruption of UBA1 has been observed in several neurodegenerative diseases. For example, UBA1 is an important modifier of polyglutamine protein

toxicity in a HD mouse model, whereby reduction in nuclear UBA1 expression correlates with mutant huntingtin accumulation in Huntington's disease (Wade et al., 2014). Similarly, UBA1 modifies toxicity of a *Tau* mutant in *Drosophila* (Blard et al., 2007) and the activity and expression of UBA1 is reduced in cytosolic fraction of AD patient brain samples (Lopez Salon et al., 2000). Furthermore, UBA1 preferentially binds to ALS-causing mutant fused in sarcoma (FUS) protein but not to wild-type FUS, again suggesting a modifying effect of UBA1 on disease pathogenesis (Wang et al., 2015). Finally, UBA1 has been implicated in the pathogenesis of idiopathic PD as exposure of rodent models to pesticides increased expression of α-synuclein, caused damage to dopaminergic neurons and motor dysfunction; changes that were specifically due to inhibition of UBA1 (Chou et al., 2008; Viquez et al., 2012). Taken together, these studies provide evidence linking altered UBA1 activity or expression with pathogenic events in a range of neurodegenerative diseases. Interestingly, however, spinal muscular atrophy is the neurodegenerative disease with the most evidence implicating UBA1 as a causative factor in disease pathogenesis.

1.2.4 UBA1 in spinal muscular atrophy

UBA1 is implicated in SMA on a number of levels, not least because mutations in *UBA1* cause a rare form of SMA (X-linked SMA) but also because widespread disruption to UBA1 expression has been identified in various models of SMA. Furthermore, as previously mentioned, therapeutically targeting UBA1 or its downstream targets rescues neuromuscular phenotypes in SMA.

1.2.4.a X-linked SMA

Mutations in *UBA1* cause a rare form of SMA known as X-linked SMA (XL-SMA). XL-SMA is clinically similar to SMA and is characterised by loss of lower motor neurons in the anterior horn of the spinal cord, muscle weakness, hypotonia and a lack of reflexes. In addition to these features shared with SMA, congenital contractures and fractures are also commonly associated with XL-SMA (Dlamini et al., 2013; Jedrzejowska et al., 2015; Ramser et al., 2008). Other pathologies seen in

XL-SMA patients include widespread involvement of the sensory neuron system, and developmental and degenerative cerebellar abnormalities (Dlamini et al., 2013). Interestingly, all the mutations identified in *UBA1* that cause XL-SMA cluster in exon 15 of the gene (Figure 1-3) (Dlamini et al., 2013; Jedrzejowska et al., 2015; Ramser et al., 2008). It is possible that these mutations lead to altered methylation patterns of exon 15 with potential implications for blocking transcription enhancers and reducing UBA1 expression (Ramser et al., 2008). However, it so far seems unlikely that mutations in UBA1 cause disruption to either the adenylation activity of UBA1 or its ability to form thioester bonds with ubiquitin.

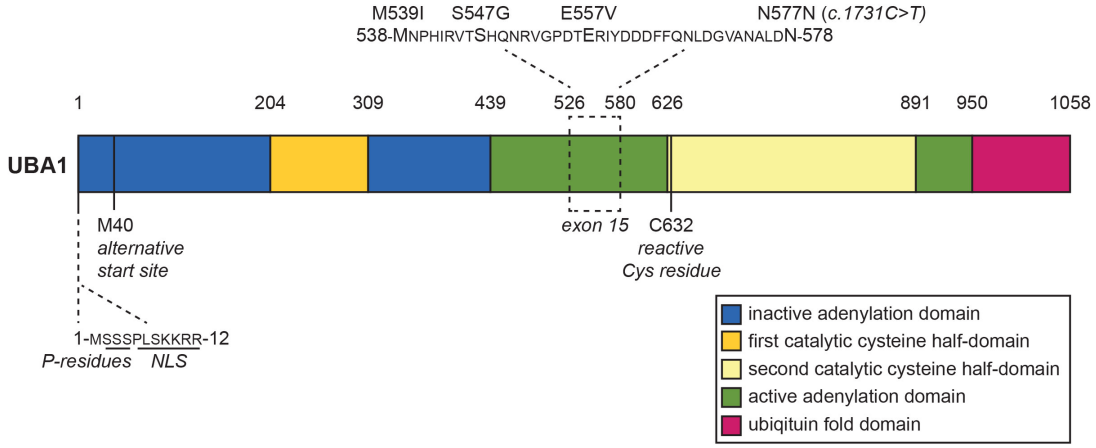

Figure 1-3 Domains of UBA1 and mutations identified in XL-SMA

UBA1 has a methionine residue at position 40 that provides an alternative translation start site leading to the generation of the UBA1b isoform. The full-length transcript produces the UBA1a isoform which contains a nuclear localisation sequence (NLS) and several serine residues which can be phosphorylated (P-residues). Mutations in UBA1 shown to cause XL-SMA cluster in exon 15 of the protein. When UBA1 is folded into its 3D structure, the first catalytic cysteine half-domain and the second catalytic cysteine half-domain are immediately adjacent to each other, as are the inactive adenylation domain and the active adenylation domain. The ubiquitin fold domain allows UBA1 to bind E2 enzymes and the cysteine residue that binds ubiquitin (C632) resides within the second catalytic cysteine half-domain. The specific amino acid domains in this figure are based on the mouse UBA1 sequence. The mouse and human UBA1 sequences are 95% identical at the amino acid level; all amino acids that surround the borders of domains, that are mutated in XL-SMA and that are in the NLS and P-residues are fully conserved between mouse and human UBA1 sequences. Figure adapted from (Groen and Gillingwater, 2015).

1.2.4.b Alterations to UBA1 in SMA

Although XL-SMA is a rare form of SMA, as previously mentioned, it has recently been shown that ubiquitin homeostasis is altered in *SMN1*-dependent SMA. Central to this disruption in ubiquitin homeostasis is a downregulation of UBA1 levels following SMN depletion. It was initially shown that in late-symptomatic severe SMA mice UBA1 levels are reduced by approximately 50% in spinal cord and by more than 60% in skeletal muscle compared to age-matched controls. This was extended to show that in skeletal muscle from early-symptomatic Taiwanese SMA mice UBA1 protein levels were reduced by approximately 30% (Wishart et al., 2014). Subsequently, it has been shown that the time course of UBA1 reduction correlates with disease progression in SMA mice with changes in several organs occurring during pre-symptomatic stages of the disease. These disruptions to UBA1 occurred in spinal cord and muscle along with a range of systemic organs, including heart and liver. Importantly, UBA1 is also significantly reduced in SMA patient-derived iPSC motor neurons compared to control (Powis et al., 2016). Although these reductions in UBA1 have been demonstrated in whole tissues in models of SMA, reduction of UBA1 has also been seen at the single cell level with significant reductions in UBA1 expression occurring in myelinating Schwann cells (Aghamaleky Sarvestany et al., 2014). However, further investigation is required to identify whether UBA1 is reduced in other cell types.

Although little is known about how UBA1 leads to these SMA phenotypes, it has been demonstrated that UBA1 and SMN bind to each other in the cytoplasm (Wishart et al., 2014) and that the ubiquitin proteasome system (UPS) mediates SMN degradation (Chang et al., 2004). Furthermore, reduction in SMN levels leads to alterations in the splicing of *UBA1* (Wishart et al., 2014) suggesting a complex interaction of these proteins involving multiple potential routes. It has also been shown in SMA spinal cord that there is a significant increase in beta-catenin levels (Wishart et al., 2014), a known downstream target of ubiquitylation. This suggests that altered function of the downstream targets of UBA1 could be contributing to UBA1-mediated degeneration in SMA. Interestingly, suppression or pharmacological inhibition of UBA1, induces an SMA-like neuromuscular phenotypes in zebrafish

(Wishart et al., 2014) and similarly, it has been shown that pharmacological inhibition of UBA1 in Schwann cells leads to a defective myelination phenotype that is observed in SMA (Aghamaleky Sarvestany et al., 2014; Hunter et al., 2014). Together this suggests that decreased UBA1 levels alone are sufficient to induce neurodegeneration.

1.2.4.c Therapeutic strategies targeting UBA1

Initial therapeutic strategies to target defective ubiquitin homeostasis focused on the known downstream targets of UBA1. Treatment with an inhibitor of beta-catenin signalling (quercetin) was sufficient to rescue the motor axon branching phenotypes seen in both SMA zebrafish and zebrafish treated with a UBA1 inhibitor. Similarly, treatment of SMA mice with quercetin increased motor neuron number in the spinal cord, rescued muscle fibre diameter, improved motor function and increased innervation of NMJs (Wishart et al., 2014).

Therapies targeted directly at UBA1 also had beneficial effects on neuromuscular phenotypes in SMA models. For example, co-injection of human *UBA1* mRNA with *Smn* morpholino in zebrafish rescued the motor axon branching phenotype and improved motor behaviour compared to zebrafish injected with *Smn* morpholino (Powis et al., 2016). Likewise, treatment of SMA mice with AAV9-UBA1 increased weight and survival compared to untreated SMA mice. The SMA mice treated with AAV9-UBA1 also showed rescue of neuromuscular, heart and liver pathology. There was an increase in the number of motor neuron cell bodies in the spinal cord, an increase in muscle fibre diameter and rescue of NMJ innervation in AAV9-UBA1 treated SMA mice compared to untreated SMA mice (Powis et al., 2016). Taken together these pre-clinical therapeutic trials indicate that UBA1 and ubiquitin homeostasis is amenable to therapeutic intervention and a viable strategy to treat SMA.

1.3 Summary

The first disease modifying therapy has recently been approved for treatment of all types of SMA. This treatment is designed to augment full-length SMN protein levels, as are several other therapies currently in clinical trial for SMA. However, there is a second wave of SMN-independent therapies in development that target cellular and molecular pathways dysregulated downstream of SMN reduction in SMA. One of the promising SMN-independent therapeutic strategies for SMA is targeting defective ubiquitin homeostasis. Central to the alteration of ubiquitin homeostasis in SMA is a reduction of the ubiquitin-like modifier activating enzyme 1. UBA1 is responsible for activating ubiquitin as the first step in the ubiquitin conjugation process, marking unwanted proteins for degradation by the proteasome. While it is known that therapies targeting UBA1 rescue neuromuscular phenotypes in SMA models, the mechanism by which UBA1 mediates neurodegeneration is unclear.

1.4 Aims

Based on the current literature, to understand the cellular and molecular mechanisms underlying UBA1-mediated pathogenesis of SMA and investigate the hypothesis that UBA1 is a key regulator of neuropathological changes in SMA via modulation of novel pathways, this thesis will address the following aims:

1. Investigate whether UBA1 is specifically disrupted within motor neurons during disease pathogenesis in SMA.
2. Identify and validate novel downstream targets of UBA1.
3. Investigate whether downstream targets of UBA1 are relevant for UBA1-mediated pathogenesis of SMA.

Chapter 2 Materials and Methods

2.1 Ethics statement

All experimental procedures were conducted in accordance with UK Animals (Scientific Procedures) Act 1986. Animal procedures and breeding were approved by a University of Edinburgh internal ethics committee and performed in accordance with institutional guidelines and Home Office regulations under project licence number 6004569 and personal licence number I4AFF2A01.

2.2 Mouse model and *in vivo* experiments

2.2.1 Taiwanese SMA mouse model and colony maintenance

Taiwanese SMA mice (Hsieh-Li et al., 2000; Riessland et al., 2010), on a congenic FVB background, were originally obtained from Jackson Laboratories (Jackson Laboratories strain no. 005058) and maintained according to breeding protocols as previously described (Riessland et al., 2010). The Taiwanese SMA mouse colony was maintained as two separate strains that were bred together to generate SMA mice and control littermates (Figure 2-1A). The first strain was maintained by breeding wild-type FVB mice (obtained from University of Edinburgh breeding stocks) with mice heterozygous for *Smn* (referred to as Thet mice: $Smn^{+/-}$). This produced homozygous $Smn^{+/+}$ mice and Thet mice ($Smn^{+/-}$). Mice with these genotypes were phenotypically normal. $Smn^{+/-}$ mice generated in these breeding pairs were used for further breeding (Figure 2-1A).

The second strain of mice was referred to as Thom and were bred to maintain a homozygous deletion of *Smn* (HRTP knock-out of *Smn* exon 7) and four copies of the human *SMN2* transgene ($Smn^{-/-}$; $SMN2^{tg/tg}$; Figure 2-1A) (Hsieh-Li et al., 2000). Thom mice show a mild phenotype of distal necrosis of the tails and ears and in some cases, older mice develop scoliosis. To generate experimental mice, breeding pairs were set up using male Thet and female Thom mice. The offspring from these breeding pairs were either SMA mice ($Smn^{-/-}$; $SMN2^{tg/0}$) or phenotypically normal heterozygous ($Smn^{+/-}$; $SMN2^{tg/0}$) littermates that were used as controls. Both SMA

and control mice have two copies of the human *SMN2* transgene (Figure 2-1A) (Hsieh-Li et al., 2000). For all mice used in this study the day of birth was counted as postnatal day 1 (P1) following standard protocol in the lab.

Wild-type FVB mice were maintained alongside the SMA mouse colony: wild-type FVB mice were obtained from University of Edinburgh breeding stocks and bred together or with *Smn*$^{+/+}$ mice obtained from Thet breeding pairs (Figure 2-1B). Wild-type CD1 and C57BL/6J mice were obtained from in-house breeding stocks. Throughout this thesis, mice with the genotype *Smn*$^{+/-}$*; SMN2*$^{tg/0}$ will be referred to as control mice, wild-type FVB mice will be referred to as FVB and other wild-type strains used will be referred to by their background strain. All mice were maintained under standard specific pathogen free conditions at the University of Edinburgh.

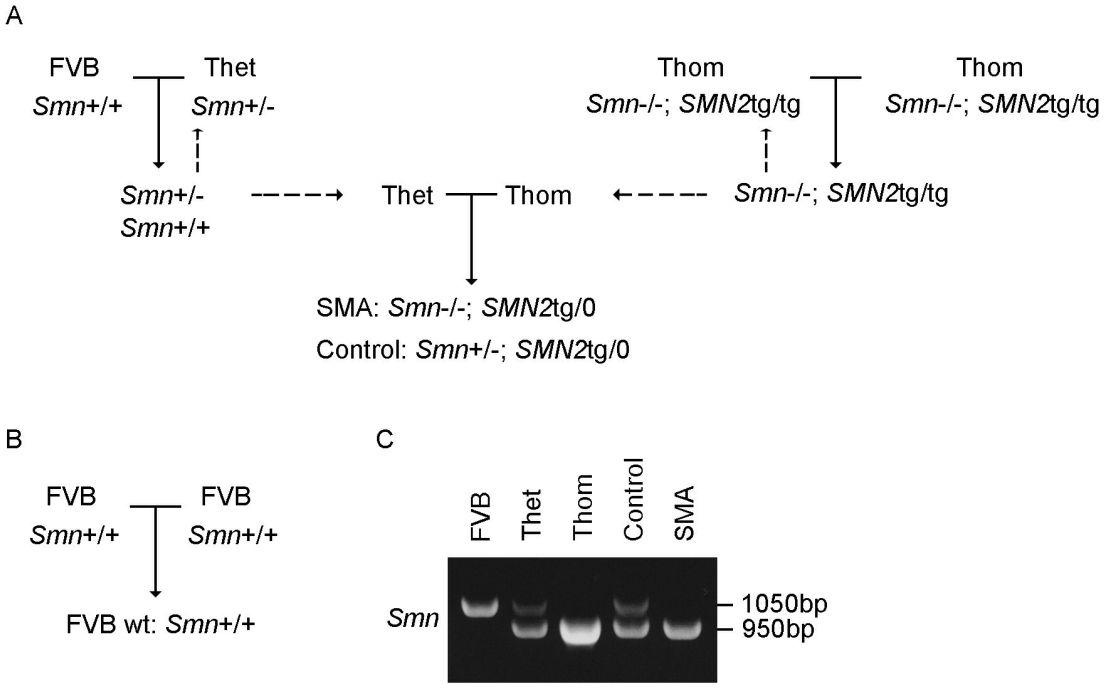

Figure 2-1 Breeding scheme and example genotypes of Taiwanese SMA mice
A Breeding scheme of Thet and Thom mouse line maintenance and generation of experimental SMA and control mice. **B** Breeding scheme showing maintenance of wild-type FVB mice used in this study. **C** Example *Smn* genotyping for all mice used in these breeding schemes: FVB, Thet, Thom, control and SMA. 1050bp band corresponds with the *Smn*$^{+}$ allele and the 950bp band represents the *Smn*$^{-}$ allele.

2.2.2 Genotyping

For DNA extraction, 500µl of lysis buffer (100mM Tris pH 8, 200mM NaCl, 5mM EDTA pH 8, 0.2% SDS in ddH_2O) containing 2.5µl Proteinase K (Life Technologies) was added to ear punches or tail tips which were then left to digest overnight at 55°C. Samples were then mixed by vortex and centrifuged for 15 minutes at 14,000 rpm. DNA was precipitated by pouring the supernatant into 500µl of isopropanol and mixed by inversion until a white precipitate formed. The samples were then centrifuged for 5 minutes at 14,000 rpm to pellet the DNA and washed twice with 1ml of 70% ethanol with a 30 seconds spin at 14,000 rpm after each wash. DNA pellets were then dried for a minimum of 30 minutes and dissolved in 200µl (tail tips) or 50µl (ear punches) of deionised water for at least 1 hour. Following this, multiplex PCR was performed using the following primers for *Smn* (Sigma Aldrich), PCR product size and allele indicated in brackets:

Forward:	ATAACACCACCACTCTTACTC	
Reverse 1:	GTAGCCGTGATGCCATTGTCA	(1050bp: Smn^+)
Reverse 2:	AGCCTGAAGAACGAGATCAGC	(950bp: Smn^-)

PCR master mix, per reaction, for genotyping *Smn* was as follows (all reagents Promega):

3µl 5x green Taq buffer
0.9µl $MgCl_2$
0.15µl dNTPs
0.2µl Taq DNA polymerase
1.5µl 10µM Forward *Smn* primer
1µl 10µM Reverse 1 *Smn* primer
1µl 10µM Reverse 2 *Smn* primer
6.25µl ddH_2O

For each sample, 1µl of DNA was added to the master mix to generate a total reaction mixture volume of 15µl. Amplification was then performed using the following program on a T100 BIO-RAD thermo cycler:

Step:	1	2	3	4	5	6
Temp:	**94°C**	**94°C**	**58°C**	**72°C**	**72°C**	**12°C**
Time:	3 min	30 secs	30 secs	30 secs	5 mins	hold
		36 cycles of steps 2 to 4				

PCR products were then separated by gel electrophoresis using 1% agarose (Scientific Laboratory Supplies) in 1x TAE (diluted from 10x UltraPure TAE; Life Technologies) gels containing SYBR safe DNA gel stain (Life Technologies). Genotypes were determined based on the presence or absence of the 1050bp and 950bp bands. For reference, *Smn* genotypes for all mice used to maintain the Taiwanese SMA mouse colony have been included (Figure 2-1C).

2.2.3 Phenotypic characterisation of SMA mice

Before control and SMA mice were sacrificed for tissue harvesting, weight was determined and motor performance was assessed. A righting test was performed to assess motor ability in the neonatal mice. The righting test is a commonly used simple assay in which mice are placed on their back on a flat surface and the time taken for the mice to turn over and place all four paws on the surface is recorded (Feather-Schussler and Ferguson, 2016). If a mouse did not respond within 30 seconds the test was terminated.

Representative control and late-symptomatic SMA mice as used throughout this thesis are shown in Figure 2-2A, illustrating a typical smaller appearance in SMA compared to control littermates. Representative weights and righting times for control and SMA mice in this colony have also been included (Figure 2-2B, C). The weight of SMA mice at postnatal day 5 (P5) begins to decline while the weight of control mice continues to increase (Figure 2-2B). This corresponds with the time point at which righting times begin to increase in SMA mice compared to control (Figure 2-2C). Furthermore, the onset of symptoms starts to become visibly apparent at P5. Therefore, throughout this study, P5 mice will be used as an early-symptomatic stage of disease progression, while P2 and P8 mice will be used as pre- and late-symptomatic stages of disease respectively.

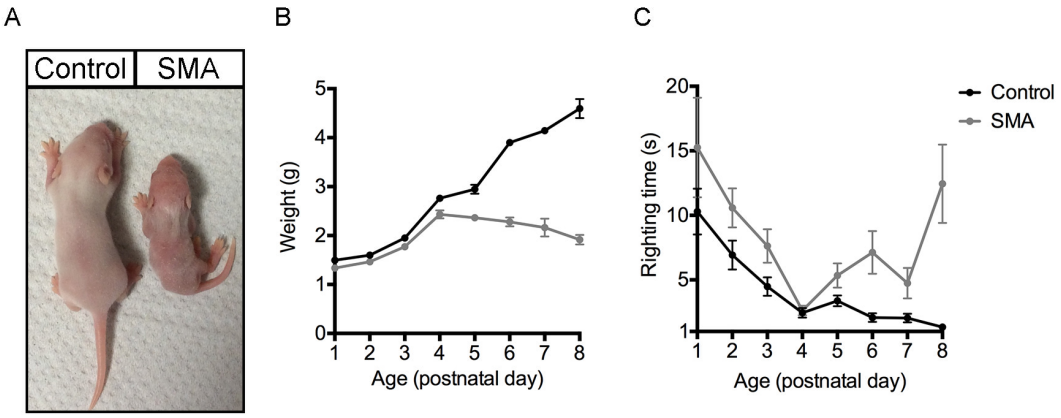

Figure 2-2 Phenotypic characterisation of SMA and control mice

A Control (left) and SMA (right) mice at P8 (late-symptomatic) showing smaller size of the SMA mouse and indicating the motor defects and weakness of the SMA mouse as its back legs are out to the side. **B** Weight and **C** righting time of control and SMA mice from day of birth (P1) to late-symptomatic stage of the disease (P8). N=3 litters per time point, n=9 mice per condition for each time point (3 mice per condition from each litter); data was collected over a 2 and a half year period showing stability of the SMA phenotype over this time period.

2.2.4 UBA1 overexpression *in vivo*

To overexpress UBA1 *in vivo* mice were injected with AAV9-UBA1 intravenously on the day of birth as previously described (Powis et al., 2016). Adeno-associated virus serotype 9 (AAV9) expressing full-length human UBA1 cDNA was custom-produced by Vigene and administered at a concentration of $7x10^{13}$ vg. Before injection, mice were weighed to check they were >1.3g (determined to be the minimum weight for safe injection of virus) and placed on crushed ice for 2 minutes for general chilled anaesthesia. Mice were then placed on a WeeSight transilluminator (Philips) to visualise the vasculature and 10µl of AAV9-UBA1 was injected into the facial vein using a Hamilton 702 RN 25µl syringe fitted with a Hamilton 33 guage RN needle. Pressure was applied to the injection site while mice were warmed in hand before returning them to their mother or a foster mouse. Mice were checked twice daily for three days to monitor health following injection of AAV9-UBA1; they were then checked daily until sacrifice at postnatal day 8.

2.2.5 Tissue preparation

SMA mice and control littermates were sacrificed by overdose of anaesthetic (sodium pentobarbitone, 300mg/kg) at post-natal day (P) 2, P5, P7 or P8. FVB mice and mice (FVB or SMA) injected with AAV9-UBA1 were sacrificed at P8 by overdose of anaesthetic. In all cases, death was confirmed by exsanguination. For immunohistochemistry of spinal cords, spinal columns were roughly dissected and 1xPBS was injected into the spinal canal through the sacral end of the column, using a 23-gauge needle on a 5ml syringe, so that the intact spinal cord was ejected through the cervical end of the spinal column. The spinal cords were fixed in 4% PFA (Electron Microscopy Sciences) in phosphate buffered saline (PBS) for 24 hours then transferred to 30% sucrose overnight at 4°C for cryoprotection. The lumbar regions of the spinal cords were embedded in optimal cutting temperature compound (OCT; Cell Path), sectioned at 25µm on a cryostat (Leica 3050S) and immediately collected onto superfrost plus microscope slides (Thermo Scientific) in a serial manner so that each section on each slide was at a 200µm interval. Slides were stored at -20°C.

For immunohistochemistry of lumbar dorsal root ganglia (DRG), spinal columns were carefully dissected from P8 mice and a scalpel was used to cut transversely at the T13 vertebrae. Spinal columns were then fixed for 6 hours in 4% PFA (Electron Microscopy Sciences) in PBS then transferred to 30% sucrose at 4°C for 24 hours for cryoprotection. The lumbar and lower thoracic regions of the spinal columns were embedded in OCT and sectioned at 12µm on a cryostat. Using the T13 DRGs, spinal columns were aligned so that the DRGs were symmetrical on both sides of the column. For each DRG pair from lumbar segment 1 to lumbar segment 4 serial sections were collected onto superfrost plus microscope slides and stored at -20°C. Example images of DRGs throughout this thesis show a single DRG, therefore, for reference, a spinal column section showing a pair of DRGs stained with Toluidine blue has been included (Figure 2-3A). All example images of DRGs are from the L2 segment.

For quantitative fluorescent Western blot analysis and fractionation preparations, spinal cord (using the same method as above), heart and *gastrocnemius*

muscle (referred to as muscle for the rest of this thesis) were rapidly dissected and quickly frozen on dry ice. Lumbar dorsal root ganglia were dissected out of the spinal cord using a previously described method (Sleigh et al., 2016). Briefly, the spinal column was dissected and a scalpel was used to perform a transverse cut at the level of T13 and then a sagittal cut through the caudal half of spinal column, starting from the dorsal surface. Each half of the spinal column was then pinned in a Sylgard-lined petri dish (VWR) containing ice-cold 1xPBS and the spinal cord and meninges were removed in a rostral to caudal direction (Figure 2-3B). Forceps were then used to grasp the distally projecting axon bundles lateral to the DRGs allowing the dorsal root ganglia to be carefully scooped out of the spinal column along with the connecting nerves (Figure 2-3B). These were then transferred to a separate Sylgard-lined dish with fresh ice-cold 1xPBS (Figure 2-3C) and projecting axons were carefully removed from the DRGs along with any remaining meninges (Figure 2-3D). The DRGs were then rapidly frozen on dry ice. For each mouse, three DRGs from each half of the lumbar spinal column were dissected so that a Western blot could be performed on six DRGs per mouse. All tissue was stored at -80°C.

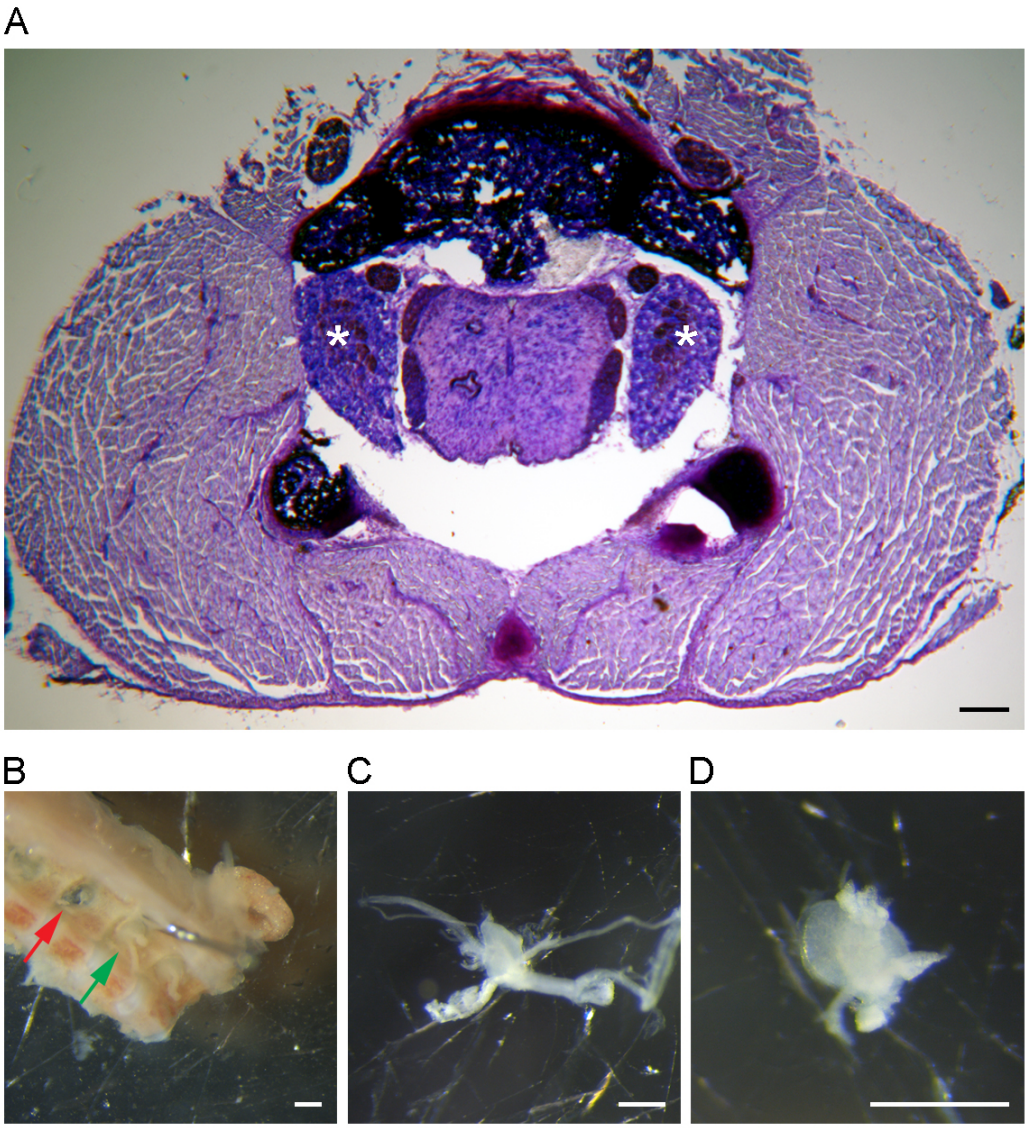

Figure 2-3 Preparation of dorsal root ganglia for immunohistochemistry and Western blot

A Example section of a spinal column containing dorsal root ganglia (indicated by white asterisks); section of DRGs from lumbar segment 2, stained with Toluidine blue solution for 3 minutes, dipped in running water and immediately mounted in 10% Mowoil solution (Polyscience). Image was captured on a Leica DMR equipped with a Retiga 2000R camera. Scale bar: 200µm. **B-D** Images of DRG dissection from P8 control mouse captured on Leica M60 dissection microscope equipped with a Leica MC170 HD camera. Scale bars: 1mm. **B** Spinal column with spinal cord and meninges removed showing DRG (green arrow) and spinal column after removal of DRG (red arrow). **C** DRG with projecting axons, **D** which were then carefully removed close to the DRG.

2.3 Zebrafish

Morpholino injections and protein extraction from zebrafish were performed by Dr Penelope Boyd.

Adult wildtype zebrafish were maintained in a fish facility at the University of Edinburgh according to standard methods. Zebrafish embryos were maintained using standard protocols at 28.5°C and were staged by hours post fertilisation (hpf).

2.3.1 UBA1 knockdown *in vivo*

To perform UBA1 knockdown *in vivo*, single cell-stage zebrafish embryos were injected with 6 ng *uba1* MO in aqueous solution containing 0.05% phenol red using age-matched un-injected embryos as controls. A previously published *uba1* morpholino (MO) (Wishart et al., 2014) was designed against the 5' start sequence of the *uba1* gene (Gene Tools LLC); 5'ACAGCGGCGAGCTGGACATCGTTTC-3'

For microinjection, adult pairs were set up using barriers in a pair mating tank. The barriers kept the females and males apart thereby controlling when they mated. This meant that fresh 1 cell stage embryos could be obtained throughout the duration of microinjection allowing for maximum numbers of embryos to be injected. Glass capillaries (Harvard apparatus, GC120T-10) were individually placed in a flaming/Brown p-97 micropipette puller which used a heated filament to pull a single glass capillary into two microinjection needles. The needle was filled with the appropriate solution using Eppendorf microloader pipette tips, and the needle end was blunted using sharp forceps. The microinjector was calibrated using a graticule, after which embryos were harvested and brushed individually in wells of a 1.5% agarose mould. Embryos were aligned to have the cell away from the injection manipulator so that the needle entered the embryo through the yolk and injected into the cell to minimise damage. Embryos were injected in rows of 25 and batches of 100 in the first 30 minutes of development, after which they were placed in fresh egg water and left to develop at 28°C. Un-injected embryos were kept as controls and fresh embryos were collected for each injection round.

2.3.2 Preparation of zebrafish for Western blot analysis

Embryos were dechorionated and deyolked in 1ml of deyolking buffer (1/2 Ginzburg Fish Ringer without Calcium: 55 mM NaCl, 1.8 mM KCl, 1.25 mM $NaHCO_3$). Embryos were pooled into batches of 30 fish, with three replicate batches per experimental group. Zebrafish were pelleted at 300x *g* for 30 seconds and the supernatant was discarded. Zebrafish were washed twice with wash buffer (110mM NaCL, 3.5 mM KCl, 2.7 mM CaCl2, 10 mM Tris pH 8.5) and pelleted again at 300x *g* for 30 seconds. The supernatant was removed and the zebrafish pellets were stored at -80°C. Western blot protocol was followed from 2.11.1.

2.4 In vitro experiments

2.4.1 Culture of HEK293 cells

HEK293 cells (human embryonic kidney cells) were originally obtained from the European Collection of Authenticated Cell Cultures (Public Health England, cat no: 85120602). HEK293 cells were grown in high glucose Dulbecco's modified Eagle medium (DMEM; Life Technologies) supplemented with 10% heat inactivated fetal bovine serum (FBS; Sigma), 1 x penicillin/streptavidin (pen/strep; Invitrogen) and 1x L-glutamine (Invitrogen). For immunocytochemistry experiments, HEK293 cells were seeded at a density of 100,000 cells per well onto 19mm^2 coverslips (VWR) and fixed at 2 days *in vitro* (DIV). For transfection, HEK293 cells were seeded at a density of 200,000 cells per well in a six well plate and grown for 48 hours before transfection.

2.4.2 Transfection of HEK293 cells

2.4.2.a UBA1 knockdown *in vitro*

HEK293 cells were transfected with RNAiMax (Invitrogen) and Silencer Select Validated UBA1 siRNA (s601, targeted against exons 24 and 25; Life Technologies). The following transfection mixtures were made up per well: 5µl RNAiMax transfection reagent was added to 125µl DMEM, 2.5µl of 10µM UBA1 siRNA was

added to 125µl DMEM. The siRNA solution was then added to the lipofectamine solution and incubated for 5 minutes before being added to the cells. For optimisation of UBA1 siRNA, scrambled siRNA and fluorescent siRNA (negative control 1, Integrated DNA technologies) were used as controls and transfected in the same manner. Cells were collected 48 hours after transfection.

2.4.2.b UBA1 overexpression *in vitro*

HEK293 cells were transfected using lipofectamine (Invitrogen) and pCMV6-XL4-UBA1 plasmid (Origene). For optimisation of UBA1 overexpression, either 6µl, 9µl, 12µl or 15µl of lipofectamine transfection reagent was added to 150µl DMEM, per well. For subsequent transfections, 7.5µl of lipofectamine was added to 125µl of DMEM, per well, and incubated for 5 minutes. This was then added to 150µl of DMEM with 3.5µg UBA1 plasmid for optimisation, or 125µl DMEM with 3µg UBA1 plasmid for subsequent transfections. The transfection mixture was incubated for a further 20 minutes before being added to the cells. Cells were harvested 24 hours after transfection.

2.4.2.c Co-transfections

All co-transfections were performed on HEK293 cells seeded at a density of 240,000 cells per well in a 6-well plate. For co-transfection of multiple plasmids, 1.25µg of each plasmid was added to 125µl of DMEM and 2.5µl of lipofectamine per plasmid was added to 125µl of DMEM. Incubation times and mixing of the transfection solutions was carried out as described in 2.4.2.b. For co-transfection of siRNA and multiple plasmids, the plasmid transfection solutions were made up and incubated as specified above and the siRNA transfection solutions were made up and incubated as specified in 2.4.2.a. Both transfection solutions were added onto the cells at the same time. For co-transfections, the same amount of DNA and lipofectamin/RNAiMax was added to each well, therefore, empty vectors and control siRNA were used when the respective constructs were not transfected to keep transfection amounts and ratios constant (Table 2-1). For all co-transfections, cells were harvested 48 hours after transfection.

Construct		Control vector	
Construct	**Supplier**	**Construct**	**Supplier**
pCMV6-XL4-UBA1	Origene	pCMV6-Entry	Origene
pcDNA3.1-SMN-V5-His	Gift from Prof Wirth	N/A	N/A
pEGFP-GARS-N2	Gift from Dr Antonellis	pEGFP-N1	Gift from Prof Cousin
pcDNA3.1-HA-Ubiquitin	Gift from Dr Yeh; Addgene #18712	pcDNA3.1+	Gift from Prof Cousin
UBA1 siRNA	Life Technologies	negative control siRNA 2	Life Technologies

Table 2-1 Constructs and respective control vectors
Constructs with supplier and respective control vectors used to maintain DNA concentration during transfections. pcDNA3.1-HA-Ubiquitin construct is as published (Kamitani et al., 1997); pEGFP-GARS-N2 construct is as published (Griffin et al., 2014).

2.4.3 Preparation of HEK293 cells for Western blot analysis

To collect HEK293 cells for Western blot, media was carefully aspirated off the cells which were then washed in pre-warmed 1xPBS (10x Dulbeccos Phosphate Buffered Saline, diluted in ddH_2O; Life Technologies) to remove remaining media. Cells were then washed off the wells using 1ml ice-cold 1xPBS and transferred to a 1.5ml tube. HEK293 cells were then pelleted by centrifugation at 500x *g* for 5minutes in a pre-cooled centrifuge (4°C). PBS was then removed from the cell pellets which were snap-frozen on dry ice and stored at -80°C.

2.4.4 Cortical neuron culture

Cortical neurons used in this study for the purpose of antibody optimisation and distribution analysis method optimisation were cultured by Dr Ewout Groen.

Cortical neurons were prepared as previously described (Groen et al., 2013). Briefly, cortices were dissected from wild-type CD1 embryonic day (E)14.5 embryos, trypsinized, triturated in DMEM/F12 medium (Life Technologies) containing 10% FBS and 2µg/ml DNaseI (Sigma) and cultured in neurobasal medium (Life Technologies) supplemented with 0.25mM glutamax (Life Technologies), 2% B27 (Invitrogen), 1x pen/strep and 18mM Hepes. Cortical neurons were fixed at DIV4 for optimisation experiments.

2.4.5 Motor neuron culture

Motor neurons used in this study to investigate UBA1 distribution were cultured by Dr Fiona Lane.

Motor neurons were prepared as previously described (Blokhuis et al., 2016). Briefly, the ventral half of spinal cords were dissected from wild-type C57BL/6J E13.5 embryos, trypsinized, dissociated in L15 medium (Life Technologies) containing 4% bovine serum albumin (BSA) and 0.1µg/ml DNaseI, and cultured in glial conditioned medium (neurobasal medium with 2% B27 which had been incubated on glial cells for 24 hours) supplemented with 10ng/ml BDNF, GDNF and CNTF. For longer-term cultures, half of the medium was changed at DIV6. Motor neurons were fixed at DIV4, DIV8 or DIV12.

2.4.6 Culture of glial cells

Glial cells were obtained during motor neuron preparations from dissociation of embryonic spinal cord ventral horns from wild-type C57BL/6J embryos and subsequent centrifugation during which glial cells were pelleted to isolate the motor neurons. Glial cells were then cultured in minimum essential medium (MEM; Life Technologies), supplemented with 10% FBS, 10mM Hepes (Invitrogen), 1x pen/strep and 10mM glucose. For immunocytochemistry, glial cells were seeded at a density of 20,000 cells per well onto 13mm^2 coverslips (VWR). For longer-term cultures, half of the medium was changed at DIV6. Glial cells were fixed at DIV4, DIV8 or DIV12.

2.5 Antibodies

A table of primary and secondary antibodies used throughout this thesis has been compiled detailing the antibodies and the manufactures along with the techniques which the antibodies were used for. For primary antibodies, the concentration for each technique and the use of the antibody (i.e. as a loading control, cytoplasmic marker, nuclear marker, motor neuron marker, sensory neuron subtype marker, protein tag or protein of interest) have also been included.

Primary antibodies				
Antibody	**Manufacturer**	**Technique**	**Use**	**Concentration**
α-tubulin	abcam	WB	Loading control	1:5000
β–III tubulin	abcam	ICC	Cytoplasmic marker	1:1000
β–III tubulin	Sigma	ICC	Cytoplasmic marker	1:1000
ChAT	Millipore	IHC	Motor neuron and cytoplasmic marker	1:100
CoxIV	abcam	WB	Loading control	1:1000
GAPDH	abcam	WB	Loading control/ cytoplasmic marker	1:2500
GARS	abcam	IHC WB	Protein of interest	1:500 1:5000
GFP	abcam	IP WB	Tag/experiment control	1µg/150µl 1:5000
H3	abcam	WB	Loading control/ nuclear marker	1:5000
HA	CST	WB	Tag on protein of interest	1:1000
IPO4	CST	WB	Protein of interest	1:2500
NF200	Sigma	IHC	Sensory neuron subtype marker	1:500
PDCD4	CST	WB	Protein of interest	1:1000
Peripherin	Merck	IHC	Sensory neuron subtype marker	1:500
RanBP1	ThermoFisher	WB	Protein of interest	1:1000
SMI32	Covance	IHC	Cytoplasmic marker	1:1000
SMN	BD transduction	IP WB	Protein of interest	1µg/150µl 1:1000
UBA1 (discontinued)	abcam	IHC	Protein of interest	1:600-1:1000
UBA1a	ThermoFisher	IHC ICC WB	Protein of interest	1:100 1:50 1:1000
UBA1a	CST	IHC ICC WB	Protein of interest	1:200 1:100 1:1000
UBA1a,b	ThermoFisher	WB	Protein of interest	1:1000
UBA6	CST	WB	Protein of interest	1:1000
Ube1	abcam	IHC	Protein of interest	N/A
Ube1	Sigma	IHC ICC WB	Protein of interest	1:800 1:200 1:1000
YARS	abcam	WB	Protein of interest	1:1000

Secondary antibodies for IHC and ICC	
Antibody	**Supplier**
Donkey anti-Rabbit 488 AlexaFluor	Life Technologies
Donkey anti-Mouse 488 AlexaFluor	Life Technologies
Donkey anti-Rabbit 594 AlexaFluor	Life Technologies
Donkey anti-Mouse 594 AlexaFluor	Life Technologies
Donkey anti-Goat 594 AlexaFluor	Life Technologies

Secondary antibodies for WB	
Antibody	**Supplier**
Donkey anti-Rabbit 680RD IRDye	LI-COR Biosciences
Donkey anti-Mouse 680RD IRDye	LI-COR Biosciences
Donkey anti-Rabbit 800CW IRDye	LI-COR Biosciences
Donkey anti-Mouse 800CW IRDye	LI-COR Biosciences

Table 2-2 Primary and secondary antibodies

All primary and secondary antibodies used in this thesis with manufacturer and application; concentrations and use also shown for primary antibodies. IHC: immunohistochemistry; ICC: immunocytochemistry; WB: Western blot; IP: Immunoprecipitation; N/A: not applicable (this antibody did not work for specified technique). For NF200 and peripherin IHC method was 2.6.2; for all other antibodies IHC method 2.6.1 was used. For ICC method 2.7 was used for all antibodies; for WB method 2.11 was used for all antibodies; for IP method 2.10.2 was used for all antibodies.

2.6 Immunohistochemistry

2.6.1 Standard immunohistochemistry protocol

Immunohistochemistry on sectioned tissues was performed using the Sequenza (Thermo Scientific) slide rack for optimal consistency. This protocol is based on optimisation of Choline Acetyltransferase (ChAT) (Powis and Gillingwater, 2016). Spinal cord and spinal column sections were permeabilised in 0.3% Triton X-100 (Sigma) in PBS for 10 minutes at RT, washed for 3 x 5 minutes in PBS and blocked in standard blocking solution (4% BSA, 0.1% Triton X-100 in PBS) for 1 hour. Subsequently the sections were incubated in the appropriate primary antibodies (Table 2-2) in a 1:4 dilution of the standard blocking solution at 4°C for 24 hours. After 3 x 10 minute PBS washes, sections were incubated with the appropriate Alexa Fluor-labelled secondary antibodies (1:400, Table 2-2; Life Technologies) in a 1:4 dilution of the standard blocking solution, for 1 hour at RT, washed for 3 x 10 minutes, incubated in 1x DAPI (Life Technologies) for 10 minutes and then washed in PBS for 3 x 10 minutes. The slides were mounted and coverslipped in a 10% Mowoil solution (Polyscience). This protocol was used when performing immunohistochemistry for all antibodies except NF200 and peripherin.

2.6.2 Immunohistochemistry for NF200 and peripherin

Spinal column sections were thawed at room temperature for 1 hour and then permeabilised in 0.3% Triton X-100 in PBS (PBST) for 3 x 10 minutes at RT, and blocked in 10% BSA in PBST for 1 hour. Subsequently the sections were incubated with NF200 (1:500, Sigma; Table 2-2) and peripherin (1:500, Merck; Table 2-2) in

blocking solution, at 4°C for 24 hours. After 3 x 10 minute PBS washes, sections were incubated with the appropriate Alexa Fluor-labelled secondary antibodies (1:400, Table 2-2; Life Technologies) in PBS, for 1 hour at RT, incubated in 1x DAPI for 10 minutes and then washed in PBS for 3 x 10 minutes. The slides were mounted and coverslipped in a 10% Mowoil solution (Polyscience).

2.7 Immunocytochemistry

Primary motor neurons, cortical neurons, glial cells and HEK293 cells were fixed in 4% PFA with 4% sucrose to preserve morphology in PBS for 10 minutes, permeabilised in 0.1% Triton X-100 for 5 minutes, washed twice in PBS and blocked in PBS containing 2.5% BSA for 30 minutes. They were subsequently incubated with primary antibodies (Table 2-2) in 2.5% BSA for 1 hour at RT. After 3 washes in PBS cells were incubated with a mixture of the appropriate Alexa Fluor-labelled secondary antibodies (1:400, Table 2-2), and phalloidin against F-actin (1:40; conjugated to Alexa Fluor 555; Life Technologies) for glial cells, in 2.5% BSA for one hour at RT. Then the cells were washed three times, incubated with 1x DAPI for 5 minutes, washed four times in PBS and mounted onto microscope slides (Thermo Scientific) using a 10% Mowoil solution.

2.8 Image acquisition and analysis

Imaging of glial cells was performed using a Nikon A1R FILM confocal microscope; images of HEK293 cells for cell counts was performed on a Leica DMi8 fluorescent microscope. Unless otherwise mentioned in the figure legend, all other imaging was performed on a Zeiss LSM710 confocal microscope. For intensity analysis, all imaging was performed at constant confocal settings for all samples in that experiment; the settings used ensured that no samples had oversaturated pixels in the channel of the protein of interest as this would preclude analysis of the intensity of signal from the antibodies detecting the proteins of interest.

To perform distribution analysis on HEK293 cells, glial cells and cultured motor neurons, Z-stack images were taken and then 3D projected (Max Intensity) to generate the images used for analysis. This ensured that UBA1 localised to different

areas of the cells would be included in the distribution analyses. Both HEK293 cells and glial cells were selected for analysis on the basis of a single nucleus per discernible cell with no overlapping of other cell bodies. At least 40 glial cells and 80 HEK293 cells from across 3 different coverslips were analysed per experimental condition. Motor neurons were selected for imaging on the basis of nuclear integrity with clearly discernible and intact axons and dendrites; at least 25 motor neurons from across 3 different coverslips were imaged and analysed per experimental condition.

To perform intensity and distribution analysis on lumbar spinal motor neurons, Z-stack images were taken for 8 spinal motor neuron pools per mouse. The Z-stacks were set up so that images from five different planes through the section were taken per motor neuron pool. Individual motor neurons were selected for analysis based on an intact nucleus and an intact cell body, as ascertained by DAPI and ChAT respectively, and were analysed in the plane where the nuclear outline was most defined.

Whole DRGs were imaged in a single plane and were selected for imaging and subsequent analysis based on structural integrity. Only sections that were a full cross-section through the centre of the DRG were imaged, i.e. sections taken from the middle of the DRG. One left and one right DRG were imaged per lumbar segment form L1-L4 for each mouse. For distribution analysis of sensory neurons, 7 larger area neurons and 7 smaller area neurons were analysed per DRG for 4 DRGs per mouse (one DRG for each of the lumbar segments 1-4).

2.8.1 Intensity and distribution analysis

Intensity and protein distribution analyses were performed in ImageJ. A nuclear marker and a cytoplasmic marker were used to draw around the circumference of the nucleus and cell body, respectively (yellow lines, Figure 2-4A). These outlines were then imposed onto the channel of the protein of interest (yellow lines, Figure 2-4A) and the XOR function was used to generate an area that contained the cytoplasm but not the nucleus, so that intensity measurements for the protein of interest in the nucleus and cytoplasm could be obtained separately (Figure 2-4B). The mean

intensity of the antibody signal for the protein of interest per area (cytoplasm only or nucleus only) was then measured using the measurement function (Figure 2-4B). The area of the nucleus, the cytoplasm and the whole cell was also measured at the same time. Results were recorded in Microsoft Excel and the ratio of the intensity of the protein of interest labelling in the nucleus to the cytoplasm (nuclear to cytoplasmic ratio [NCR]) was then calculated (Figure 2-4B).

Some distribution analysis (on HEK293 cells and cultured motor neurons) was performed by Amr Maani as part of a student project.

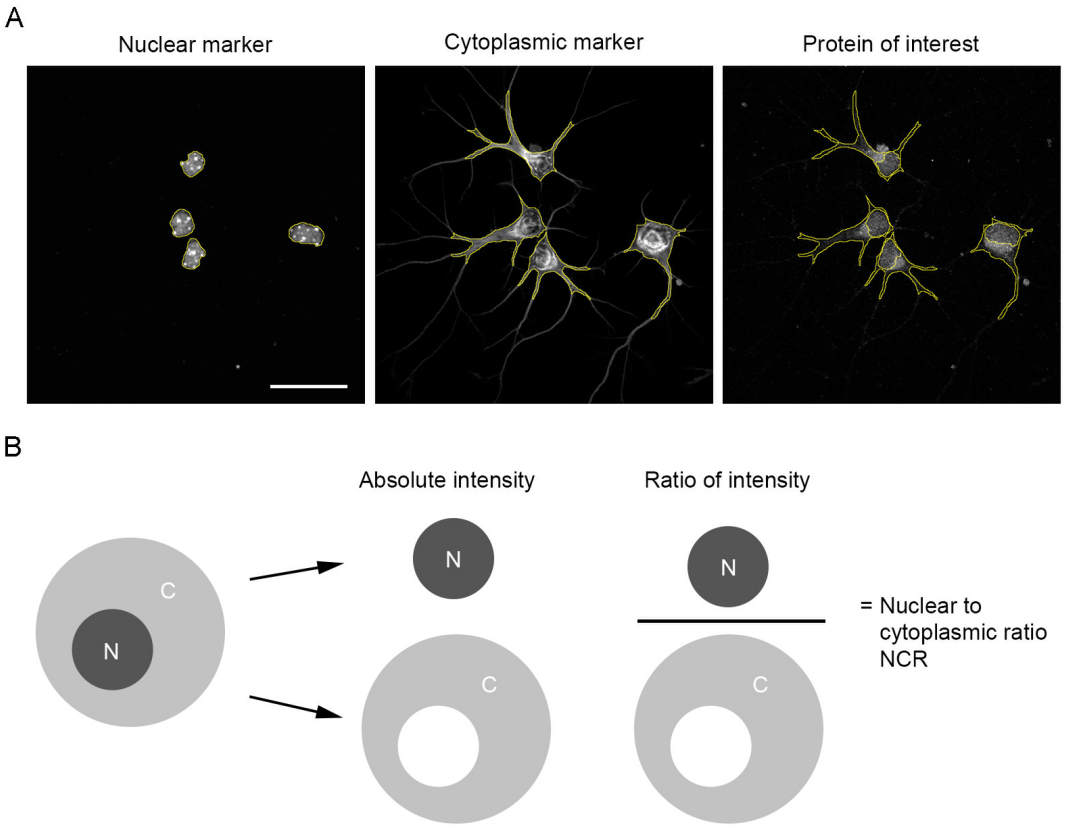

Figure 2-4 Intensity and distribution analysis

Intensity and distribution analysis optimisation was performed on DIV4 cortical neurons labelled with DAPI (nuclear marker), β-III tubulin (cytoplasmic marker) and pan-UBA1. **A** Nuclear and cytoplasmic markers were used to outline the nucleus and cell body respectively (yellow lines). These outlines were then imposed onto the channel of the protein of interest. Scale bar: 20μm. **B** The XOR function was used so that the intensity of the protein of interest labelling could be measured separately in the nucleus and the cytoplasm.

The intensity can then be presented as the absolute intensity for each cellular compartment or the ratio of nuclear to cytoplasmic intensity (NCR).

2.8.2 Sensory neuron and HEK293 cell counts

The cell counter plugin in ImageJ was used to count the number of sensory neurons positive for NF200, peripherin or both NF200 and peripherin. This avoided recounting any neurons. The total numbers of neurons positive for each antibody labelling were exported into Microsoft Excel where they were converted into a percentage of each labelling per DRG. The total numbers of neurons positive for each labelling were also added together to generate a total number of neurons per DRG. For control and SMA mice, 8 DRGs comprising 4 left-right pairs for lumbar segments 1-4 were analysed. For SMA mice and SMA mice injected with AAV9-UBA1, 4 DRGs comprising 2 left-right pairs for lumbar segments 1 and 2 were analysed. The cell counter plugin was also used to count HEK293 cells in eight 150μm^2 areas from across four coverslips.

2.8.3 Neuron area measurements

For analyses involving intensity or distribution analysis, the neuron area was measured at the same time of the mean intensity of the antibody labelling of the protein of interest (see 2.8.1). To investigate the area of NF200 positive and peripherin positive sensory neurons, the labelling of these markers was used to draw around the circumference of cell profiles in ImageJ. The measurement function was then used to measure area of the whole sensory neuron cell body.

2.9 Subcellular fractionation

For biochemical fractionation of late-symptomatic mouse spinal cords (P8 control and SMA mice), a modified version of the protocol by Cox and Emili (Cox and Emili, 2006) was used (Figure 2-5). Spinal cords were washed three times by centrifugation at 100x *g* for 1 minute in ice-cold PBS and then they were washed once in lysis buffer containing 0.25 M sucrose, 50 mM Tris-HCl, 5 mM $MgCl_2$, 1 mM DTT, 25$\mu g\ ml^{-1}$ spermine, 25$\mu g\ ml^{-1}$ spermidine and 1% protease inhibitor

cocktail (Life Technologies). The spinal cords were then gently homogenised on ice in 250µl of the lysis buffer using a glass dounce homogenizer. The homogenates were centrifuged at 800x *g* for 15 minutes at 4°C to pellet nuclei from the soluble, cytoplasmic lysate which was subsequently cleared of contaminants by centrifugation at 1000x *g* for 15 minutes at 4°C (Figure 2-5A). The supernatant contained a pure cytoplasmic fraction and was stored on dry ice while nuclei were extracted.

Although it was not possible to present data from nuclear fractions in this thesis (due to limitations of tissue quantity; see 3.3), for completeness: the crude nuclear pellet was re-homogenised in lysis buffer and centrifuged at 800x *g* for 15 minutes at 4°C. The pellet contained a clean nuclear pellet which was then resuspended in lysis buffer containing 2M sucrose and pure nuclei were isolated by ultracentrifugation at 80,000x *g* for 35 minutes (Figure 2-5A). The nuclei were lysed and soluble nuclear proteins were extracted in buffer containing 20% glycerol, 0.02M HEPES, 50 mM Tris-HCl, 5 mM $MgCl_2$, 1 mM DTT and 1% protease inhibitor cocktail. The lysed nuclei were centrifuged at 9,000x *g* for 30 minutes at 4°C and the resulting supernatant contained soluble nuclear proteins (Figure 2-5A) which were then Western blotted immediately along with the cytoplasmic fractions; Western blot method was followed from section 2.11.2. An example Western blot of cytoplasmic and nuclear fractions from P60 FVB spinal cords for cytoplasmic (GAPDH) and nuclear (Histone H3) markers has been included for reference (Figure 2-5B).

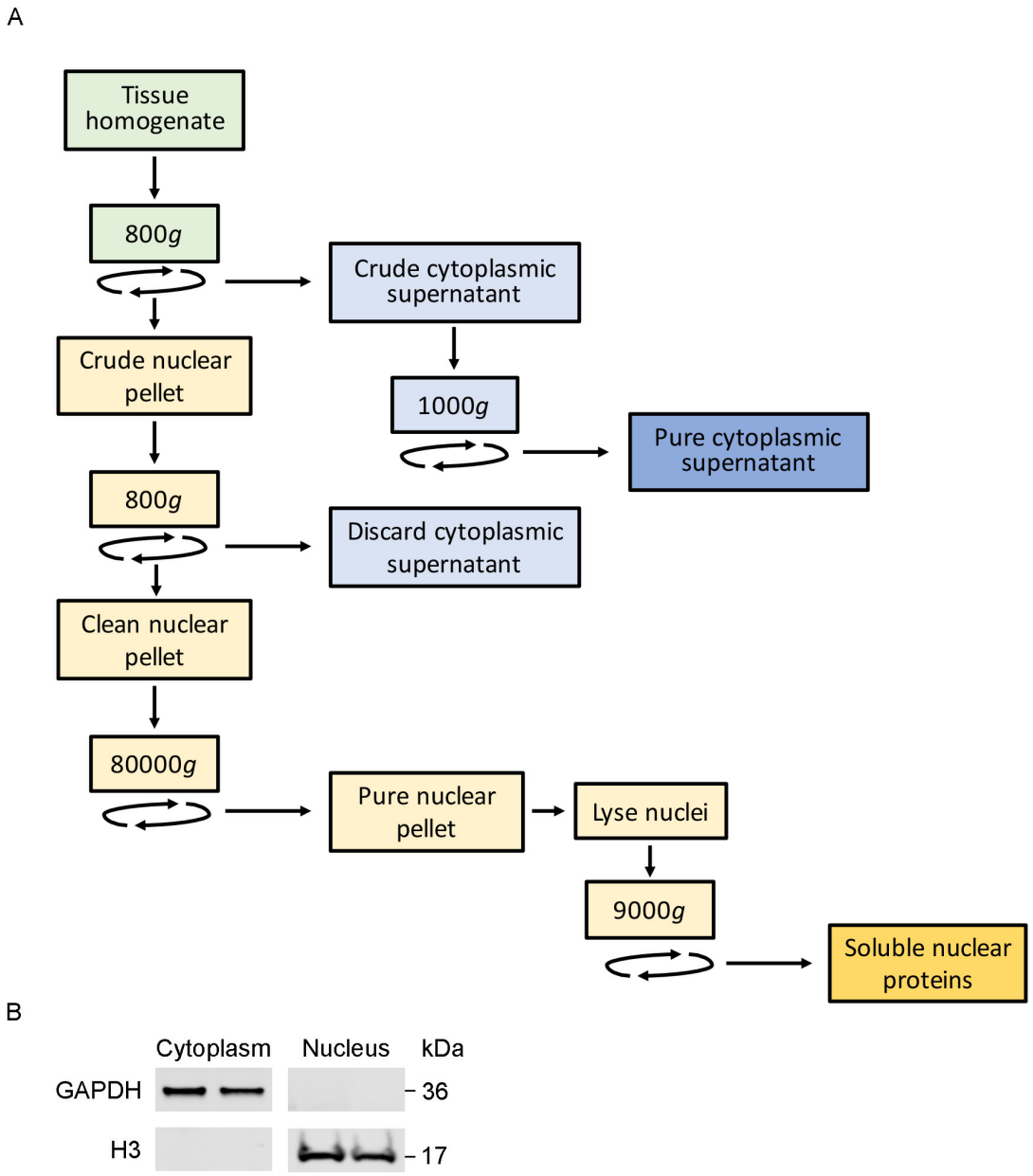

Figure 2-5 Schematic of subcellular fractionation protocol with example Western blot
A Schematic of fractionation protocol, showing extraction of a pure cytoplasmic fraction and a soluble nuclear protein fraction. **B** Example Western blot of cytoplasmic and nuclear fractions from P60 FVB spinal cords for a cytoplasmic marker (GAPDH) and a nuclear marker (histone H3 [H3]) showing purity of sample preparation method and generation of clean nuclear fractions. MW of proteins detected by antibodies indicated in kDa.

2.10 Ubiquitylation assay

2.10.1 Sample processing

Following transfection for 48 hours, 10µM of MG132 proteasome inhibitor was added to each well of HEK293 cells for 90 minutes. Cells were then lysed in the wells with 150µl of radioimmunoprecipitation assay (RIPA) buffer (Fisher Scientific) containing 1% protease inhibitor cocktail (Life Technologies), 1% phosphatase inhibitor (Life Technologies) and 10mM N-Ethylmaleimide. Cells were left on ice for 10 minutes and then centrifuged at 14,000 rpm for 10 minutes at 4°C. The supernatant was then used for immunoprecipitation (2.10.2).

2.10.2 Immunoprecipitation

From the supernatant prepared above, 7.5µl was removed and added to 7.5µl 2x NuPAGE LDS sample buffer (Life Technologies) for use as input control. The rest of the supernatant was incubated with primary antibody (Table 2-2) on a rotor at 4°C for 1 hour and 20 minutes. Solution was separated from Dynabeads protein A (for rabbit primary antibody) or Dynabeads protein G (for mouse primary antibody; both Life Technologies) using a magnetic stand. The protein/primary antibody solution was added to the Dynabeads and incubated on a rotor at 4°C for 40 minutes. The Dynabeads (now bound to the primary antibody/protein complexes) were then washed four times in 400µl NP40 buffer consisting of 20mM Tris-HCl [pH 7.5], 150mM NaCl, 1% Nonidet P-40 substitute and 10% glycerol. All remaining NP40 buffer was removed and the Dynabeads were gently suspended in 25µl of 1x NuPAGE LDS sample buffer and incubated at 95°C for 5 minutes to separate the primary antibody/protein complexes from the Dynabeads. The Dynabeads were then separated on a magnetic stand and the sample was transferred to a new tube. Samples and input control samples were subsequently Western blotted to detect proteins; Western blot method was followed from section 2.11.3.

2.11 Quantitative fluorescent Western blotting

2.11.1 Protein extraction

Protein was extracted from tissue and cell pellets in RIPA buffer with 1% protease inhibitor cocktail. Tissue was homogenised using a motorised disposable pestle mixer (VWR) and cell pellets were homogenised by repeated pipetting with a P200 pipette; all homogenisation was performed on ice. Dorsal root ganglia were homogenised in 25µl of buffer, zebrafish were lysed in 50µl of buffer, all other tissues and cell pellets were homogenised in at least 100µl of buffer, depending on tissue size and quantity of cells, with same amount of lysis buffer used for all samples in one experiment.

2.11.2 Protein quantification

Protein concentration was then determined by bicinchoninic acid (BCA) assay (Thermo Scientific). Extracted protein was then diluted to a final concentration of 30µg per well (for HEK293 cells, heart, spinal cord and muscle) in deionised water and NuPAGE LDS sample buffer. The final protein concentration for dorsal root ganglia was 17µg per well and the final protein concentration for cytoplasmic fractions of spinal cords was 25µg per well. For reducing Western blot conditions 5mM of dithiothreitol (DTT, Life Technologies) or 5% β-mercaptoethanol was added to the sample buffer. Following dilution to appropriate final concentrations, protein samples were incubated at 70°C for 10 minutes and then mixed by vortex.

2.11.3 Polyacrylamide gel electrophoresis, protein detection and Western blot analysis

Extracted protein was then separated by SDS-polyacrylamide gel electrophoresis at 150 volts on precast NuPage 4-12% BisTris gradient gels (Invitrogen). Samples were run alongside a Novex sharp pre-stained protein standard (3.5-260 kDa; Life Technologies). Gel embedded proteins were then transferred to polyvinylidene difluoride (PVDF) membranes using an iBlot 2 device (Life Technologies), with a 6 minutes 30 seconds semi-dry blotting program. The membranes were incubated in

Ponceau solution (0.2% Ponceau, 30% acetic acid; total protein stain) for 20 minutes and then transferred to blocking solution (LI-COR Biosciences) for 30 minutes at RT. Quantitative western blots were performed using primary antibodies (Table 2-2) diluted in blocking solution at 4^{o}C overnight.

A loading control protein was included during primary antibody incubation. For Western blots on samples used for the proteomics screen due to variability of histone H3 in UBA1 knockdown samples and reduction of CoxIV in UBA1 overexpression samples, it was necessary to use different loading controls for control compared to UBA1 knockdown (CoxIV) and control compared to UBA1 overexpression (histone H3; Figure 2-6A). For tissue the loading control was normally GAPDH or α-Tubulin, however, sometimes it was necessary to use Ponceau total protein stain as the loading control (for example when performing Western blot on control and SMA heart; Figure 2-6B). In Western blot figures where Ponceau has been used as the loading control, a representative section of Ponceau staining has been shown; full lanes of Ponceau stain were quantified for normalisation. Loading controls were also diluted in blocking solution and incubated with the membranes at 4^{o}C overnight.

After 6 x 5 minute washes in PBS, membranes were incubated in the appropriate secondary antibodies (1:5000, Table 2-2; LI-COR Biosciences) in blocking solution for 1 hour at RT. The membranes were then washed in PBS for 3 x 30 minutes, dried and imaged using an Odyssey Infrared Imaging System (LI-COR Biosciences) with Image Studio software (LI-COR Biosciences). Analysis was performed in Image Studio where the intensity of the fluorescent band was measured for the protein of interest and the loading control. The intensity of the protein of interest was then normalised to the intensity of the loading control to determine relative protein expression for each sample; experimental conditions were then normalised to the control condition for that experiment.

Some quantitative fluorescent Western blots (on zebrafish, hearts from FVB mice and HEK293 cells for ubiquitylation experiments) were performed by Dinja van der Hoorn as part of a student project.

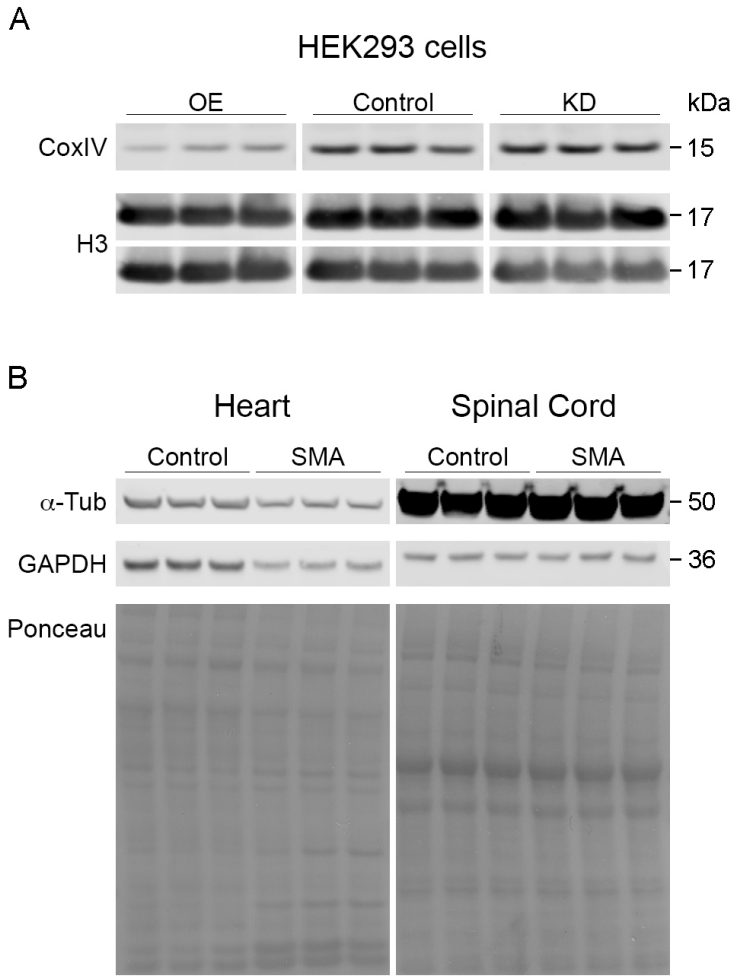

Figure 2-6 Loading controls for Western blot analysis

Example loading controls used for quantitative fluorescent Western blot analysis. **A** Western blot on HEK293 cells with UBA1 overexpression or UBA1 knockdown and control showing reduction of CoxIV following UBA1 overexpression and variability of histone H3 (H3) following UBA1 knockdown. **B** Western blot on heart and spinal cord from P8 control and SMA mice (30µg protein loaded per sample). GAPDH and α-Tubulin were both suitable loading controls for spinal cord. Neither α-Tubulin nor GAPDH were appropriate loading controls for heart, therefore it was necessary to normalise to the total protein stain (Ponceau). MW of proteins detected by antibodies indicated in kDa. Ponceau is shown for whole lane.

2.12 Label-free proteomic screen and analysis

2.12.1 Protein extraction

For the label-free proteomic screen HEK293 cells were collected as previously described (see 2.4.3) except three wells of cells were collected into one 15ml tube so that for each condition (control, UBA1 overexpression and UBA1 knockdown) there were three samples each containing the cells from three separate wells. Protein was extracted from the HEK293 cell pellets in SDT lysis buffer containing 100 mM Tris-HCl (pH 7.6; Sigma), 4% (W/V) Sodium dodecyl sulfate (VWR) by repeated homogenisation using a P200 pipette. Protein concentration was determined using a BCA assay (ThermoScientific).

2.12.2 Label-free proteomics

HEK293 cell lysates were sent to Douglas Lamont at the 'FingerPrints' Proteomics Facility, University of Dundee, where the mass spectrometry and necessary preparations were performed for the label-free proteomics screen. Assignment of proteins in Mascot was also performed by Dr Douglas Lamont.

2.12.2.a Mass spectrometry

Aliquots (100 µg) of each HEK293 lysate were processed through FASP (filter-aided sample preparation) involving buffer exchange to 8M urea and alkylation with 50mM iodoacetamide. Double digestion with trypsin (Roche, sequencing grade) was then performed, initially for 4 hours, then overnight, both at 30°C. Samples were then desalted to remove unwanted buffer salts by washes with 0.1% trifluoroacetic acid and then 70% acetonitrile. Each sample was then separated by injecting it onto a nanoflow LC-MS/MS Ultimate 3000 RSLC (Thermo Scientific) system coupled to a linear ion trap Orbitrap hybrid mass spectrometer (LTQ- Orbitrap Velos Pro, Thermo Scientific) via a nanoelectrospray ion source (Thermo Scientific). The peptides from each digest were separated with a linear gradient of 2-40% acetonitrile, 0.1 % formic acid over 124 minutes with a constant flow of 300 nL/min. Full-scan MS survey spectra were acquired in the LTQ Oribitrap with a resolution of 60,000; this was

followed by IT-MS/MS scans for the 15 most intense peptide ions. Data were acquired using Xcalibur software. Alongside the nine samples, four quality control samples were processed, each of which consisted of a mixture of the nine samples.

2.12.2.b Assigning peptides and proteins in Progenesis and Mascot

The raw proteomic data was then imported into Progenesis for analysis of relative ion abundance and peptide characterisation. The MS/MS output were converted into 2D representations for each sample; these were then aligned to one of the quality control samples (quality control sample 3) with all alignment scores >90%. The data was subsequently filtered where all ions with a charge >5 were removed from the dataset, as were features detected below 23 minutes and above 137 minutes (Figure 2-7A); this filter on retention time corrected for elution variability. The runs for the different biological replicates of each condition were combined and statistical p-values were automatically generated for the peptides in Progenesis software through a One-way ANOVA on the ArcSinh transform of the normalized data. The peptides were then filtered and those with a p-value > 0.05 or a power < 0.8 were removed (Figure 2-7A).

The remaining data was then exported for identification of individual proteins using the IPI-*Homo sapiens* database via Mascot Search Engine (V2.3.2) in which 712 proteins were identified (Figure 2-7A); the statistical analysis of this data was carried out automatically in Mascot. The proteins identified in Mascot were then imported into Progenesis for filtering and further analysis. Peptide conflicts were removed and proteins were filtered to eliminate those with < 2 unique peptides; proteins with a p-value < 0.05 or a fold change < 1.1 in both UBA1 overexpression compared to control and knockdown compared to control were also removed (Figure 2-7A). This resulting dataset contained the 222 proteins which showed the largest significant variation in expression following modulation of UBA1 expression levels (Figure 2-7A-C; Appendix 2). During data processing in Progenesis, a correlation analysis of proteins (following filtering) was performed to group the proteins based on the similarity of their expression profiles across the three conditions.

Graphs showing the fold-change of proteins following UBA1 overexpression compared to control (Figure 2-7B) and UBA1 knockdown compared to control (Figure 2-7C) were generated to indicate the spread of proteins both pre- and post-filtering. UBA1 was highlighted in red and was the protein with the most significant fold-change compared to control in both datasets post-filtering. UBA1 was removed from the dataset for all subsequent analysis so that the results would not be skewed by the manipulation of protein expression used to generate the samples for this proteomic screen.

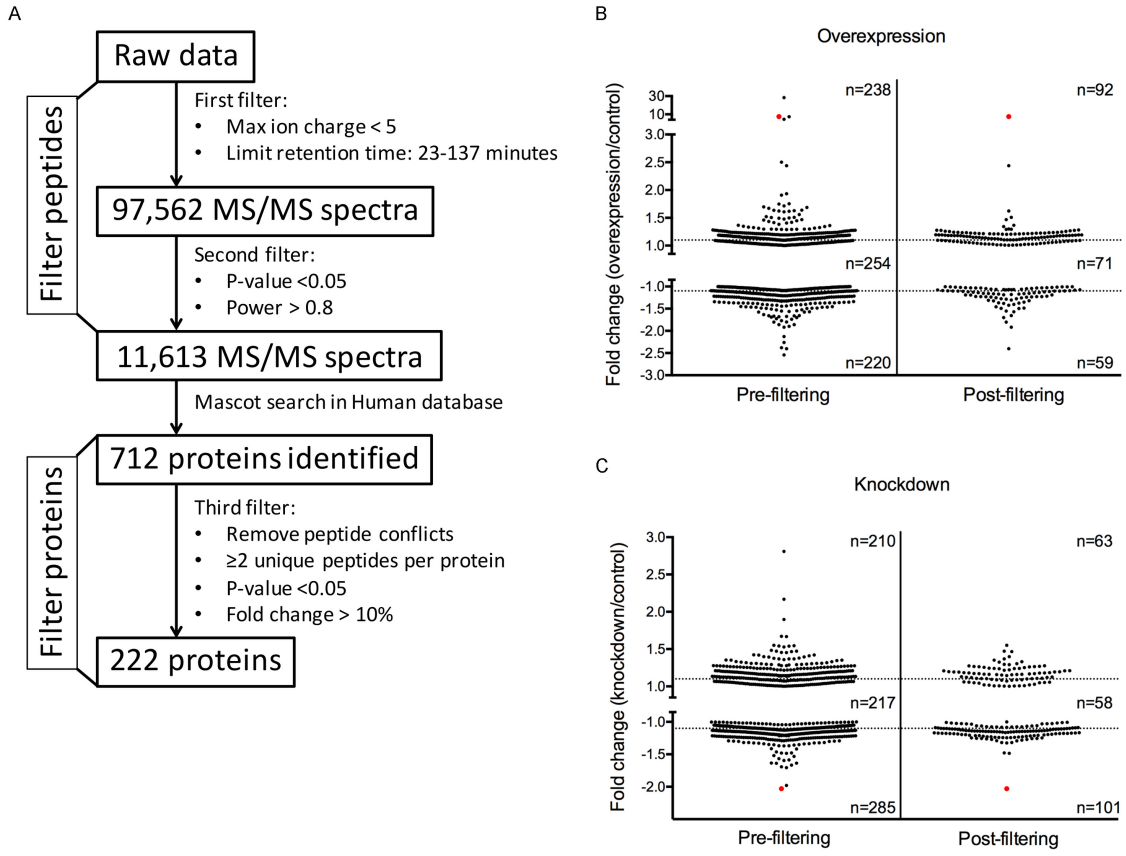

Figure 2-7 Filtering of the proteomics dataset

A Filtering steps performed in progenesis during filtering of the raw data, the peptides identified and then the filtering of the proteins that were identified in Mascot. Overall this generated a dataset of 222 proteins. **B** Fold change of proteins changed following UBA1 overexpression compared to control and **C** UBA1 knockdown compared to control, both pre-filtering (after identification of protiens in Mascot) and post-filtering (dataset used for subsequent analysis). UBA1 is indicated by a red dot and was removed from the dataset for all subsequent analysis.

2.12.3 *In silico* analysis of the proteomic screen

2.12.3.a Gene ontology term enrichment in DAVID

The Database for Annotation, Visualization and Integrated Discovery (DAVID; available at http://david.abcc.ncifcrf.gov) provides a comprehensive set of functional annotation tools to identify biological meaning for large datasets (Huang da et al., 2009a, b). DAVID was used to identify enriched biological themes within the filtered proteomics dataset; both functional annotation clustering and gene functional annotation were performed. Both of these analyses rely on grouping together enriched terms to identify either enriched functional clusters or functionally related groups of genes. In both cases, the protein list is compared against a background list (in this case *H. sapiens*) and enriched terms associated with the gene list are identified. Modified Fischer's exact p-values for each term are automatically calculated during this analysis; these are used to determine the enrichment of each term. To then generate either a functional annotation clustering or gene functional classification report, annotation terms that belong to the same gene group or the same proteins are grouped. This group of annotations or gene group is then assigned an enrichment score (ES) which is the geometric mean of the p-values for all the terms in that cluster. The ES is the $-\log_{10}$ of the p-value and so represents the significance of the enrichment of that gene group or functional group in this dataset compared to a generic background dataset. For reference, an ES of 1.3 is equivalent to a p-value of 0.05. This software was also used to characterise the functions associated with the protein clusters generated in BioLayout (see 2.12.3.b); for this analysis, functional annotation clustering was performed.

2.12.3.b Protein expression profiling in Biolayout

BioLayout (developed at the Roslin Institute, University of Edinburgh, http://www.biolayout.org) was used to identify UBA1-dependent clusters of proteins based on the expression of the proteins across UBA1 overexpression, control and UBA1 knockdown. This software uses a pattern recognition algorithm to enable the visualisation and analysis of network graphs based on the expression profiles of the

proteins. The network graphs in this study were generated using a Pearson correlation (set to 0.98) and Markov clustering algorithm (Enright et al., 2002). Each protein is represented by a coloured node and the proximity to its neighbour indicates the similarity in protein expression. The colour of the node indicates the cluster that protein belongs to; all proteins in one cluster have a similar expression profile. The expression profiles are displayed as mean normalised abundance (on a pareto scale) with SEM for each condition. These clusters can be further analysed for functional annotation using other *in silico* tools such as DAVID (see 2.12.3.a).

2.12.3.c Network and canonical pathway analysis in IPA

Ingenuity pathway analysis (IPA; www.qiagenbioinformatics.com/products/ingenuity-pathway-analysis/) was used as previously described (Wishart et al., 2010; Wishart et al., 2007). Data analysis and interpretation of expression analysis experiments in IPA is based on the manually curated Ingenuity Knowledge Base in which more than 90% of the information in the database is drawn from the full text of peer reviewed journals; less than 10% of interactions have been identified by natural language processing and subsequent manual verification. Two different analysis platforms in IPA were used during this study. The first was network analysis which identifies causal relationships within the dataset based on the curated Knowledge Base; the analysis also includes regulators not present within the dataset. Within each network relative expression changes of the proteins are displayed: red symbols indicate upregulated proteins and green symbols indicate downregulated proteins compared to control.

The canonical pathways function and functional annotation tool were also used for the identification of known biological pathways within this dataset. Canonical pathway analysis compares the library of published biological pathways within the curated Knowledge Base with the dataset being analysed. The significance of the association between the dataset and the canonical pathway is defined by a Fischer's exact p-value (generated during the analysis) that determines if the probability of association between the proteins in the dataset and in the canonical pathway are due to chance, along with the overlap of the number of proteins from the

dataset that are present in the canonical pathway (Savli et al., 2008). A 1.1 fold-change threshold filter was applied in IPA to each dataset analysed and only experimentally observed interactions were selected for each analysis.

2.13 Statistical analysis

All statistical analyses were performed in Microsoft Excel and Prism 6 (GraphPad), individual statistical tests are reported in figure legends. For all analyses, statistical significance was considered to be $P \leq 0.05$. Data are reported as mean ± standard error of the mean (SEM) throughout this thesis. All frequency distributions were generated as relative frequencies and are presented as percentages. Figures were created using Adobe Photoshop CS6 or Adobe Illustrator CS6 software. Flowcharts were created in Microsoft PowerPoint.

Chapter 3 Characterising the distribution of UBA1

3.1 Introduction

Spinal muscular atrophy (SMA) is a motor neuron disease characterized by the loss of lower motor neurons from the anterior horn of the spinal cord (Kolb and Kissel, 2011). SMA primarily affects children and is the most common genetic cause of infant mortality (Lunn and Wang, 2008; Sugarman et al., 2012). It is now well characterised that ubiquitin homeostasis is altered in SMA and that reduction of ubiquitin-like modifier-activating enzyme 1 (UBA1) is central to this disruption (Aghamaleky Sarvestany et al., 2014; Fuller et al., 2015; Wishart et al., 2014). While it is known that therapies targeting UBA1, or downstream proteins, rescue neuromuscular phenotypes in SMA models (Powis et al., 2016; Wishart et al., 2014), the mechanism by which UBA1 mediates degeneration in SMA is unclear. In fact, very little is known about the function of UBA1 in cells beyond its canonical role in the ubiquitylation pathway (Groen and Gillingwater, 2015).

In SMA, the reduction of UBA1 is well characterised at late-symptomatic stages of the disease when reduction of UBA1 occurs in the neuromuscular system and in non-neuronal organs (Aghamaleky Sarvestany et al., 2014; Powis et al., 2016; Wishart et al., 2014). As previously mentioned (see 1.2.4.b), the time course of UBA1 reduction correlates with disease progression in SMA mice with changes in several organs occurring during pre-symptomatic stages of the disease (Powis et al., 2016). The characterisation of UBA1 pathology in SMA has been conducted on whole tissues and while changes in the whole spinal cord are modest compared to UBA1 reduction in other organs such as heart and liver (Powis et al., 2016), the primary pathological target in SMA is the motor neuron (Lunn and Wang, 2008; Powis and Gillingwater, 2016). Therefore, to tease out the role of UBA1 reduction in SMA pathogenesis it is now necessary to go beyond the whole tissue level and examine UBA1 distribution and function at the single cell level.

One of the few known functions of UBA1 is its involvement in regulation of the cell cycle, with mutations in *UBA1* leading to cell cycle arrest and apoptosis (Lao

et al., 2012; Lee et al., 2008). Indeed, UBA1 distribution is well characterised throughout the cell cycle in dividing cultures of cells. UBA1 exists as two isoforms, UBA1a and UBA1b. UBA1a contains 40 amino acids at its N-terminal that are lacking from UBA1b (Figure 1-3) (Groen and Gillingwater, 2015; Handley-Gearhart et al., 1994). The first 40 amino acids (unique to UBA1a) contain a nuclear localization sequence (NLS) and a series of serine residues that are phosphorylated (Figure 1-3) in a cell cycle dependent manner by cyclin-dependent kinase 1 (Cdk1) (Cook and Chock, 1995; Handley-Gearhart et al., 1994; Rona et al., 2014; Stephen et al., 1997). Due to the NLS, UBA1a is mainly localized to the nucleus, while UBA1b is mostly cytoplasmic (Grenfell et al., 1994; Handley-Gearhart et al., 1994). Cdk1 has maximal activity in the nucleus during G2 where it phosphorylates UBA1a (Rona et al., 2014). This phosphorylation ensures that after mitosis, UBA1a is exclusively localized in the nuclei of the daughter cells enabling the degradation of mitotic cyclins to occur (Grenfell et al., 1994; Seufert et al., 1995). Following the G1 phase, UBA1a becomes more cytoplasmic until G2 when it returns to the nucleus (Grenfell et al., 1994).

Furthermore, using immunoelectron microscopy it has been shown that UBA1 localises to different subcellular compartments. In HepG2 cells, 37% of UBA1 was present in the nucleus (primarily localised to the heterochromatin), 56% was present in the cytosol and 7% resided within the mitochondria. Within the cytosol, UBA1 showed enhanced association with desmosomal junctions, with the cytoplasmic surfaces of lysosomes, and the rough endoplasmic reticulum (Schwartz et al., 1992). This information gives a clear overview of the subcellular localisation of UBA1 during interphase.

Interestingly, redistribution of UBA1 in neuronal populations has been observed in several neurodegenerative diseases (Lopez Salon et al., 2000; Wade et al., 2014; Wishart et al., 2014). In SMA, UBA1 is initially lost from the neuronal cytoplasm (as evidenced by experiments on hippocampal synaptosomes) of pre-symptomatic SMA mice (Wishart et al., 2014), suggesting that subtle pre-symptomatic changes in UBA1 levels or subcellular distribution may be involved in SMA pathogenesis. Furthermore, in both Huntington's disease (HD) and

Alzheimer's disease (AD), redistributions of UBA1 occur in specific neuronal populations (Lopez Salon et al., 2000; Wade et al., 2014). For example, there is a reduction of UBA1 in the cytosolic fraction of AD patients' cortex (Lopez Salon et al., 2000). In HD, UBA1 expression levels decline during disease progression in the nuclear fraction of mouse cortex (Wade et al., 2014). Together this suggests that subcellular changes in UBA1 distribution may play a role in the pathogenesis of a range of neurodegenerative diseases. However, although the distribution of UBA1 in dividing cells has been well characterised (Grenfell et al., 1994; Groen and Gillingwater, 2015; Stephen et al., 1997), little is known about the distribution and localisation of UBA1 in healthy neuronal populations *in vitro* or *in vivo*.

To better understand the role of UBA1 in motor neuron degeneration it will be vital to characterise UBA1 distribution in healthy populations of post mitotic cells. This will enable the investigation of UBA1 distribution in SMA motor neurons throughout disease progression, which may help to identify when UBA1 reduction becomes important in SMA pathogenesis. In this study, tools to investigate UBA1 were optimised and used to confirm published distribution profiles of UBA1. The expression patterns of UBA1 in cultured motor neurons were then characterised to provide a baseline for the distribution of UBA1 in post-mitotic cells. Finally, to better understand the role of UBA1 in SMA pathogenesis, UBA1 distribution in spinal motor neurons was characterised throughout disease progression.

3.2 Results

3.2.1 Optimisation of UBA1 antibodies

To investigate the distribution and role of UBA1 in SMA, the availability of antibodies that produce reliable and reproducible results across a range of laboratory techniques is essential. The manufacturer has since discontinued the anti-UBA1 antibody used previously in the lab and it was not clear which commercially available antibodies can reliably differentiate between the different isoforms of UBA1. Therefore, several antibodies that detect UBA1 or UBA1a (according to manufacturer specifications) were purchased in order to identify 'gold standard' UBA1 antibodies that work well for immunohistochemistry (IHC), immunocytochemistry (ICC) and Western blot (Table 3-1). Due to the extra 40 amino acids (Stephen et al., 1997), the UBA1a isoform can be detected if antibodies are directed against this sequence and, in contrast, antibodies directed against any other part of the protein detect both UBA1a and UBA1b isoforms (referred to here as pan-UBA1 antibodies). Because it had previously been identified that the limiting function of the antibody was its ability to work for IHC, all antibodies were initially screened for their suitability for IHC. Subsequently, those that worked were tested for ICC and Western blot suitability.

Number	Manufacturer	Name	Cat. no	Species	Epitope	IHC (SPC)	ICC	WB
1	Abcam (discontinued)	Ube1	ab24623	Mouse (mono)	Full recombinant protein	1:600 to 1:1000	Not tested	Yes
2	Sigma	Ube1	E3152	Mouse (mono)	Full recombinant protein	1:800	1:100	1:1000
3	Abcam	Ube1	ab34711	Rabbit (poly)	Full recombinant protein	No	No	1:1000
4	Thermo	Ube1a,b	PA5-17274	Rabbit (poly)	C-term	No	Not tested	Not tested
5	Thermo	Ube1a	PA5-17262	Rabbit (poly)	N-term	1:50	1:100	1:1000
6	CST	Ube1a	4890S	Rabbit (poly)	N-term	1:200	1:100	1:1000

Table 3-1 Overview of UBA1 antibodies

UBA1 antibodies with screening results for immunohistochemistry (IHC), immunocytochemistry (ICC) and Western blot suitability, including optimal antibody concentrations. Mono: monoclonal; poly: polyclonal.

For IHC, all antibodies were tested on spinal cord sections from control mice ($Smn^{+/-}$; $SMN2^{tg/0}$) to identify their suitability for IHC. Antibodies 1 and 2 were produced from the same hybridoma clone and raised against full-length recombinant UBA1 protein. For both antibodies, positive nuclear and cytoplasmic staining was observed (Figure 3-1A and D). Antibody 2 also non-specifically labelled the vasculature (Figure 3-1D). Using the other pan-UBA1 antibodies (3 and 4) specific UBA1 staining could not be identified, although pronounced non-specific labelling of the vasculature was observed for antibody 4 (Figure 3-1B and E). The specific epitope sequence that the UBA1a antibodies (5 and 6) were raised against was not disclosed but was confirmed to be within the first 40 amino acids by the manufacturers. Antibody 6 appeared to have a better signal-to-noise ratio and more pronounced nuclear staining than antibody 5 (Figure 3-1C and F).

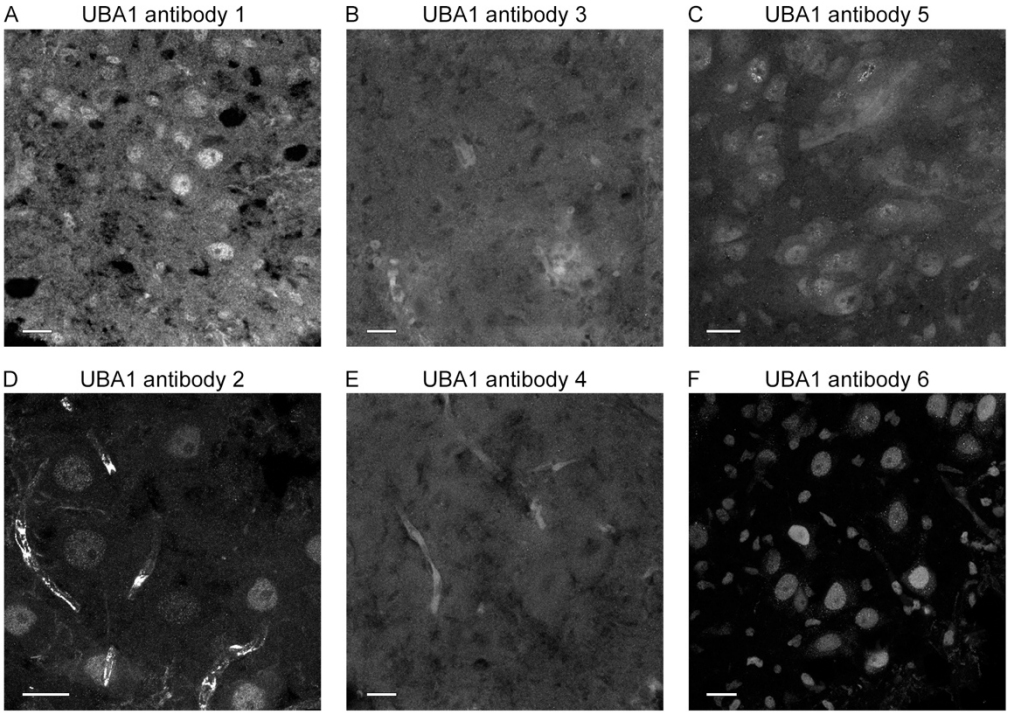

Figure 3-1 Immunohistochemistry screen of UBA1 antibodies on spinal cord
Antibodies 1, 2, 5 and 6 showed specific UBA1 staining on 25μm spinal cord sections from P8 control mice ($Smn^{+/-}$; $SMN2^{tg/0}$). **A, D** Positive nuclear and cytoplasmic staining. **B**, **D** Non-specific staining of the vasculature. **B**, **E** No specific UBA1 staining. **C** Positive nuclear and diffuse cytoplasmic staining. **F** Pronounced nuclear staining with low background. Scale bars: 20μm.

Subsequently, the antibodies that were suitable for IHC (antibodies 2, 5 and 6), were tested for ICC on cortical neurons *in vitro*. Antibody 2 showed positive nuclear, cytoplasmic and axonal staining (Figure 3-2A) while, in contrast, the UBA1a antibodies (5 and 6) both showed bright nuclear staining with minor amounts of cytoplasmic staining (Figure 3-2B, C). Therefore, antibody 2 will be used for detection of both UBA1 isoforms for IHC and ICC. Although both antibodies 5 and 6 show clear and consistent staining patterns for both techniques, due to the reduced signal to noise ratio for IHC, antibody 6 will be used for detection of UBA1a for IHC and ICC.

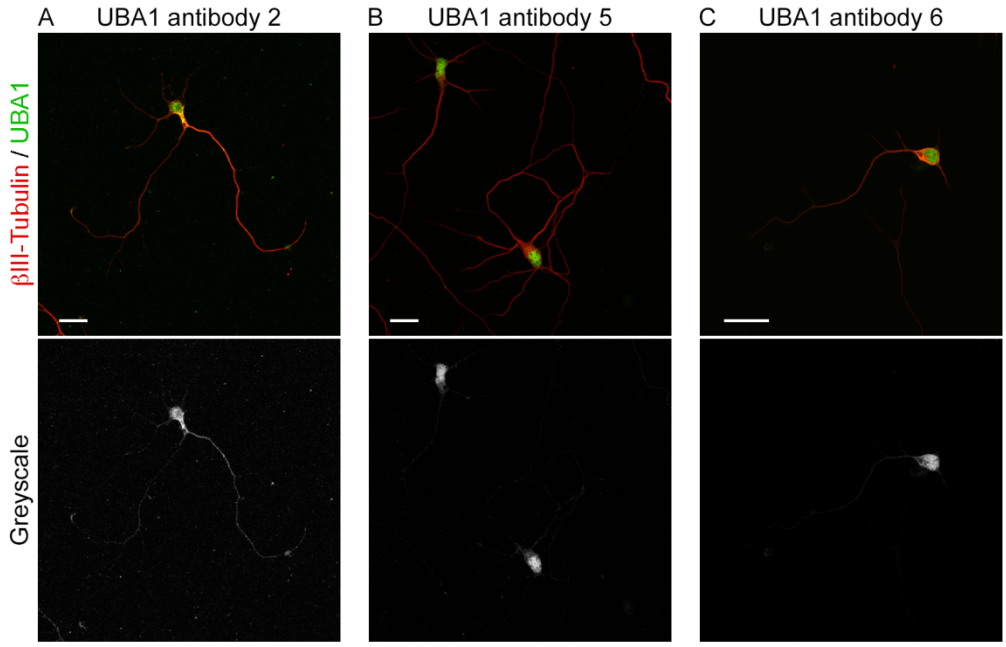

Figure 3-2 Immunocytochemistry screen of UBA1 antibodies 2, 5 and 6
Primary cortical neurons cultured from wild-type CD1 embryos were fixed at 4 days *in vitro*, beta III-tubulin was used as a cytoplasmic marker. **A** Positive nuclear, cytoplasmic and axonal staining. **B**, **C** bright nuclear staining and weak cytoplasmic staining. Scale bars: 20μm.

Following this, antibodies 2, 5 and 6 were tested on brain and spinal cord dissected from control mice ($Smn^{+/-}$; $SMN2^{tg/0}$) to identify their suitability for Western blot. Previously in the lab, antibody 4 had been the standard antibody for detecting pan-UBA1 in quantitative fluorescent Western blotting; therefore antibody 4 was used for comparison with the other antibodies. Antibody 4 showed a clear doublet with two bands at 110 and 117kDa representing UBA1 and UBA1 bound to ubiquitin (UBA1~Ub), respectively (Figure 3-3). This doublet was also seen with antibody 2, however, non-specific bands were also observed. The UBA1a antibodies (5 and 6) both showed the 110 and 117kDa bands without any non-specific bands (Figure 3-3); due to antibody 6 being used for IHC and ICC, antibody 6 will also be used to detect the UBA1a isoform on Western blots.

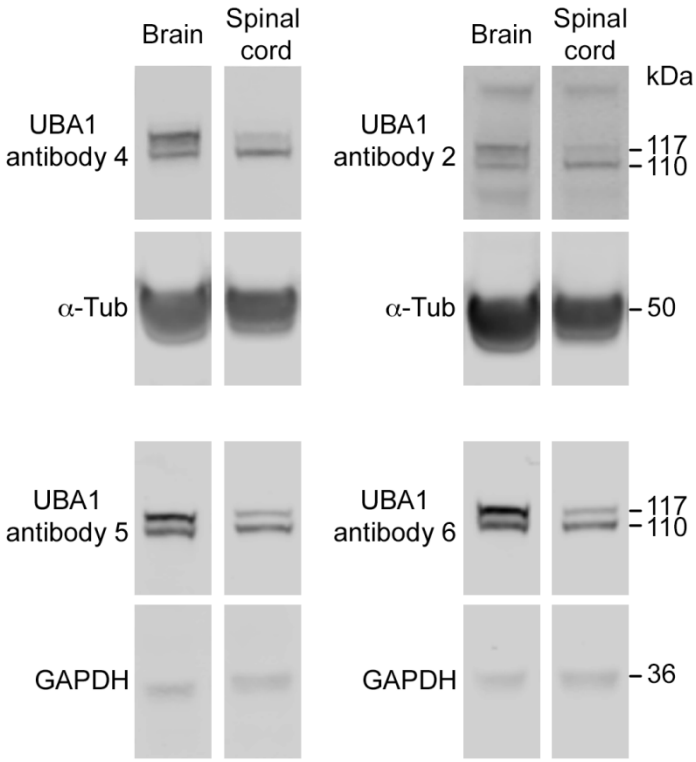

Figure 3-3 Western blot screen for UBA1 antibodies 4, 2, 5 and 6

UBA1 antibodies were tested on brain and spinal cord lysates from P7 control mice ($Smn^{+/-}$; $SMN2^{tg/0}$). Antibodies 4, 5 and 6 showed two clear bands at 100kDa (UBA1) and 117kDa (UBA1~Ub). Antibody 2 detected two bands at 100kDa and 117kDa along with some non-specific bands. Alpha-tubulin (α-Tub) used as loading control for antibodies 4 and 2; GAPDH used as loading control for antibodies 5 and 6.

It has previously been reported that the 117kDa band of UBA1~Ub is not present on a Western blot under reducing conditions, as this breaks the UBA1~Ub thioester bond (Kitagaki et al., 2009; Xu et al., 2010). Indeed, when a reducing agent was added the 117kDa band was not present with any of the antibodies tested. This was observed across all the tissues for both SMA and control mice (Figure 3-4). The difference between non-reducing and reducing conditions was particularly pronounced for antibody 2 in muscle. This antibody produced more non-specific bands in muscle than in the other tissues that were tested, resulting in the UBA1

doublet being unclear in non-reducing conditions (Figure 3-4). Antibody 4 detected pan-UBA1 without producing the non-specific bands of antibody 2; therefore, antibody 4 will be used to detect UBA1 for quantitative fluorescent Western blot.

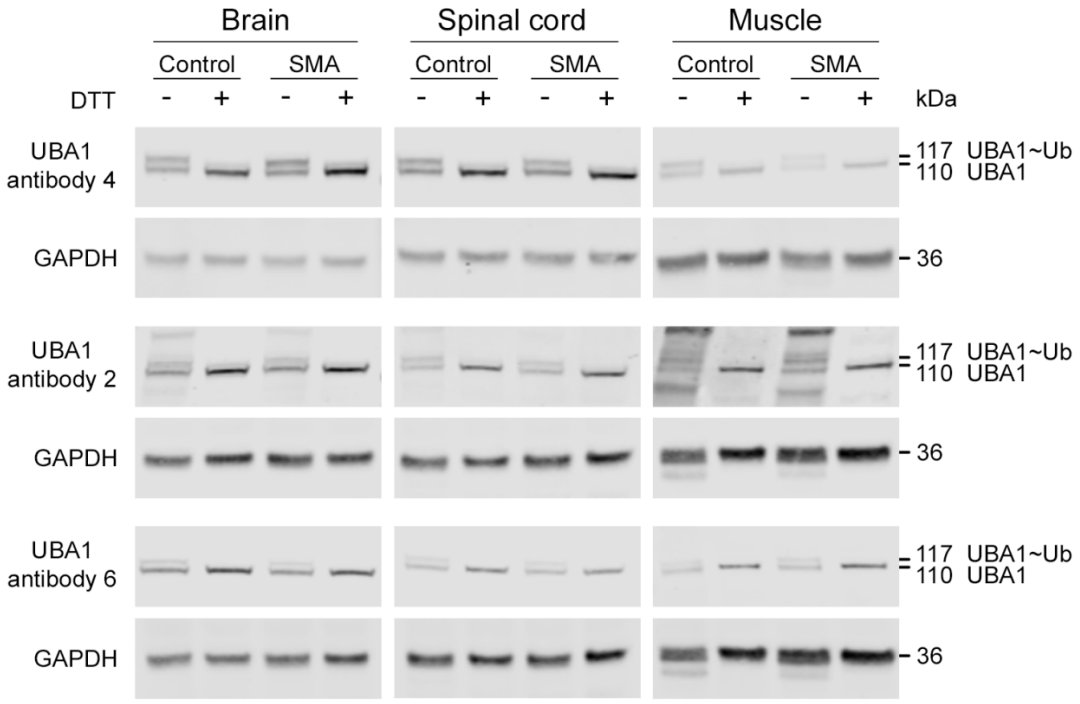

Figure 3-4 Reducing Western blot conditions break the UBA1~Ub thioester bond
Representative fluorescent Western blot bands for UBA1 in brain, spinal cord and muscle lysates from P8 Taiwanese control and SMA mice, with GAPDH as a loading control. DTT was used as a reducing agent. Antibody 4 and antibody 6 show two clear bands in non-reducing conditions and one band at 110kDa in reducing conditions. Reducing conditions with antibody 2 removed non-specific bands as well as the 117kDa band.

To summarise, antibody 2 will be used to detect both isoforms of UBA1 for IHC and ICC as it showed clear distribution patterns with positive staining following the optimisation of antibodies for immunolabelling on spinal cord sections and primary cortical neurons. Similarly, antibody 6 showed clear nuclear localisation and easily discernible distribution patterns for both IHC and ICC and so this antibody will be used to detect the UBA1a isoform for these techniques. Antibody 4 will be

used to detect both isoforms of UBA1 on Western blot as this gave a clear doublet band which became a single band under reducing conditions. Antibody 6 will be used to detect UBA1a for Western blot as this showed a clear doublet band and responded well to reducing conditions under which it produced a single band.

When mentioning UBA1 in the subsequent text of this thesis, I refer to the protein; when using pan-UBA1 or UBA1a I refer to the different antibodies that will be used to detect UBA1. Antibodies 2 and 4 will be referred to as pan-UBA1 while antibody 6 will be referred to as UBA1a. Unless otherwise stated, reducing conditions will be used for Western blots of UBA1 to ensure accurate quantification of total UBA1 protein levels.

3.2.2 Characterisation of UBA1 distribution in cultures of dividing cells

3.2.2.a UBA1a and pan-UBA1 antibodies show different distribution patterns

After defining which antibodies to use for detection of UBA1, the antibodies were used to confirm the distribution of UBA1 reported in the literature and to establish a method for distribution analysis (see 2.8.1). To do this, UBA1 distribution was initially investigated in a culture of dividing cells. HEK293 cells were chosen due to their clear cellular morphology and rapidly dividing nature. The cells were fixed at two days *in vitro* (DIV2) and labelled for pan-UBA1 or UBA1a in conjunction with cytoplasmic (tubulin) and nuclear (DAPI) markers after which the absolute intensity of pan-UBA1 and UBA1a in the nucleus and cytoplasm was quantified.

Consistent with the literature (Grenfell et al., 1994; Handley-Gearhart et al., 1994; Stephen et al., 1997), pan-UBA1 revealed both nuclear and cytoplasmic localisation of UBA1 with uniform distribution across the cell. There was no discernible localisation of UBA1 to subcellular structures (Figure 3-5A). In contrast, UBA1a showed a strong nuclear localisation with very little UBA1a in the cytoplasm (Figure 3-5A). These observations were then quantified to allow comparison of the absolute intensity of pan-UBA1 and UBA1a. Consistent with these observations, UBA1a was significantly more nuclear than pan-UBA1 (UBA1a=42.33a.u., pan-UBA1=25.55a.u; $P \leq 0.0001$; Figure 3-5B). In the cytoplasm, there was less UBA1a than pan-UBA1 (UBA1a=6.39a.u., pan-UBA1=21.14a.u.; $P \leq 0.0001$; Figure 3-5C).

The nuclear to cytoplasmic ratio (NCR) of intensity can also be a useful measure to, for example, compare samples across different time points or when quantifying absolute intensities is not suitable or feasible. The closer the NCR is to 1, the more evenly distributed the protein was between the nucleus and the cytoplasm. In line with the above observations and quantifications, pan-UBA1 had an NCR of 1.27 indicating a slightly higher intensity in the nucleus than in the cytoplasm. Conversely, UBA1a had a much higher NCR (6.64) because it preferentially detects

UBA1a, which was primarily localised to the nucleus rather than the cytoplasm (Figure 3-5D).

In the literature, the distribution patterns of UBA1 at different stages of the cell cycle have been described (Grenfell et al., 1994). To ensure the variation in distribution patterns was captured, the number of cells suitable for intensity analysis was quantified. For a cell to meet analysis criteria, it had to have an intact nucleus as established by DAPI, thereby excluding cells undergoing division. In a 150μm^2 area, on average 88.2% of cells were suitable for intensity analysis, while the remaining 11.8% were classified as undergoing mitosis based on their nuclear morphology (Figure 3-5E). Therefore, it was the distribution of UBA1 during interphase that was observed and analysed here, and the variation in distribution patterns throughout interphase was captured in this analysis. Overall, these results are consistent with the published literature, where UBA1a shows a predominantly nuclear localisation while pan-UBA1 reveals both nuclear and cytoplasmic localisation of UBA1 (Grenfell et al., 1994; Handley-Gearhart et al., 1994). Importantly, these observations can be quantified to reliably identify differences in distribution patterns, allowing the antibodies to be used for further investigation of UBA1 distribution.

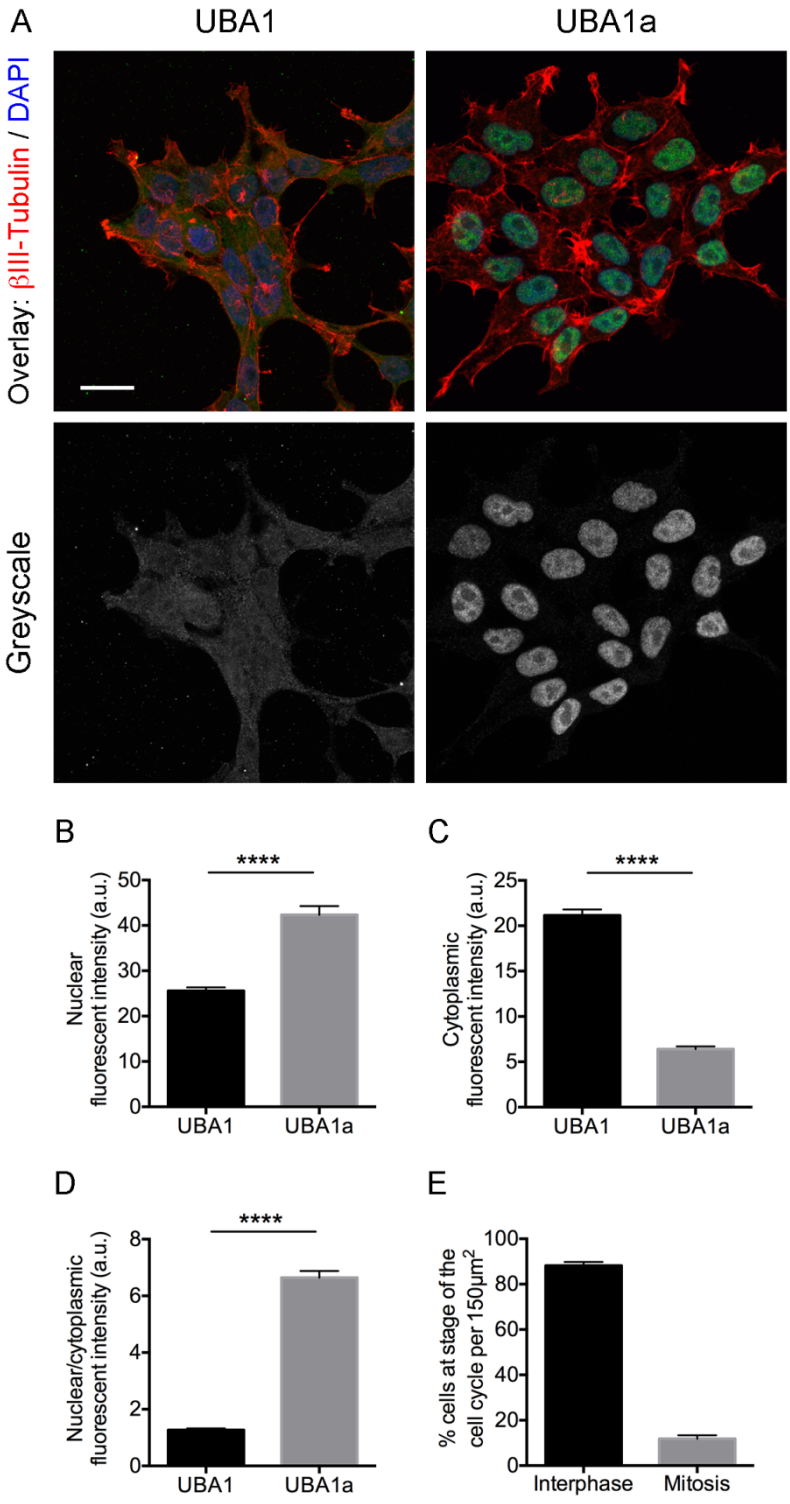

Figure 3-5 Distribution patterns of UBA1 and UBA1a antibodies in dividing cells

HEK293 cells were fixed at DIV2 and labelled with pan-UBA1 or UBA1a, cytoplasmic (βIII-tubulin) and nuclear (DAPI) markers. **A** Pan-UBA1 showed evenly distributed staining across the cell body, UBA1a showed specific nuclear localisation. **B** Quantification of the absolute intensity of pan-UBA1 and UBA1a in the nucleus. **C** Quantification of the absolute intensity of

pan-UBA1 and UBA1a in the cytoplasm. **D** Nuclear to cytoplasmic ratio for pan-UBA1 and UBA1a. **B-D** Pan-UBA1, N=3 coverslips, n=82 cells; UBA1a, N=3 coverslips, n=95 cells. **E** Percentage of dividing cells per 150μm^2, classified by nuclear morphology based on DAPI. n=8 150μm^2 areas. Scale bar: 25μm. Unpaired 2-tailed Student's t test; **** $P \leq 0.0001$.

3.2.2.b UBA1 distribution patterns were consistent over time in culture

To investigate UBA1 distribution in a long-term culture of cells, glial cells were cultured from wild-type C57BL/6J E13.5 embryos, fixed at DIV4, DIV8 or DIV12 and labelled for pan-UBA1 or UBA1a in conjunction with cytoplasmic and nuclear markers. Glial cells were chosen as they could be kept in culture for longer than HEK293 cells yet also have clear cellular morphology. At all time-points, pan-UBA1 revealed both nuclear and cytoskeletal staining (Figure 3-6A). UBA1a was predominantly nuclear with few cells showing cytoplasmic UBA1a (Figure 3-6B). As previously observed in HEK293 cells, this indicates that the antibodies detect different combinations of the UBA1 isoforms. On quantification, the NCR of UBA1a was significantly more nuclear than that for pan-UBA1. This difference was consistent over time in culture with the NCR for pan-UBA1 ranging from 3.29 to 4.89 whilst the NCR for UBA1a ranged from 10.60 to 13.93 ($P \leq 0.0001$ at all time points; Figure 3-6C). Again, pan-UBA1 had a NCR closer to 1 than that for UBA1a, as it detects both the nuclear and cytoplasmic UBA1 isoforms, while UBA1a detects the nuclear isoform.

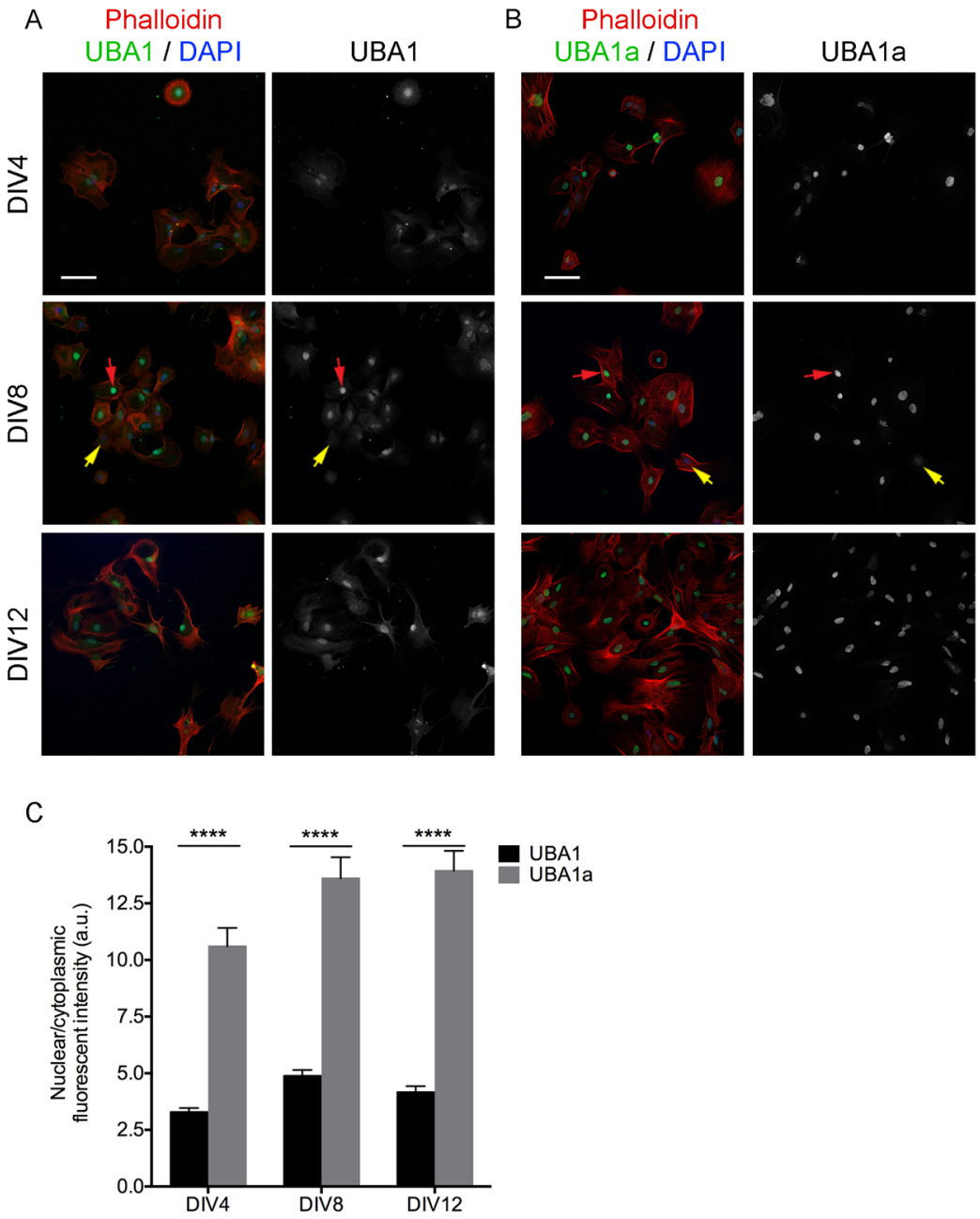

Figure 3-6 UBA1 distribution in a long-term culture of dividing cells

Glial cells were fixed at DIV4, DIV8 or DIV12 and labelled with pan-UBA1 or UBA1a, cytoplasmic (phalloidin) and nuclear (DAPI) markers. **A** Pan-UBA1 revealed cytoskeletal and variable nuclear localisation. **B** UBA1a showed variable nuclear intensity, very little cytoskeletal localisation. **A**, **B** Clearly discernible, bright nuclei (red arrows), less intense nuclear staining (yellow arrows). **C** Nuclear to cytoplasmic ratio of pan-UBA1 and UBA1a at each time point. UBA1a was consistently more nuclear than pan-UBA1. N=3 coverslips, n>40 glial cells per age per antibody. Scale bars: 100μm. One-way ANOVA with Tukey's post-hoc test; **** $P \leq 0.0001$.

3.2.2.c UBA1 is differentially distributed in cultures of dividing cells

It has previously been reported that UBA1 has different distribution patterns within dividing cultures of cells dependent on the stage of the cell cycle (Grenfell et al., 1994; Trausch et al., 1993). To investigate whether this could be detected with pan-UBA1 and UBA1a, the variation of UBA1 localisation in glial cells was observed. A variety of distribution patterns were identified for both pan-UBA1 and UBA1a. Some glial cells showed clearly discernible nuclei (red arrows, Figure 3-6A, B) and others had nuclei with the same intensity of UBA1 as the cytoplasm, or with very little UBA1 (yellow arrows, Figure 3-6A, B). This is consistent with the published literature discussing the changes of UBA1 distribution patterns throughout the cell cycle, with strongly nuclear localisation of UBA1 during the G2 phase and less nuclear UBA1 in the S phase when there is an increase in its cytoplasmic localisation (Grenfell et al., 1994).

Also of note is the difference in staining patterns between HEK293 cells and glial cells (Figure 3-5A, Figure 3-6A, B). Overall, UBA1 was present in the cytoplasm of HEK293 cells to a greater extent than in glial cells, reflected by the differences in NCR values for the two cell types; this was evident for both pan-UBA1 and UBA1a, suggesting differential requirements of cell types for UBA1. Indeed, it has previously been reported that, in dividing cultures of cells, UBA1 distribution varies between different cell types (Trausch et al., 1993); therefore, the antibodies used here reliably detect distribution patterns and behaviours of UBA1 previously described in the literature.

To summarise, I have shown that, consistent with the literature, pan-UBA1 and UBA1a present different distribution patterns (Handley-Gearhart et al., 1994). I expanded on this finding and demonstrated that these differences are consistent in longer-term cultures of dividing cells. Furthermore, I have also demonstrated that the optimised antibodies showed a range of distribution patterns, as previously reported (Grenfell et al., 1994; Handley-Gearhart et al., 1994; Trausch et al., 1993), and that the distribution patterns vary between different cell types.

3.2.3 Characterisation of UBA1 distribution in motor neurons *in vitro*

3.2.3.a Characterising UBA1 distribution in motor neurons *in vitro*

Next, to assess the distribution of UBA1 in post-mitotic cells, intensity analysis was performed on wildtype primary motor neurons. Motor neurons were cultured from wild-type C57BL/6J E13.5 mouse embryos, fixed at DIV4, DIV8 or DIV12 and labelled for pan-UBA1 or UBA1a along with cytoplasmic (βIII-tubulin) and nuclear (DAPI) markers. As observed for glial cells, pan-UBA1 was more cytoplasmic than UBA1a, which was predominantly localised to the nucleus. For pan-UBA1, axonal localisation was observed (Figure 3-7A) whereas UBA1a was only observed in the proximal axon (Figure 3-7B). The respective distribution patterns of pan-UBA1 and UBA1a in motor neurons were consistent and significantly different, with UBA1a showing a more nuclear distribution (NCR=3.81-1.87) than pan-UBA1 (NCR=1.80-1.32; $P \leq 0.0001$ at DIV4 and DIV8; $P \leq 0.05$ at DIV12; Figure 3-7C). Interestingly, the NCR for both pan-UBA1 and UBA1a decreased over time in culture, indicating an increase in cytoplasmic UBA1 (Figure 3-7C).

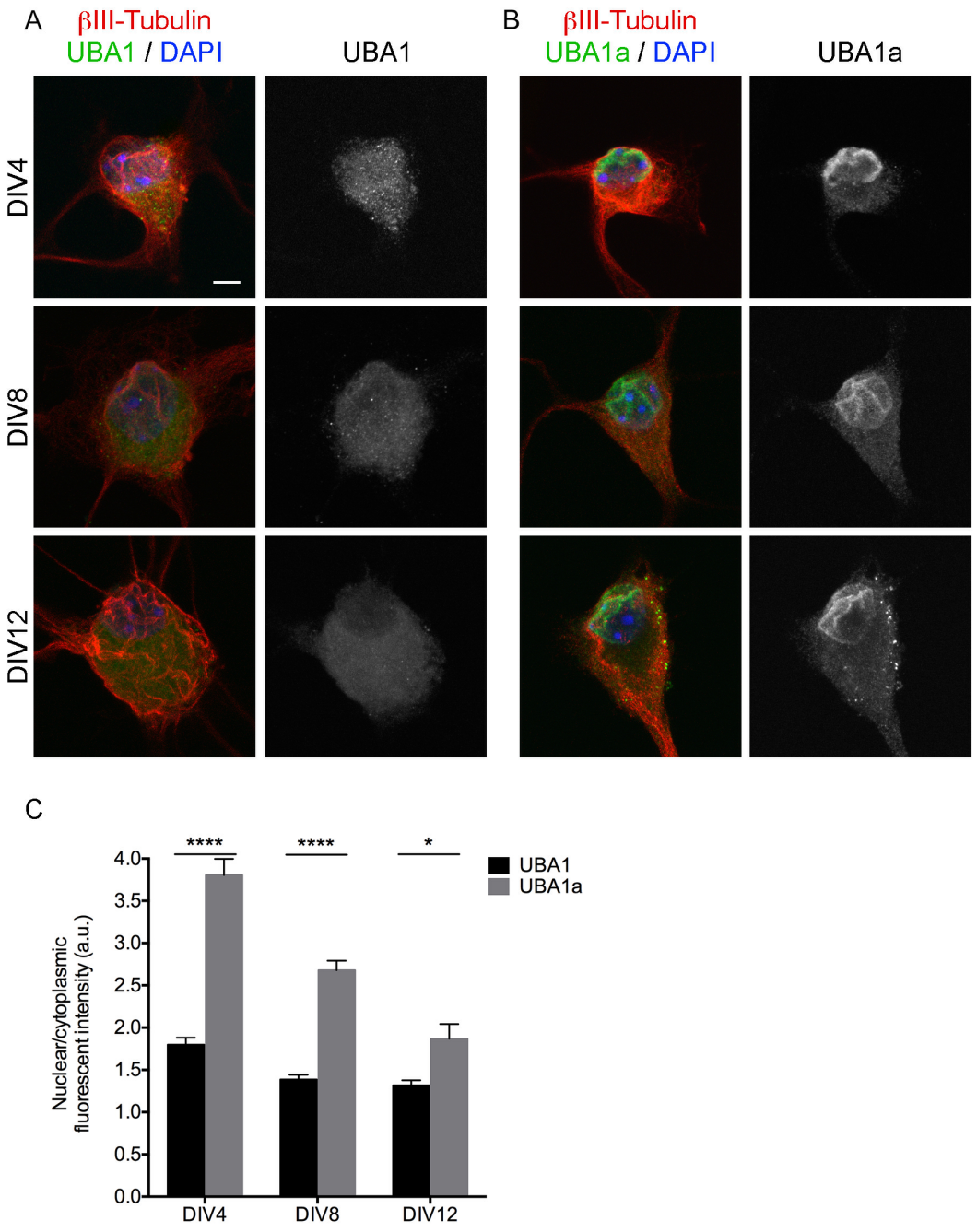

Figure 3-7 UBA1 distribution in cultured primary motor neurons

Motor neurons were fixed at DIV4, DIV8 or DIV12 and labelled with pan-UBA1 or UBA1a, cytoplasmic (βIII-tubulin) and nuclear (DAPI) markers. **A** Pan-UBA1 revealed cytoplasmic and nuclear localisation with a reduction in nuclear intensity over time in culture. **B** UBA1a showed clear nuclear localisation with an increase of cytoplasmic intensity over time in culture. **C** Nuclear to cytoplasmic ratio of pan-UBA1 and UBA1a at each time point. UBA1a was consistently more nuclear than pan-UBA1. Both pan-UBA1 and UBA1a showed a reduction in NCR over time in culture. N=3 coverslips, n>25 motor neurons per time point per

antibody. Scale bars: 20μm. One-way ANOVA with Tukey's post-hoc test; *P≤ 0.05, **** P ≤ 0.0001.

3.2.3.b UBA1 distribution changes over time in motor neurons *in vitro*

To further dissect the extent of the shift of UBA1 distribution in motor neurons, UBA1 distribution in a long-term culture of dividing cells (glial cells) was used as a baseline to compare with the distribution of UBA1 in a culture of motor neurons. In glial cells, the NCR for pan-UBA1 increased between DIV4 (NCR=3.29) and DIV8 (NCR=4.89, P≤0.0001) but there was no significant difference in the NCR between DIV8 and DIV12 (Figure 3-8A). In motor neurons, the NCR of pan-UBA1 reduced from 1.80 at DIV4 to 1.32 at DIV12 (P≤0.0001; Figure 3-8A). Similarly, for UBA1a, glial cells showed a small shift towards a more nuclear localisation between DIV4 (NCR=10.60) and DIV8 (NCR=13.60, P≤0.05) with no significant difference between DIV8 and DIV12 (Figure 3-8B). In motor neurons, there was a consistent and significant decrease in the NCR between all time-points investigated. The NCR for UBA1a dropped from 3.81 at DIV4 to 2.68 at DIV8 and then to 1.87 at DIV12 (P≤0.0001; Figure 3-8B). Therefore, there was a consistent reduction in UBA1 NCR in motor neurons over time that did not occur in glial cells. While the same trend was observed for pan-UBA1 and UBA1a in motor neurons, the relative reduction in nuclear staining was more pronounced for UBA1a (Figure 3-8A, B). As the shift in NCR was detected by both antibodies, it suggests that it was due to a redistribution of UBA1a from the nucleus into the cytoplasm rather than an increase in the translation of UBA1b, the cytoplasmic isoform.

As mentioned above, UBA1 distribution varies between different cell types (Trausch et al., 1993), however, only dividing cultures of cells have previously been investigated. Here, UBA1 distribution was investigated in long-term cultures of both dividing and post-mitotic cells. In dividing cultures, pan-UBA1 NCR was consistently more nuclear than in motor neurons (NCR=3.29-4.89 for glial cells, NCR=1.32-1.80 for motor neurons; Figure 3-8A). This difference also occurred with UBA1a, which was exclusively nuclear in glial cells but showed nuclear and cytoplasmic localisation in motor neurons (NCR=10.60-13.93 for glial cells,

NCR=1.87-3.81 for motor neurons; Figure 3-8B). Overall, it can be seen that UBA1 was more cytoplasmic in motor neurons than in glial cells; this differential distribution of UBA1 could influence the relative susceptibility of the cell type to UBA1 reduction in conditions such as SMA (Powis et al., 2016).

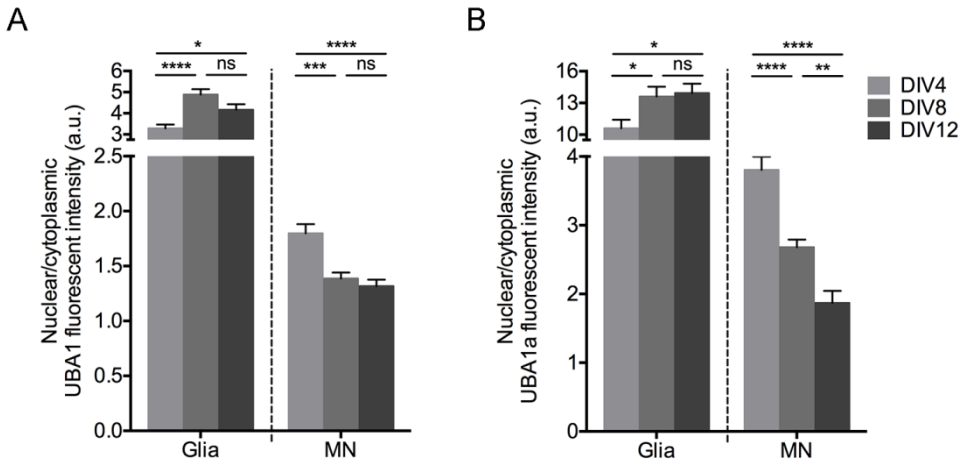

Figure 3-8 UBA1 distribution changes over time in primary motor neurons
A Nuclear to cytoplasmic ratio (NCR) of pan-UBA1 in glial cells and primary motor neurons over time in culture. **B** NCR of UBA1a in glial cells and primary motor neurons over time in culture. **A, B** Motor neurons showed a consistent reduction in NCR, glial cells showed a small increase in NCR between DIV4 and DIV8. One-way ANOVA with Tukey's post-hoc test; ns – not significant, * P≤ 0.05, ** P≤ 0.01, *** P≤ 0.001, **** P ≤ 0.0001.

Here, UBA1 distribution in post-mitotic cells was characterised revealing that differences between UBA1 and UBA1a were consistent over time in cultured motor neurons. Both UBA1a and pan-UBA1 showed a consistent reduction in NCR overtime in motor neurons and UBA1 was consistently more cytoplasmic in motor neurons than in glial cells at each time point investigated.

3.2.4 Characterisation of UBA1 distribution *in vivo*

3.2.4.a Reduction of UBA1 levels in pre- and late-symptomatic SMA motor neurons

To better understand the role of UBA1 in motor neuron pathology in SMA and to characterise UBA1 distribution in motor neurons *in vivo*, lumbar spinal cord sections from SMA mice and control littermates at P2 (pre-symptomatic) and P8 (late-symptomatic) (Figure 2-2) were labelled for UBA1a, a motor neuron specific marker (Choline Acetyltransferase; ChAT) and a nuclear marker (DAPI). Spinal motor neuron pools were imaged at constant confocal settings to allow quantification of nuclear and cytoplasmic UBA1. The UBA1a antibody was used due to the clear staining patterns and reliability of identifying changes in distribution of UBA1 (Figure 3-1C). Furthermore, pan-UBA1 showed non-specific labelling of blood vessels (Figure 3-1D) that could interfere with distribution analysis.

It has previously been shown that UBA1 is reduced across a wide range of tissues at various stages of disease progression in SMA mice (Powis et al., 2016). Previously, UBA1 levels in spinal motor neurons have been reported in SMA (Wishart et al., 2014), however, since publication, the manufacturer changed the description of the antibody used in that study; it is now understood that the antibody used detects UBA7. Therefore, a comprehensive characterisation of UBA1 levels in spinal motor neurons throughout disease progression is essential.

At both pre- and late-symptomatic time points UBA1a was reduced in the nucleus and cytoplasm of SMA motor neurons compared to control (Figure 3-9A, B). Pre-symptomatically there was a 48.3% reduction of nuclear UBA1a and a 41.4% reduction of cytoplasmic UBA1a (Figure 3-9C). Similarly, the late-symptomatic reduction of nuclear UBA1 in SMA was 44.1%; however, the cytoplasmic reduction of UBA1a (28.2%) was less than in pre-symptomatic mice (Figure 3-9D). Whilst at the whole tissue level the reduction of UBA1 in the spinal cord can only be observed late-symptomatically, here, UBA1 was reduced, at the single cell level, in motor neurons at both pre- and late-symptomatic stages of disease. Furthermore, the pre-symptomatic reduction was greater than that seen at late-symptomatic stages.

Overall, this suggests that UBA1 reduction in SMA motor neurons is implicated in the early stages of disease pathogenesis. Moreover, as studies in Drosophila have shown that motor neurons are particularly susceptible to perturbations in UBA1, changes in UBA1 expression may contribute to the motor neuron susceptibility in SMA (Liu and Pfleger, 2013).

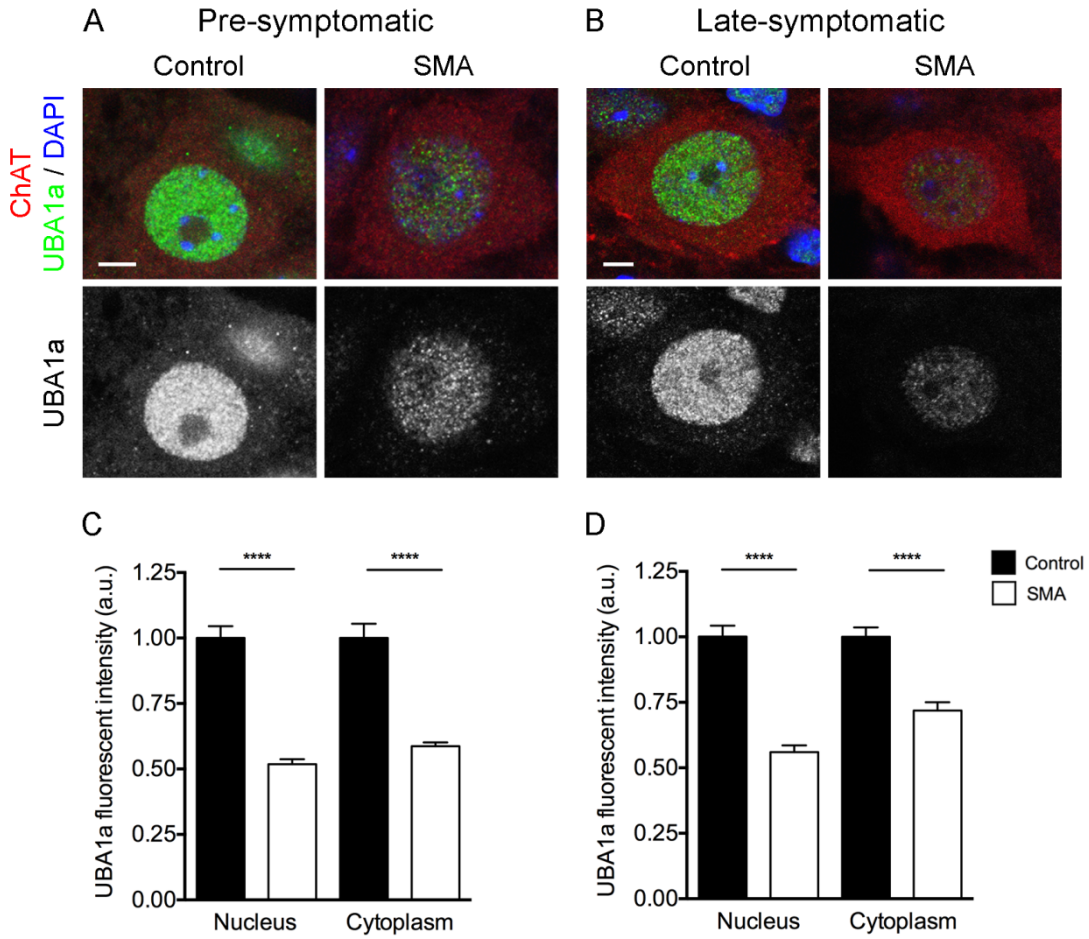

Figure 3-9 UBA1 is reduced in pre- and late-symptomatic SMA spinal motor neurons
Spinal cord sections from SMA and control mice at P2 (pre-symptomatic) and P8 (late-symptomatic) were labelled with UBA1a, a cytoplasmic and motor neuron specific marker (ChAT), and a nuclear marker (DAPI). **A** Pre-symptomatic SMA spinal motor neurons showed a reduction of UBA1a in the nucleus and cytoplasm compared to control mice. **B** Late-symptomatic SMA spinal motor neurons showed a reduction of nuclear and cytoplasmic UBA1a compared to control mice. Scale bars: 5μm. **C** Quantification of absolute intensity of nuclear and cytoplasmic UBA1a in pre-symptomatic SMA motor neurons showed significant reduction of UBA1. Control N=3 mice, n=188 motor neurons; SMA N=3 mice, n=244 motor neurons. **D** Quantification of absolute intensity of nuclear and cytoplasmic UBA1a in late-

symptomatic SMA motor neurons showed significant reduction of UBA1. Control N=3 mice, n=262 motor neurons; SMA N=2 mice, n=168 motor neurons. SMA normalised to control. One-way ANOVA with Tukey's post-hoc test; **** P ≤ 0.0001.

3.2.4.b UBA1 levels are increased in early-symptomatic SMA motor neurons

To investigate why UBA1 reduction in SMA motor neurons is more pronounced at pre- rather than late-symptomatic stages of disease, UBA1 protein levels and distribution at an additional intermediate time point were characterised. To do this, P5 (early-symptomatic) (Figure 2-2) lumbar spinal cords from SMA and control mice were stained for UBA1a and absolute intensity analysis was performed. Surprisingly, at early-symptomatic stages of disease progression a prominent increase in both nuclear and cytoplasmic UBA1a levels was observed (Figure 3-10A). When quantified, the nuclear increase in UBA1a was 41.7% and the cytoplasmic increase was 61.7% compared to controls (P≤0.0001; Figure 3-10B). This is the opposite of what was seen at both pre- and late-symptomatic stages of disease (Figure 3-9), suggesting that this may be the result of an attempted compensatory response by the motor neurons during the early stages of disease.

To investigate this increase in UBA1 levels, NCRs were compared for control and SMA mice at all time points to see if UBA1 distribution was consistently changed over time. There was a significant reduction in the NCR of UBA1a at both pre- and late-symptomatic time points but at early-symptomatic stages there was no significant difference (Figure 3-10C). At pre- and late-symptomatic stages of disease SMA motor neurons had an NCR indicative of more cytoplasmic staining to less nuclear staining compared to controls (pre-symptomatic control=3.16, SMA=2.53, P≤0.01; late-symptomatic control=4.25, SMA=3.69, P≤0.05). This is consistent with the absolute intensity results which show a larger reduction of nuclear than cytoplasmic UBA1a in SMA mice compared to control (Figure 3-9).

Interestingly, both control and SMA mice showed an increase in NCR over time: the highest NCR for both control and SMA mice was at the late-symptomatic stage of disease progression (control=4.25, SMA=3.69; Figure 3-10D). For control

mice, there was no significant difference in UBA1a NCR between P2 and P5, however, between P5 and P8 there was a significant increase in NCR (P5=3.39, P8=4.25; P≤0.0001, Figure 3-10D). In SMA, UBA1a NCR significantly increased between pre- and early-symptomatic stages (P2=2.53, P5=3.46; P≤0.0001). However, there was no significant difference in NCR between early-and late-symptomatic stages of disease progression (Figure 3-10D). To summarise, UBA1a became more nuclear over time in both control and SMA mice, however, the change in control mice occurred between P5 and P8 and the change in SMA mice occurred between P2 and P5.

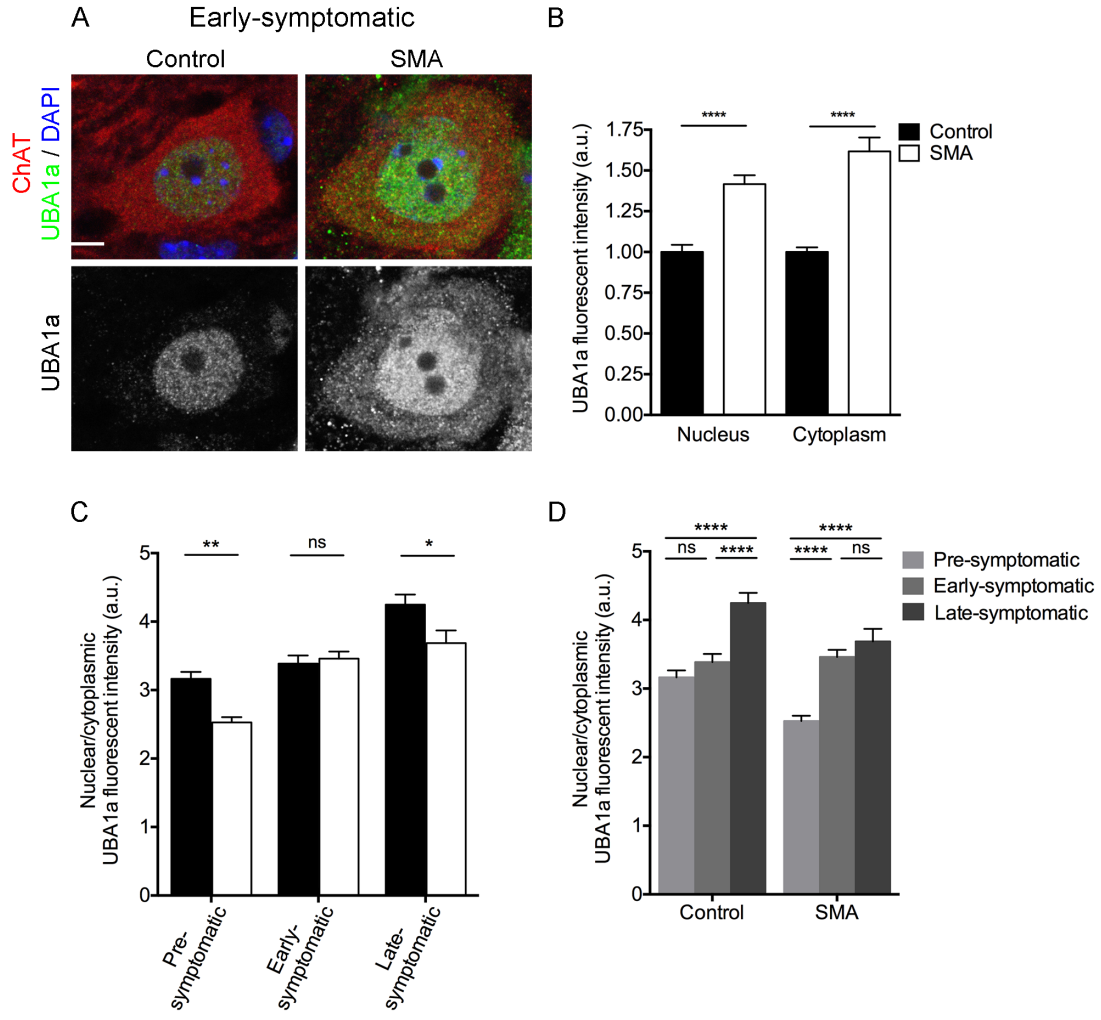

Figure 3-10 UBA1 expression is increased in early-symptomatic SMA spinal motor neurons

Spinal cord sections from SMA and control mice at P5 (early-symptomatic) were labelled with UBA1a, a cytoplasmic and motor neuron specific marker (ChAT), and a nuclear marker

(DAPI). **A** Early-symptomatic SMA spinal motor neurons showed an increase of nuclear and cytoplasmic UBA1a compared to control mice. Scale bar: 5μm. **B** Quantification of absolute intensity of nuclear and cytoplasmic UBA1a showed a significant increase of UBA1 levels in early-symptomatic SMA motor neurons. Control N=3 mice, n=229 motor neurons; SMA N=3 mice, n=243 motor neurons. SMA normalised to control. One-way ANOVA with Tukey's post-hoc test; **** P ≤ 0.0001. **C** Nuclear to cytoplasmic ratio (NCR) of UBA1a for control and SMA mice at each stage of disease progression. Significant reduction in NCR at pre- and late-symptomatic stages of disease progression in SMA mice compared to control. **D** NCR of UBA1a for control and SMA mice at each stage of disease progression, showing increasing NCR for control and SMA from P2 to P8. **C, D** One-way ANOVA with Tukey's post-hoc test; ns – not significant, *P ≤ 0.05, **P ≤ 0.01, **** P ≤ 0.0001.

3.2.4.c Biochemical validation of cytoplasmic specific reduction of UBA1

To biochemically confirm the changes in UBA1 levels observed *in vivo* using IHC, subcellular fractionation was performed on spinal cords from SMA mice and littermate controls at late-symptomatic stage of disease. Late-symptomatic mice were used for these experiments due to the larger volume of tissue available. Spinal cords were homogenised and centrifuged, as previously described (Cox and Emili, 2006) (Figure 2-5), to extract the cytoplasm and quantify UBA1a protein expression by Western blot. The UBA1a antibody was used to allow for reliable comparison between the independent techniques used to study UBA1 distribution *in vivo*. This preparation produced a clean cytoplasmic fraction with minimal nuclear contamination (Figure 3-11A). A clear reduction in UBA1a was seen in the SMA spinal cord cytoplasmic fraction compared to controls (Figure 3-11A), when quantified the cytoplasmic reduction of UBA1a was 46.6% (Figure 3-11B, Exp 1). To ensure this reduction was not due to an artefact of the preparation or technical error, two more preparations were conducted, both of which showed a significant reduction in UBA1a expression. On average, UBA1a was significantly reduced by 38.0% in the cytoplasmic fraction of SMA spinal cords compared to controls (Figure 3-11B).

The reduction in cytoplasmic UBA1a as detected by IHC and biochemically by subcellular fractionation was then compared (Figure 3-11C). There was a 10%

difference in the reduction of cytoplasmic UBA1a detected by IHC (28.2%) and subcellular fractionation (38.0%). However, while both techniques showed a significant reduction in cytoplasmic UBA1a compared to control, there was no significant difference between the two techniques (Figure 3-11C). Subcellular fractionation of SMA and control spinal cords therefore provides a biochemical validation of the cytoplasmic reduction of UBA1 *in vivo*.

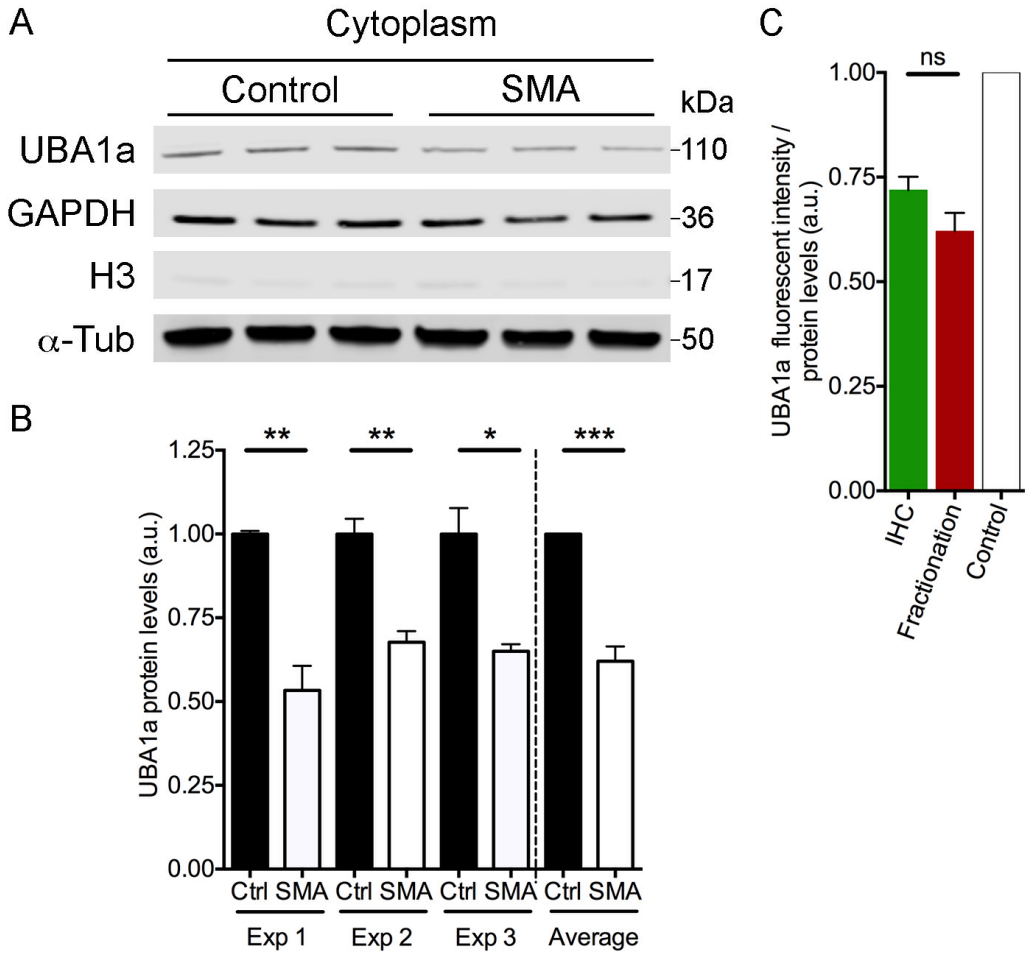

Figure 3-11 Subcellular fractionation of spinal cords confirms cytoplasmic reduction of UBA1 in late-symptomatic SMA mice

Subcellular fractionation was performed on spinal cords from late-symptomatic SMA mice and control littermates to extract the cytoplasmic fraction. **A** Representative quantitative fluorescent Western blot of cytoplasmic fraction from control and SMA spinal cords showed a reduction in UBA1a; cytoplasmic marker (GAPDH), nuclear control (Histone H3), loading control (α-Tubulin). Protein sizes are as indicated (kDa). **B** Quantification of UBA1a in cytoplasmic fraction from SMA and control spinal cords for 3 preparations (experiment [Exp]

1 to 3) and the average. Normalised to α-Tubulin loading control, and then normalised to control mice. N=3 preparations, n=3 mice per condition per preparation. Unpaired 2-tailed Student's t test per preparation and for average; * P ≤ 0.05, ** P ≤ 0.01, *** P ≤ 0.001. **C** Comparison of UBA1a reduction in the cytoplasmic compartment of late-symptomatic SMA spinal cord or spinal motor neurons, quantified by immunohistochemistry (IHC) and fractionation followed by Western blot, with a control shown for reference. Unpaired 2-tailed Student's t test; ns – not significant.

In this section, I demonstrated that UBA1 levels were reduced in SMA spinal motor neurons at both pre-symptomatic and late-symptomatic stages of disease progression. However, at an intermediate stage of disease, UBA1 levels were elevated in SMA mice motor neurons when compared to control mice. Interestingly, both control and SMA spinal motor neurons showed an overall increase in NCR over time; however, this increase occurred at different time points in SMA and control mice. Finally, subcellular fractionation of spinal cords was used to biochemically validate the cytoplasmic reduction of UBA1 in late-symptomatic SMA spinal cords.

3.3 Discussion

Despite the fact that redistribution of UBA1 in specific neuronal populations has been identified in several neurodegenerative diseases (Lopez Salon et al., 2000; Wade et al., 2014; Wishart et al., 2014), the distribution of UBA1 in healthy neuronal cells has until now remained uncharacterised. To improve our understanding of UBA1 distribution, I optimised antibodies to study the localisation of UBA1 for immunolabelling of spinal cord sections and primary neurons, as well as for Western blot. I then validated these antibodies by characterising UBA1 distribution in dividing cultures of cells, which showed the same patterns as described in the literature (Grenfell et al., 1994; Handley-Gearhart et al., 1994; Trausch et al., 1993). I also extended this to show that these differences are consistent over time in culture. Furthermore, I demonstrated that different distribution patterns exist within dividing cultures of cells and I used this finding to establish a quantification method that captures this variation. Next, I determined UBA1 distribution in post-mitotic cells and found that in primary motor neurons UBA1 consistently becomes more cytoplasmic over time, this does not occur in cultures of dividing cells. Finally, to further characterise the role of UBA1 in SMA pathogenesis, I investigated the distribution of UBA1 in spinal motor neurons from control and SMA mice. I observed a reduction of UBA1 in pre- and late-symptomatic SMA mice; however, intriguingly, I identified a prominent increase in UBA1 in early-symptomatic SMA mice. Overall, this indicates that UBA1 reduction in motor neurons is an early pathological feature in SMA and suggests that changes in UBA1 distribution could be an important factor during normal growth and development of neonatal mice.

After having optimised antibodies to reliably detect UBA1, it was possible to observe and quantify variations in UBA1 distribution patterns between different cell types. For example, in glial cells, a range of distribution patterns were observed at all time points investigated, however, there was little change between the different time-points. Conversely, in motor neurons, whilst at each time point there was a relatively specific distribution pattern, this pattern was different for each time point with UBA1 becoming more cytoplasmic the longer the neurons were kept in culture. In glial cells, UBA1 was localised to the nucleus as detected with both antibodies, while in

motor neurons UBA1 showed relatively more cytoplasmic localisation. In comparison to both HEK293 cells and the localisation of UBA1 reported in HepG2 cells (Schwartz et al., 1992), the drastically different localisation of UBA1 isoforms between different cell types and throughout development of specific cell types is striking (Appendix 1). The differential distribution of UBA1 between different cell types could influence the susceptibility of the cell type to UBA1 reduction. As previously mentioned (see 1.1.5), one working theory for the presence of extra-neuronal pathology in SMA is the 'threshold hypothesis' where differential thresholds for low SMN levels exist in different cell types (Hamilton and Gillingwater, 2013; Sleigh et al., 2011). It is plausible that cell type-specific UBA1 distribution patterns could contribute to the sensitivity of that cell type to low levels of SMN.

Furthermore, on investigating UBA1 distribution patterns in spinal motor neurons it became evident that there are clear differences between UBA1 localisation *in vitro* and *in vivo*. In primary motor neurons, UBA1 becomes relatively more cytoplasmic than nuclear over time. This might, for example, correspond to the sustained growth of motor axons possibly requiring a higher demand of UBA1 in the cytoplasm for protein turnover. Interestingly, a different distribution change is observed over time in motor neurons *in vivo*. As neonatal mice grow and begin to mature, UBA1 becomes relatively more nuclear. One reason that could account for this difference is that primary motor neurons are cultured from E13.5 embryos while the spinal motor neurons analysed were from neonatal mice, suggesting that the developmental stage could influence UBA1 distribution. It would be interesting to investigate UBA1 distribution in spinal motor neurons from control mice during embryonic development and after post-natal day 8 to extend the time course of UBA1 distribution in spinal motor neurons. Not only would this allow the role of UBA1 during development to be further investigated, but would also help to tease apart the differences between primary motor neurons and spinal motor neurons and identify whether these differences are due to the stage of development investigated.

Investigating UBA1 distribution in spinal motor neurons also highlighted the changes in UBA1 protein levels and localisation throughout SMA disease

progression. Initially, UBA1 was reduced pre-symptomatically before a potential compensatory response of increased UBA1 levels at the early-symptomatic stage of disease corrected the altered UBA1 distribution. Despite this, due to the large change in the distribution of UBA1 in control mice between P5 (early-symptomatic) and P8 (late-symptomatic), this potential compensatory response may not be sufficient to correct UBA1 protein levels, to remain at control levels between these time points. In this situation, it is possible that the reduction in UBA1 levels may exhibit its main downstream damage during the pre-symptomatic phase, when UBA1 protein levels exhibited their greatest reduction in SMA motor neurons compared to control.

Previously, pre-symptomatic implication of UBA1 in SMA was restricted to neuronal populations outside the spinal cord or to non-neuronal organs (Powis et al., 2016; Wishart et al., 2014). Here reduction of UBA1 was observed in spinal motor neurons for the first time, showing a significant reduction of UBA1 pre-symptomatically. Not only does this suggest that UBA1 reduction could be a driving force in motor neuron degeneration in SMA but also supports the idea that for full therapeutic correction SMA must be treated before clinical symptoms appear (Kariya et al., 2014; Robbins et al., 2014). Furthermore, UBA1 is also differentially distributed between motor neurons of pre-symptomatic SMA and control mice, suggesting that mislocalisation of UBA1 may be harmful during development.

Interestingly, subcellular fractionation of spinal cords biochemically validated the late-symptomatic reduction of UBA1 seen in the cytoplasm of SMA mice. While subcellular fractionation of P8 spinal cords produces robust and reliable data that can be suitably quantified from cytoplasmic fractions, several technical limitations prevented this from being possible for nuclear fractions. The primary issue was tissue quantity, when performing subcellular fractionation on spinal cords of this size, the amount of protein present in the final nuclear fraction was too minimal to detect UBA1. Therefore, while the cytoplasmic fraction can be easily and reliably quantified, the nuclear fraction did not lend itself to quantification in this situation. In contrast to this, nuclear UBA1 can be reliably quantified by distribution analysis on IHC of spinal cord sections. In fact, while the nuclear analysis is based on DAPI which provides a clear outline to the nucleus, the cytoplasmic outline is

based on ChAT staining which provides a less clear-cut edge of the cell body. Therefore, while fractionation can accurately measure cytoplasmic UBA1 levels to validate the IHC cytoplasmic results, the nuclear results from IHC are likely to be more accurate than those for the cytoplasm.

In conclusion, a robust set of antibodies for both *in vivo* and *in vitro* work to study UBA1 have been identified. Existing data on the distribution of UBA1 in dividing cultures of cells has been extended to confirm that differences between UBA1 and UBA1a localisation are consistent over long-term cultures of cells. Moreover, for the first time UBA1 distribution has been investigated in a healthy neuronal population, which showed pronounced variation and changes over time in distribution patterns compared to long-term cultures of dividing cells. Finally, a novel characterisation of UBA1 distribution throughout disease progression in SMA spinal motor neurons has been performed and validated by biochemical fractionation. From this work, it is evident that UBA1 reduction may be an important pre-symptomatic molecular feature of SMA in motor neurons. To understand the role of UBA1 in motor neuron degeneration it will be essential to determine what causes the reduction of UBA1 and what effect the reduction in UBA1 has on the proteome. As the primary canonical function of UBA1 is to charge the ubiquitin system (Bedford et al., 2011; Groen and Gillingwater, 2015), it will be interesting to investigate if defects in the ubiquitin proteasome system occur downstream of UBA1 reduction or whether other protein families and pathways are disrupted following changes in UBA1 protein levels.

Chapter 4 Identification of downstream targets of UBA1

4.1 Introduction

The ubiquitin-like modifier activating enzyme 1 (UBA1) is a major downstream target of the SMN protein with clear applications as a therapeutic target in SMA (Powis et al., 2016; Wishart et al., 2014). In Chapter 3 of this thesis I showed that UBA1 expression is reduced pre-symptomatically in SMA spinal motor neurons implicating UBA1 in the pathogenesis of SMA. Moreover, I demonstrated that there is also an early-symptomatic compensatory phase where UBA1 protein levels increase within the spinal motor neurons in SMA. In order to understand the role of UBA1 in motor neuron degeneration it will be important to unravel the relevance of these changes in UBA1 expression and the effect these changes in UBA1 expression have on the rest of the proteome.

UBA1 is the enzyme at the apex of the ubiquitylation cascade, being responsible for the activation of ubiquitin and thus functionality of ubiquitin signalling pathways (Bedford et al., 2011). It is therefore not surprising that UBA1 accounts for ~2% of the protein in all cells (Clague et al., 2015; Yang et al., 2013). Despite the abundance of UBA1, very little is known about the functions of the enzyme outside the ubiquitin proteasome system. Indeed, even within the pathway where UBA1 has its canonical function, there are still large gaps in our knowledge.

While the role of UBA1 itself is well defined within the ubiquitin-proteasome system (see 1.2.1), the relationship between UBA1 and the other enzymes in the system is less well understood. To elaborate, there are approximately 40 E2 enzymes known to conjugate ubiquitin downstream of UBA1 and around 600 E3 enzymes that ligate ubiquitin to the substrate protein (Bedford et al., 2011). The E2 enzymes are not only responsible for delivering the activated ubiquitin to the E3 ligase but they also determine the topology of ubiquitin-chain linkage and switch between initiation and elongation of polyubiquitin chains (Kulathu and Komander, 2012; Ye and Rape, 2009). Thus, E2 enzymes are responsible for mediating ubiquitin chain assembly.

Despite this, the selectivity of E2 enzymes for the much greater number of E3 enzymes remains uncharacterised.

The E3 ubiquitin ligase enzymes are reasonably well characterised in terms of their general properties and can be split into four categories based on their structure and function. Three classes of E3 enzymes function as adaptors by binding a ubiquitin loaded E2 and a substrate protein to promote ubiquitylation, these are U-box E3s, monomeric RING finger E3s and multi-subunit E3 complexes containing a RING finger protein (Bedford et al., 2011). The fourth class of E3 enzymes are HECT domain E3s which form a thioester intermediate with ubiquitin before transferring the ubiquitin to a substrate (Ambrozkiewicz and Kawabe, 2015; Bedford et al., 2011). Regardless of the subclass of the E3 enzyme, the enzyme is responsible for the recruitment of specific substrate proteins to enable ubiquitylation. Although there is an increasing number of protein substrates whose E3 enzymes are known, these are generally one-to-one relationships without understanding or knowing the full range of substrates for each E3 (Kwon et al., 2013; Teixeira et al., 2016). Likewise, some E2-E3 pairs have been identified but again without characterising how the wide range of E3 enzymes relates to the smaller number or E2 enzymes (Clague et al., 2015).

Although several E2 enzymes have been shown to mediate ubiquitylation downstream of UBA1, other E2s have been shown to associate with another E1 that also activates ubiquitin (Liu et al., 2017b). The ubiquitin-like modifier activating enzyme 6 (UBA6) is the only other E1 enzyme that has been shown to activate ubiquitin. Although, until recently, it was thought that UBA6 was merely a ‘back-up’ ubiquitin activating enzyme with its main function to activate FAT10, a ubiquitin-like protein (UBL) (Bedford et al., 2011). Indeed, FAT10ylation mediated by UBA6 is responsible for signalling UBA1 for degradation (Bialas et al., 2015). A recent study has, however, shown that UBA6-mediated ubiquitylation may be more common place that initially thought; identifying that UBA6 may be responsible for mediating ubiquitylation of 697 substrates with only 258 of these substrates overlapping with UBA1. The study also identified two UBA6 specific E2 enzymes and a further four E2 enzymes that mediate ubiquitylation by both UBA1 and UBA6

(Liu et al., 2017b). This adds further complexity to understanding the relationships between E1, E2 and E3 enzymes. Moreover, due to the increased understanding of the possible role of UBA6 in ubiquitin conjugation pathways and the overlap of these two E1 enzymes, to identify UBA1-dependent substrates it will be necessary to investigate whether or not UBA6 may be influencing the ubiquitylation of the substrates.

Interestingly, specific downstream pathways dependent on UBA1 mediated ubiquitylation have been identified. As previously described (see 3.1), UBA1 has differential localisation throughout the cell cycle, this corresponds to the ubiquitylation and deubiquitylation of proteins required for progression through the cell cycle; for example, p53 and Histone H2A (Joo et al., 2007; Kitagaki et al., 2009; Yang et al., 2007). Temperature-sensitive mutations of UBA1 show that loss of UBA1 leads to cell cycle arrest due to reduction in overall ubiquitylation and protein degradation (Ghaboosi and Deshaies, 2007; Sugaya et al., 2014). Interestingly, UBA1 has also been shown to be essential for ubiquitylation-mediated repair of double-strand DNA breaks, thus implicating UBA1 in DNA repair pathways (Moudry et al., 2012). The influence of UBA1 on these pathways require its ability to activate ubiquitin and the canonical ubiquitylation pathway.

There are, however, suggestions that UBA1 may have functions outside the canonical ubiquitylation cascade. For example, it has been demonstrated that there may be crosstalk between UBA1 and autophagy: the normal E1 (Atg7) and E2 (Atg3) enzymes required for autophagy are bypassed and Uba1 instead is required for Atg8-dependent autophagy, although not by direct activation of the UBL Atg8 (Chang et al., 2013). Moreover, it has also been demonstrated that Uba1 is required for axon development in Drosophila and that inhibition of Uba1 leads to increased miniature and spontaneous synaptic currents in cultured hippocampal neurons (Rinetti and Schweizer, 2010; Watts et al., 2003). Although it is uncertain how this is mediated (whether through ubiquitylation or a non-canonical function of UBA1) it indicates the broad range of pathways in which UBA1 is implicated and the possibility of UBA1 having multiple non-canonical functions.

In order to understand the role of UBA1 in the pathogenesis of SMA it will be essential to identify the key consequences of the widespread reduction of UBA1 expression. Similarly, it is still unclear whether the primary consequence of disruption to UBA1 expression is dysfunction to the ubiquitin-proteasome system or pathways downstream of the ubiquitylation cascade. Interestingly, very little is known about the specificities of E2 and E3 enzymes and therefore, it is unclear which E2s, E3s or indeed protein substrates might be relevant for UBA1-mediated degeneration in SMA. However, there remains the possibility that reduction of UBA1 might be altering a non-canonical function of the enzyme and thus contributing to pathogenesis of SMA. Therefore, to delineate the effects of changes in UBA1 expression levels on downstream proteins and to identify UBA1-dependent pathways that may be relevant for SMA, a proteomics screen was performed. To do this, a model system where UBA1 protein levels could be modulated was optimised and a label-free proteomics screen was performed to identify the effects of changes in UBA1 expression on the proteome. Proteins from UBA1-dependent protein families were then validated both *in vitro* and *in vivo* with the aim of understanding the downstream effects of UBA1 dysregulation in SMA.

4.2 Results

4.2.1 Experimental design for proteomic profiling of the effects of UBA1 modulation *in vitro*

4.2.1.a Optimisation of UBA1 overexpression and knockdown

To investigate downstream targets of UBA1 by performing a proteomics screen, a suitable *in vitro* model system was required. As UBA1-dependency of downstream targets will be key to understanding the role of UBA1 in SMA, the model system needed to be amenable to both overexpression and knockdown of UBA1. HEK293 cells were chosen as high transfection efficiencies can be achieved, which is essential to achieve a homogeneous population of cells necessary for the proteomics screen. Overexpression of UBA1 was tested with different concentrations of transfection reagent (Lipofectamine 2000), to identify the optimal conditions for maximum transfection efficiency. UBA1 overexpression increased with increasing amounts of the transfection reagent (Figure 4-1A), 9µl of transfection reagent was selected for use in the proteomics experiments due to the robust overexpression achieved (Figure 4-1C). For UBA1 knockdown, untreated, transfection reagent only, and scrambled siRNA control conditions were compared to siRNA targeting exons 24 and 25 of UBA1 (Figure 4-1B). Transfection with the UBA1 siRNA led to a 71.87% knockdown of UBA1 compared to average control levels (Figure 4-1D), comparable to the SMN-dependent reduction in UBA1 seen in SMA (Powis et al., 2016; Wishart et al., 2014). Use of a fluorescent siRNA indicated that transfection efficiency of siRNA was greater than 95% (data not shown). Overall, this system is suitable to achieve robust overexpression and knockdown of UBA1 in an experimentally tractable cell system.

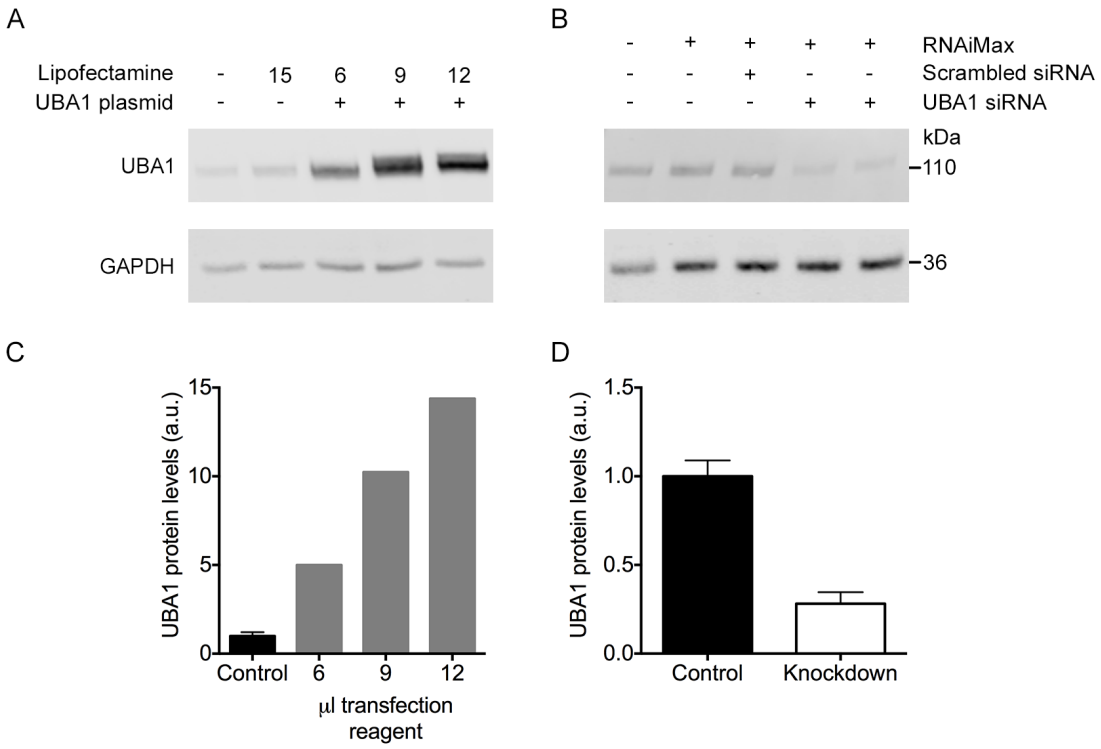

Figure 4-1 Optimisation of UBA1 overexpression and knockdown *in vitro*
Optimisation of UBA1 overexpression and knockdown was performed on HEK293 cells. **A** Representative fluorescent Western blot of HEK293 cells: control cells, lipofectamine only control, HEK293 cells transfected with UBA1 plasmid and increasing volume of lipofectamine (values shown as µl) showing increasing overexpression of UBA1. **B** Representative fluorescent Western blot of HEK293 cells: control cells, RNAiMax only control, scrambled siRNA control, and siRNA directed against UBA1 showing reduction of UBA1 protein levels. **A** and **B** GAPDH used as a loading control, protein sizes are as indicated (kDa). **C** Quantification of UBA1 protein levels (normalised to GAPDH loading control), control represents control cells and lipofectamine only control. **D** Quantification of UBA1 knockdown (normalised to GAPDH loading control) control represents the first three bands from panel **B**.

4.2.1.b Validation of changes in UBA1 protein levels in samples to be used for proteomics analysis

Following optimisation of UBA1 overexpression and knockdown, samples for label-free proteomics were generated by applying the same experimental design from the optimisation phase. HEK293 cells were transfected 48 hours after plating. For overexpression samples, the cells were collected 24 hours after transfection and

knockdown samples were collected 48 hours after transfection (Figure 4-2A). Three biological replicates were included for each experimental condition along with three control (non-transfected) samples.

To confirm UBA1 protein expression in the samples used for the proteomics screen, Western blots using both pan-UBA1 and UBA1a antibodies were performed. The UBA1 plasmid encoded full-length UBA1 i.e. UBA1a, however, the siRNA used was targeted against exons common to both isoforms of UBA1. Therefore, UBA1 protein levels were quantified with both antibodies to get an accurate assessment of the changes to UBA1 protein levels in the HEK293 cells. Again, as with optimisation, there was a robust knockdown of UBA1 (Figure 4-2B), detected by both antibodies with reduction of 76.15% ($P \leq 0.01$) detected by pan-UBA1 and of 74.22% ($P \leq 0.001$) with UBA1a (Figure 4-2C). Similarly, the overexpression of UBA1 was significant, with a 10.11 fold change increase ($P \leq 0.001$) detected by pan-UBA1 and an increase of 4.37 fold ($P \leq 0.01$) detected by UBA1a (Figure 4-2D, E). Interestingly pan-UBA1 detected the greatest relative overexpression (Figure 4-2E), which could be due to antibody affinity. This demonstrates that UBA1 levels were significantly up- and down-regulated in the proteomics samples. Importantly, however, following UBA1 knockdown, UBA1 protein levels were not knocked-down beyond biologically relevant levels (e.g. completely depleted) with respect to reduction in UBA1 protein that is seen in SMA (Powis et al., 2016; Wishart et al., 2014).

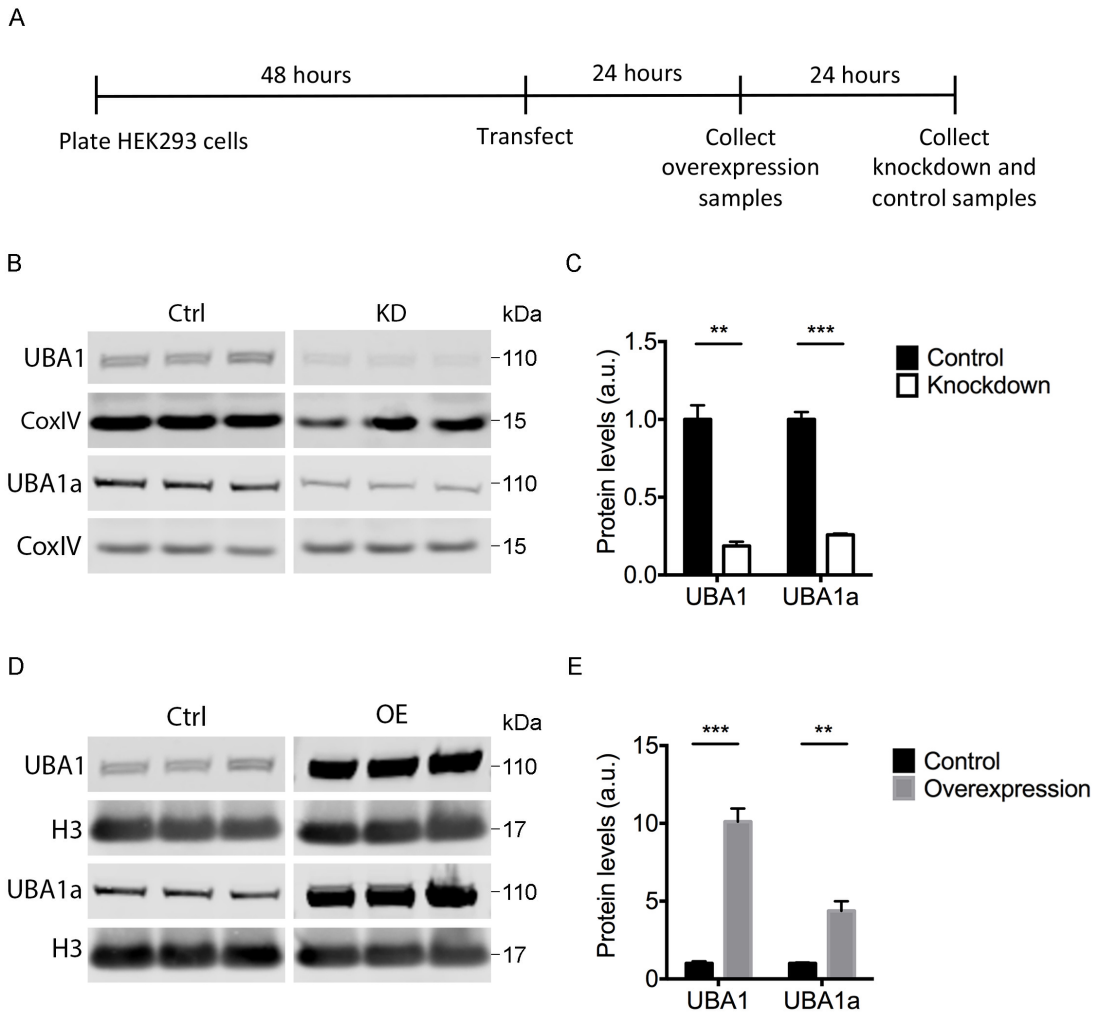

Figure 4-2 UBA1 protein levels in samples to be used for proteomic analysis
Quantification of UBA1 protein levels in HEK293 cells used for the proteomics screen. **A** Timeline of sample preparation. **B** Fluorescent Western blot of UBA1 protein levels, detected by pan-UBA1 and UBA1a, after knockdown of UBA1. CoxIV as loading control. **C** Quantification of UBA1 protein levels after UBA1 overexpression showing significant downregulation detected by both antibodies. **D** Fluorescent Western blot of UBA1 protein levels, detected by pan-UBA1 and UBA1a, after overexpression of UBA1. Histone H3 (H3) as loading control. **E** Quantification of UBA1 protein levels after UBA1 overexpression showing significant downregulation detected by both antibodies. **B, D** Samples run on the same gel in non-contiguous lanes. Protein sizes are as indicated (kDa). **C, E** Samples were normalised to loading control and then overexpression and knockdown samples were normalised to control. Unpaired two-tailed Student's t-test; ** $P \leq 0.01$, *** $P \leq 0.001$; n=3 separate transfections per condition.

4.2.1.c Characterising SMN and UBA6 protein levels in samples to be used for proteomic analysis

After validating the changes in UBA1 protein levels in the samples used for the proteomics screen, protein levels of SMN and UBA6 were characterised in the proteomics samples. As the aim of this chapter is to tease out UBA1-dependent pathways that may be relevant for SMA it was necessary to investigate whether protein expression changes are independent of changes in SMN expression. It was also important to determine UBA6 protein levels in these samples due to its role in degradation of UBA1 and the recent identification of its wider role in the ubiquitylation process (Bialas et al., 2015; Liu et al., 2017b).

Interestingly, following knockdown of UBA1, the protein levels of both SMN and UBA6 remained unchanged (Figure 4-3A, B). This indicates that any changes in protein levels following UBA1 knockdown were not due to influences from either SMN or UBA6. Following UBA1 overexpression, SMN protein levels remained unchanged (Figure 4-3C, D) however, UBA6 was upregulated by 65.13% ($P \leq 0.05$) compared to control HEK293 cells (Figure 4-3D). This upregulation of UBA6 could be due to a feedback mechanism to mediate a reduction in the protein levels of UBA1. However, due to the increase in its expression it needs to be noted that UBA6 may influence proteins changed upon UBA1 overexpression. Despite this it can be seen that neither SMN nor UBA6 are influencing proteins changed upon knockdown of UBA1 which is of particular importance as UBA1 reduction is the primary dysregulation of UBA1 seen in SMA (Wishart et al., 2014).

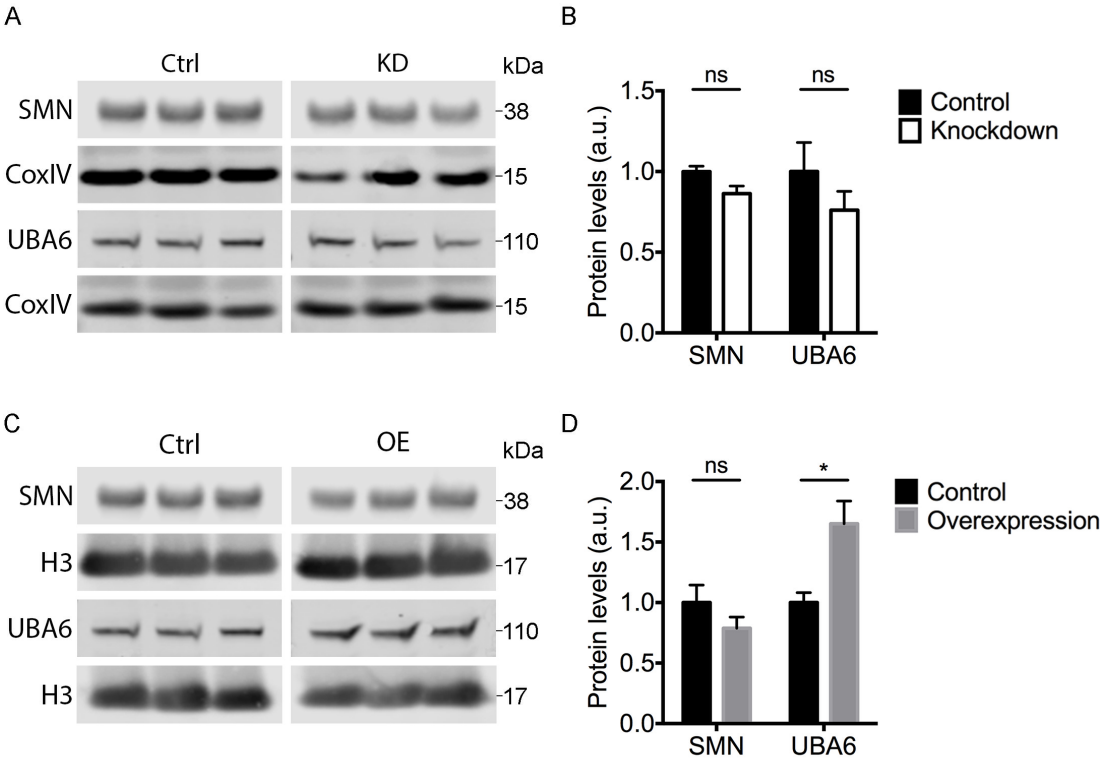

Figure 4-3 UBA6 was upregulated following UBA1 overexpression

Quantification of SMN and UBA6 protein levels in HEK293 cells used for the proteomics screen. **A**, **C** Fluorescent Western blot of SMN and UBA6 protein levels after (**A**) knockdown and (**C**) overexpression of UBA1. **A** CoxIV, **C** Histone H3 (H3) as loading control. **B**, **D** Quantification of SMN and UBA6 protein levels after (**B**) knockdown and (**D**) overexpression of UBA1. **D** Significant upregulation of UBA6 following UBA1 overexpression. **A, C** Samples run on the same gel in non-contiguous lanes. Protein sizes are as indicated (kDa). **B, D** Samples were normalised to loading control and then overexpression and knockdown samples were normalised to control HEK293 cells. Unpaired two-tailed Student's t-test; ns – not significant, * $P \leq 0.05$; n=3 separate transfections per condition.

To summarise, here I optimised transfection conditions for overexpression and knockdown of UBA1 in HEK293 cells and used this experimental design to generate samples for a label-free proteomics screen. I validated that UBA1 expression was significantly changed in the samples used for the proteomics screen. Then I identified that SMN expression was not changed in these samples, but that UBA6 may affect the expression of proteins changed on UBA1 overexpression.

4.2.2 Proteomic analysis

In order to identify downstream targets of UBA1, whether they be E2 and E3 enzymes, specific protein substrates, or targets of non-canonical functions of UBA1, label-free proteomics was performed on HEK293 cells with modulated UBA1 protein levels. Label-free proteomics was chosen due to the larger proteome coverage attained compared to proteomic approaches relying on labelling, as well as the better quantitation that can be achieved as the output is an average absolute abundance for each protein instead of a relative abundance (Gstaiger and Aebersold, 2009). The analysis of the proteomics dataset focused on identifying proteins that were changed in opposite directions in the two experimental conditions compared to control. Therefore, proteins that were upregulated following UBA1 overexpression and downregulated following UBA1 knockdown, compared to control, were classified as UBA1-dependent, as were proteins downregulated following UBA1 overexpression and upregulated following UBA1 knockdown, compared to control. This analysis focuses on identifying pathways and proteins that behave in one of these UBA1-dependent manners. For reference, the filtered dataset (see method 2.12.2.b, Figure 2-7) can be found in Appendix 2 and a table containing proteins with a change in expression greater than 20% following both UBA1 overexpression and knockdown can be found in Appendix 3.

4.2.2.a Gene ontology term enrichment

To generate an initial overview of the protein families and pathways changed in the dataset, gene ontology term enrichment analysis was performed in DAVID (see method 2.12.3.a). Both gene functional classification and functional classification were performed, where the first identifies gene families that are enriched and the latter identifies enrichment of specific protein functions otherwise known as gene ontology (GO) terms. The enrichment score (ES) represents the enrichment of the different terms in this dataset compared to a generic background dataset. For reference, an ES of 1.3 is equivalent to a p-value of 0.05, an ES of 3 is equivalent to a p-value of 0.001 and an ES of 4 is equivalent to a p-value of 0.0001.

Within the dataset, four gene groups were enriched: tRNA ligases, translation elongation factors, small molecule synthesis and nuclear transport. The ESs for these groups ranged from 4.14 to 6.17 showing clear significance of the enrichment of these gene groups in the dataset. Interestingly, there is no enrichment of genes related to the ubiquitin-proteasome system (Table 4-1A). When identifying gene ontology term enrichment (protein functions), all of the enriched gene groups were represented with ESs ranging from 2.95 to 4.56 (Table 4-1A, B). Gene ontology terms enriched with lower ESs included ubiquitin-like conjugation, protein complex assembly, and ATP and nucleotide binding (Table 4-1B); functions related to the ubiquitin conjugation process. From this initial analysis, it is evident that modulation of UBA1 protein levels does not cause massive disruption to E2 and E3 enzymes. Therefore, this dataset is comprised of novel downstream targets of the ubiquitin conjugation process or targets of non-canonical functions of UBA1.

A

Gene functional classification

Gene group	Enrichment score
tRNA ligases	6.17
Eukaryotic translation elongation factors	6.11
Small molecule synthesis	5.31
Nuclear transport	4.14

B

Functional classification

GO term cluster	Enrichment score
Translation elongation	4.56
tRNA ligase activity	4.31
Nucleic acid synthesis	4.10
Cytoskeleton	3.30
Protein transport and localisation	3.03
RNA transport and localisation	2.95
Protein complex assembly	2.85
ATP and nucleotide binding	2.55
Glycolysis	2.45
Cytoskeletal binding	2.36
Ubl conjugation	2.25
Membrane bound vesicle	2.04
GTPase binding	2.02

Table 4-1 Gene ontology term enrichment

A Enrichment of different gene families within the dataset. **B** Enrichment of functional protein groups within the dataset.

4.2.2.b Identification of UBA1-dependent expression profiles

As the primary aim of this proteomic screen was to detect UBA1-dependent proteins, it was necessary to identify groups of proteins with expression profiles that show UBA1-dependency. To begin this process, a correlation analysis was performed in progenesis (see method 2.12.2.b) to group proteins based on the similarity of their expression profiles. The dendrograms in Figure 4-4A and B show all the proteins in the dataset with the vertical distance between each protein representing expression profile similarity. The left-hand side of the dendrogram was highlighted in blue in Figure 4-4A and the bottom panel of Figure 4-4A displays the expression profiles of these proteins; similarly, Figure 4-4B shows the expression profiles of proteins on the right hand side of the dendrogram. The expression profiles show the standardised normalised abundance of each protein. Each line in the expression profile represents a protein and each point represents the standardised normalised abundance of that protein in one sample (3 replicates per condition).

The proteins highlighted in Figure 4-4A showed a general trend of upregulation following UBA1 overexpression and downregulation following UBA1 knockdown compared to control. Conversely in Figure 4-4B, where the proteins on the right-hand side of the dendrogram were highlighted, the generalised expression profile showed a downregulation following UBA1 overexpression and upregulation following UBA1 knockdown. Interestingly, and perhaps counterintuitively, more proteins were upregulated on UBA1 overexpression than downregulated (Figure 4-4A, B). Although the broad generalised expression profiles were clear for each of the two main clusters in the dendrogram, there were proteins that did not conform completely to either of these expression profiles and therefore do not classify as UBA1-dependent. Thus, it will be necessary to further subdivide the groups of proteins into clusters with greater similarity or more refined protein expression profiles to tease out UBA1-dependency.

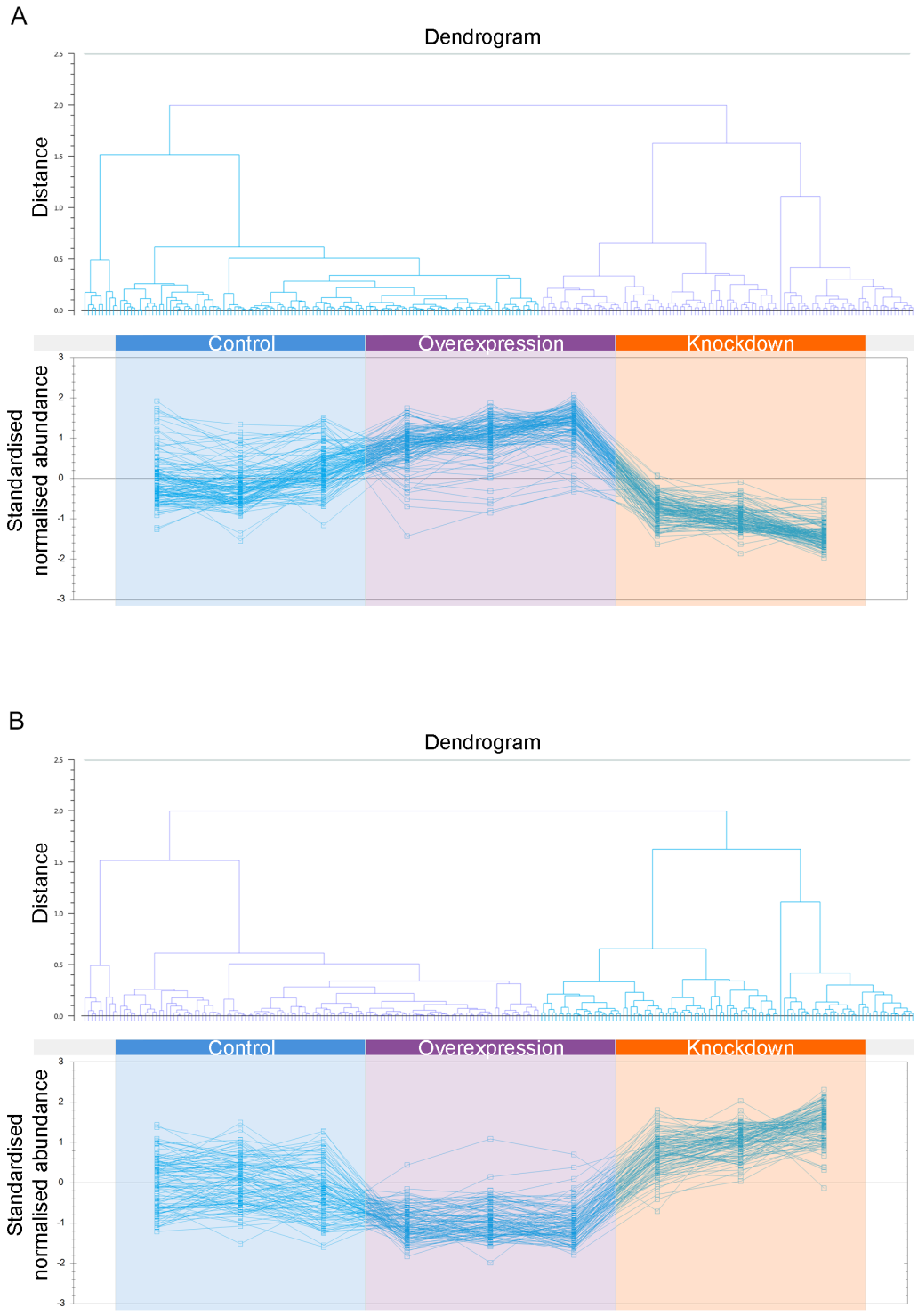

Figure 4-4 Characterisation of protein expression profiles

Overview of protein expression profiles across control, UBA1 overexpression and UBA1 knockdown conditions. **A** Top panel: left side of dendrogram highlighted in blue showing similarity of expression profiles. Bottom panel: protein expression profiles displayed as standardised normalised abundance of proteins on left side of dendrogram. Proteins have a

trend of increased expression following UBA1 overexpression and decreased expression following UBA1 knockdown compared to control. **B** Top panel: right side of dendrogram highlighted in blue. Bottom panel: protein expression profiles displayed as standardised normalised abundance of proteins on right side of dendrogram. Proteins have a trend of decreased expression following UBA1 overexpression and increased expression following UBA1 knockdown compared to control.

4.2.2.c Analysis in Biolayout identified two UBA1-dependent protein clusters

In order to identify groups of UBA1-dependent proteins, the protein groups were further divided into clusters based on their expression profiles by performing analysis in Biolayout (see method 2.12.3.b). This software allows the visualisation and analysis of network graphs based on the relationship between proteins: in this case the networks and derived clusters were based on the similarity of the protein expression profiles. Each protein was represented by a coloured node, and the relationships between the proteins were represented by edges (pale blue). The colour of the node indicates the cluster that protein belongs to.

As was seen in Figure 4-4, the analysis reveals two main groups of proteins (Figure 4-5A), each of which can be further subdivided, generating 6 smaller clusters of proteins. Three proteins do not fit into a cluster (turquoise, left of top group; Figure 4-5A). Each cluster showed its own expression profile which was displayed as the mean expression profile for that cluster with SEM (Figure 4-5B-D). Two of the clusters showed UBA1-dependent expression profiles (Figure 4-5B, C), while the other four clusters showed a prominent expression change in one experimental condition (Figure 4-5D). The first UBA1-dependent cluster of proteins, Cluster 1, contained proteins that are upregulated following UBA1 overexpression and downregulated following UBA1 knockdown (Figure 4-5B). Subsequent analysis using DAVID revealed that the proteins in this cluster function in glycolysis, translation elongation, assembly of protein complexes or as tRNA ligases (Table 4-2). Cluster 4 also showed a UBA1-dependent expression profile with proteins downregulated following UBA1 overexpression and upregulated following UBA1 knockdown (Figure 4-5C). Proteins in Cluster 4 function in transport and localisation

of protein, RNA and nucleic acids (Table 4-2). Interestingly, the functions of the UBA1-dependent clusters overlap with the enriched gene ontology terms (Table 4-1). Thus, indicating that these are key protein families and functions changed on modulation of UBA1 protein levels.

Although the other clusters do not show UBA1-dependency they provide useful information about the proteomic screen and the function of UBA1. Based on the expression profiles, it can be suggested that Clusters 2 and 3 may be affected by changes in ubiquitin activation by UBA1 (Figure 4-5D). Cluster 3 showed an expression profile with the main change in the samples with UBA1 overexpression (Figure 4-5D), as UBA6 was upregulated in these samples (Figure 4-3D) this E1 enzyme may influence the expression profile of the proteins in Cluster 3. This was the only cluster with a change in expression profile only when UBA1 was overexpressed (Figure 4-5B-D), indicating that UBA6 is unlikely to have a widespread effect on the proteins in the dataset. Assessing the functions of proteins in Cluster 5 suggested that following UBA1 knockdown there was an overall reduction in ubiquitylation (Table 4-2), which could be expected on knockdown of the key E1 ubiquitin activating enzyme. Furthermore, Cluster 6 highlighted the role of UBA1 in the progression of the cell cycle and suggests that disruption to this pathway occurs when UBA1 expression is reduced (Figure 4-5D, Table 4-2).

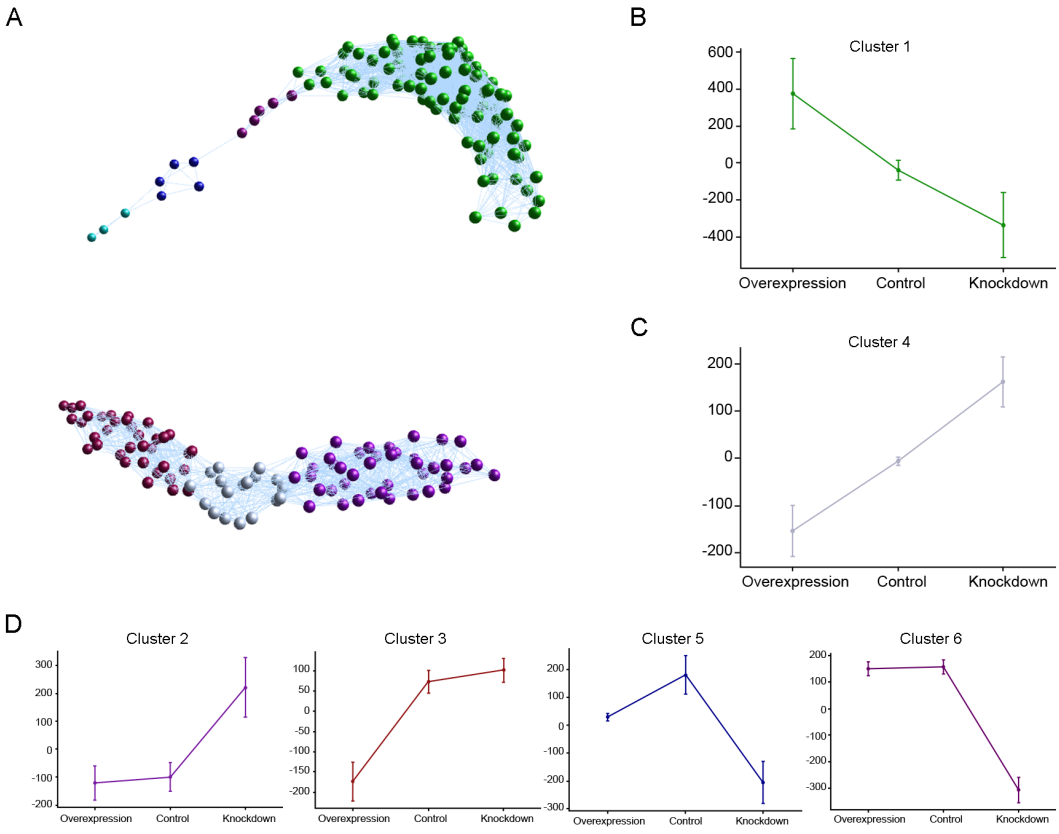

Figure 4-5 Analysis in Biolayout revealed two UBA1-dependent protein clusters

Identification of UBA1-dependent protein expression profiles. **A** Overview of clustering based on similarity of protein expression profiles, two main groups of proteins can be seen. Each node represents a protein and the colour of the node indicates the cluster the protein belongs to. **B** Proteins in Cluster 1 (green nodes) show a UBA1-dependent protein expression profile. **C** Proteins in Cluster 4 (silver nodes) show the opposite UBA1-dependent protein expression profile to those in Cluster 1. **D** Clusters 2,3,5 and 6 show other expression profiles. **B**, **C**, **D** Protein expression profiles are shown as mean normalised abundance on a pareto scale with the SEM for that cluster.

Protein cluster	Number of proteins	Gene ontology term enrichment
Cluster 1	110	tRNA ligase activity, glycolysis, translation elongation, protein complex assembly
Cluster 4	18	Protein, RNA and nucleic acid transport and localisation
Cluster 2	41	Mitochondrial processes, membrane proteins
Cluster 3	36	Cytoskeleton and scaffolding proteins, cell-cell junctions
Cluster 5	5	Ligase activity and ubiquitin pathway binding
Cluster 6	5	Molecular chaperones, cell cycle progression

Table 4-2 Functional classification of protein clusters

Table showing functions of proteins in clusters from Figure 4-5 based on gene ontology term enrichment for Clusters 1 to 4 (in DAVID) and manual searching of protein functions for

Clusters 5 and 6. For functional annotation classification of Cluster 1, enrichment scores (ES) were > 5; for all other clusters analysed in DAVID, ES > 1.5.

4.2.2.d Ingenuity pathway analysis revealed UBA1-dependency in protein networks

To investigate UBA1-dependency at the level of individual proteins and to assess the relationships between the UBA1-dependent protein families, a network analysis was performed using the ingenuity pathway analysis (IPA) software (see method 2.12.3.c). IPA uses both statistical analyses and a curated knowledge base of published protein interactions and associations to identify causal relationships within the dataset. One of the analysis platforms within IPA can generate networks showing associations and relationships between proteins in the dataset, as well as showing relative expression changes of the proteins - red symbols indicate upregulated proteins and green symbols indicate downregulated proteins.

Here, networks were generated for proteins changed following UBA1 overexpression compared to control (Figure 4-6A) and for proteins changed following UBA1 knockdown compared to control (Figure 4-6B). Interestingly, the network for each condition was composed of the same proteins and of these 35 proteins only 5 were not present in the dataset (white symbols). From the remaining 30 proteins, 25 behave in a UBA1-dependent manner (Figure 4-6), suggesting that modulations in UBA1 protein levels cause widespread reciprocal changes in expression of a range of proteins. These networks include proteins with tRNA ligase activity (YARS, GARS, HARS, WARS), translation elongation factors (EEF1G, EEF1B2, EEF1A1, EEF1D) and nuclear transport proteins (IPO4), all of which show UBA1-dependency across the two conditions (Figure 4-6). This further establishes the relevance of these protein families to the dataset and extends this to identify specific proteins within these families that are UBA1-dependent. The networks shown here also highlight crossover between the proteins from the different UBA1-dependent protein families.

A

UBA1 overexpression

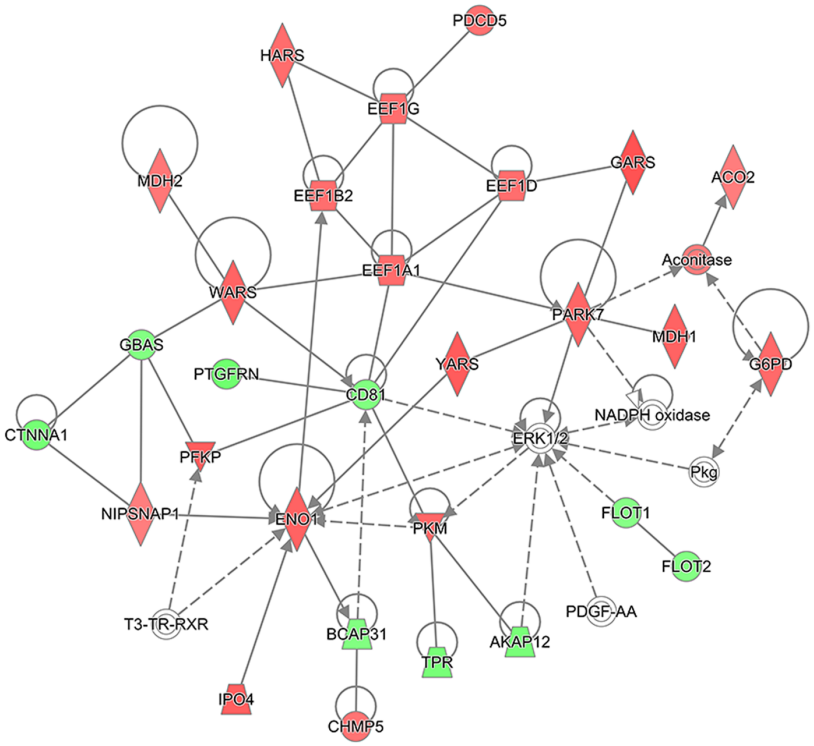

B

UBA1 knockdown

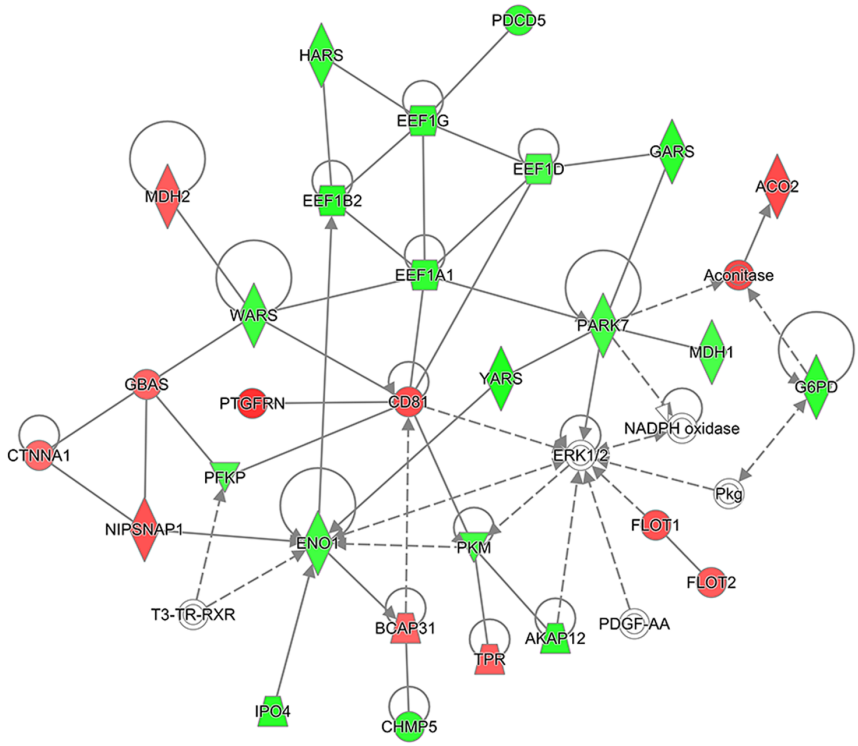

Figure 4-6 Protein networks showed UBA1-dependency

Networks of proteins generated in Ingenuity pathway analysis for (**A**) proteins changed on UBA1 overexpression compared to control and (**B**) proteins changed on UBA1 knockdown compared to control. **A, B** Proteins within red shapes are upregulated, proteins in green shapes are downregulated, proteins in white shapes are not present in the dataset. The shape of the protein in the network depicts the protein function: diamonds represent enzymes, triangles represent kinases, hexagons indicate translation regulators, trapeziums represent transporters, circles indicate other protein classes and circles with an inner circle depict a protein complex. Solid lines show direct binding of proteins, dotted straight lines show indirect interaction by protein binding. Solid arrow heads indicate when a protein acts on another protein and clear arrow heads show when a protein translocates to another protein or complex. Both networks contain the same proteins, most proteins show opposite expression changes in the two networks.

4.2.2.e The canonical pathways RAN signalling and tRNA charging are enriched within the dataset

To further investigate the functions of proteins in the dataset, an analysis using IPA was performed to identify canonical pathways that had significant overlap with proteins in the dataset. Previously in this chapter, analyses that investigate enrichment of specific protein functions were performed (see 4.2.2.a and 4.2.2.c), this analysis differs in that it identifies enrichment of pathways in which proteins exhibit their known function. The canonical pathway with the greatest overlap with the dataset was RAN signalling, a pathway involved in nuclear transport (Table 4-3). Importantly, several proteins within this pathway show UBA1-dependency including importin β and RanBP1 (Figure 4-7A, B). Furthermore, this analysis also identified tRNA charging (a function of tRNA synthetases) as a significantly enriched canonical pathway, with 9 of the 39 proteins involved in this pathway present in the dataset (Table 4-3). This further reinforces the relevance of both nuclear transport proteins and tRNA synthetases as key UBA1-dependent protein families.

Canonical pathway	p-value	Overlap	Number of proteins
RAN Signalling	2.76E-12	47.1%	8/17
Glycolysis I	1.14E-10	32.0%	8/25
Gluconeogenesis I	1.14E-10	32.0%	8/25
tRNA Charging	2.00E-10	23.1%	9/39
Purine Nucleotides De Novo Biosynthesis II	5.32E-10	54.5%	6/11

Table 4-3 Canonical pathways enriched on modulation of UBA1 expression

Canonical pathways that are enriched in both UBA1 overexpression compared to control and UBA1 knockdown compared to control. P-value indicates the significance of enrichment. Overlap and number of proteins show the percentage and number, respectively, of proteins in the dataset that function in that canonical pathway.

A UBA1 overexpression

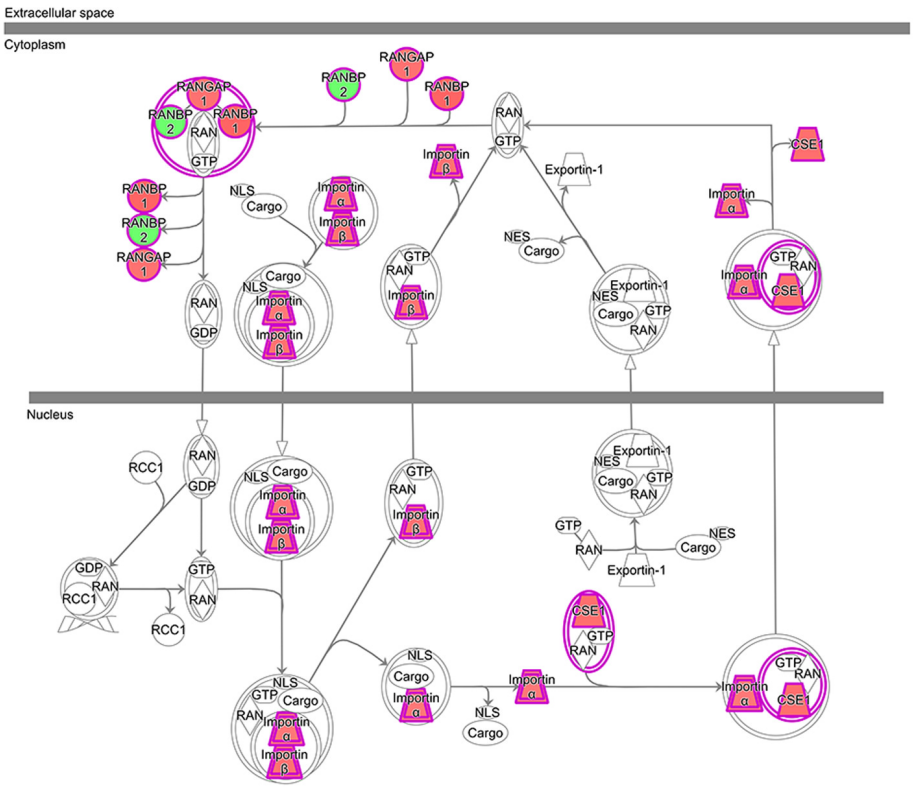

B UBA1 knockdown

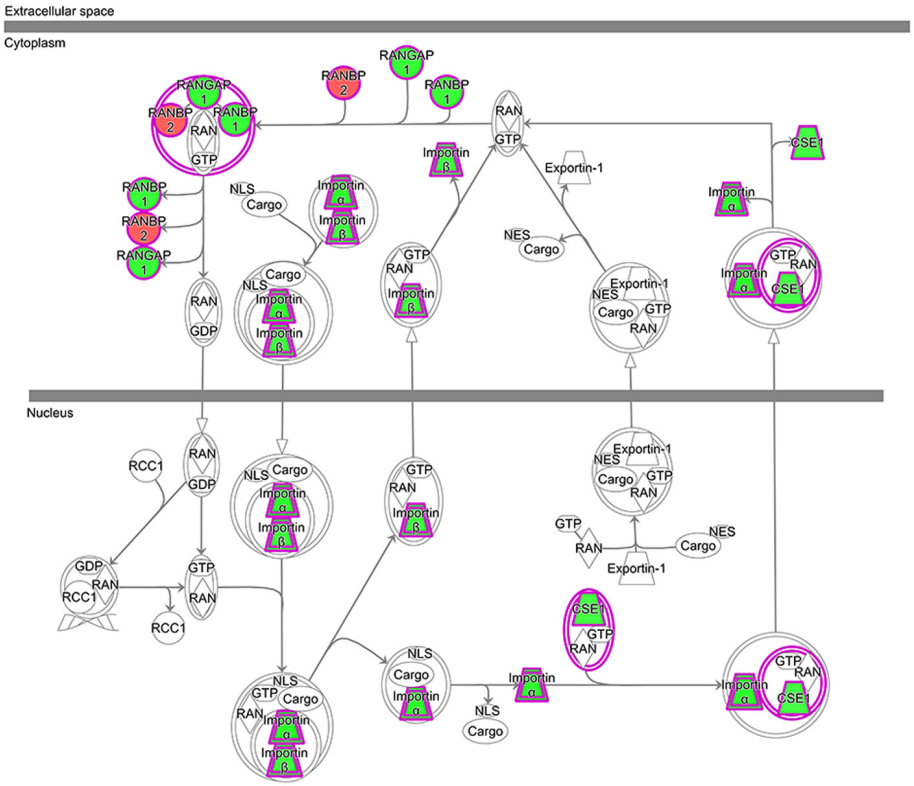

Figure 4-7 UBA1-dependency within an enriched canonical pathway
Schematic of the RAN-signalling canonical pathway – the most significantly enriched canonical pathway in the dataset. **A, B** Proteins in red shapes are upregulated, green shapes are downregulated and white shapes are not present in the dataset. The shape of the protein depicts its function: trapeziums represent transporters, circles indicate other protein classes and circles with an inner circle depict a protein complex. Solid arrowheads indicate when a protein acts on another protein and clear arrow heads show when a protein translocates to another location or complex. Proteins in the dataset show opposite changes in expression following (**A**) UBA1 overexpression and (**B**) UBA1 knockdown.

4.2.2.f Proteomics analysis revealed tRNA synthetases, nuclear transport and translation elongation as UBA1-dependent pathways of interest

In order to provide an overview of the proteins in the UBA1-dependent protein families and select candidates for further investigation, a table was compiled to identify proteins of interest. The table is split into three different groups based on gene groups from Table 4-1: tRNA synthetases, proteins involved in nuclear transport and proteins involved in translation elongation. Proteins selected for further investigation were highlighted in blue. The tRNA synthetases YARS and GARS were chosen for validation as they have the largest fold changes in that gene group and there were readily available antibodies for these proteins (Table 4-4). Similarly, IPO4 and RanBP1 were chosen for validation of nuclear transport pathways due to size of their fold changes and as these proteins are active in different aspects of nuclear transport (Table 4-4) (Mor et al., 2014). Finally, due to various tissue specific and developmental regulation related expression changes of different translation elongation factors (Abbott et al., 2009), PDCD4 was chosen for validation of this gene group (Table 4-4). PDCD4 inhibits the interaction of EIF4A1 and EIF4G causing an inhibition of translation initiation (Loh et al., 2009; Suzuki et al., 2008). PDCD4 was also chosen because it is changed in the opposite direction to the other proteins selected for further investigation, thus allowing UBA1-dependency to be assessed in relation to both possible directional changes of downstream proteins.

Gene group	Gene name	Protein name	Unique peptides	Score	p-value	Fold change OE	Fold change KD
tRNA synthetase	YARS	Tyrosine--tRNA ligase, cytoplasmic	2	101.88	2.88E-03	1.29	-1.32
	GARS	Glycine--tRNA ligase	2	102.71	1.43E-03	1.37	-1.24
	WARS	Tryptophan--tRNA ligase, cytoplasmic	2	146.73	1.12E-02	1.23	-1.14
	SARS	Serine--tRNA ligase	2	107.24	5.83E-04	1.30	-1.14
Nuclear transport	IPO4	Importin-4	2	99.74	2.69E-03	1.26	-1.25
	KPNA2	Importin subunit alpha-1	9	590.84	3.87E-03	1.06	-1.25
	RANGAP1	Ran GTPase-activating protein 1	2	147.36	2.21E-04	1.12	-1.18
	RANBP1	Ran-specific GTPase-activating protein	2	99.01	3.67E-03	1.22	-1.18
	KPNB1	Importin subunit beta-1	7	450.51	6.35E-04	1.22	-1.07
	RANBP2	E3 SUMO-protein ligase RanBP2	2	122.72	8.85E-04	-1.24	1.16
Translation elongation	EEF1B2	Elongation factor 1-beta	2	167.21	4.26E-04	1.15	-1.27
	EIF5A	Eukaryotic translation initiation factor 5A-1	2	177.28	8.48E-04	1.15	-1.24
	EEF2	Elongation factor 2	6	364.92	4.59E-03	1.10	-1.23
	EEF1A1	Elongation factor 1-alpha 1	3	182.89	9.15E-05	1.17	-1.21
	EEF1G	Elongation factor 1-gamma	3	176.86	2.19E-04	1.15	-1.21
	PDCD4	Programmed cell death protein 4	3	156.83	1.41E-04	-1.57	1.33

Table 4-4 Target proteins from UBA1-dependent protein families

Proteins of interest belonging to the three UBA1-dependent protein families identified in this screen: tRNA synthetases, nuclear transport and translation elongation. Proteins highlighted in blue were chosen for further investigation. Score indicates the mascot score and the p-value is the significance of the maximal change between the three conditions. Fold changes are represented as overexpression compared to control and knockdown compared to control.

To summarise, here a label-free proteomics screen was performed and analysed to identify UBA1-dependent protein families. Gene ontology term enrichment analysis revealed tRNA synthetases, nuclear transport and translation elongation as key functions dysregulated within this dataset. Subsequent analysis identified that these protein families behave in a UBA1-dependent manner with UBA1-dependency also identified at the level of individual proteins belonging to these pathways. Proteins from each UBA1-dependent protein family were chosen for further investigation: GARS, YARS, IPO4, RanBP1 and PDCD4.

4.2.3 Validation of target protein changes following UBA1 modulation *in vitro*

After identification of UBA1-dependent pathways and selection of proteins to take forwards for further investigation it was necessary to validate the proteomics screen using an independent methodology. To do this Western blot was performed on the samples used for the proteomics screen. There were, however, some technical limitations with the Western blot, mainly that the sample size was restricted to the three samples used per condition for the proteomics screen and that the samples had already been depleted due to their prior use. Furthermore, the fold changes expected based on changes seen in proteomics screen are small adding another layer of difficulty. It is also worth mentioning that several potential loading control proteins were found to be changed in the proteomics screen (including GAPDH and tubulin proteins; Appendix 2) and so it was necessary to use different loading controls for overexpression and knockdown samples. Therefore, the following data is presented separately for overexpression compared to control and for knockdown compared to control.

4.2.3.a Confirmation of changes in tRNA synthetase expression levels following UBA1 modulation *in vitro*

In order to independently validate the UBA1-dependency of tRNA synthetases, GARS and YARS were chosen for Western blot (Table 4-4). Following knockdown of UBA1, GARS was downregulated by 48.26% although this was not a significant difference ($P=0.1690$). In the same samples, YARS was reduced to 44.16% of control levels following knockdown of UBA1 ($P\leq0.05$; Figure 4-8A, B). When UBA1 was overexpressed, GARS showed a non-significant up regulation by 43.52% ($P=0.0788$); YARS was also increased by 42.16% compared to control levels ($P\leq0.05$; Figure 4-8C, D). Interestingly, although GARS did not show a significant difference, the directional changes in expression of both GARS and YARS were consistent with those seen in the proteomics screen; thereby validating the UBA1-dependency of these proteins with an independent methodology.

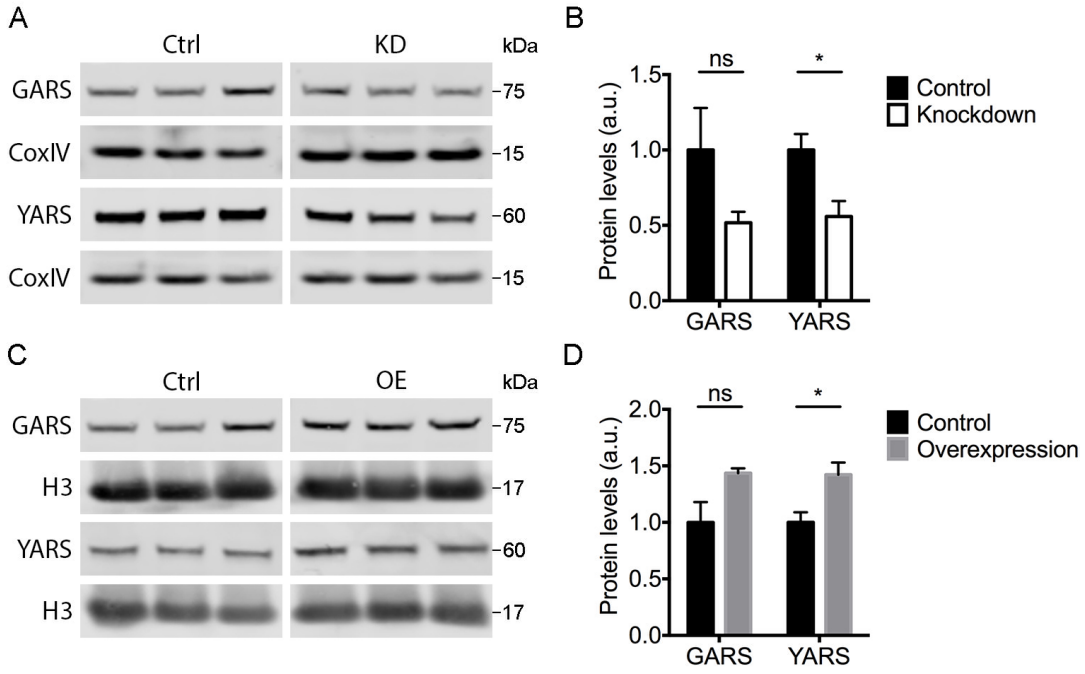

Figure 4-8 The tRNA synthetases GARS and YARS showed UBA1-dependency *in vitro*
Quantification of GARS and YARS protein levels in HEK293 cells used for the proteomics screen. **A**, **C** Fluorescent Western blot of GARS and YARS protein levels after (**A**) knockdown and (**C**) overexpression of UBA1. Samples run on the same gel in non-contiguous lanes. Protein sizes are as indicated (kDa). **A** CoxIV as loading control. **C** Histone H3 (H3) as loading control. **B**, **D** Quantification of GARS and YARS protein levels after (**B**) knockdown and (**D**) overexpression of UBA1. Samples were normalised to loading control and then overexpression and knockdown samples were normalised to control. **B** Significant downregulation of YARS following UBA1 knockdown. **D** Significant upregulation of YARS following UBA1 overexpression. Unpaired two-tailed Student's t-test; ns – not significant, * $P \leq 0.05$; n=3 separate transfections per condition.

4.2.3.b Validation of expression changes of nuclear transport proteins following modulation of UBA1 expression *in vitro*

Similarly, two proteins involved in nuclear transport (RanBP1 and IPO4) were selected for independent validation of the UBA1-dependency of this protein family (Table 4-4). Following knockdown of UBA1, RanBP1 was significantly downregulated (20.94%, $P \leq 0.05$) and IPO4 showed a trend indicating downregulation (58.23%, $P=0.0827$; Figure 4-9A, B). When UBA1 was overexpressed neither protein showed a significant difference (Figure 4-9C, D).

Despite this, the downregulation of both RanBP1 and IPO4 on UBA1 knockdown provides an independent validation of the effect of UBA1 modulation on the expression of these proteins.

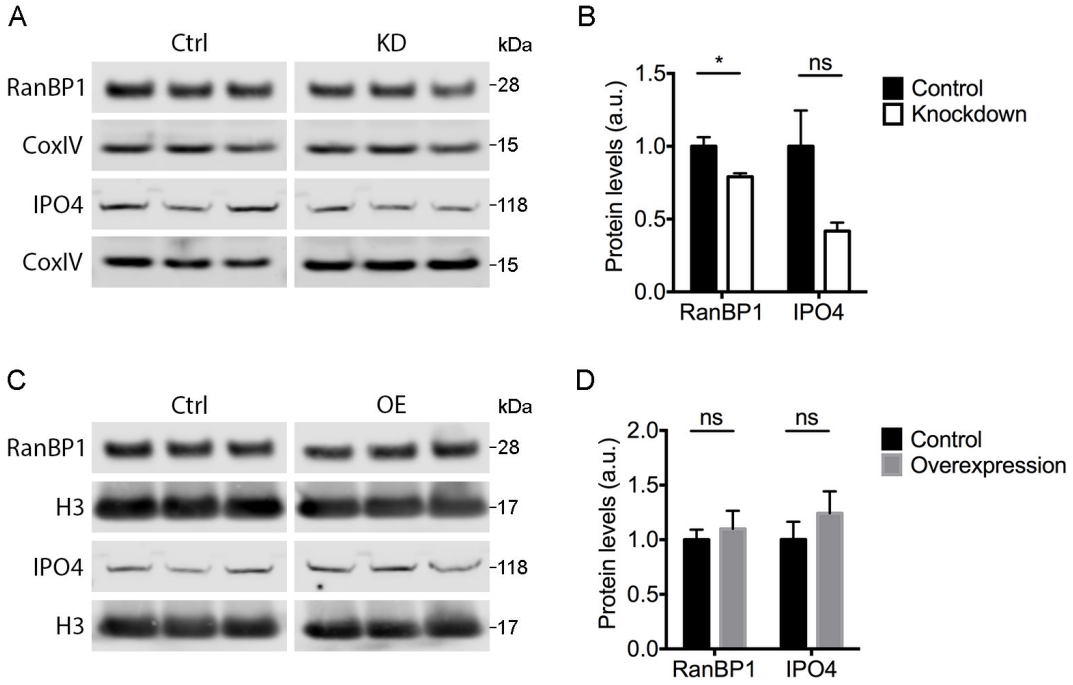

Figure 4-9 Significant downregulation of RanBP1 following UBA1 knockdown *in vitro*
Quantification of RanBP1 and IPO4 protein levels in HEK293 cells used for the proteomics screen. **A**, **C** Fluorescent Western blot of RanBP1 and IPO4 protein levels after (**A**) knockdown and (**C**) overexpression of UBA1. Samples run on the same gel in non-contiguous lanes. Protein sizes are as indicated (kDa). **A** CoxIV as loading control. **C** Histone H3 (H3) as loading control. **B**, **D** Quantification of RanBP1 and IPO4 protein levels after (**B**) knockdown and (**D**) overexpression of UBA1. Samples were normalised to loading control and then overexpression and knockdown samples were normalised to control. **B** Significant downregulation of RanBP1 following UBA1 knockdown. Unpaired two-tailed Student's t-test; ns – not significant, * $P \leq 0.05$; n=3 separate transfections per condition.

4.2.3.c An inhibitor of translation initiation was significantly changed following modulation of UBA1 expression *in vitro*

Finally, to independently validate the UBA1-dependency of the translation elongation protein family, Western blot was performed on the proteomic samples for PDCD4. There was a small and variable, non-significant upregulation of PDCD4

following UBA1 knockdown (19.01%, P=0.2928; Figure 4-10A, B). Following UBA1 overexpression, there was a significant downregulation of PDCD4 expression by 50.31% compared to control (P≤0.05; Figure 4-10A, C). As PDCD4 expression was changed in the opposite direction to the rest of the target proteins investigated, here, it has been possible to validate UBA1-dependency in the opposite direction to previously shown (see Figure 4-8).

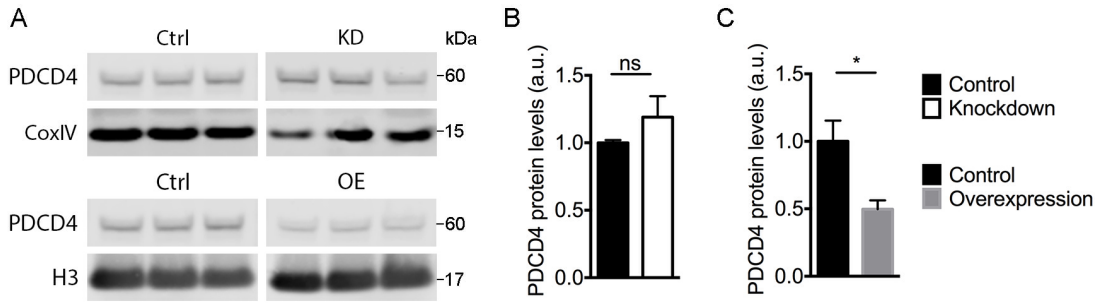

Figure 4-10 PDCD4 was significantly downregulated following UBA1 overexpression *in vitro*

Quantification of PDCD4 protein levels in HEK293 cells used for the proteomics screen. **A** Fluorescent Western blot of PDCD4 protein levels after (top panels) knockdown and (bottom panels) overexpression of UBA1. Samples run on the same gel in non-contiguous lanes. Top panel, CoxIV as loading control. Bottom panel, Histone H3 (H3) as loading control. Protein sizes are as indicated (kDa). **B**, **C** Quantification of PDCD4 protein levels after (**B**) knockdown and (**C**) overexpression of UBA1. Samples were normalised to loading control and then overexpression and knockdown samples were normalised to control. **C** Significant downregulation of PDCD4 following UBA1 overexpression. Unpaired two-tailed Student's t-test; ns – not significant, * P ≤ 0.05; n=3 separate transfections per condition.

To summarise, here I used an independent methodology to validate changes in protein expression identified in the proteomic screen. Quantitative Western blot revealed that the tRNA synthetases GARS and YARS, showed UBA1-dependency while the nuclear transport proteins IPO4 and RanBP1 were both downregulated on UBA1 knockdown. Finally, PDCD4 also showed UBA1-dependency when quantified by Western blot analysis.

4.2.4 Investigating UBA1-dependency of target proteins *in vivo*

4.2.4.a Characterisation of UBA1, UBA6 and SMN expression following UBA1 overexpression *in vivo*

Following validation of the novel downstream targets of UBA1 *in vitro*, validation of the UBA1-dependent target proteins was performed *in vivo*. To do this, wild-type FVB mice were injected intravenously with AAV9-UBA1 on the day of birth and hearts were harvested at postnatal day 8 for Western blot analysis. Hearts were chosen as it has previously been shown that a robust overexpression of UBA1 with this vector occurs in this organ (Powis et al., 2016). Before analysing the target proteins, it was first necessary to confirm UBA1 overexpression and assess whether either SMN or UBA6 may influence the expression of the target proteins *in vivo*. UBA1 was significantly overexpressed when detected either by pan-UBA1 (fold change increase of 2.05, $P \leq 0.001$) or by UBA1a (fold change increase of 5.84, $P \leq 0.01$; Figure 4-11A, B), indicating that this was a robust model of UBA1 overexpression *in vivo*. There was no change in the expression of SMN; however, there was a significant upregulation of UBA6 (25.91%, $P \leq 0.05$; Figure 4-11C, D). This was also the case with Western blot on HEK293 cells overexpressing UBA1 (see Figure 4-3), again indicating that UBA6 may influence the expression of proteins changed following UBA1 overexpression.

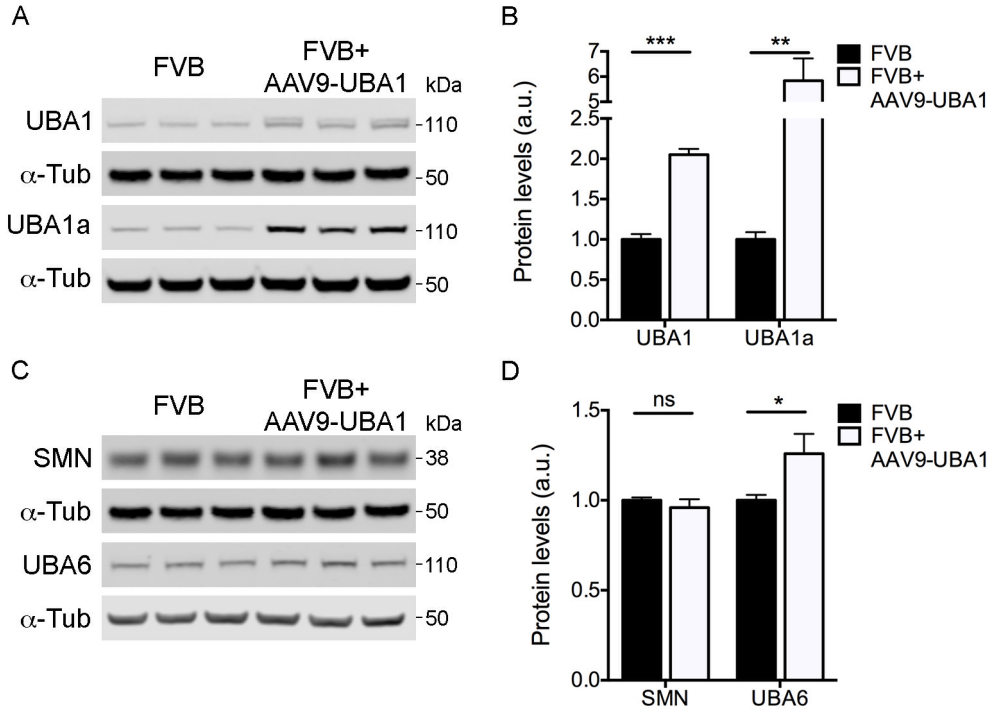

Figure 4-11 UBA1 and UBA6 protein expression was significantly upregulated in AAV9-UBA1 injected FVB mice

Quantification of UBA1, UBA6 and SMN protein levels in heart from AAV9-UBA1 injected wild-type FVB mice. **A** Fluorescent Western blot of UBA1 protein levels, detected by pan-UBA1 and UBA1a after overexpression of UBA1 *in vivo*. **B** Quantification of UBA1 protein levels showing significant upregulation detected by both antibodies; n=3 mice per condition. **C** Representative fluorescent Western blot of SMN and UBA6 protein levels after overexpression of UBA1 *in vivo*. **D** Quantification of SMN and UBA6 protein levels showing significant upregulation of UBA6; n=6 mice per condition. **A**, **C** α-Tubulin (α-Tub) as loading control. Protein sizes are as indicated (kDa). **B**, **D** Protein expression was normalised to loading control and then protein expression from AAV9-UBA1 injected mice was normalised to control FVB mice. Unpaired two-tailed Student's t-test; ns – not significant, * $P \leq 0.05$, ** $P \leq 0.01$, *** $P \leq 0.001$.

4.2.4.b Target proteins were changed following UBA1-overexpression *in vivo*

In order to investigate whether the target proteins were also UBA1-dependent *in vivo*, Western blot of the five proteins (GARS, YARS, IPO4, RanBP1 and PDCD4) was performed on hearts from mice overexpressing UBA1. The tRNA synthetase GARS showed a significant upregulation by 25.51% ($P \leq 0.01$) following UBA1

overexpression *in vivo*, while there was no change in the expression of YARS (Figure 4-12A, B). The nuclear transport protein IPO4 was also upregulated in the hearts overexpressing UBA1 (40.85%, P≤0.05) but there was no change in the expression of RanBP1 (Figure 4-12C, D). Finally, PDCD4 was also upregulated following UBA1 overexpression *in vivo* (41.65%, P≤0.05; Figure 4-12E, F). Interestingly, neither YARS nor RanBP1 showed any change in expression indicating that these proteins may not respond to UBA1 overexpression *in vivo*. The expression of both GARS and IPO4 were changed in the same direction as in the proteomics screen; however, PDCD4 was changed in the opposite direction, suggesting that other factors are modulating the expression of this protein *in vivo*.

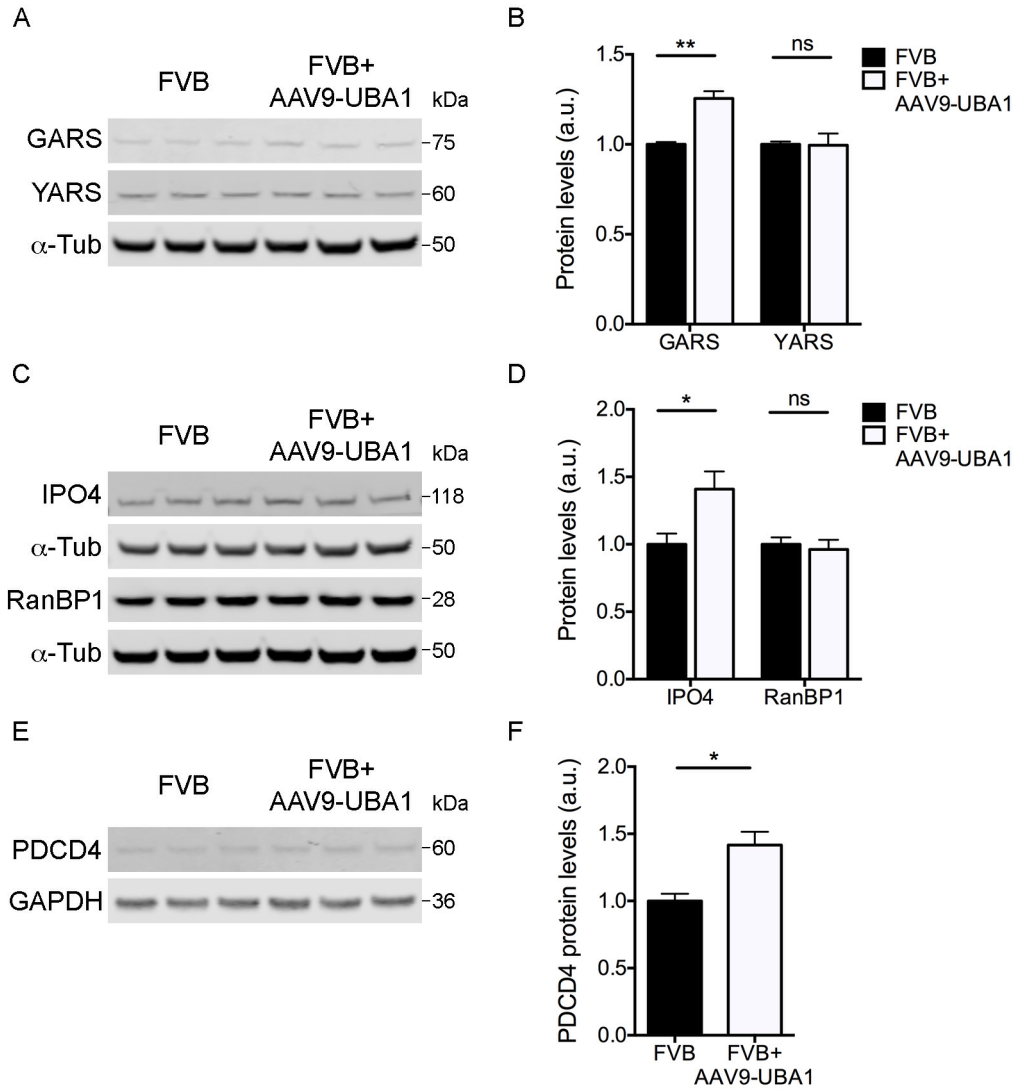

Figure 4-12 GARS, IPO4 and PDCD4 were upregulated following overexpression of UBA1 *in vivo*.

Quantification of target protein expression levels in heart from AAV9-UBA1 injected wild-type FVB mice. **A** Representative fluorescent Western blot of GARS and YARS and (**B**) quantification of GARS and YARS protein levels after overexpression of UBA1 *in vivo*, showing a significant upregulation of GARS. **C** Representative fluorescent Western blot of IPO4 and RanBP1 and (**D**) quantification of IPO4 and RanBP1 protein levels after overexpression of UBA1 *in vivo*, showing a significant upregulation of IPO4. **E** Representative fluorescent Western blot and (**F**) quantification of PDCD4 expression after overexpression of UBA1 *in vivo*, showing a significant upregulation of PDCD4. **A**, **C** α-Tubulin (α-Tub) as loading control; **E** GAPDH as loading control. Protein sizes are as indicated (kDa). **B**, **D**, **F** Protein expression was normalised to loading control and then protein expression from AAV9-UBA1 injected mice was normalised to control mice. Unpaired two-tailed Student's t-test; ns – not significant, * P ≤ 0.05, ** P ≤ 0.01. GARS, IPO4, PDCD4 n=3 mice per condition; YARS, RanBP1 n=6 mice per condition.

4.2.4.c Expression of the tRNA synthetase GARS was changed in neuronal tissue overexpressing UBA1

To confirm the change in GARS expression and to rule out any tissue specific effects, Western blot was performed on nervous tissue from mice overexpressing UBA1. To do this, dorsal root ganglia (DRGs) were chosen as they are a more refined cell population than heart and are an experimentally accessible part of the nervous system (see Figure 2-3 B-D); for further relevance of DRGs see Chapter 5. In DRGs from mice injected with AAV9-UBA1 there was an increase in UBA1 expression by 33.22% (P≤0.01) but no change in SMN expression levels (Figure 4-13A, B). This overexpression of UBA1 in the DRGs led to an upregulation of GARS by 42.13% (P≤0.01; Figure 4-13A, B) further cementing the relationship between UBA1 overexpression and GARS upregulation.

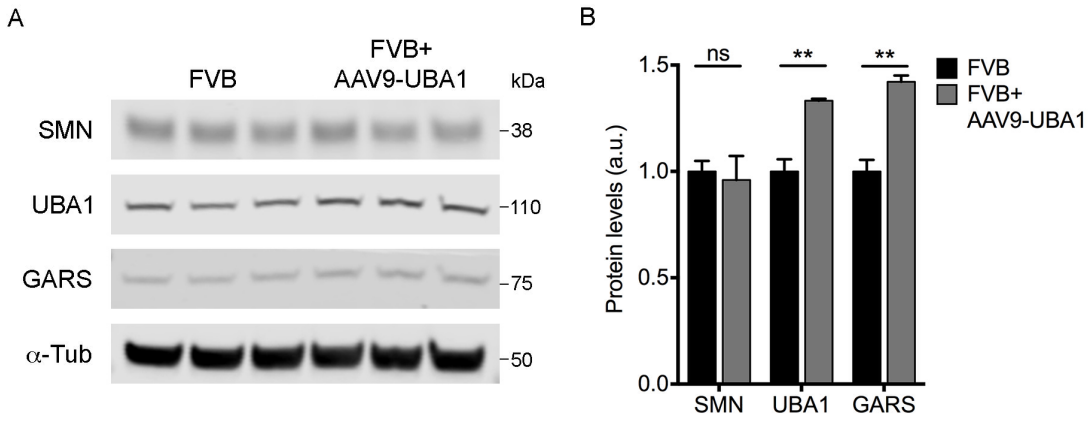

Figure 4-13 GARS was upregulated following overexpression of UBA1 in neuronal tissue

Quantification of SMN, UBA1 and GARS expression levels in dorsal root ganglia from AAV9-UBA1 injected wild-type FVB mice. **A** Representative fluorescent Western blot of SMN, UBA1 and GARS, α-Tubulin (α-Tub) as loading control. Protein sizes are as indicated (kDa). **B** Quantification of SMN, UBA1 and GARS protein levels after overexpression of UBA1 *in vivo*, showing a significant upregulation of UBA1 and GARS. Protein expression was normalised to loading control and then protein expression from AAV9-UBA1 injected mice was normalised to control. Unpaired two-tailed Student's t-test; ns – not significant, ** P ≤ 0.01; n=3 mice per condition.

4.2.4.d Expression of the tRNA synthetase GARS showed UBA1-dependency *in vivo*

In order to confirm the UBA1-dependency of GARS *in vivo*, a model system where UBA1 could be downregulated was required. Therefore, zebrafish were injected with a morpholino directed against *Uba1* to knockdown its expression (Wishart et al., 2014). Interestingly, the knockdown of *Uba1* caused a modest but significant increase in Smn expression in the zebrafish (15.88%, P≤0.05; Figure 4-14A, B), suggesting interplay between the regulation of SMN and UBA1 protein levels. The morpholino caused a 33.66% reduction of Uba1 expression in the zebrafish (P≤0.05) which in turn caused a 35.30% reduction in Gars expression (P≤0.05; Figure 4-14A, B). This confirms the UBA1-dependency of GARS *in vivo* and demonstrates that of the target proteins investigated, the tRNA synthetase GARS was the most consistently UBA1-dependent protein on validation (Table 4-5).

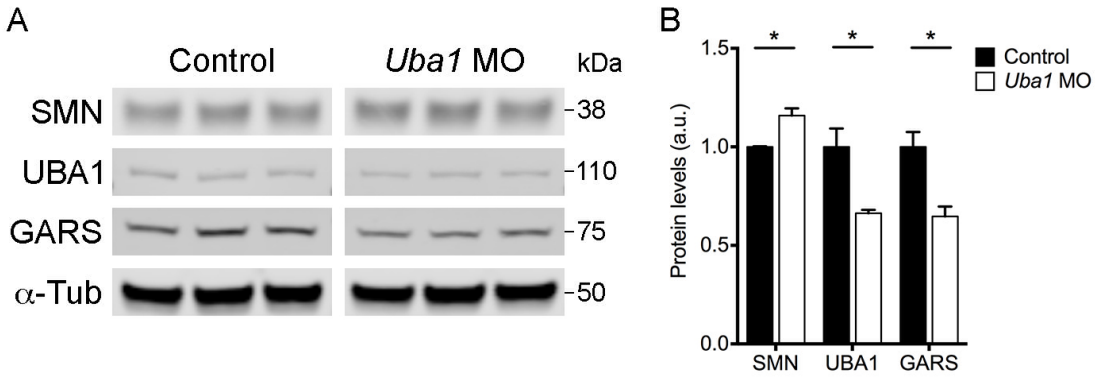

Figure 4-14 The tRNA synthetase GARS is downregulated on UBA1 knockdown *in vivo*
Quantification of SMN, UBA1 and GARS expression levels in zebrafish injected with *Uba1* morpholino (MO). **A** Representative fluorescent Western blot with SMN, UBA1 and GARS antibodies, α-Tubulin (α-Tub) as loading control. Samples run on the same gel in non-contiguous lanes. **B** Quantification of Smn, Uba1 and Gars protein levels after knockdown of *Uba1 in vivo*. Significant upregulation of Smn and significant downregulation of Uba1 and Gars. Protein expression was normalised to loading control and then protein expression from *Uba1* MO zebrafish was normalised to control. Unpaired two-tailed Student's t-test; * P ≤ 0.05; n=3 batches of zebrafish per condition.

Model	UBA1	GARS
HEK293 OE	10.11	1.44
HEK293 KD	-1.76	-1.48
Heart OE	2.05	1.26
DRG OE	1.33	1.42
Zf MO	-1.33	-1.35

Table 4-5 UBA1-dependency of the tRNA synthetase GARS
UBA1 and GARS expression changes in different model systems with modulation of UBA1 levels, detected by Western blot. Expression changes are shown as fold change compared to control. Red cells indicate upregulation of the protein, green cells indicate downregulation. See 4.2.1.b, 4.2.3.a and 4.2.4.a - d for more information on validation experiments.

Overall, here I have validated changes in target proteins identified in the proteomic screen *in vivo*. Following UBA1 overexpression *in vivo,* three of the five target proteins (GARS, IPO4 and PDCD4) were changed in heart, while the

remaining two target proteins (YARS and RanBP1) did not respond to UBA1 overexpression *in vivo*. The expression of GARS was also significantly upregulated in DRGs from AAV9-UBA1 injected mice and, following UBA1 knockdown *in vivo*, GARS was significantly downregulated. Thus, clearly showing that GARS behaves in a UBA1-dependent manner *in vivo* across multiple tissues and model systems (Table 4-5).

4.2.5 UBA1 influences GARS expression through a non-canonical mechanism

In this chapter, several novel downstream targets of UBA1 have been identified and validated as proteins with UBA1-dependent expression profiles. As the canonical role of UBA1 is in the ubiquitylation cascade, the role of ubiquitylation in mediating the UBA1-dependency of these downstream targets was investigated. Several studies have examined ubiquitylation of UPS target proteins by using ubiquitylation assays (Chang et al., 2004; Liu et al., 2017b; Lu et al., 2007; Vingill et al., 2016). This consists of transfecting cells with the protein of interest and ubiquitin along with modulating the expression of the protein hypothesised to be involved in the ubiquitylation of the target protein. Therefore, in this situation, the cells would be transfected with GARS, ubiquitin and expression of UBA1 would be modulated. Firstly however, it was necessary to investigate whether modulation of UBA1 expression could lead to changes in ubiquitylation to identify whether UBA1 may influence the expression of its downstream targets through its canonical function in the UPS.

4.2.5.a Modulation of UBA1 protein levels causes changes in overall ubiquitylation *in vitro*

To investigate the effect of modulation of UBA1 expression on overall ubiquitylation, HEK293 cells were transfected with ubiquitin conjugated to a haemagglutinin tag (Ub-HA) alongside a control vector, or UBA1 overexpression vector (Figure 4-15A), or UBA1 siRNA (Figure 4-15B) (see Table 2-1 for control vector details). It can be seen that, as expected, following overexpression of UBA1 overall polyubiquitylation of substrate proteins was increased; interestingly, monoubiquitin (free ubiquitin) levels were also increased (Figure 4-15A). Following UBA1 knockdown, there was a concomitant but less prominent change in overall ubiquitin with a modest reduction in polyubiquitylation of substrate proteins (Figure 4-15B). Overall, this confirms that modulation of UBA1 levels leads to changes in ubiquitylation of substrate proteins, confirming that UBA1 can influence the

expression of its downstream targets through differential ubiquitylation in this model system.

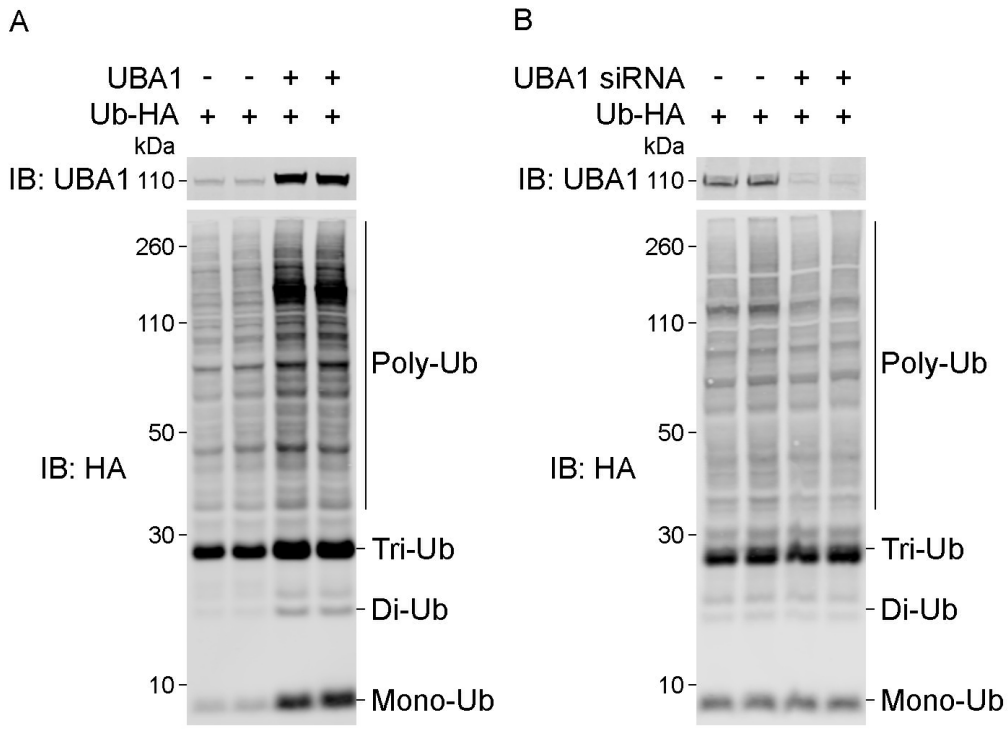

Figure 4-15 Overexpression of UBA1 increases overall levels of ubiquitylation
Modulation of UBA1 expression leads to alteration in overall ubiquitylation of substrate proteins. HEK293 cells were transfected with ubiquitin-HA (Ub-HA) and (**A**) pCMV6-UBA1 or pCMV6 as a control vector, and (**B**) UBA1 siRNA or negative control 2 siRNA. Representative fluorescent Western blot of pan-UBA1 and ubiquitin (immunoblotted with antibody for HA tag); showing polyubiquitylated substrate proteins (Poly-Ub), and free Triubiquitin (Tri-Ub), diubiquitin (Di-Ub) and monoubiquitin (Mono-Ub). **A** Overall ubiquitylation is increased following overexpression of UBA1, and **B** decreased following knockdown of UBA1. Molecular weight of protein ladder markers are indicated in kDa.

4.2.5.b Optimisation of ubiquitylation assay

To optimise the ubiquitylation assay to ensure that ubiquitylation can be reliably detected, SMN was chosen as a positive control, as there are several accounts of a clear ubiquitylation pattern for this protein (Abera et al., 2016; Chang et al., 2004). HEK293 cells were transfected with a tagged SMN construct (tSMN) and a control

vector, or tSMN and Ub-HA; control HEK293 cells were also included (see method 2.10; Figure 4-16). An IP was then performed for SMN followed by Western blot for both SMN and HA to detect ubiquitin. It can be seen that SMN has been successfully immunoprecipitated and that ubiquitylated tSMN has been detected (Figure 4-16). This replicates known SMN ubiquitylation patterns in the literature (Abera et al., 2016; Chang et al., 2004) and demonstrates that the ubiquitylation assay can reliably detect ubiquitylated target proteins.

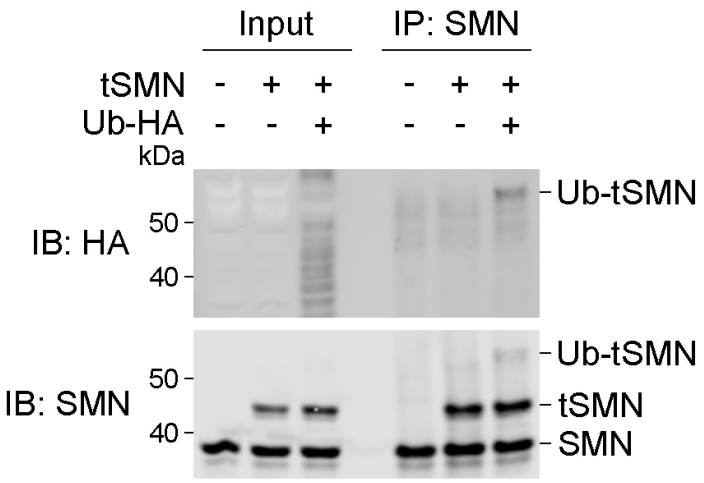

Figure 4-16 Optimisation of ubiquitylation assay

Ubiquitylation of SMN can be reliably detected by performing a ubiquitylation assay. HEK293 cells were transfected with a tagged SMN construct (tSMN) and Ub-HA or pcDNA3.1 as a control vector, SMN was immunoprecipitated (IP) and immunoblot (IB) for both SMN and HA tag (to detect ubiquitin) was performed; Ub-tSMN indicates ubiquitylated tSMN. Molecular weight of protein ladder markers are indicated in kDa.

4.2.5.c Modulation of UBA1 expression *in vitro* does not affect the ubiquitylation of GARS

After optimisation of the ubiquitylation assay, it was possible to investigate whether downstream targets identified in the proteomics screen were differentially ubiquitylated on modulation of UBA1 expression. GARS was selected for this assay as it was the downstream target of UBA1 shown to be most reliably UBA1-dependent. Like many other proteins in the literature, the ubiquitylation pattern of GARS showed a classic polyubiquitylation smear at high molecular weights (Liu et

al., 2017b; Lu et al., 2007; Vingill et al., 2016). Following overexpression of UBA1, in the presence of both GARS and ubiquitin, there was no change in the overall ubiquitylation of GARS (Figure 4-17A). Similarly, following UBA1 knockdown, there was also no change in the ubiquitylation of GARS compared to control UBA1 expression (Figure 4-17B). A negative control GFP vector was included to ensure that any changes in ubiquitylation were not due to the presence of the GFP tag on GARS; importantly there was no difference in the polyubiquitin smears in these control conditions on modulation of UBA1 expression (Figure 4-17A, B). Therefore, this shows that modulation of UBA1 expression does not affect the ubiquitylation of GARS, suggesting that UBA1 influences the expression of GARS through a non-canonical mechanism, independent of its role in the ubiquitylation cascade.

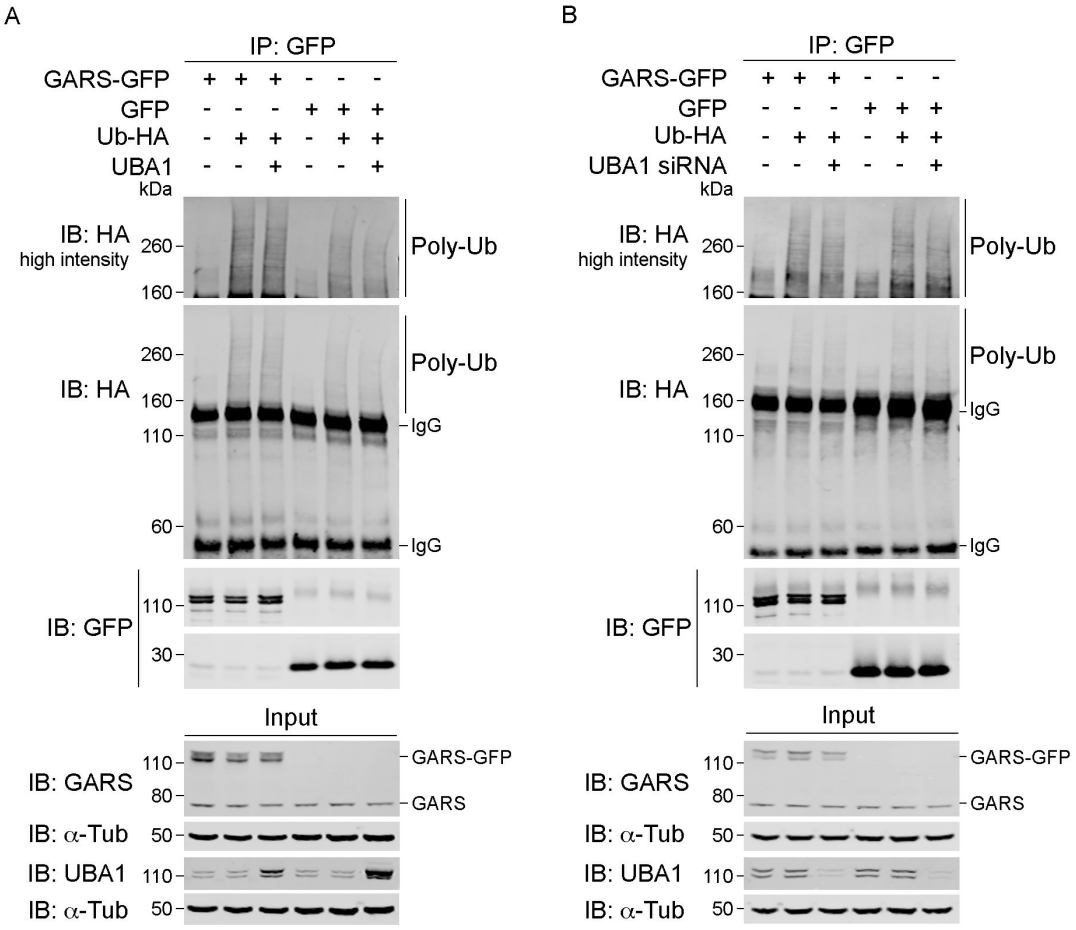

Figure 4-17 UBA1 is not required for polyubiquitylation of the tRNA synthetase GARS
The tRNA synthetase GARS is polyubiquitylated but is not differentially ubiquitylated by UBA1. HEK293 cells were transfected with GARS-GFP or GFP as well as Ub-HA and **A**

UBA1 or **B** UBA1 siRNA or the equivalent control vectors (see Table 2-1). Immunoprecipitation (IP) of GFP was performed on all samples. Input control samples were immunoblotted (IB) for UBA1 and GARS. IP samples were immunoblotted for GFP, showing successful IP of both GARS-GFP and GFP (**A** and **B**), and HA (to detect ubiquitin). IgG bands and polyubiquitylation (Poly-Ub) smears are indicated. High intensity immunoblots show Poly-Ub smears imaged at an increased laser power. **A** and **B** There is no change in the overall ubiquitylation of GARS following overexpression (**A**) or knockdown (**B**) of UBA1. Molecular weight of protein ladder markers are indicated in kDa.

Here I have shown that modulation of UBA1 expression can lead to changes in overall ubiquitylation of target substrates. This difference is most pronounced following UBA1 overexpression compared to control UBA1 expression. I then went on to optimise a ubiquitylation assay to successfully detect ubiquitylated SMN. This assay was then used to investigate the effect of modulation of UBA1 expression on the ubiquitylation of the UBA1-dependent protein GARS. I showed that although GARS was polyubiquitylated, changes in UBA1 expression did not lead to differential ubiquitylation of GARS.

4.2.6 Meta-analysis of UBA1 proteomics *in vitro* and related datasets

To assess the relevance of the protein families identified here for UBA1-mediated degeneration in SMA, a comparison of this dataset with screens previously performed on SMA tissue or in which UBA1 was dysregulated was conducted (Table 4-6). One dataset showed UBA1 overexpression and so was compared with the expression changes seen following UBA1 overexpression *in vitro*. The screen was a label-free proteomics screen on hearts from wild-type mice that were injected with AAV9-UBA1 on the day of birth. Proteins that were dysregulated in hearts from mice injected with AAV9-GFP on the day of birth were excluded from the study (Powis, 2016). This dataset therefore represents proteins changed following UBA1 overexpression *in vivo* (Table 4-6).

The translation elongation factor EEF2 showed the same directional change in both datasets, while EIF4A1 was upregulated *in vivo*. This was the same directional change as the other translation elongation and initiation factors *in vitro* suggesting consistency between the datasets. Proteins involved in nuclear transport showed less consistency between the two datasets. The nuclear import factor KPNB1 was changed in the same direction in both datasets, however, KPNA2 was changed in the opposite direction *in vivo* compared to the other nuclear transport proteins *in vitro*. Although none of the same tRNA synthetases were present in the two datasets, all of the tRNA synthetases present in each dataset were upregulated (Table 4-6), thus demonstrating consistency of protein families dysregulated following UBA1 overexpression *in vitro* and *in vivo*. Interestingly, some proteins not identified as UBA1-dependent in this screen show overlap between the datasets. Importantly, CTNNB1 (β-catenin), a known downstream target of UBA1 (Wishart et al., 2014), shows downregulation across both datasets (Table 4-6), highlighting the reliability of the screen performed in this study.

To investigate the relevance of UBA1-dependent protein families to SMA, comparisons with several screens on SMA tissue were performed. The first study was a label-free proteomics screen on pre-symptomatic skeletal muscle (rostral

levator auris longus [LALr]) from control and SMA mice (Mutsaers et al., 2011). Saravestany et al. performed a label-free proteomics screen on Schwann cells isolated from peripheral nerves of control and symptomatic SMA mice (Aghamaleky Sarvestany et al., 2014). In the study by Wishart et al., iTRAQ comparative proteomics was performed on hippocampal synaptosomes from pre-symptomatic SMA and control mice (Wishart et al., 2014). Finally, Boyd et al., performed a microarray analysis of differentially vulnerable motor neuron pools (Boyd et al., 2017). Apart from the study by Mutsaers et al. (2011), UBA1 expression was downregulated in all these studies and thus they were compared to the UBA1 knockdown dataset (Table 4-6).

As with the UBA1 overexpression comparison, proteins involved in each of the UBA1-dependent pathways were dysregulated in these datasets. Translation elongation and initiation factors were represented in each dataset; however, two of the four datasets show downregulation of EEF1G and EIF4A1 while they were upregulated in the UBA1 knockdown dataset. There was considerably less overlap between proteins involved in nuclear transport and marked variability in the directional changes of proteins involved in this pathway across the datasets (Table 4-6). Again, several tRNA synthetases were identified in two of the screens, all of which were downregulated; this is consistent with the expression changes in the UBA1 knockdown dataset (Table 4-6). This comparison therefore, demonstrated the consistency of changes to tRNA synthetase expression and implicates the protein family as a relevant downstream pathway of UBA1 for SMA. A known downstream target of UBA1, UCHL1 (Powis et al., 2014), was changed in opposite directions between UBA1 knockdown and the SMA datasets (Table 4-6). Thus, indicating that other aspects of SMA molecular pathology may influence or modulate some of the proteins downstream of UBA1.

Overall, there were both considerable overlap and marked variability of proteins and transcripts disrupted across these datasets. While the overlap of known downstream targets of UBA1 (UCHL1 and β-catenin) demonstrated the reliability of this screen, the most consistently changed UBA1-dependent protein family was tRNA synthetases, clearly suggesting these proteins are relevant for SMA.

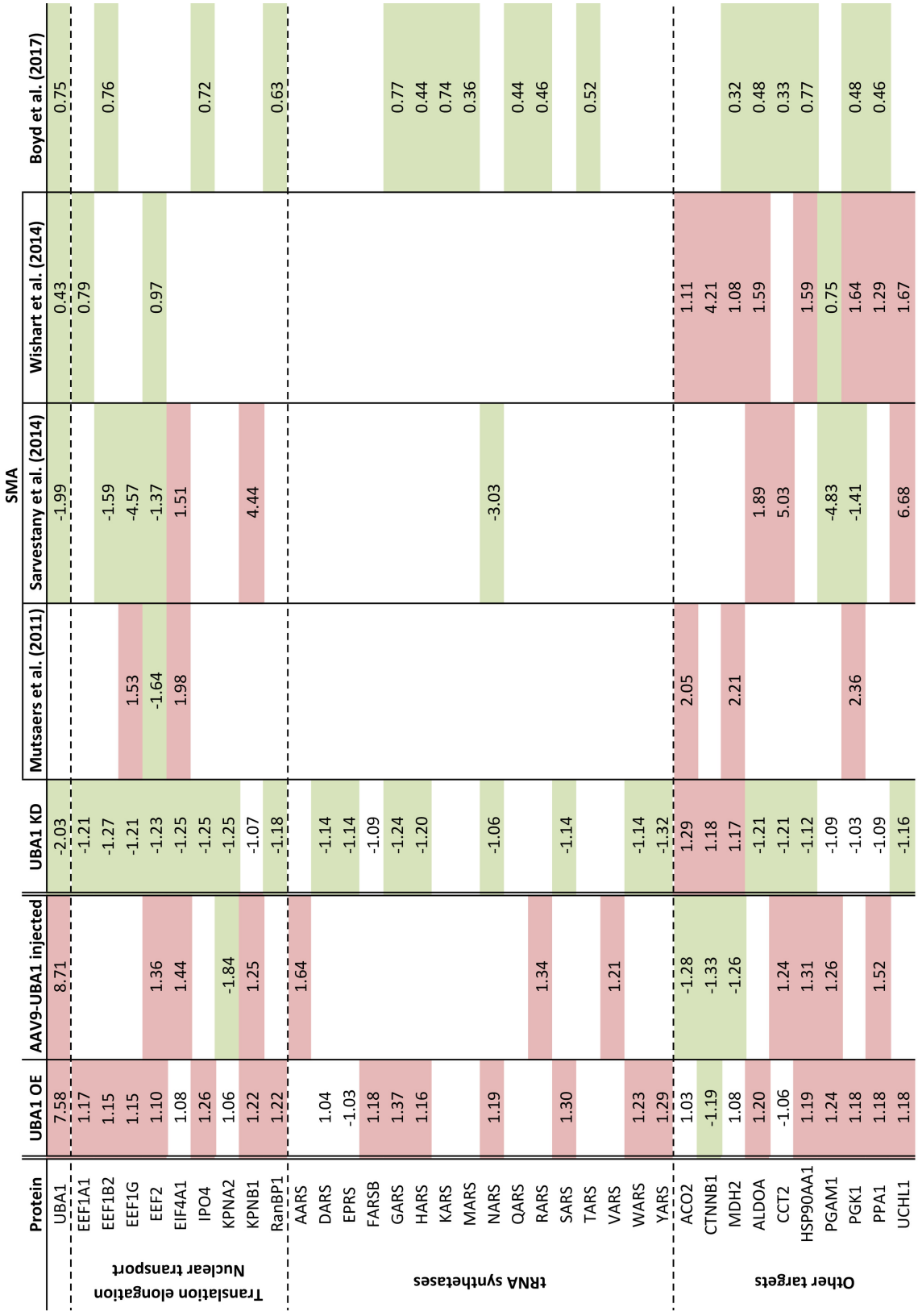
SMA
Protein
UBA1 OE
AAV9-UBA1 injected
UBA1 KD
Mutsaers et al. (2011)
Sarvestany et al. (2014)
Wishart et al. (2014)
Boyd et al. (2017)
Translation elongation
Nuclear transport
tRNA synthetases
Other targets
UBA1 7.58 8.71 -2.03 -1.99 0.43 0.75
EEF1A1 1.17 -1.21 0.79
EEF1B2 1.15 -1.27 -1.59 0.76
EEF1G 1.15 1.53 -1.21 -4.57
EEF2 1.10 1.36 -1.23 -1.64 -1.37 0.97
EIF4A1 1.08 1.44 -1.25 1.98 1.51
IPO4 1.26 -1.25 0.72
KPNA2 1.06 -1.84 -1.25
KPNB1 1.22 1.25 -1.07 4.44
RanBP1 1.22 -1.18 0.63
AARS 1.64
DARS 1.04 -1.14
EPRS -1.03 -1.14
FARSB 1.18 -1.09
GARS 1.37 -1.24 0.77
HARS 1.16 -1.20 0.44
KARS 0.74
MARS 0.36
NARS 1.19 -1.06 -3.03
QARS 0.44
RARS 1.34 0.46
SARS 1.30 -1.14
TARS 0.52
VARS 1.21
WARS 1.23 -1.14
YARS 1.29 -1.32
ACO2 1.03 -1.28 1.29 2.05 1.11
CTNNB1 -1.19 -1.33 1.18 4.21
MDH2 1.08 -1.26 1.17 2.21 1.08 0.32
ALDOA 1.20 1.24 -1.21 1.89 1.59 0.48
CCT2 -1.06 -1.21 5.03 0.33
HSP90AA1 1.19 1.31 -1.12 1.59 0.77
PGAM1 1.24 1.26 -1.09 -4.83 0.75
PGK1 1.18 -1.03 2.36 -1.41 1.64 0.48
PPA1 1.18 1.52 -1.09 1.29 0.46
UCHL1 1.18 -1.16 6.68 1.67

Table 4-6 tRNA synthetases are consistently dysregulated across a range of datasets
Overlap of proteins changed following UBA1 overexpression or UBA1 knockdown with other screens performed on SMA tissue or with modulated UBA1 levels. Red cells indicate upregulated proteins, green cells indicate downregulated proteins. White cells represent proteins changed below the 10% threshold used in this study. Cells with no values show that the protein was not detected in that screen or no change was reported in the dataset. UBA1 OE, AAV9-UBA1 injected (Powis, 2016), UBA1 KD, Mutsaers et al., (2011) and Sarvestany et al., (2014) are presented as fold changes compared to control; Wishart et al., (2014) is presented as ratios compared to control. Ratios for Boyd et al., (2017) represent the transcript changes between motor neurons innervating the extensor digitorum longus (resistant to motor neuron pathology in SMA mice) and the tibialis anterior (vulnerable to motor neuron pathology in SMA mice) in wild-type mice.

4.3 Discussion

The studies described here were initiated to characterise the molecular consequences of disruption to UBA1 protein levels and identify pathways that may be relevant for UBA1-mediated degeneration in SMA. In the previous chapter, I demonstrated that in spinal motor neurons UBA1 expression is first decreased compared to control, then increased and then the expression is decreased again as the disease progresses (see Chapter 3). Therefore, to understand the effects of disruption to UBA1 levels in SMA, a model system where UBA1 could be both up- and downregulated was required.

I began by optimising overexpression and knockdown of UBA1 in HEK293 cells to generate samples for a label-free proteomics screen. The label-free proteomics was performed on control HEK293 cells, UBA1 overexpression and UBA1 knockdown samples, thereby allowing identification of UBA1-dependent expression profiles. Initial analysis revealed that tRNA synthetases, small molecule synthesis, translation elongation and nuclear transport were functions enriched within the dataset. On investigation of UBA1-dependent expression profiles, two broad groups of proteins were identified with one cluster from each group showing clear UBA1-dependency: proteins upregulated following UBA1 overexpression and downregulated following UBA1 knockdown or vice versa. Interestingly, the functions of the UBA1-dependent clusters of proteins were tRNA synthetases, translation elongation and nuclear transport. By generating networks and investigating enrichment of canonical pathways, it was possible to see UBA1-dependency at the level of the individual protein within these protein families.

Five proteins from the three UBA1-dependent protein families were chosen for further investigations: GARS and YARS (tRNA synthetases), RanBP1 and IPO4 (nuclear transport proteins), and PDCD4 (inhibitor of translation initiation factors). Changes in the expression of these proteins were validated by Western blot on HEK293 cells with modulated UBA1 levels and then their UBA1-dependency was investigated *in vivo*. Although three of the five proteins showed expression changes on UBA1 overexpression *in vivo*, the tRNA synthetase GARS showed consistency in

expression changes across both the *in vitro* and *in vivo* validation experiments (Table 4-5); clearly showing that this protein is UBA1-dependent and amenable to experimental modulation of UBA1 levels *in vivo*.

As the aim of this screen was to identify UBA1-dependency that may be relevant for UBA1-mediated degeneration in SMA it was necessary to ascertain whether or not SMN could be having an influence on the proteins in this dataset. As there was no change in SMN expression in the samples used for this screen, it was possible to tease out UBA1-dependency and identify proteins that may be relevant for UBA1-mediated degeneration in SMA. Despite the expression of SMN remaining unchanged, due to top functional pathway changes in the dataset being neurological disorders, and skeletal and muscular disorders (Appendix 4), it is evident that this dataset is relevant for neuromuscular diseases. Interestingly, changes in cell growth and proliferation, and cell death and survival are the two most changed functional pathways in this dataset which correlates with the known role of UBA1 in the cell cycle and the effects of temperature sensitive mutations of UBA1 (Ghaboosi and Deshaies, 2007; Joo et al., 2007; Sugaya et al., 2014). Thus, further establishing the validity of this dataset as capturing known UBA1 specific effects but extending this to be able to identify downstream proteins relevant for disease pathways.

One of the striking findings of the study was the lack of proteins involved in the ubiquitin proteasome system, with only a few proteins related to the UPS identified in the screen. These included BAG6, which is involved in ubiquitin-mediated degradation of newly synthesised defective polypeptides (Minami et al., 2010), and DCAF7, a substrate receptor for a cullin E3 ligase complex (Peng et al., 2016). Interestingly, proteins involved in other ubiquitin-like signalling pathways were dysregulated within the dataset such as COPS3 (involved in deneddylation) (Lyapina et al., 2001) and RanBP2 which as well as being a nuclear import and export factor is an E3 ligase enzyme for SUMO (Pichler et al., 2002). Overall, this suggests that UBA1 may mediate some overlap between the different UBL pathways and indicates that this dataset has largely not identified proteins acting downstream of UBA1 within the UPS.

Despite this, the proteomic screen performed here may have identified proteins that are differentially ubiquitylated following changes in UBA1 protein levels, or proteins that are effectors or targets of non-canonical pathways of UBA1. UBA1 accounts for ~2% of the protein in all cells and so is thought not to be the rate-limiting factor in the UPS (Clague et al., 2015; Yang et al., 2013). Therefore, it is potentially unsurprising that very few changes in UPS enzymes have been identified. However, it may be possible to infer the role UBA1 had on specific clusters of proteins by analysing the expression profiles of these clusters. For example, proteins in Cluster 4 (see 4.2.2.c) may be changed due to an increase or decrease in the ubiquitylation activity of UBA1, while the expression changes of proteins in Cluster 1 may be caused by a different mechanism or function of UBA1. Moreover, a protein belonging to Cluster 5, proliferating cell nuclear antigen (PCNA), is known to have different functions within DNA repair pathways depending on whether it is mono-ubiquitylated or poly-ubiquitylated through K63 (Cazzalini et al., 2014). This therefore, provides further insight into the role of UBA1 in DNA-repair pathways and raises the possibility that UBA1 confers different functions on its downstream targets by the process of differential ubiquitylation.

Another pathway that has been highlighted as relevant to UBA1 in this dataset is the glycolytic pathway. Interestingly, the glycolytic enzyme phosphoglycerate kinase 1 (PGK1) was dysregulated on modulation of UBA1 protein levels. A recent study has implicated bioenergetics pathways and PGK1 in mediating motor neuron vulnerability in SMA (Boyd et al., 2017), therefore, showing clear links between the relevance of this study and SMA. As PGK1 is upregulated on UBA1 overexpression this also suggests that amelioration of disruption to this pathway could be one way UBA1 overexpression has beneficial effects on SMA mice (Powis et al., 2016). Moreover, it has previously been shown that a therapy targeting PGK1, which improved motor axon branching phenotypes in SMA zebrafish (Boyd et al., 2017), may influence HSP90 through PGK1, thus conferring protective phenotypes (Chen et al., 2015). Interestingly, heat-shock protein HSP90-alpha (HSP90AA1) is upregulated on UBA1 overexpression (*in vitro* and *in vivo*) and down regulated on UBA1 knockdown – as it is in vulnerable pools of motor neurons (Boyd et al., 2017) (Table 4-6). Moreover, it has been shown that UBA1 and

HSP90 interact *in vitro* (Falsone et al., 2005). Thus, raising the possibility of UBA1 overexpression exerting some of its neuroprotective effects through modulation of bioenergetics pathways.

One of the key UBA1-dependent protein families identified in this screen was nuclear transport. Although this pathway showed less overlap with SMA datasets than other UBA1-dependent pathways identified, several studies have implicated defective nuclear transport as a mechanism contributing to motor neuron degeneration in amyotrophic lateral sclerosis (ALS) - an adult onset form of motor neuron disease. These studies focused on the effects of aggregated proteins on nucleocytoplasmic transport and identified that a wide range of proteins involved in different aspects of nucleocytoplasmic transport are modifiers of toxicity in ALS (Dormann et al., 2010; Freibaum et al., 2015; Jovicic et al., 2015; Woerner et al., 2016; Zhang et al., 2015). This included proteins involved in RAN signalling such as RanGAP (also present in this dataset, see Appendix 2) (Freibaum et al., 2015; Zhang et al., 2015) and several importins including KPNA3 and IPO9 (Jovicic et al., 2015). Thus, indicating the relevance of defective nucleocytoplasmic transport in motor neuron degeneration in both ALS and, potentially, SMA. Although not present in one of the UBA1-dependent protein families, it is worth noting the presence of profilin-1 (PFN1) in the dataset (see Appendix 2). PFN1 is involved in the regulation of actin dynamics and mutations in PFN1 have been shown to cause familial forms of ALS (Wu et al., 2012). This further establishes the overlap of ALS and downstream proteins of UBA1, suggesting relevance of these proteins and pathways for SMA pathogenesis.

In the UBA1-dependent gene group translation elongation, the most biological relevance potentially comes from elongation factor 1-alpha 1 (eEF1A1) (Abbott et al., 2009; Doig et al., 2013; Newbery et al., 2005). eEF1A1 is an individually encoded variant of the translation elongation factor eEF1A, and has 98% similarity at the gene level and 92% similarity at the amino acid level with the other variant of eEF1A, eEF1A2. It is known that peptides identified during proteomic screens are often from completely conserved regions between the two variants making the identification of the protein challenging (Abbott et al., 2009). While

eEF1A1 is almost ubiquitously expressed, eEF1A2 is only expressed in neurons and muscle – with the expression of eEF1A2 replacing the expression of eEF1A1 in muscle during postnatal development. Interestingly, mutations in eEF1A2 specifically cause an early-onset neurodegenerative phenotype in mice referred to as the wasted mouse model (Abbott et al., 2009; Doig et al., 2013; Newbery et al., 2005). This clearly implicates the relevance of proteins identified in this dataset to neurodegeneration. However, due to the fact that commercially available antibodies for eEF1A recognise both variants equally and that the variants have differential distribution and developmental timings (Abbott et al., 2009), it was decided instead to further investigate PDCD4 from the translation elongation gene family.

As previously mentioned, PDCD4 inhibits the interaction between translation initiation factors EIF4A1 and EIF4G, thereby inhibiting translation initiation and cap-dependent translation (Loh et al., 2009; Suzuki et al., 2008). Along with this PDCD4 is a tumour suppressor protein and may have a role in apoptosis (Palamarchuk et al., 2005). It is becoming apparent that cell death pathways are involved in the neurodegenerative process of the lower motor neurons in SMA (Murray et al., 2015; Sareen et al., 2012; Simon et al., 2016). Therefore, this could be a very important target to look into, not only because UBA1 has also been implicated in cancer but because it may provide more detail on the role of cell death in SMA. Moreover, investigating PDCD4 allowed the assessment of UBA1-dependency in the opposite direction to the other target proteins investigated and it was possible to validate this *in vitro*, a very important aspect of this study.

The final UBA1-dependent protein family identified was tRNA synthetases. These enzymes function to attach specific amino acids to their corresponding tRNA(s), with most enzymes responsible for a single amino acid. For example, glycyl-tRNA synthetase (GARS) is responsible for catalysing the ligation of glycine to the 3’ end of its cognate tRNAs (Pang et al., 2014). Interestingly, mutations in several tRNA synthetases - GARS, YARS, KARS, AARS, MARS and HARS - have now been shown to cause Charcot-Marie-Tooth disease (CMT) (Antonellis et al., 2003; Gonzalez et al., 2013; Jordanova et al., 2006; McLaughlin et al., 2012; McLaughlin et al., 2010; Vester et al., 2013). CMTs are hereditary peripheral

neuropathies with motor and sensory involvement. They primarily manifest with muscle weakness and wasting, and depending on the subtype, greater or lesser sensory involvement (Reilly et al., 2011). What was striking about this family of proteins was the consistency of their expression changes across a range of datasets (see Table 4-6). Furthermore, the range of different tRNA synthetases identified in SMA proteomic screens or screens with UBA1 expression changes is intriguing and even more so as when detected, the tRNA synthetases behave in exactly the same UBA1-dependent manner as each other (Table 4-6). Moreover, throughout the validation experiments performed in this study, the tRNA synthetases were the most consistently UBA1-dependent of the proteins investigated with GARS showing strikingly consistent UBA1-dependency on validation *in vitro* and *in vivo* (Table 4-5). This clearly implicates tRNA synthetases as a protein family consistently disrupted in SMA or on modulation of UBA1 levels and suggests the importance of disruption to this protein family for UBA1-mediated degeneration in SMA, not least because mutations in several tRNA synthetases cause a related neuromuscular disease (Reilly et al., 2011).

Finally, it was identified that UBA1 does not influence the ubiquitylation of its downstream target GARS. This is in line with recent work in which an interactomics screen to determine the ubiquitylation targets of UBA1 and UBA6 identified GARS as one of the proteins specifically ubiquitylated by UBA6 (Liu et al., 2017b). Although this study did not validate GARS as a specific UBA6 target (Chang et al., 2013), the work performed here suggests that UBA1 does not have a role in mediating the degradation of GARS, thereby indirectly supporting the fact that GARS is specifically targeted for ubiquitylation by UBA6. Overexpression of UBA1 seems to have a more pronounced effect on overall protein ubiquitylation than UBA1 knockdown (Figure 4-15). This suggests that targets of UBA1 that are changed only after overexpression of UBA1 may be changed because of the canonical role of UBA1 as the main E1 ubiquitin activating enzyme. In contrast, proteins that are changed in a UBA1-dependent manner, including GARS, must be influenced by an independent, non-canonical mechanism of UBA1 that remains to be determined.

Overall, through comparative analysis with SMA and other UBA1 proteomic screens and a range of validation experiments, it is apparent that of the UBA1-dependent protein families, the tRNA synthetases show the most consistent UBA1-dependency. Furthermore, the alterations of tRNA synthetases in the range of datasets investigated here suggest some degree of molecular overlap between the two neuromuscular diseases SMA and CMT. There are however, several questions to address. Although it is clear that GARS itself behaves in a robustly UBA1-dependent manner, it has yet to be seen whether GARS or indeed other tRNA synthetases are disrupted in SMA. Finally, in order to investigate whether tRNA synthetases are involved in UBA1-mediated degeneration in SMA, it will be essential to ascertain if they are contributing to the pathogenesis of this disease.

Chapter 5 UBA1-mediated dorsal root ganglia pathology in SMA

5.1 Introduction

It is now well established that disruption to UBA1 is a key molecular feature of SMA. Although the therapeutic applications of UBA1 targeted therapies in SMA have been thoroughly investigated, the mechanism by which UBA1-mediates degeneration in SMA is unknown. In Chapter 4, I demonstrated that tRNA synthetases are one of the main UBA1-dependent protein families, with the tRNA synthetases GARS and YARS showing UBA1-dependency *in vivo* and *in vitro* respectively. The identification of the UBA1-dependency of tRNA synthetases raises the possibility of overlap between two neuromuscular disorders: SMA and Charcot-Marie-Tooth disease (CMT).

The canonical function of tRNA synthetases is to covalently couple each amino acid to its appropriate tRNA molecule (Pang et al., 2014). This happens in a two-step reaction whereby the tRNA synthetase first activates the amino acid and then it covalently links the amino acid to the tRNA, using ATP in this process. There is a different tRNA synthetase for each amino acid; for example, one tRNA synthetase will attach glycine to all tRNAs that recognise codons for glycine, this tRNA synthetase is called GARS and is encoded by the *GARS* gene (Ibba and Soll, 2000). This one-to-one ratio of tRNA synthetase for amino acid is almost entirely adhered to with only one bifunctional tRNA synthetase: EPRS which catalyses the aminoacylation of both glutamic acid and proline tRNAs. The one-to-one ratio is necessary to ensure accurate amino acid selection by tRNA synthetases which, along with hydrolytic editing following the aminoacylation reaction, ensures accurate protein synthesis (Pang et al., 2014).

The tRNA synthetases can be divided into two classes based on their chemical properties, the architecture of the catalytic domain and the consensus sequences. Class I aminoacyl tRNA synthetases mainly function as monomers while class II enzymes are almost exclusively oligomeric, functioning as homodimers or trimers (Pang et al., 2014). These two classes of tRNA synthetases bind ATP and

tRNA in different manners and so carry out the aminoacylation reaction by different mechanisms (Ibba and Soll, 2000). Interestingly, there are both cytoplasmic and mitochondrial tRNA synthetases and while mutations in mitochondrial tRNA synthetases are associated with mitochondrial diseases (Nafisinia et al., 2017; Pang et al., 2014), mutations in several cytoplasmic tRNA synthetases cause Charcot-Marie-Tooth disease (Antonellis et al., 2003; Pang et al., 2014).

CMT is a group of inherited neuromuscular disorders specifically affecting peripheral nerves with an estimated prevalence of approximately 1 in 2500 worldwide (Reilly et al., 2011). CMT is characterised by progressive motor impairment leading to distal muscle weakness, alongside progressive sensory degeneration. Skeletal deformities are also present in some cases; however, life span is usually unaffected (El-Abassi et al., 2014). CMT can be caused by demyelination of axons, referred to as CMT type 1 (CMT1), axonal degeneration (CMT2) or a combination of both pathologies, referred to as intermediate CMT. The different types of CMT have different propensities for motor and sensory involvement and can be further subdivided depending on the gene containing the causative mutation (El-Abassi et al., 2014; Reilly et al., 2011).

CMT is genetically diverse with a range of causative mutations identified in more than 50 disease associated genes (El-Abassi et al., 2014). Interestingly, the gene products do not represent a single functional category with mutations occurring in genes encoding everything from myelin proteins and mitochondrial components to DNA binding proteins and proteins involved in proteins synthesis (El-Abassi et al., 2014; Reilly et al., 2011). Not surprisingly therefore, the mechanisms underlying sensory and motor dysfunction remain unresolved. The largest gene family implicated in CMT is the tRNA synthetases. Mutations in six different tRNA synthetases – *GARS*, *YARS*, *HARS*, *AARS*, *KARS* and *MARS* – have been shown to cause CMT in patients. Mutations in all of these tRNA synthetases cause axonal degenerating or intermediate forms of CMT (Antonellis et al., 2003; Gonzalez et al., 2013; Jordanova et al., 2006; McLaughlin et al., 2012; McLaughlin et al., 2010; Vester et al., 2013). Of these six tRNA synthetases, GARS and YARS are the most well documented and characterised.

One of the tRNA synthetases that causes CMT is the tyrosyl-tRNA synthetase (YARS). Two heterozygous missense mutations and one *de novo* deletion in *YARS* have been identified in three unrelated families affected with dominant intermediate CMT type C (DI-CMTC) (Jordanova et al., 2006; Thomas et al., 2016). DI-CMTC takes a slowly progressive course with distal muscle weakness primarily affecting lower limbs. Sensory complaints were less common than motor symptoms in DI-CMTC pedigrees, however, sural nerve biopsies (sensory nerve) showed age-dependent axonal degeneration and some segmental remyelination indicating the presence of some sensory pathology (Thomas et al., 2016).

Similarly, mutations in the tRNA synthetase *GARS* cause CMT type 2D (CMT2D) (Antonellis et al., 2003). This is an axonal degenerating type of CMT and has limited sensory involvement compared to other forms of CMT (Motley et al., 2010). The typical onset of CMT2D is during adolescence or young adulthood and it initially manifests as weakness and atrophy of the hand muscles (Antonellis et al., 2003; Liao et al., 2015). This is unique within CMTs as they usually present as a length dependent peripheral neuropathy affecting the feet more than the hands (Reilly et al., 2011). Interestingly, some patients with dominant *GARS* mutations are diagnosed with distal SMA type V (dSMA-V), which is characterised by atrophy and weakness of distal muscles in the absence of the mild-to-moderate sensory involvement present in CMT2D (Antonellis et al., 2003; Eskuri et al., 2012). Moreover, a *de novo* mutation in *GARS* (Gly598Ala) has been shown to cause infantile SMA (Eskuri et al., 2012; James et al., 2006). This clearly indicates overlap between SMA and CMT, suggesting that GARS may have a pathogenic role in SMA.

GARS was the first tRNA synthetase to be shown to be associated with CMT and so it is not surprising that CMT2D is the most studied tRNA synthetase mediated CMT to date. In particular, there are more animal models of CMT2D, and it is the only tRNA synthetase mediated CMT that currently has published mouse models. The mouse models of CMT were caused by spontaneous mutations or ENU mutagenesis and interestingly, the mutations in both of the mouse models correspond to mutations found in CMT2D patients (Achilli et al., 2009; Seburn et al., 2006). Homozygous mutations in *GARS* can cause embryonic lethality of the mice, while

the heterozygous mutations cause a variety of phenotypes ranging from mice with a life expectancy of six weeks and sensory and motor deficits to mice with a normal life expectancy and poor motor function and mild sensory involvement (Achilli et al., 2009; Motley et al., 2010; Seburn et al., 2006).

Interestingly, the sensory pathology in CMT2D is poorly understood. The greatest sensory deficit in CMT2D patients is in the perception of vibration (Sivakumar et al., 2005), a sensation that is detected by sensory neurons with large cell bodies and large diameter axons (Lallemend and Ernfors, 2012; Le Pichon and Chesler, 2014). However, biopsies from patient sural nerves show a selective loss of small sensory axons (Sivakumar et al., 2005); thus, bringing uncertainty to the sensory defects and pathology present in CMT2D. Due to the availability of mouse models with differing severity it has been possible to investigate the sensory deficits present in CMT2D models caused by different mutations.

It has recently been shown, in two different mouse models, that there is a disruption to the fate of sensory neurons in the dorsal root ganglia (DRGs) in CMT2D (Sleigh et al., 2017a). The dorsal root ganglia reside within the spinal column and contain the sensory neuron cell bodies. These receive inputs from the periphery and synapse onto motor neurons in the ventral horn by sending projections into the spinal cord through the dorsal root (Le Pichon and Chesler, 2014; Sleigh et al., 2016). Sensory neurons within DRGs can be split into different subtypes depending on their function. Large area sensory neurons are generally either mechanoreceptors (sense touch) or proprioceptors (sense position and movement) both of which stain positive for NF200, a heavy neruofilament protein. Smaller area sensory neurons stain positive for peripherin (an intermediate neurofilament protein) and are nociceptive neurons sensing either noxious mechanical or noxious thermal stimuli (Lallemend and Ernfors, 2012; Le Pichon and Chesler, 2014; Sleigh et al., 2017a). In CMT2D mice there is a severity dependent disruption to the fate of sensory neurons with an increase in the percentage of NF200 positive neurons and a decrease in the percentage of peripherin positive neurons. This in turn caused heightened sensation to painful stimuli and poor performance on balance specific

motor tests (Sleigh et al., 2017a). Thus, providing a clear overview of sensory pathology and phenotypes in CMT caused by mutations in *GARS*.

I have previously identified that the tRNA synthetases are a major UBA1-dependent protein family that show UBA1-dependency across multiple wild-type systems with modulated UBA1 protein levels (see 4.2.4). Interestingly, a range of tRNA synthetases show changes in SMA datasets and related screens (Table 4-6), indicating that they may be relevant for UBA1-mediated pathogenesis of SMA. However, it has yet to be seen whether GARS or indeed other tRNA synthetases are disrupted in SMA and whether they may be contributing to UBA1-mediated degeneration in SMA. In order to investigate this, I performed Western blots for UBA1, GARS and YARS on a range of tissues from the Taiwanese mouse model of SMA. After ascertaining that GARS expression is disrupted in neuronal tissues from SMA mice, I identified that the SMA mice have a disruption to sensory neuron fate consistent with the phenotype in CMT2D mice and that this phenotype is dependent on changes in UBA1 and GARS protein expression. Thus, clearly drawing parallels between the two neuromuscular disorders CMT and SMA.

5.2 Results

5.2.1 Characterisation of tRNA ligase protein levels in SMA

5.2.1.a Reduction of UBA1 protein levels in SMA mice

To begin to understand the role and relevance of tRNA synthetases in SMA, it was first necessary to ascertain whether or not specific tRNA synthetases previously identified as being UBA1-dependent (Chapter 4) were also disrupted in SMA. For this, GARS and YARS were investigated as these tRNA synthetases are known to cause CMT. However, before investigating the expression levels of GARS and YARS in SMA models, it was essential to confirm that UBA1 expression was being consistently modified across the range of tissues used for these experiments. Therefore, the levels of UBA1 were quantified by fluorescent Western blot on spinal cord, dorsal root ganglia (DRG), muscle and heart from late symptomatic SMA mice and littermate controls. DRGs were chosen due to the recent implication of GARS in sensory neuron cell fate (Sleigh et al., 2017a) (see Figure 2-3). Spinal cord, muscle and heart were chosen as they represent a range of other tissues previously shown to be affected in SMA (Hamilton and Gillingwater, 2013; Powis et al., 2016). UBA1 protein levels were reduced in SMA across all the tissues investigated, compared to control (Figure 5-1A). In spinal cord, DRG and muscle UBA1 was reduced by 17.57% ($P \leq 0.05$), 27.59% ($P \leq 0.05$) and 21.45% ($P \leq 0.05$) respectively in SMA compared to control mice (Figure 5-1B), showing a similar disruption to UBA1 expression across these tissues. However, the reduction of UBA1 expression in heart was much greater, with a reduction of 52.29% in SMA mice compared to control ($P \leq 0.001$, Figure 5-1B). While this demonstrates variability in the reduction of UBA1 protein levels seen at the whole tissue level in SMA, it indicates that in all tissues investigated UBA1 was reduced.

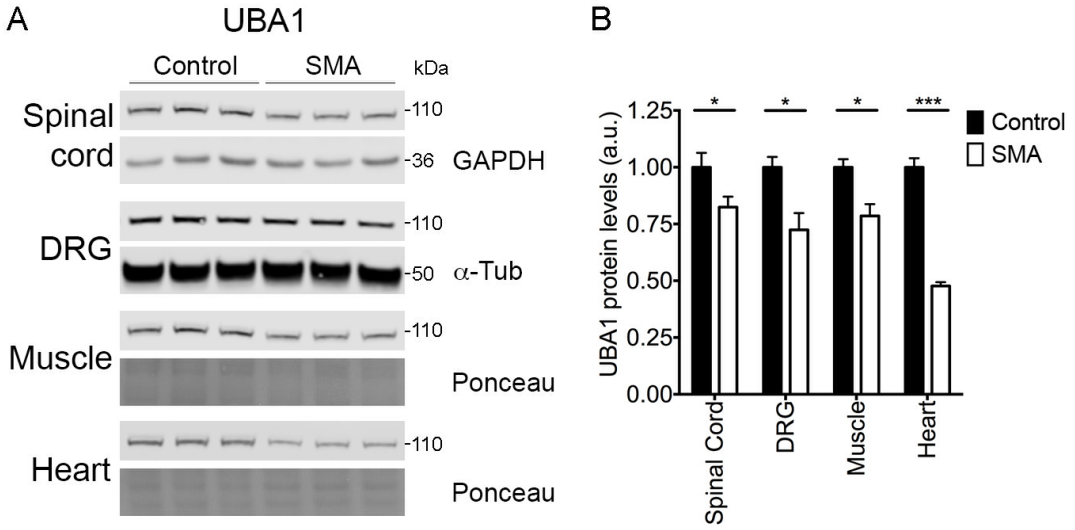

Figure 5-1 UBA1 expression is reduced in SMA mice

Quantification of UBA1 protein levels in the Taiwanese mouse model of SMA. **A** Representative fluorescent Western blot of UBA1 protein levels, detected by pan-UBA1, in spinal cord, dorsal root ganglia (DRG), muscle and heart from late-symptomatic SMA mice and control littermates. GAPDH, α-Tubulin (α-Tub) and total protein (Ponceau) as loading controls. Protein sizes are as indicated (kDa). **B** Quantification of UBA1 protein levels in late-symptomatic SMA mice showed significant downregulation of UBA1 across all tissues. UBA1 expression was normalised to loading control, and then expression in SMA tissue was normalised to the control tissue. Unpaired two-tailed Student's t-test; * $P \leq 0.05$, *** $P \leq 0.001$; spinal cord: n=6 mice per condition; DRG, muscle, heart: n=3 mice per condition.

5.2.1.b Dysregulation of tRNA synthetases in a mouse model of SMA

After confirming that UBA1 expression was reduced in the tissues used for this experiment, the protein levels of GARS and YARS were investigated. Interestingly, the two tRNA synthetases were both dysregulated across a range of SMA tissues. However, the two tRNA synthetases showed different tissue specific effects and directional changes (Figure 5-2A, B). GARS showed no change in either muscle or heart but was significantly dysregulated in both nervous tissues investigated (Figure 5-2A, C): in spinal cord GARS showed an increase of 100.02% compared to control ($P \leq 0.05$) and in DRG the increase was 55.75% ($P \leq 0.05$; Figure 5-2C). YARS remained unchanged in both DRG and muscle (Figure 5-2B) but the protein was significantly downregulated by 36.89% in spinal cord compared to control ($P \leq 0.05$)

and by 36.00% in heart (P≤0.05; Figure 5-2D). Importantly, increased levels of GARS in SMA are consistent with changes in GARS protein levels reported in CMT2D (Achilli et al., 2009; Motley et al., 2010), where they are increased during neonatal development, further drawing parallels between the two neuromuscular diseases of SMA and CMT.

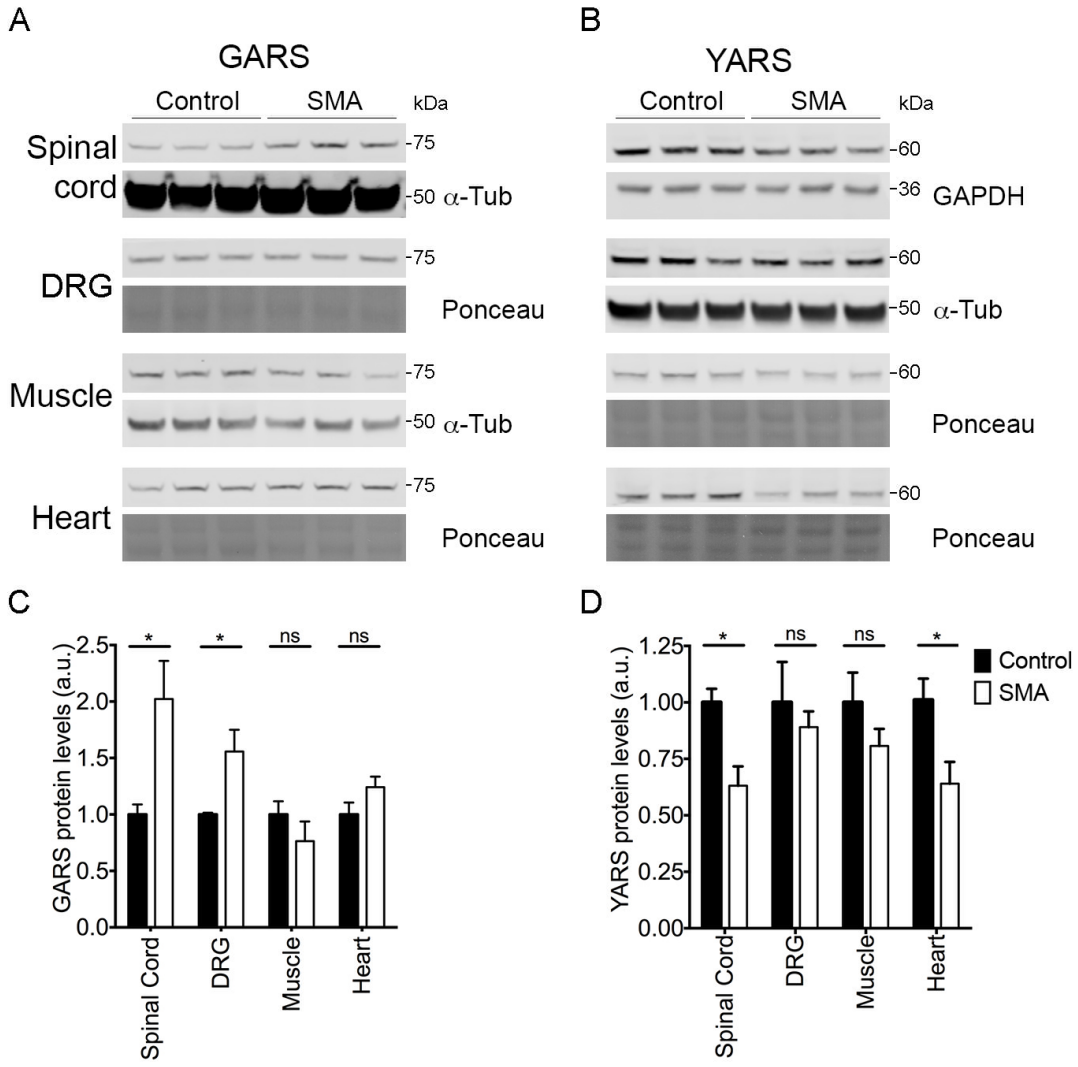

Figure 5-2 GARS and YARS are dysregulated in tissue from SMA mice

Quantification of GARS and YARS protein levels in the Taiwanese mouse model of SMA. **A, B** Representative fluorescent Western blot of (**A**) GARS and (**B**) YARS protein levels in spinal cord, dorsal root ganglia (DRG), muscle and heart from late-symptomatic SMA mice and control littermates. GAPDH, α-Tubulin (α-Tub) and total protein (Ponceau) as loading controls. Protein sizes are as indicated (kDa). **C, D** Quantification of (**C**) GARS and (**D**) YARS protein levels in late-symptomatic SMA mice, protein expression was normalised to

loading control, and then expression in SMA tissue was normalised to the control tissue. **C** Significant upregulation of GARS in spinal cord and DRGs in SMA mice. **D** Significant downregulation of YARS in spinal cord and heart. Unpaired two-tailed Student's t-test; ns – not significant, * P ≤ 0.05; n=3 mice per condition.

5.2.1.c SMN is downregulated in dorsal root ganglia from SMA mice

As protein levels of SMN have not previously been reported for DRGs in SMA, the expression of SMN in SMA DRGs was quantified by Western blot analysis. As expected, a significant reduction of SMN was seen in the DRG (Figure 5-3A) with an overall reduction of 92.27% in SMA compared to control (P≤0.001; Figure 5-3B). This is in line with the reduction of SMN protein seen in patients (Lefebvre et al., 1997) and the lack of *Smn* transcript in DRGs from delta 7 SMA mice (Mentis et al., 2011). Thus, this clearly shows that the relationship between SMN reduction and UBA1 reduction within the DRG is the same as that reported for other tissues previously investigated (Powis et al., 2016; Wishart et al., 2014).

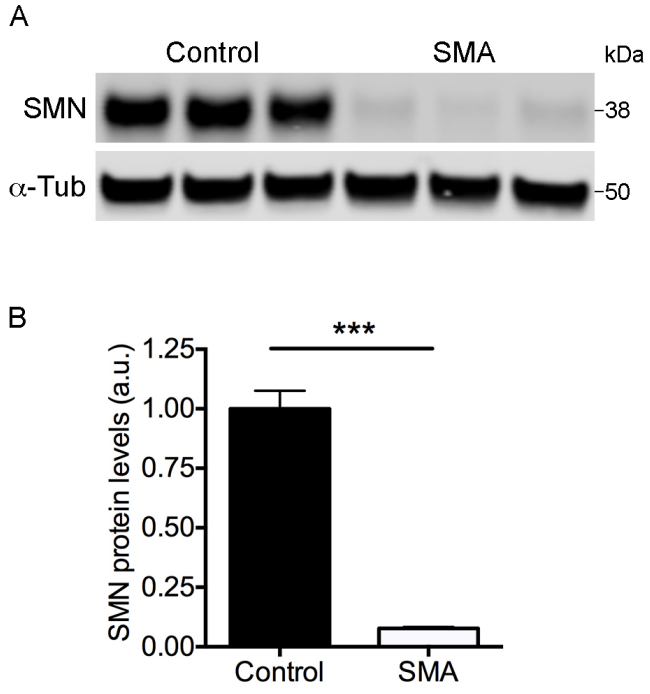

Figure 5-3 SMN protein levels are reduced in DRGs from SMA mice
Quantification of SMN protein levels in dorsal root ganglia from SMA mice and control littermates. **A** Fluorescent Western blot of SMN protein levels, α-Tubulin (α-Tub) as loading

control. Protein sizes are as indicated (kDa). **B** Quantification of SMN protein levels in late-symptomatic SMA DRGs showed significant downregulation of SMN. SMN expression was normalised to loading control, and then expression in SMA DRGs was normalised to the control. Unpaired two-tailed Student's t-test; *** P ≤ 0.001; n=3 mice per condition.

Here I have shown that UBA1 protein expression is reduced across a range of tissues, including dorsal root ganglia, in the Taiwanese mouse model of SMA. I then showed that the tRNA synthetases GARS and YARS are dysregulated across a range of SMA tissues. Interestingly, GARS expression is changed in the same direction in SMA tissue as it is in mouse models of CMT2D.

5.2.2 Identification of a novel sensory neuron phenotype in a mouse model of SMA

5.2.2.a SMA mice have fewer mechano- and proprioceptive sensory neurons

To identify whether the disruption to tRNA synthetases in SMA was relevant for UBA1-mediated pathogenesis of SMA, the disruption to sensory neuron fate seen in GARS mediated CMT was used as a phenotypic readout. To do this, spinal columns with DRGs were sectioned at 12μm and labelled for NF200 and peripherin, markers of larger area mechano- and proprioceptors, and of the smaller area nociceptors, respectively. The percentage of neurons positive for NF200, peripherin or both NF200 and peripherin were quantified for each pair of lumbar DRGs from lumbar segment 1 to segment 4 (L1-L4) (see Figure 2-3A) for three SMA mice and three control littermates.

In the SMA mice the DRGs appeared smaller and had fewer NF200 positive neurons compared to the control mice (Figure 5-4A). There was a 17.41% reduction in NF200 positive neurons relative to control ($P \leq 0.01$; Figure 5-4B), with a concomitant increase in peripherin positive cells by 6.32% relative to control ($P \leq 0.01$; Figure 5-4C). Interestingly, there was no difference in the percentage of cells that stained positive for both NF200 and peripherin between control and SMA (Figure 5-4D). This clearly indicates the presence of a disruption to sensory neuron fate in SMA mice and therefore highlights symptomatic overlap between SMA and CMT2D, indicating that disruption to GARS protein levels may be contributing to disease phenotypes in SMA.

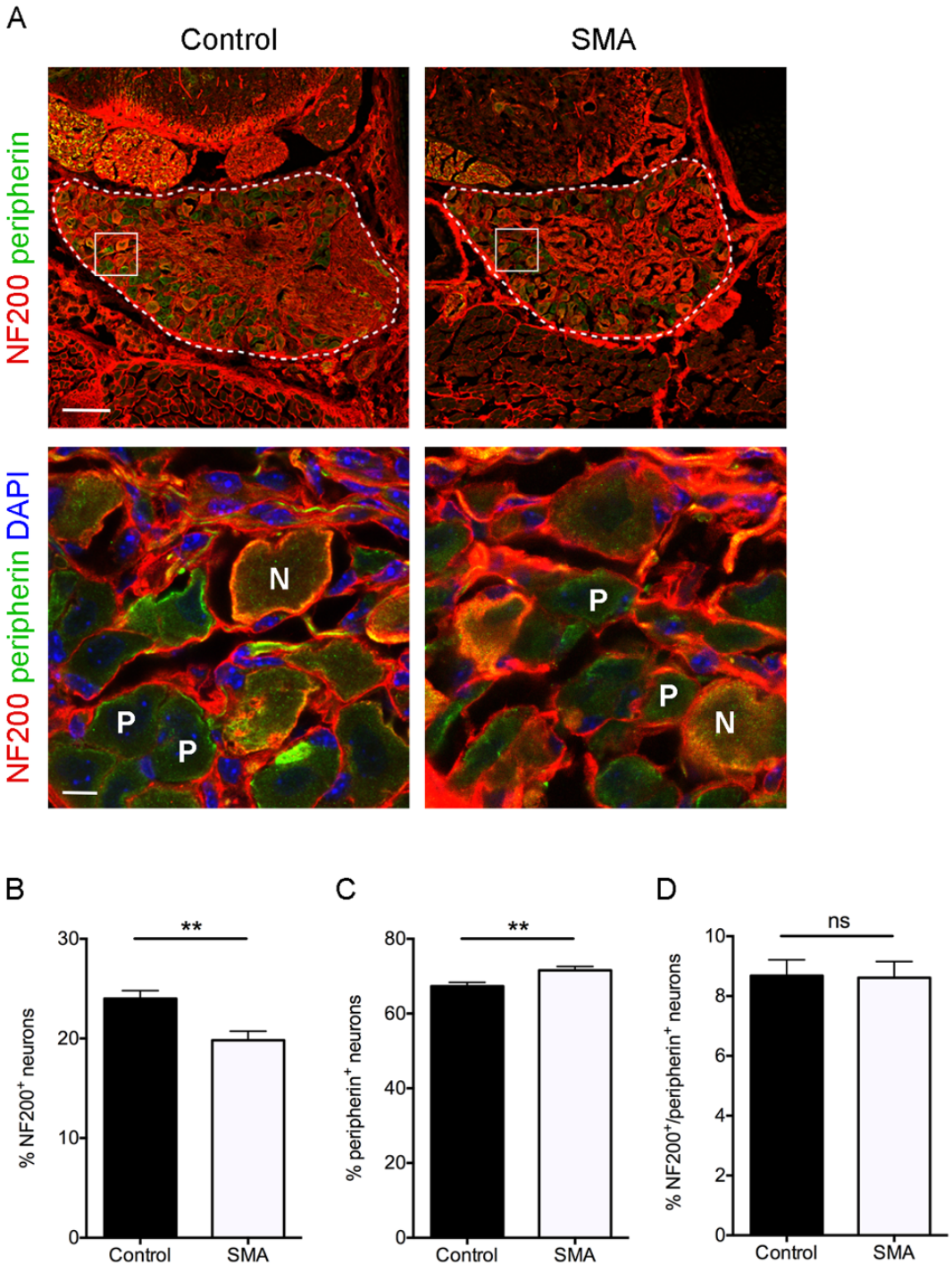

Figure 5-4 Disruption to sensory neuron fate in SMA dorsal root ganglia

Spinal column sections from late-symptomatic SMA and control mice were labelled with NF200, peripherin and DAPI. **A** DRGs in SMA and control spinal columns labelled for NF200 and peripherin; images of L2 DRGs. Top panels: dotted line indicates outline of DRG, box indicates area in bottom panel, scale bar = 100μm. Bottom panels: DRGs also labelled for DAPI, N indicates NF200 positive neurons, P indicates peripherin positive neruons, scale bar

= 10μm. **B** Quantification of the percentage of NF200 positive ($NF200^+$) sensory neurons, showing a reduction in SMA mice. **C** Quantification of the percentage of peripherin positive ($peripherin^+$) neurons, showing an increase in SMA mice. **D** Quantification of the percentage of sensroy neruons positive for both NF200 and peripherin. N=3 mice, n=8 DRGs per mouse. Mann-Whitney test; ns – not significant, ** P ≤ 0.01.

5.2.2.b Sensory neurons and dorsal root ganglia are smaller in SMA mice

The DRGs in SMA mice appeared qualitatively smaller than those in control mice. Therefore, to quantify changes in the overall size of the DRGs, the total cell number per DRG was analysed. Interestingly, CMT2D mice also showed a reduction in the area of sensory neuron cell bodies compared to control and so the area of NF200 and peripherin positive neurons was quantified. In SMA mice there was an overall reduction in total number of sensory neurons per DRG by 13.76% ($P \leq 0.05$), representing an average of 32 fewer neurons per DRG compared to control (Figure 5-5A). The area of NF200 positive cells was also reduced in SMA with an average reduction of $105\mu m^2$ per NF200 positive neuron compared to control ($P \leq 0.001$; Figure 5-5B). In contrast, there was no difference in the area of the peripherin positive neurons in SMA mice compared to control (Figure 5-5C). This suggests that sensitivity to changes in GARS levels in populations of NF200 positive sensory neurons drives the DRG phenotypes seen in SMA.

After measuring the area of sensory neuron cell bodies in SMA and control mice, the range of areas of NF200 and peripherin positive neurons was analysed. In both control and SMA DRGs there was a clear distinction between the area range of peripherin positive and NF200 positive neurons, with a small ($100\mu m^2$) region of overlap between the two (Figure 5-5D, E). Although the smallest peripherin positive neurons were the same size in both control and SMA mice, the largest peripherin positive neurons were smaller in SMA (Figure 5-5E). Which, along with the smaller size of NF200 positive neurons in SMA, resulted in a $50\mu m^2$ shift of the overlap range of NF200 and peripherin positive neuron area in SMA (Figure 5-5D, E). Overall, this provides a useful tool to be able to identify whether a sensory neuron is

likely to be NF200 or peripherin positive, based on the neuron area, in both control and SMA mice.

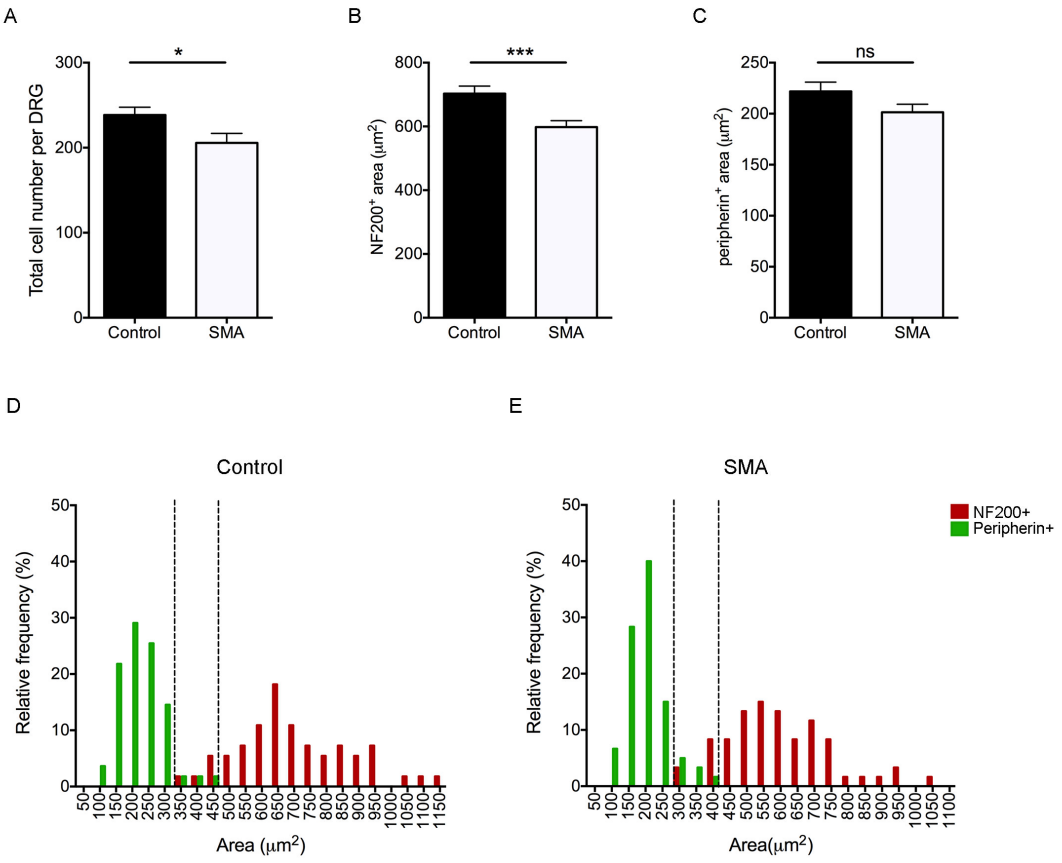

Figure 5-5 Reduction in the area of NF200 positive neurons in SMA mice
Characterisation of DRG phenotypes in late-symptomatic SMA mice. **A** Quantification of total cell number in control and SMA mice, showing a reduction of sensory neuron number in SMA mice. N=3 mice, n=8 DRGs per mouse. **B, C** Quantification of the area of NF200 (**B**) and peripherin (**C**) positive neurons. N=3 mice, n=20 neurons per mouse. **B** Reduction in the area of NF200 positive neurons. **A-C** Unpaired two-tailed Student's t-test; ns – not significant, * $P \leq 0.05$, *** $P \leq 0.001$. **D, E** Frequency distribution of the area of NF200 and peripherin positive neurons for (**D**) control and (**E**) SMA mice represented as percentage of neurons per 50µm^2 area range. Dotted lines indicate range of overlap of areas for NF200 positive and peripherin positive neurons for both control and SMA mice.

5.2.2.c Dorsal root ganglia in lumbar segments 1-2 are preferentially affected in SMA

The sensory neurons within the DRGs of the lumbar region receive inputs from the lower limbs and lower aspects of the trunk, with each DRG receiving inputs from a defined anatomical region. As an overview, DRGs within the lumbar segments 1 and 2 (L1-L2) receive inputs from the proximal lower limb, while L3-L4 receive inputs from the distal lower limb. As the proximal muscles of the body are primarily affected from the motor perspective in SMA, differences between the two groups of DRGs were investigated (Hamilton and Gillingwater, 2013; Kolb and Kissel, 2011; Ladak et al., 2014). Within L1 and L2 DRGs, there were significant differences in the percentages of NF200 (23.57% relative reduction, $P \leq 0.01$) and peripherin positive neurons (8.47% relative increase, $P \leq 0.05$) in SMA compared to control (Table 5-1). However, within the L3-L4 DRGs, there was only a significant difference in the percentage of NF200 positive neurons (12.01% relative reduction, $P \leq 0.05$; Table 5-1). This further suggests that the NF200 positive neurons are primarily affected in SMA and that the phenotype is more consistent in the L1 and L2 DRGs which receive the inputs from the body regions primarily affected in SMA.

Similarly, there was only a significant difference in the total number of cells per DRG within DRGs from lumbar segments 1 and 2 and not in DRGs from lumbar segments 3 and 4 (Table 5-1). NF200 positive neurons were significantly smaller in SMA mice than in control mice in both L1-L2 and L3-L4 DRGs (Table 5-1), again suggesting that the NF200 positive sensory neurons are primarily affected in SMA. Interestingly, although there was no significant difference in the area of peripherin positive neurons in DRGs from all lumbar regions investigated, peripherin positive neurons were significantly smaller in L1-L2 DRGs (Table 5-1). Thereby indicating that the primary DRG pathology is present within the L1-L2 DRGs, thus reflecting the pattern of muscle weakness seen in SMA.

DRG level	L1-L2			L3-L4		
	Control	SMA	p-value	Control	SMA	p-value
% NF200$^+$	22.36 ± 1.063	17.09 ± 1.107	** 0.0036	25.65 ± 1.035	22.57 ± 0.9689	* 0.0447
% peripherin$^+$	68.97 ± 1.663	74.81 ± 1.212	* 0.0121	65.65 ± 1.217	68.31 ± 1.101	ns 0.1266
% NF200$^+$/peripherin$^+$	8.667 ± 0.8516	8.104 ± 0.8139	ns 0.6197	8.697 ± 0.6681	9.119 ± 0.7193	ns 0.7010
Total cell number per DRG	220.8 ± 9.998	181.9 ± 13.26	* 0.0285	255.9 ± 13.65	229.3 ± 15.93	ns 0.217
NF200$^+$ cell area (μm^2)	673.0 ± 34.17	568.6 ± 29.30	* 0.0240	736.4 ± 31.14	625.6 ± 27.24	** 0.0095
Peripherin$^+$ cell area (μm^2)	205.9 ± 10.85	175.7 ± 7.980	* 0.0290	239.7 ± 14.39	225.5 ± 11.79	ns 0.4449

Table 5-1 DRGs in lumbar segments 1-2 are primarily affected in SMA
Quantification of phenotypes in DRGs from lumbar segments 1-2 (L1-L2) and 3-4 (L3-L4) in SMA mice compared to control. Values shown are mean ± SEM. P-values are calculated from Mann-Whitney test for percentage of neurons and from unpaired two-tailed Student's t-test for total neuron number and neuron area, ns – not significant; * P ≤ 0.05, ** P ≤ 0.01; N=3 mice per condition, n=4 DRGs per mouse; for area measurements N=3 mice per condition, n=10 neurons per mouse.

Here I have identified that there is a disruption to sensory neuron fate in SMA mice. The dorsal root ganglia in SMA have a reduction in the percentage of NF200 positive neurons with a concomitant increase in the percentage of peripherin positive neurons. The area of NF200 positive sensory neurons is also reduced in SMA mice compared to control. Importantly, the phenotypes are more pronounced in dorsal root ganglia from lumbar regions 1 and 2, which are those that receive inputs from the body regions primarily affected in SMA.

5.2.3 Changes in UBA1 and GARS protein levels lead to the DRG phenotypes seen in SMA

5.2.3.a Reduction in the nuclear to cytoplasmic ratio of UBA1 in SMA dorsal root ganglia

To investigate whether disruption to UBA1 expression was directly responsible for the disruption to sensory neuron fate in SMA, the ratio of UBA1 expression was investigated at the level of individual sensory neurons within the DRG. In order to do this spinal column sections containing DRGs from late-symptomatic SMA and control mice were stained for UBA1 (using the UBA1a antibody), along with SMI32 as a cytoplasmic marker and DAPI for a nuclear marker. The DRGs were imaged at constant confocal settings and an intensity analysis was performed to quantify the nuclear to cytoplasmic ratio (NCR) of the intensity of the staining (see method 2.8.1). In DRGs from SMA mice there was less prominent nuclear labelling and more pronounced cytoplasmic labelling of UBA1a, suggesting a shift in the distribution of UBA1 (Figure 5-6A). Quantification revealed a reduction of the NCR by 23.83% in SMA mice compared to controls (control=5.34, SMA=4.07; $P \leq 0.0001$; Figure 5-6B). Moreover, the distribution of the NCR showed a clear shift in the range from an NCR of 1 to 15 for control to an NCR range of 0 to 11 for SMA (Figure 5-6C). Therefore, this indicates that UBA1 protein expression is changed within sensory neurons in SMA.

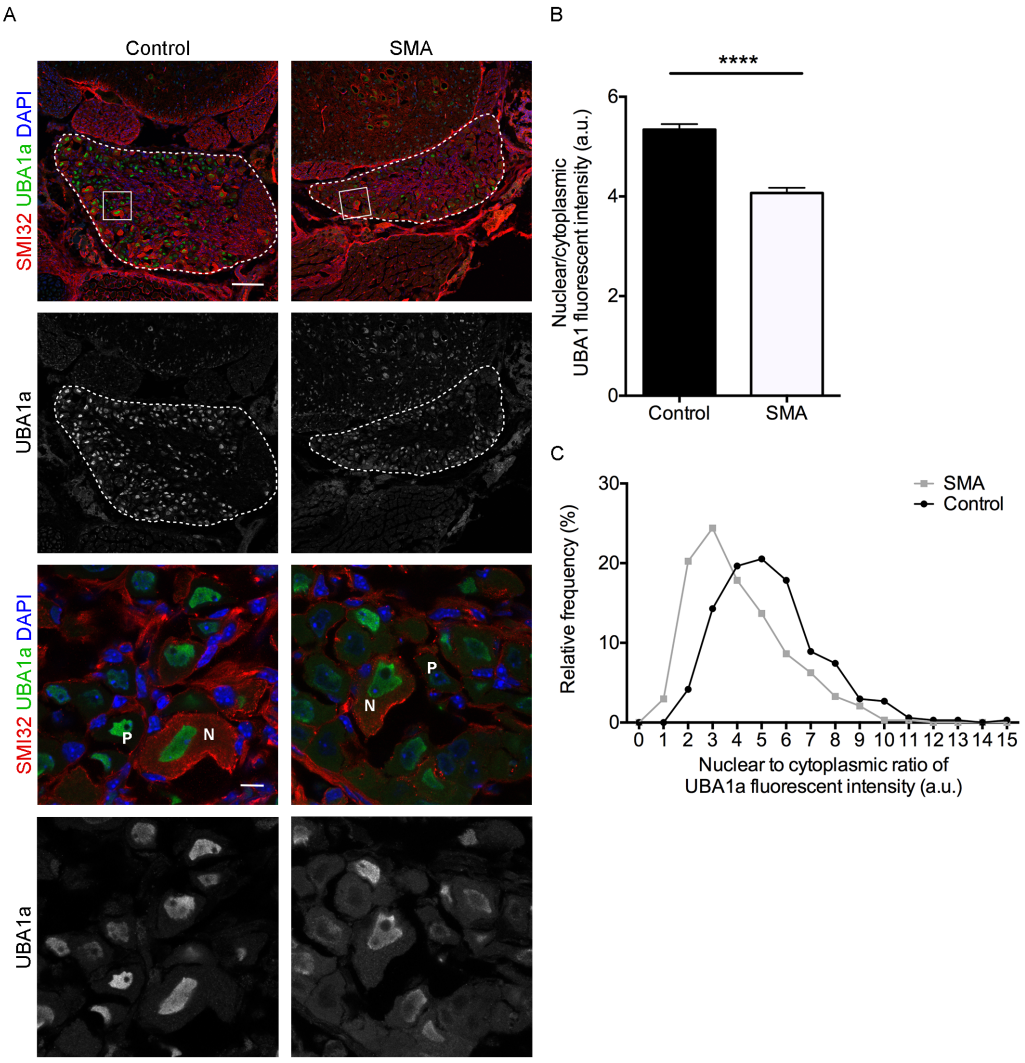

Figure 5-6 Nuclear UBA1 expression is reduced in sensory neurons in SMA dorsal root ganglia

Spinal column sections from late-symptomatic SMA and control mice were labelled with UBA1a, cytoplasmic (SMI32) and nuclear (DAPI) markers. **A** DRG sensory neruons show a reduction in nuclear UBA1a in SMA mice compared to control; images of L2 DRGs. Top panels: dotted line indicates outline of DRG, box indicates area in bottom panels, scale bar = 100µm. Bottom panels: N indicates NF200 positive-like neurons, P indicates peripherin positive-like neruons, scale bar = 10µm. **B** Late-symptomatic SMA DRG sensory neurons show a reduction in the nuclear to cytoplasmic ratio of UBA1a compared to control mice. Unpaired two-tailed Student's t-test; **** $P \leq 0.0001$. **C** Frequency distribution of the NCR of UBA1a in sensory neurons from control and SMA mice shows a shift to lower NCR in SMA mice; represented as percentage of neurons per NCR range, bin width=1. N=3 mice per condition, n=112 sensory neurons per mouse.

5.2.3.b The nuclear to cytoplasmic ratio of GARS expression is increased in DRGs from SMA mice

After identifying that UBA1 protein levels were changed within sensory neurons, to investigate if downstream changes in GARS expression were responsible for the disruption to sensory neuron fate in SMA, GARS expression in sensory neurons was quantified. To do this, the same experimental procedure was used as for UBA1 but the immunohistochemistry was performed for GARS, SMI32 and DAPI. The sensory neurons in the SMA mice showed an increase in the NCR of GARS by 5.06% compared to control (control=0.9627, SMA=1.011; $P \leq 0.001$; Figure 5-7A, B). However, it appeared that the larger area neurons had a selective increase in the intensity of GARS labelling (Figure 5-7A). This was confirmed by analysing the distribution of GARS NCR, where there was no change in the range of GARS NCR but there was an increase in the percentage of neurons with a higher NCR: 43.53% of SMA sensory neurons were present in the bin centred on an NCR of 1.2, compared to only 34.71% of control sensory neurons (Figure 5-7C). Interestingly, here changes in GARS expression occurred in the opposite direction to changes in UBA1 expression which was the same trend as seen by Western blot of whole DRGs and spinal cord. Therefore, this indicates that changes in the expression of UBA1 and downstream changes in GARS expression are likely to be causing the disruption to sensory neuron fate in SMA mice.

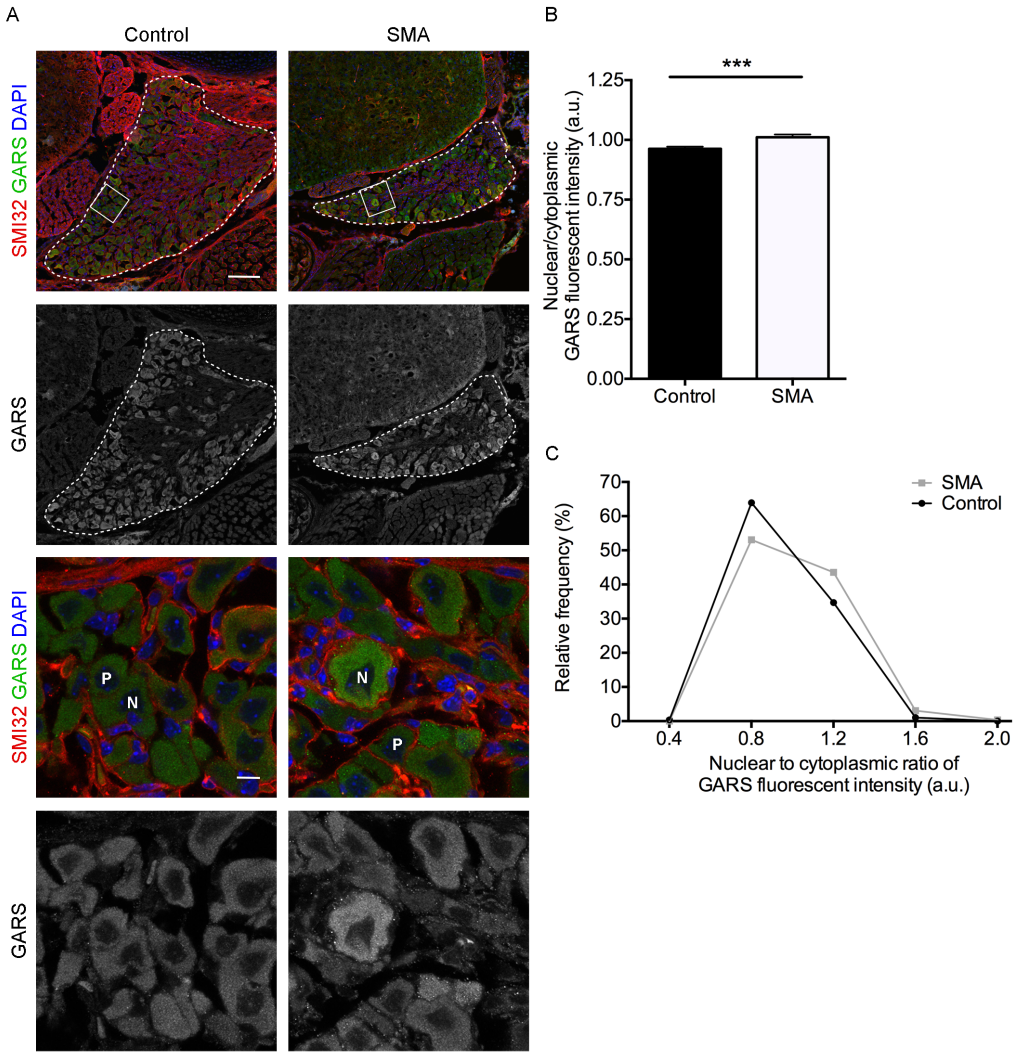

Figure 5-7 Nuclear GARS expression is increased in sensory neurons in SMA dorsal root ganglia

Spinal column sections from late-symptomatic SMA and control mice were labelled with GARS, cytoplasmic (SMI32) and nuclear (DAPI) markers. **A** DRG sensory neruons show an increase in GARS intensity in SMA mice compared to control; images of L2 DRGs. Top panels: dotted line indicates outline of DRG, box indicates area in bottom panels, scale bar = 100μm. Bottom panels: N indicates NF200 positive-like neurons, P indicates peripherin positive-like neruons, scale bar = 10μm. **B** Late-symptomatic SMA DRG sensory neurons show an increase in the nuclear to cytoplasmic ratio of GARS compared to control mice. Unpaired two-tailed Student's t-test; *** $P \leq 0.001$. **C** Frequency distribution of the NCR of GARS in sensory neurons from control and SMA mice show an increase in the percentage of neurons with a higher GARS NCR in SMA; represented as percentage of neurons per NCR range, bin width=0.4. N=3 mice per condition, n=112 sensory neurons per mouse.

5.2.3.c Expression of GARS and UBA1 are consistently changed in NF200 positive neurons from lumbar segments 1-2

In order to investigate whether changes in UBA1 and GARS expression were responsible for NF200 positive neurons being primarily affected in SMA, the expression of these proteins was quantified in different sub-populations of sensory neurons within the DRG. To do this, the area ranges of peripherin positive and NF200 positive neurons for both control and SMA were used to classify neurons as NF200 positive-like (control $\geq 450\mu m^2$; SMA $\geq 400\mu m^2$) or peripherin positive-like sensory neurons (control $\leq 350\mu m^2$; SMA $\leq 300\mu m^2$; Figure 5-5D, E). There was a significant reduction in UBA1a NCR in NF200 (31.16%; P≤0.0001) and peripherin (32.97%; P≤0.0001) positive like neurons in lumbar DRGs from L1-L2 in SMA mice compared to control (Table 5-2). In SMA mice there was also a significant reduction in the NCR of UBA1a in peripherin positive neurons from DRGs L3-L4 (37.86% reduction compared to control; P≤0.0001; Table 5-2). Interestingly, however, the NCR of GARS was only significantly changed in the NF200 positive like neurons in DRGs from regions L1-L2 (8.41% increase in SMA compared to control; P≤0.01; Table 5-2). Consistent with previous findings, UBA1a and GARS expression was changed in opposite directions within the NF200 positive sensory neurons in the dorsal root ganglia from L1-L2. Therefore, this confirms that NF200 positive neurons in DRGs from L1-L2 are primarily affected in SMA and identifies that it is changes in UBA1 and GARS expression within these cells that drives this phenotype.

DRG level		L1-L2			L3-L4		
		Control	SMA	p-value	Control	SMA	p-value
UBA1a	NF200$^+$ NCR	5.301 ± 0.2200 n=69	3.649 ± 0.1948 n=63	**** 0.0001	5.914 ± 0.2078 n=78	5.646 ± 0.2190 n=73	ns 0.3767
	peripherin$^+$ NCR	4.516 ± 0.1823 n=88	3.027 ± 0.1332 n=80	**** 0.0001	5.571 ± 0.2759 n=76	3.462 ± 0.1918 n=69	**** 0.0001
GARS	NF200$^+$ NCR	0.9381 ± 0.02102 n=56	1.017 ± 0.01886 n=57	** 0.0060	0.9173 ± 0.01720 n=66	0.9572 ± 0.01865 n=70	ns 0.1192
	peripherin$^+$ NCR	0.9835 ± 0.01751 n=84	1.039 ± 0.02621 n=87	ns 0.0840	0.9938 ± 0.01759 n=85	1.025 ± 0.02001 n=80	ns 0.2370

Table 5-2 GARS and UBA1 expression are consistently changed in NF200 positive neurons in L1-L2 dorsal root ganglia

Quantification of UBA1 and GARS NCR in sensory neuron cell bodies from SMA mice compared to control from lumbar DRGs in segments L1 to L2 and L3 to L4. Values shown as mean ± SEM. P-values are calculated from an unpaired two-tailed Student's t-test; ns – not significant, ** P ≤ 0.01, **** P ≤ 0.0001. N=3 mice per condition, the number of sensory neurons per condition are recorded in the table as n number.

Here I have shown that UBA1 is dysregulated in sensory neurons in dorsal root ganglia from SMA mice compared to control littermates. Likewise, dysregulation of GARS was observed in SMA mice sensory neurons, being particularly evident in larger area sensory neurons. By using the known area ranges of NF200 and peripherin positive neurons, I then identified that the disruption to expression of GARS and UBA1 was particularly pronounced in NF200 positive neurons from DRGs in lumbar segments 1 and 2. Thus, changes in the expression of GARS and UBA1 are likely a key driver of the disruption to sensory neuron fate in SMA.

5.2.4 Overexpressing UBA1 in SMA mice rescues the disruption to sensory neuron fate

5.2.4.a Overexpression of UBA1 *in vivo* reduces GARS expression in dorsal root ganglia

To identify whether the disruption to sensory neuron fate in SMA mice was dependent on, and not just correlated with, changes in UBA1 and GARS expression, the effect of UBA1 overexpression on sensory neuron fate in SMA was investigated. To do this, SMA mice were injected with AAV9-UBA1 on the day of birth and tissue was harvested at postnatal day 8. Before analysing the proportions of NF200 and peripherin positive sensory neurons, it was necessary to identify whether the overexpression of UBA1 was causing changes in GARS expression. Therefore, quantitative Western blot was performed on lumbar DRGs from SMA mice and SMA mice treated with AAV9-UBA1 to investigate protein levels of UBA1, GARS and SMN. There was no significant difference in SMN expression between SMA mice and AAV9-UBA1 SMA mice (Figure 5-8A, B) indicating that SMN was unlikely to be causing changes in protein expression or alterations to sensory neuron fate in these mice. The expression of UBA1 was increased by 16.60% ($P \leq 0.05$) in the DRGs from treated SMA mice compared to untreated SMA mice (Figure 5-8A, B), confirming that UBA1 had been upregulated *in vivo* by treatment with AAV9-UBA1. This upregulation of UBA1 lead to a reduction in GARS expression by 29.22% ($P \leq 0.05$; Figure 5-8A, B). This demonstrates that UBA1 overexpression in SMA mice leads to a reduction in GARS expression in DRGs, with GARS changed in the opposite direction to UBA1 and returning towards expression levels in control mice.

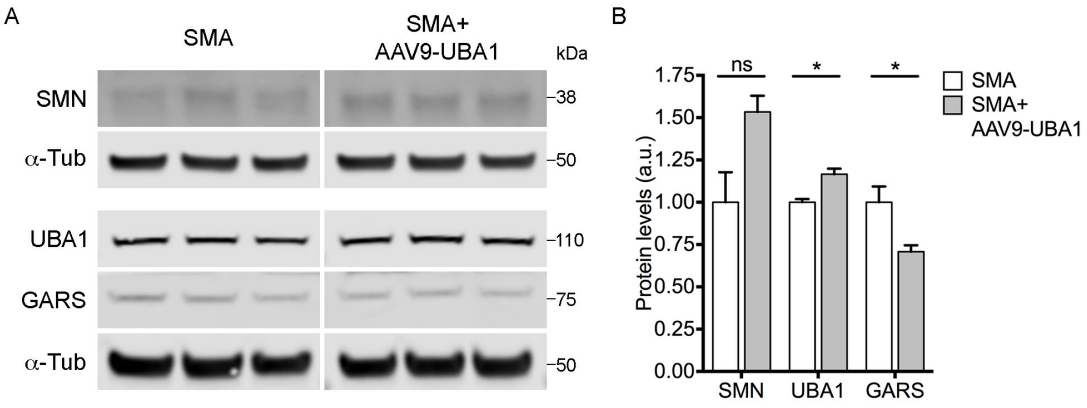

Figure 5-8 Overexpression of UBA1 in SMA mice leads to a reduction of GARS protein levels in dorsal root ganglia

Quantification of SMN, UBA1 and GARS protein levels in dorsal root ganglia from SMA mice and SMA mice treated with AAV9-UBA1. **A** Representative fluorescent Western blot of SMN, UBA1 and GARS in dorsal root ganglia from late-symptomatic SMA mice and SMA mice injected with AAV9-UBA1 (SMA+AAV9-UBA1), α-Tubulin (α-Tub) as loading control. Protein sizes are as indicated (kDa). **B** Quantification of SMN, UBA1 and GARS protein levels showing significant upregulation of UBA1 and downregulation of GARS. Protein expression was normalised to loading control, and then protein expression in SMA+AAV9-UBA1 DRGs was normalised to SMA DRGs. Samples run on the same gel in non-contiguous lanes. Unpaired two-tailed Student's t-test; ns – not significant, * $P \leq 0.05$; n=3 mice per condition.

5.2.4.b Treatment with AAV9-UBA1 rescues the disruption to sensory neuron fate in SMA mice

To investigate whether the reduced GARS expression caused by UBA1 overexpression *in vivo* lead to a rescue of sensory neuron fate, the percentage of NF200 and peripherin positive neurons was quantified in SMA mice and SMA mice treated with AAV9-UBA1. The sensory neuron fate phenotype was investigated in DRGs from lumbar segments 1 to 2, as these were the lumbar DRGs in which the disruption to sensory neuron fate was present in the SMA mice (see section 5.2.2.c). The results from control mice have been included for reference. Overexpression of UBA1 in SMA mice fully rescued the disruption to sensory neuron fate (Figure 5-9A). The percentage of NF200 positive neurons was increased by 45.89% in SMA mice treated with AAV9-UBA1 relative to untreated SMA mice ($P \leq 0.01$; Figure 5-9B). There was also a significant reduction in the percentage of peripherin positive

neurons in SMA mice treated with AAV9-UBA1 by 8.59% relative to untreated SMA mice (P≤0.05; Figure 5-9C). Interestingly, there was no difference in the percentage of sensory neurons positive for both NF200 and peripherin (Figure 5-9D). Compared to the reference data from control mice, there was no significant difference in the percentage of NF200 positive, peripherin positive or NF200 and peripherin positive neurons in SMA mice treated with AAV9-UBA1 (Figure 5-9B-D). This therefore indicates that overexpression of UBA1 *in vivo*, and the resulting reduction in GARS protein levels, fully rescues the disruption to sensory neuron fate in SMA mice, thereby confirming that this novel SMA phenotype is dependent on disruption to UBA1 and GARS protein levels.

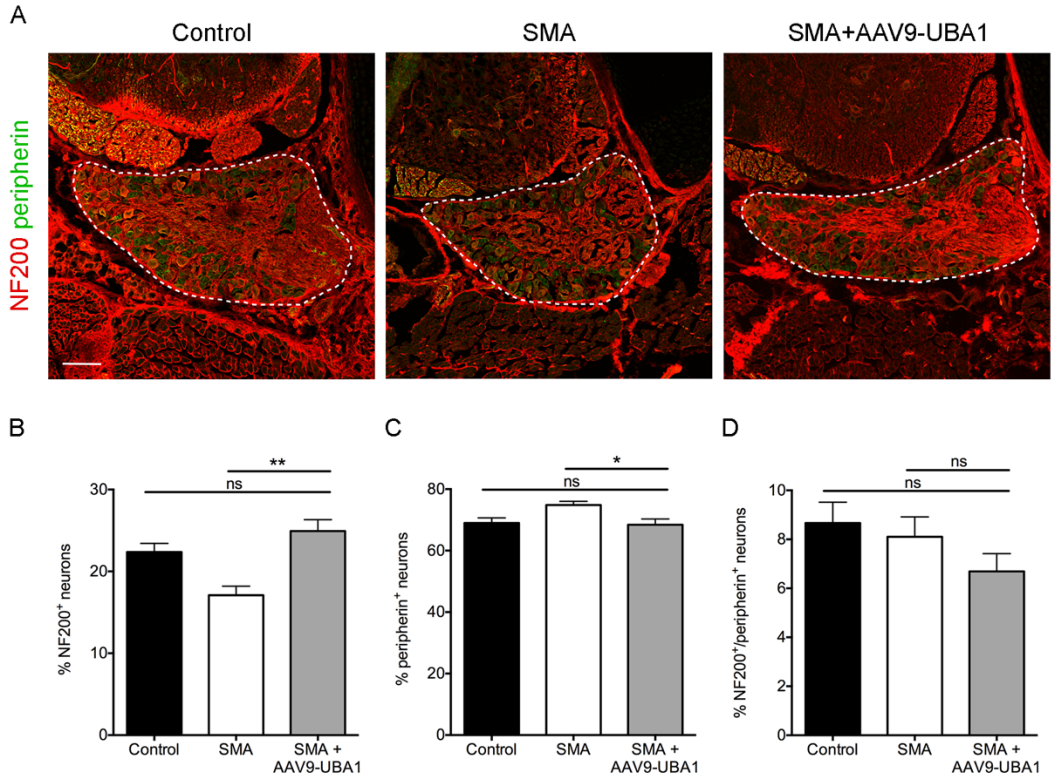

Figure 5-9 UBA1 overexpression *in vivo* rescues disruption to sensory neuron fate in SMA mice

Spinal column sections from SMA mice and SMA mice treated with AAV9-UBA1 were labelled with NF200 and peripherin. Data from control mice is shown as reference. **A** DRGs in spinal columns labelled for NF200 and peripherin, dotted line indicates outline of DRG, scale bar = 100μm; images of L2 DRGs. **B** Quantification of the percentage of NF200 positive ($NF200^+$) neurons showing an increase in SMA mice treated with AAV9-UBA1 compared to untreated SMA mice. **C** Quantification of the percentage of peripherin positive

(peripherin$^+$) sensory neurons showing a reduction in SMA mice treated with AAV9-UBA1 compared to untreated SMA mice. **D** Quantification of the percentage of sensory neurons positive for both NF200 and peripherin. N=3 mice per condition, n=4 DRGs per mouse. Kruskal-Wallis test with Dunn's multiple comparisons test; ns – not significant, * P ≤ 0.05, ** P ≤ 0.01.

5.2.4.c Overexpression of UBA1 *in vivo* rescues sensory neuron number and area in SMA mice

To investigate whether treatment with AAV9-UBA1 fully rescued the DRG phenotypes seen in SMA mice, the total number and area of sensory neurons was quantified. In SMA mice treated with AAV9-UBA1 there was an increase by 72.42% in the total cell number per DRG in SMA mice overexpressing UBA1 compared to untreated SMA mice (P≤0.0001; Figure 5-10A). There was also an increase in the area of NF200 positive neurons by an average of 129μm^2 per neuron in treated SMA mice compared to untreated SMA mice (P≤0.01; Figure 5-10B). Similarly, peripherin positive neurons showed an average increase of 40μm^2 in the SMA mice injected with AAV9-UBA1 (P≤0.01; Figure 5-10C). This therefore shows that treatment with AAV9-UBA1 fully rescues the range of dorsal root ganglia phenotypes seen in SMA mice.

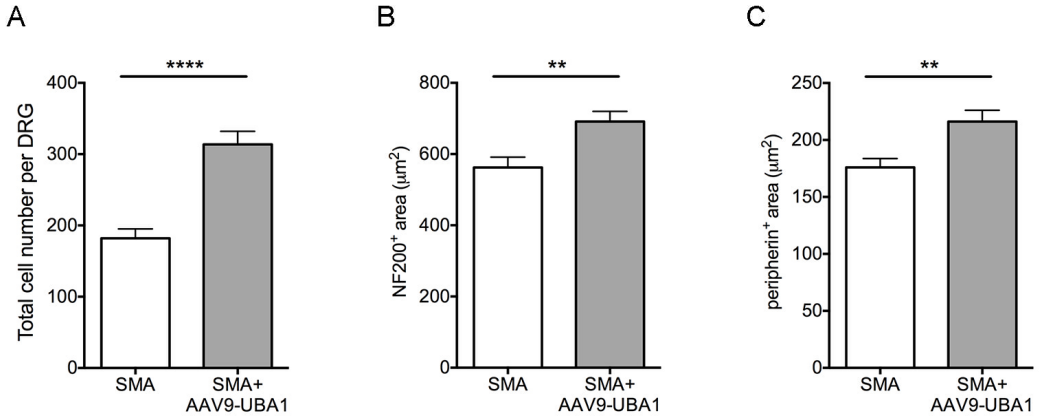

Figure 5-10 Overexpression of UBA1 rescues DRG phenotypes in SMA mice
DRG phenotypes are rescued in SMA mice treated with AAV9-UBA1. **A** Quantification of total cell number in SMA mice and SMA mice injected with AAV9-UBA1 (SMA+AAV9-UBA1) showed an increase in sensory neuron number following overexpression of UBA1 in SMA

mice. N=3 mice per condition, n=4 DRGs per mouse. **B, C** Quantification of the area of (**B**) NF200 and (**C**) peripherin positive neurons. N=3 mice per condition, n=10 neurons per mouse. **B** Increase in the area of NF200 positive neurons. **C** Increase in the area of peripherin positive neurons. **A-C** Unpaired two-tailed Student's t-test; ns – not significant, ** $P \leq 0.01$, **** $P \leq 0.0001$.

In this section, I have shown that treatment with AAV9-UBA1 leads to a robust overexpression of UBA1 and a downregulation of GARS expression in DRGs from SMA mice. I then demonstrated that this results in a complete rescue of the disruption to sensory neuron fate seen in SMA mice as well as increasing the total neuron number per DRG. Finally, I showed that UBA1 overexpression in SMA mice rescued the reduction in area of NF200 and peripherin positive sensory neurons. Overall, this shows that the disruption to sensory neuron fate in SMA is both reversible and regulated by a UBA1 and GARS-dependent mechanism.

5.3 Discussion

The studies described here were initiated to investigate the effect of UBA1-dependent changes in tRNA synthetases on the pathogenesis of SMA. Initially I showed that the expression of the tRNA synthetases GARS and YARS was disrupted across a range of tissues from SMA mice. Importantly, all of the tissues investigated also showed a reduction in the expression of UBA1. I then characterised a novel phenotype in SMA whereby the fate of sensory neurons within the dorsal root ganglia was perturbed. Interestingly, the total number of sensory neurons and the area of the larger, NF200 positive neurons were both reduced in SMA mice compared to control littermates. I then showed that in the NF200 positive neurons the reduction in UBA1 NCR leads to an increase in the NCR of GARS and it is these expression changes that drive the sensory neuron phenotypes in SMA mice (Figure 5-11). Finally, by treating SMA mice with AAV9-UBA1, I demonstrated that overexpression of UBA1 in SMA DRGs causes a reduction of GARS protein expression. This rescued not only the disruption to sensory neuron fate, but also the area of sensory neurons and the total number of sensory neurons per DRG (Figure 5-11). Overall, here I have shown that the disruption to sensory neuron fate and sensory neuron area in SMA mice is reversible and dependent on a UBA1 and GARS-dependent pathway.

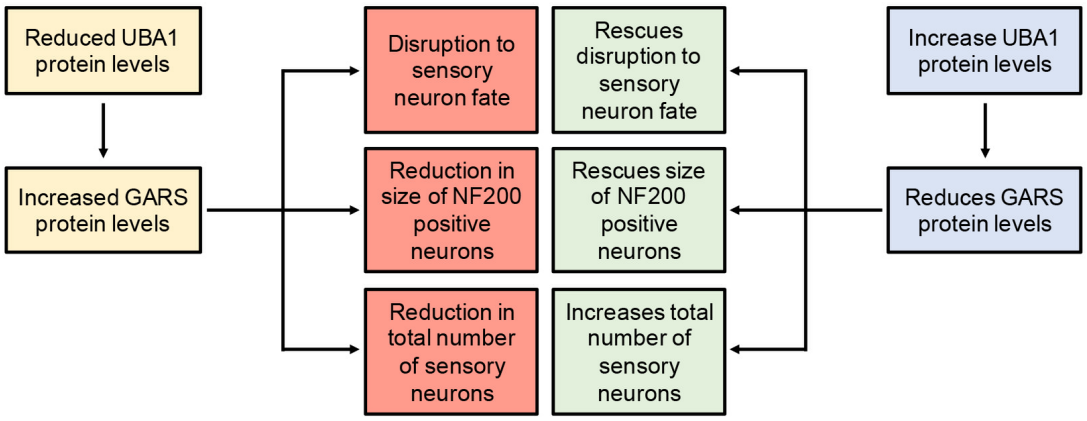

Figure 5-11 Overview of sensory neuron phenotypes in SMA mice

Reduced protein levels of UBA1 in dorsal root ganglia from SMA mice resulted in an increase in the expression of the tRNA synthetase GARS. This disruption to GARS expression distorted the proportions of sensory neuron subpopulations in the DRG, resulting

in a reduction of the medium to large area, NF200 positive neurons and an increase of the small area, peripherin positive sensory neurons. The NF200 positive neurons were also smaller in SMA and there is a reduction in the total number of sensory neurons per DRG. Treating SMA mice with AAV9-UBA1 increased UBA1 expression in the DRG which reduced GARS expression levels. This in turn rescued the disruption to sensory neuron fate, increased the area of NF200 positive neurons and increased the total cell number per DRG.

A disruption to sensory neuron fate was recently described in mouse models of CMT2D, which are caused by mutations in *Gars* leading to increased expression of GARS (Achilli et al., 2009; Motley et al., 2010). Compared to other CMTs, CMT2D has relatively mild sensory involvement (Antonellis et al., 2003; El-Abassi et al., 2014; Liao et al., 2015) and in a severe mouse model of CMT2D there is approximately a 20% absolute shift in the proportions of the different sensory neuron subtypes (Sleigh et al., 2017a). In the milder mouse model of CMT there is a 10% shift in the proportions of NF200 and peripherin positive sensory neurons (Sleigh et al., 2017a). In the study performed here an absolute reduction of NF200 positive neurons by 5% and concomitant 5% increase in peripherin positive neurons in SMA was identified. Based on the changes in sensory neuron proportions in mouse models of CMT2D, the level of disruption to sensory neuron fate identified here is in line with the phenotypic involvement of the sensory system in SMA.

To elaborate, several studies have investigated changes in the sensory system in various models of SMA. For example, one study identified that sensory neurons cultured from a severe mouse model of SMA do not develop properly due to defects in neurite outgrowth and growth cone morphology. The cultured neurons also showed a reduction of β-actin protein and mRNA in growth cones (Jablonka et al., 2006) – a phenotype that is seen in SMN deficient motor neurons (Rossoll et al., 2003). Interestingly, the study also found that there was no difference in the total number of sensory neurons per L5 DRG in SMA mice compared to control (Jablonka et al., 2006). This agrees with the results presented here as there was no significant difference in the number of sensory neurons per DRG from lumbar segments L3-L4,

but this difference was present in L1-L2 DRGs, thus indicating a consistent finding of no change in total cell number in lower lumbar DRGs.

Two other studies also investigated sensory neurons within the DRG using antibodies against paravalbumin - a specific marker of proprioceptive neurons (Lallemend and Ernfors, 2012; Le Pichon and Chesler, 2014). One study showed no significant difference in the number of paravalbumin positive neurons in L1 DRGs from P13 (late-symptomatic) SMA delta 7 mice (Mentis et al., 2011), while the other study showed a significant reduction in the number of paravalbumin positive neurons in L4 DRGs from P14 SMA delta 7 mice (~13% reduction compared to control) (Ling et al., 2010). This suggests some variation in the presence of a sensory neuron phenotype in SMA mice. However, the quantification methods were strikingly different between the two studies indicating the relevance and reliability of a quantification method that relies on relative percentages, as used in this study, as opposed to quantification of total numbers of neurons and then in one case, multiplication to arrive at an estimated number of paravalbumin positive neurons per DRG (Ling et al., 2010; Mentis et al., 2011; Sleigh et al., 2017a). Importantly, the DRGs from SMA mice shown in both studies appear considerably smaller than their control counterparts, indicating a consistent reduction in size of dorsal root ganglia in SMA (Ling et al., 2010; Mentis et al., 2011).

It has also been shown that there is a reduction in myelinated dorsal root axons (Ling et al., 2010) and a reduction in the number of synapses from proprioceptive sensory neurons onto motor neurons in SMA mice compared to control (Ling et al., 2010; Mentis et al., 2011). This suggests that the reduction in NF200 positive cells identified here may result in a reduction of processes of this sensory neuron subtype to the spinal column and thus a reduction of synapse number on motor neurons. Interestingly, the reduction in proprioceptive synapses onto motor neurons is differentially affected by the spinal cord level within the lumbar region. Synapses onto L1 motor neurons and medial L5 motor neurons are primarily lost, while synapses onto L5 lateral motor neurons are largely spared (Mentis et al., 2011). Importantly, the difference identified between these different pools of motor neurons are consistent with the differences seen in sensory neuron fate between L1-L2 DRGs

and L3-L4 DRGs. As previously mentioned the L1-L2 region receive inputs from and innervate trunk and proximal lower-limb body regions, while L3-L5 lumbar regions receive inputs from and innervate more distal lower limb regions, that is excluding the medial motor neurons in L5 which innervate trunk regions (Ladak et al., 2014; Mentis et al., 2011). This demonstrates that phenotypes affecting the sensory system in SMA consistently affect DRGs and motor neurons related to the body regions primarily affected in SMA.

Furthermore, it has also been shown that the reduction of proprioceptive synapses onto motor neurons can be reversed by increasing SMN expression specifically in motor neurons (Gogliotti et al., 2012). Similarly, a study in maternal-zygotic *smn* mutant zebrafish showed a reduction in the number of dorsal root ganglia neurons and that this could be rescued by overexpressing SMN in motor neurons (Hao le et al., 2015). However, another study showed that an increase in SMN expression in paravalbumin positive neurons was necessary, alongside SMN increase in motor neurons, to fully restore the number of proprioceptive synapses onto motor neurons in SMA mice (Fletcher et al., 2017). This study also showed that selective upregulation of SMN in proprioceptive neurons was required to normalise the hyperexcitability of motor neuron membranes seen in SMA and restore firing frequency of the motor neurons. It was also identified that blocking neurotransmission specifically in proprioceptive neurons caused severe motor defects, shortened lifespan of wild-type mice and rendered the motor neurons dysfunctional (Fletcher et al., 2017). This suggests that the reduction of NF200 positive neurons in SMA mice may be causing additional defects to motor neurons, including hyperexcitability and reduced firing frequency.

Moreover, there are several reports that identify sensory pathology in SMA patients. For example, an evaluation of electroneuromyographic studies in 15 SMA type 1 patients revealed that 26.7% of the patients had abnormal sensory conduction (Duman et al., 2013). In another study, sural nerve biopsies were performed on 19 patients with infantile SMA. All 7 of the type 1 SMA patients showed axonal degeneration, 5 of which had abnormal sensory conduction; however, none of the patients with type 2 or 3 SMA showed signs of sensory involvement (Rudnik-

Schoneborn et al., 2003). Furthermore, a recent case report described a 3-month-old boy who presented with hypotonia and weak muscles. Genetic diagnosis confirmed type 1 SMA however, the patient also had an absence of sensory responses on nerve conduction studies (Reid et al., 2016) further suggesting sensory involvement in some cases of SMA. Interestingly, several studies conducted on presumed SMA cases (patients diagnosed with SMA before genetic testing was available for the disease) also identified sensory pathology in SMA, finding not only degeneration of sensory nerves but also ballooned neurons and chromatolysis within the dorsal root ganglia (Carpenter et al., 1978; Marshall and Duchen, 1975; Murayama et al., 1991). Interestingly, a genetically-confirmed case of XL-SMA (caused by mutations in *UBA1*) showed nodules within the dorsal root ganglia, indicating a loss of sensory neurons (Dlamini et al., 2013). Together these studies demonstrate that not only are sensory phenotypes present in SMA patients as well as the models used to study the disease, but that the DRGs themselves may also be affected in SMA patients showing the relevance of the phenotypes identified here. The involvement of sensory phenotypes in SMA also starts to draw overlap between CMT and SMA at the patient level.

One of the key features of this study was highlighting the overlap of SMA and CMT at both the phenotypic and molecular level. The identification of sensory phenotypes in SMA patients starts to shed some light on the phenotypic overlap of these diseases in patients. The identification of individuals with genetically confirmed cases of co-segregation of SMA and CMT further highlights phenotypic overlap of these diseases. For example, an 11-month-old patient presented with muscle weakness and genetic diagnosis confirmed SMA type 2, however, the patient also showed an absence of sensory nerve conduction and slow motor conduction velocities, symptoms typical of peripheral neuropathy (Fernandez et al., 2016). Through investigation of the patient's family history, a paternal uncle with CMT1A was identified and genetic testing confirmed the patient had a duplication of *PMP22* and therefore, along with SMA type 2 received a diagnosis of CMT1A (Fernandez et al., 2016). Similarly, a second patient from a family with several members affected by CMT1A presented with muscle weakness and bilateral foot deformities. Genetic

analyse confirmed diagnosis of SMA type 3 and CMT1A (Jedrzejowska et al., 2008), indicating that the pathologies of these two diseases can occur simultaneously.

Furthermore, and perhaps more interestingly, several genes have now been identified in which mutations can cause a range of phenotypes including both CMT and SMA-like diseases. As previously mentioned, mutations in *GARS* can cause classical infantile SMA, distal SMA type 5 and most commonly CMT2D (Antonellis et al., 2003; Eskuri et al., 2012; James et al., 2006). Similarly, mutations in *MORC2*, which encodes a nuclear protein involved in transcriptional regulation and DNA repair, can cause CMT type 2Z or SMA (Schottmann et al., 2016; Sevilla et al., 2016). Patients with CMT2Z generally present in the second decade of life with distal weakness and sensory impairment, while the patients with an SMA-like disease present in infancy with an SMA-like phenotype that progresses with increasing sensory loss and weakness and atrophy of muscles (Schottmann et al., 2016). Mutations in *MORC2* have also been shown to cause an SMA-like disease with neuropathy, paralysis of the diaphragm and cerebellar atrophy but with an absence of sensory involvement (Sevilla et al., 2016).

Likewise, mutations in *IGHMBP2* have been shown to cause both CMT type 2S and SMA with respiratory distress type 1 (SMARD1) (Cottenie et al., 2014; Jedrzejowska et al., 2014; Liu et al., 2017a; Pedurupillay et al., 2016). Patients with mutations in *IGHMBP2* can present with sensorimotor axonal neuropathy, progressive weakness and wasting of muscles and are thus diagnosed with CMT2S; these patients do not generally have compromise of the respiratory system (Cottenie et al., 2014; Liu et al., 2017a). Conversely, mutations in *IGHMBP2* also cause SMARD1 where patients present with infantile SMA and generally die within the first year of life due to respiratory failure (Jedrzejowska et al., 2014; Pedurupillay et al., 2016). It is predicted that the mutations in *IGHMBP2* that cause SMARD1 are more severe and lead to lower protein expression of IGHMBP2 than mutations that cause CMT2S; thus, suggesting a spectrum of phenotypes distinguished by the specific mutations in *IGHMBP2* (Cottenie et al., 2014; Pedurupillay et al., 2016). Together, not only does this highlight considerable overlap between the phenotypes

of CMT and SMA, but it also demonstrates overlap of genetic pathways and molecular causes of these diseases.

Moreover, molecular overlap of CMT and SMA is further emphasised by a range of rare cases with mutations in genes in pathways known to be affected or involved in one of these diseases. For example, mutations in *LRSAM1*, an E3 ubiquitin ligase, cause CMT type 2G (Peeters et al., 2016). Patients with CMT2G display mild lower-limb axonal sensorimotor neuropathy and fatty atrophy in musculature. Interestingly, it has been shown that mutations in *LRSAM1* do not cause reduced levels of the protein or disrupt the enzymes ubiquitylation activity but they do lead to several transcriptional changes, including increased levels of NEDD4L (an E3 ligase) and *TNFRSF21* a regulator of axonal degeneration (Peeters et al., 2016). This suggests that mechanisms of degeneration in CMT2G may be similar to UBA1-mediated degeneration in SMA, as it is unlikely that alteration of canonical ubiquitylation activity is responsible for pathogenesis of either of these diseases.

Finally, mutations in *PIEZO2* can cause a neuromuscular disease characterised by muscle atrophy, mild sensory involvement, delayed motor milestones and scoliosis (Delle Vedove et al., 2016). *PIEZO2* encodes a mechanosensitive ion channel responsible for mechanosensation of light touch and proprioception. Therefore, loss of PIEZO2 protein due to these mutations causes disturbed proprioception leading to aberrant muscle development and function (Delle Vedove et al., 2016), suggesting that defects within sensory neurons themselves can lead to muscle defects and delayed motor development.

Together, these studies have demonstrated that tRNA synthetases are dysregulated within several tissues from a mouse model of spinal muscular atrophy and that UBA1-dependent dysregulation of the tRNA synthetase GARS is responsible for mediating a novel sensory neuron phenotype in SMA mice. Although disruption to sensory neurons has previously been identified in models of SMA, this is the first study to demonstrate disruption to sensory neuron fate and reduction in the size of sensory neurons within the dorsal root ganglia. Importantly, by targeting the molecular pathway responsible for these phenotypes it was possible to correct the disruption to sensory neuron fate and area, revealing a truly UBA1-dependent

phenotype in SMA mice and elucidating a mechanism of UBA1-mediated pathogenesis of SMA. The work here also suggests a reason for disruption to the sensory neurons identified in other studies on SMA models and draws closer the link between SMA and CMT from both a phenotypic and molecular perspective.

Chapter 6 General discussion

6.1 Overview of results

In this thesis, several questions were addressed to increase our understanding of the cellular and molecular mechanisms underlying UBA1-mediated pathogenesis of SMA.

The first of these was to investigate whether UBA1 expression was disrupted at the single cell level in motor neurons (section 1.4, Aim 1). Following on from work previously reported in the literature I was able to show that UBA1 distribution varied between different cell types and for the first time characterise UBA1 distribution in a healthy population of neurons. Interestingly, in these motor neurons a dramatic cellular redistribution of UBA1 was seen over-time in culture, a feature that was not present in long term cultures of dividing cells. I also showed that the NCR of UBA1 changed during neonatal development in lower motor neurons in healthy mice *in vivo*. Perhaps the most important finding of this section of work, was the identification of a significant reduction of UBA1 expression in spinal motor neurons from pre-symptomatic SMA mice compared to control littermates. This significantly builds upon and extends previous work, suggesting that UBA1 reduction is likely to be a driving force of motor neuron degeneration in SMA. Furthermore, the identification that UBA1 is mislocalised in pre-symptomatic SMA spinal motor neurons and the different distribution patterns seen in different cell types suggests that disruption to UBA1 distribution may contribute to motor neuron susceptibility in SMA.

Secondly, I sought to investigate what effect the pre-symptomatic reduction in UBA1 had on the proteome by identifying and validating novel downstream targets of UBA1 (section 1.4, Aim 2). Analysis of a label-free proteomic screen on HEK293 cells in which UBA1 expression levels had been modulated revealed three UBA1-dependent protein families: nuclear transport, translation elongation and tRNA synthetases. Individual proteins from each of these families were validated as being UBA1-dependent, both *in vitro* and *in vivo*. By performing a cross-comparison of the dataset generated here with SMA proteomic screens and related studies, I

identified that several different tRNA synthetases are disrupted across a range of studies suggesting that this protein family may be relevant for UBA1-mediated pathogenesis of SMA. Following this I demonstrated that, while changes to UBA1 expression levels lead to alterations in overall ubiquitylation, one of the main UBA1-dependent proteins identified in this screen, GARS, is not differentially ubiquitylated by UBA1. Therefore, this suggests that UBA1 influences the changes in expression of some of its downstream targets through non-canonical mechanisms.

Finally, I investigated whether the novel downstream targets identified here were relevant for UBA1-mediated pathogenesis of SMA (section 1.4, Aim 3). To address this, Western blots were performed on SMA tissue which revealed that both YARS and GARS showed significant dysregulation across a range of tissues in SMA mice. To investigate whether this dysregulation was relevant for pathogenesis of SMA, the proportions of different sensory neuron subtypes were quantified in SMA mice as there is disruption to sensory neuron fate in CMT2D mice which have mutated *GARS* and elevated expression of GARS (Sleigh et al., 2017a). Not only did SMA mice show a disruption to sensory neuron fate in DRGs, but the sensory neurons themselves were smaller and there was reduction in the overall number of sensory neurons. Importantly, there was disruption to both UBA1 and GARS distribution in SMA sensory neurons. Following overexpression of UBA1 in SMA mice, the disruption to GARS expression seen in DRGs was reversed and all sensory neuron pathologies were rescued. Therefore, this work identified a novel SMA phenotype that is caused by UBA1-dependent disruption of GARS expression.

Together the data presented in this thesis clearly implicates the pre-symptomatic reduction of UBA1 in SMA pathogenesis, identifies downstream targets of UBA1 that are relevant for UBA1-mediated degeneration, and reveals a novel sensory neuron phenotype in SMA, dependent on one of the downstream targets of UBA1. This work has implications for a wider range of neurodegenerative and neuromuscular disorders than SMA, not least because disruption to ubiquitin homeostasis is a common feature of multiple neurodegenerative conditions but also because part of this study focused on characterising a phenotype shared by two neuromuscular diseases.

6.2 Ubiquitin pathways in disease

In the first instance the studies performed here have clear relevance for XL-SMA as the causative mutations for this form of SMA reside within *UBA1* (Dlamini et al., 2013; Jedrzejowska et al., 2015; Ramser et al., 2008). Interestingly, the mutations for XL-SMA all cluster within exon 15 of *UBA1* which forms part of the active adenylation domain (Figure 1-3) (Ramser et al., 2008). The active adenylation domain is responsible for binding both ATP and ubiquitin and so is essential for the catalytic activity of the enzyme (Lee and Schindelin, 2008). However, mutations identified in the active adenylation domain of *UBA1* demonstrate only a partial loss of function (Tokgoz et al., 2006). Furthermore, mutations within UBA1 that do cause a reduction in adenylation activity do not completely eliminate the ability of UBA1 to activate ubiquitin and transfer it to an E2 enzyme (Lao et al., 2012). Therefore, it is unlikely that mutations in *UBA1* cause XL-SMA through alterations in the ability of the enzyme to perform its function in the ubiquitylation cascade. Interestingly, it has also been shown that mutations in *UBA1* cause the enzyme to become less stable than wild-type UBA1 and thus lead to increased degradation (Lao et al., 2012). It is therefore conceivable that there may be reduced levels of UBA1 in XL-SMA and so while the mechanisms behind SMA pathogenesis in XL-SMA have yet to be elucidated, the work performed here may shed some light onto pathways disrupted downstream of UBA1 in XL-SMA.

Similarly, as the proteomic screen was performed on HEK293 cells in which overexpression and knockdown of UBA1 had been performed, the data generated here may be relevant for a variety of diseases in which UBA1 expression is disrupted. However, different aspects of the screen may be more relevant for different diseases. For example, downstream targets of UBA1 changed following UBA1 overexpression may be relevant to understand cancers, such as leukemia and multiple myeloma, where UBA1 is over active and leads to increased protein ubiquitylation (Xu et al., 2010). Protein families identified as UBA1-dependent may be relevant for different neurodegenerative conditions. For example, as previously mentioned, it has recently been shown that nuclear transport is disrupted in ALS and that UBA1 binds to mutant FUS (one of the genetic causes of ALS) (Dormann et al.,

2010; Wang et al., 2015; Woerner et al., 2016). Wild-type FUS protein primarily resides within neuronal nuclei but mutant FUS forms aggregates within the cytoplasm (Dormann et al., 2010; Wang et al., 2015). As UBA1 only binds to mutant FUS, sequestration of UBA1 into FUS aggregates may contribute to the defective nuclear transport seen in this disease and may also disrupt UBA1 localisation; a feature that could itself lead to detrimental effects on neuron health and function. Indeed, it has been shown that UBA1 is sequestered in Lewy bodies in models of PD (McNaught et al., 2002), demonstrating that UBA1 does get sequestered into disease-associated protein aggregates. Moreover, it has also been shown that redistribution of SMN to mutant FUS aggregates leads to reduction in axonal SMN (Groen et al., 2013), thus demonstrating that sequestration of proteins in disease-associated protein aggregates can lead to a redistribution of the protein.

Furthermore, in this study I demonstrated that UBA1 does not regulate expression of its downstream target GARS through differential ubiquitylation. This raises the possibility of UBA1 influencing GARS, and perhaps other tRNA synthetases and downstream targets, through a non-canonical mechanism. A non-canonical role of UBA1 has previously been identified in the regulation of autophagy (Chang et al., 2013). Moreover, the possible non-canonical function of UBA1 in mediating axon development (Watts et al., 2003), along with the work presented here, indicate that UBA1 may have multiple non-canonical functions. Not only does this expand our knowledge of the basic biology of UBA1 but it could also be crucial for a range of neurodegenerative conditions. Both UPS activity and autophagy are important for clearing damaged and misfolded proteins but both pathways are affected in several neurodegenerative conditions (Bedford et al., 2011; Kubben and Misteli, 2017; Shen and Mizushima, 2014), and UPS activity is known to decline with age (Tydlacka et al., 2008). Although activation of ubiquitin by UBA1 is not thought to be the rate limiting step in the UPS (Bedford et al., 2011), if UBA1 is redistributed, as occurs in AD and HD (Lopez Salon et al., 2000; Wade et al., 2014), or inhibited as in some cases of idiopathic PD (Chou et al., 2008; Viquez et al., 2012), the requirement of UBA1 for both canonical and non-canonical functions (including autophagy) may not be met. Indeed, it has been shown for HD that UBA1 function eventually declines below a critical threshold required to maintain protein

homeostasis (Wade et al., 2014). Therefore, these alterations in UBA1 localisation or expression may exasperate disruption to the UPS and autophagy in a range of neurodegenerative conditions characterised by accumulation of ubiquitylated proteins.

6.3 tRNA synthetases in health and disease

It is now well established that mutations in several different tRNA synthetases cause a variety of subtypes of Charcot-Marie-Tooth disease (Antonellis et al., 2003; Gonzalez et al., 2013; Jordanova et al., 2006; McLaughlin et al., 2012; McLaughlin et al., 2010; Vester et al., 2013). Here, two different tRNA synthetases were shown to be dysregulated in SMA tissue and the UBA1-dependent disruption to one of these tRNA synthetases was shown to cause a novel sensory neuron phenotype in SMA mice. Thus, extending the range of diseases in which tRNA synthetases, in particular GARS, are implicated in. Despite this, it is still unclear how mutations and dysregulation of tRNA synthetases lead to degeneration.

6.3.1 Non-canonical functions of tRNA synthetases

Of the tRNA synthetases that harbour mutations causative for CMT, GARS and YARS are the most studied. As previously mentioned (see 5.1), mutations in *GARS* cause CMT2D (Antonellis et al., 2003) and mutations in *YARS* cause DI-CMTC (Jordanova et al., 2006). In both of these diseases loss of aminoacylation activity is not a common feature of the different mutant GARS and YARS proteins (Motley et al., 2010; Niehues et al., 2015; Seburn et al., 2006). Recent work on CMT2D has identified that mutant GARS aberrantly binds to the transmembrane receptor protein neuropilin 1 (Nrp1) and disrupts the interactions of Nrp1 with its natural binding partners (He et al., 2015; Sleigh et al., 2017b). Therefore, the current understanding is that mutations most likely cause a toxic gain-of-function of GARS or lead to aberrant interaction with the wild-type GARS protein (He et al., 2015; Malissovas et al., 2016; Sleigh et al., 2017b). In contrast, the disruption to sensory neuron fate identified in SMA mice is unlikely to be due to either of these mechanisms as GARS expression is dysregulated in the absence of *GARS* mutations.

Interestingly, however, several non-canonical functions of tRNA synthetases have recently been identified where tRNA synthetases are adapted for dual roles that coexist with their aminoacylation activity (Pang et al., 2014). For example, GARS can be secreted from macrophages and exhibits cytokine-like properties by binding cadherin which leads to inhibition of growth of ERK-activated tumour cells (Park et al., 2012). It has also been demonstrated that GARS functions as a chaperone that critically supports neddylation by stabilising NEDD8 conjugated to E2 enzymes (Mo et al., 2016). This indicates a role of GARS in a related pathway to the UPS and suggests that dysregulation of GARS expression may indeed lead to disruption of sensory neuron fate through a mechanism not reliant on the aminoacylation activity of the enzyme.

Similarly, YARS has been shown to have a non-canonical function in which it is cleaved into N- and C-terminal halves during apoptosis to generate two distinct cytokines with immunological activity (Wakasugi and Schimmel, 1999). Moreover, YARS has also been shown to become highly acetylated during oxidative stress which leads to a reduction in the aminoacylation activity of the enzyme and an increase in its nuclear translocation. Once in the nucleus, the acetylated YARS then protects against DNA damage caused by oxidative stress by activating DNA repair genes (Cao et al., 2017). Together this indicates that tRNA synthetases may have multiple non-canonical functions alongside their role in aminoacylation. Several other non-canonical functions of a range of tRNA synthetases have been identified including roles in mitochondrial functions, translation and transcriptional regulation and a wide range of immunological processes (Ibba and Soll, 2000; Pang et al., 2014). Therefore, disruption of any one or any combination of these non-canonical functions of tRNA synthetases could contribute to neuronal degeneration in diseases such as CMT2D, DI-CMTC and SMA.

6.3.2 tRNA synthetases in neurodegeneration

Aside from their involvement in CMT and the dysregulation of tRNA synthetases in SMA, tRNA synthetases have also been implicated in other neuronal and neurodegenerative conditions (Park et al., 2008). For example, mutations in the

editing domain of the alanyl-tRNA synthetase gene (*AARS*) does not impair aminoacylation activity of AARS but reduces the accuracy of the enzyme leading to mistranslation (inclusion of the wrong amino acid at codons for alanine) (Nangle et al., 2006; Park et al., 2008). Mistranslation in turn leads to accumulation of misfolded proteins and a severe ataxia phenotype caused by Purkinje cell loss in the cerebellum in mice harbouring editing domain mutations in *AARS* (Lee et al., 2006; Nangle et al., 2006). Mutations in the editing domain of *AARS* have also been shown to cause cardioproteinopathy characterised by ubiquitylated protein aggregates and mitochondrial dysfunction in cardiomyocytes (Liu et al., 2014). This again suggests overlap of ubiquitin pathways and disruption to specific tRNA synthetases in disease pathogenesis. It has also been demonstrated that lysyl-tRNA synthetase interacts with mutant Cu/Zn superoxide dismutase 1 (SOD1) in ALS but not wild-type SOD1 (Kunst et al., 1997), again suggesting a modifying effect on ALS disease pathogenesis by a disruption of a specific tRNA synthetase.

Moreover, there is considerable evidence implicating disruption to aminoacyl-tRNA synthetase complex interacting multifunctional protein-2 (AIMP2) in Parkinson's disease (Park et al., 2008). The multisynthetase complex is composed of nine tRNA synthetases and three non-synthetase proteins (AIMP1, AIMP2 and AIMP3). While it is thought that there may be cell-type specific differences in the tRNA synthetases that are part of this complex, it is known that the three AIMPs form the core of the multisynthetase complex (Ibba and Soll, 2000; Pang et al., 2014). On release from the complex, the tRNA synthetases trigger specific signalling activities dependent on the non-canonical activities of the enzymes (Pang et al., 2014). Therefore, it is understood that the multisynthetase complex acts as a 'functional depot' for these tRNA synthetases (Ibba and Soll, 2000).

It has been shown that AIMP2 is a substrate of the E3 ligase Parkin which, when mutated in PD, causes upregulation of AIMP2. This upregulation of AIMP2 leads to apoptosis in neuronal cells (Ko et al., 2005; Park et al., 2008). Indeed, transgenic overexpression of AIMP2 in mice leads to an age-dependent loss of dopaminergic neurons and PD-like phenotypes (Lee et al., 2013). This is thought to occur via activation of poly(ADP-ribose) polymerase-1 (PARP1) which is also

known to be activated by YARS (Lee et al., 2013; Sajish and Schimmel, 2015). This clearly suggests a pathological connection of AIMP2 and tRNA synthetases to PD. Furthermore, this suggests that the involvement of UBA1 in idiopathic PD pathogenesis (Chou et al., 2008; Viquez et al., 2012) and the sequestration of UBA1 to Lewy bodies (McNaught et al., 2002) may lead to UBA1-mediated degeneration through alterations in the functions of the UBA1-dependent tRNA synthetases identified in this thesis.

6.4 The importance of investigating overlapping disease mechanisms

One of the main strengths of this study was the ability to draw on recent findings concerning a related neuromuscular disorder and use this as a phenotypic readout for molecular involvement of specific proteins in SMA disease pathogenesis (Sleigh et al., 2017a). This highlights not only the feasibility, but also the importance, of investigating overlap between different diseases. In many neurodegenerative conditions, there is no clear picture of the mechanisms mediating selective degeneration of neuronal populations or how mutations lead to disease (Kubben and Misteli, 2017). Moreover, in most neurodegenerative conditions, a range of individual cellular defects have been implicated in disease pathogenesis (Ehrnhoefer et al., 2011). However, there are invariably extensive connections between the different cellular defects that contribute to neurodegeneration and so it is largely unclear where the molecular tipping point between health and disease lies within this complex network of interrelated cellular processes. While the sequence of events leading to degeneration may vary between different diseases, the interconnected nature of these processes may provide the opportunity to learn lessons from one disorder that have an impact for other disorders and may provide insight into therapeutic strategies beneficial for multiple neurodegenerative conditions by targeting specific cellular pathways disrupted across a range of these diseases (Ehrnhoefer et al., 2011; Kubben and Misteli, 2017).

6.5 Implications of novel phenotypes for treatment of SMA

The work presented in this thesis also has implications for SMA from a therapeutic perspective. One of the issues that remains to be resolved in terms of SMN-dependent therapy is whether restoration of SMN levels will be more important in the central nervous system (CNS), or in both the CNS and peripheral tissues, to successfully treat SMA (Hua et al., 2015; Hua et al., 2011; McGovern et al., 2015). Several studies in rodent models of the disease have shown that SMN restoration in extra-neural tissues and organ systems will likely be necessary for amelioration of the systemic SMA phenotype (Hua et al., 2015; Hua et al., 2011). The disruption to sensory neuron fate identified here further suggests the need to target tissues other than the motor neuron to fully rescue the SMA phenotype. Furthermore, this study has also shown that systemic administration of therapy is sufficient to rescue the disruption to sensory neuron fate in SMA mice (see Chapter 5); thus, highlighting the relevance of therapy delivery via systemic routes.

One other major issue that is yet to be fully addressed concerns the presence of a 'therapeutic time-window' after which therapy delivery can only have a minimal effect. Several studies have indicated that for maximal benefit, SMN-replacement therapies will need to be delivered before the onset of overt symptoms (Kariya et al., 2014; Robbins et al., 2014). It will therefore be essential to understand how this mouse work relates to the temporal development of SMA pathogenesis in human patients. In this thesis, I identified a pre-symptomatic disruption to a key downstream protein of SMN, occurring in the primary site of pathology, indicating that the consequences of SMN reduction are seen at the molecular level before the onset of symptoms (see Chapter 3). This suggests that molecular pathways not directly linked to SMN reduction may be involved in the early stages of disease pathogenesis and are likely to be less responsive to SMN-dependent therapies than the direct consequences of SMN reduction. Indeed, this work also highlights that targeted therapies to treat the molecular cause of specific phenotypes is a viable strategy. Therefore, raising the point that successful treatment of SMA by combinatorial approach may need to target the immediate molecular cause of phenotypes rather

than the result. Together this emphasizes the importance of pre-symptomatic diagnosis of SMA to enable early treatment for the best outcomes of SMN-targeted therapies. Moreover, this indicates that moving towards preventative rather than curative treatment may be necessary to have substantial effects on the disease course of SMA.

6.6 Conclusion

The work presented in this thesis demonstrates that SMA is a complex disease and is not solely characterised by motor neuron dysfunction due to defects in SMN specific pathways. I have shown that UBA1 is reduced pre-symptomatically in motor neurons from SMA mice and identified that disruption to UBA1 expression can cause dysregulation of multiple cellular pathways including translation elongation, nuclear transport and tRNA synthetases. I also identified that UBA1 leads to dysregulation of the tRNA synthetase GARS through a non-canonical mechanism. I then went on to characterise a novel SMA phenotype - a disruption to sensory neuron fate - caused by UBA1-dependent alterations in the expression of the tRNA synthetase GARS. Finally, I showed that by targeting the molecular cause, this phenotype could be fully rescued. This work has not only improved our understanding of the basic biology of UBA1 and the mechanisms of disease pathogenesis in SMA, but it also has wide reaching implications in terms of SMA therapeutics and UBA1-mediated degeneration in a range of neuronal diseases.

References

Abbott, C.M., Newbery, H.J., Squires, C.E., Brownstein, D., Griffiths, L.A., and Soares, D.C. (2009). eEF1A2 and neuronal degeneration. Biochem Soc Trans 37, 1293-1297.

Abera, M.B., Xiao, J., Nofziger, J., Titus, S., Southall, N., Zheng, W., Moritz, K.E., Ferrer, M., Cherry, J.J., Androphy, E.J.*, et al.* (2016). ML372 blocks SMN ubiquitination and improves spinal muscular atrophy pathology in mice. JCI Insight 1, e88427.

Achilli, F., Bros-Facer, V., Williams, H.P., Banks, G.T., AlQatari, M., Chia, R., Tucci, V., Groves, M., Nickols, C.D., Seburn, K.L.*, et al.* (2009). An ENU-induced mutation in mouse glycyl-tRNA synthetase (GARS) causes peripheral sensory and motor phenotypes creating a model of Charcot-Marie-Tooth type 2D peripheral neuropathy. Dis Model Mech 2, 359-373.

Acsadi, G., Lee, I., Li, X., Khaidakov, M., Pecinova, A., Parker, G.C., and Huttemann, M. (2009). Mitochondrial dysfunction in a neural cell model of spinal muscular atrophy. J Neurosci Res 87, 2748-2756.

Aghamaleky Sarvestany, A., Hunter, G., Tavendale, A., Lamont, D.J., Llavero Hurtado, M., Graham, L.C., Wishart, T.M., and Gillingwater, T.H. (2014). Label-free quantitative proteomic profiling identifies disruption of ubiquitin homeostasis as a key driver of Schwann cell defects in spinal muscular atrophy. J Proteome Res 13, 4546-4557.

Ambrozkiewicz, M.C., and Kawabe, H. (2015). HECT-type E3 ubiquitin ligases in nerve cell development and synapse physiology. FEBS Lett 589, 1635-1643.

Antonellis, A., Ellsworth, R.E., Sambuughin, N., Puls, I., Abel, A., Lee-Lin, S.Q., Jordanova, A., Kremensky, I., Christodoulou, K., Middleton, L.T.*, et al.* (2003). Glycyl tRNA synthetase mutations in Charcot-Marie-Tooth disease type 2D and distal spinal muscular atrophy type V. Am J Hum Genet 72, 1293-1299.

Arrasate, M., and Finkbeiner, S. (2012). Protein aggregates in Huntington's disease. Exp Neurol 238, 1-11.

Baumer, D., Lee, S., Nicholson, G., Davies, J.L., Parkinson, N.J., Murray, L.M., Gillingwater, T.H., Ansorge, O., Davies, K.E., and Talbot, K. (2009). Alternative splicing events are a late feature of pathology in a mouse model of spinal muscular atrophy. PLoS Genet 5, e1000773.

Bechade, C., Rostaing, P., Cisterni, C., Kalisch, R., La Bella, V., Pettmann, B., and Triller, A. (1999). Subcellular distribution of survival motor neuron (SMN) protein: possible involvement in nucleocytoplasmic and dendritic transport. Eur J Neurosci 11, 293-304.

Bedford, L., Lowe, J., Dick, L.R., Mayer, R.J., and Brownell, J.E. (2011). Ubiquitin-like protein conjugation and the ubiquitin-proteasome system as drug targets. Nat Rev Drug Discov 10, 29-46.

Beevor, C. (1902). A case of congenital spinal muscular atrophy (family type) and a case of hemorrhage into the spinal cord at birth, giving similar symptoms. Brain 25, 85-108.

Bertini, E., Dessaud, E., Mercuri, E., Muntoni, F., Kirschner, J., Reid, C., Lusakowska, A., Comi, G.P., Cuisset, J.M., Abitbol, J.L.*, et al.* (2017). Safety and efficacy of olesoxime in patients with type 2 or non-ambulatory type 3 spinal muscular atrophy: a randomised, double-blind, placebo-controlled phase 2 trial. Lancet Neurol 16, 513-522.

Bialas, J., Groettrup, M., and Aichem, A. (2015). Conjugation of the ubiquitin activating enzyme UBE1 with the ubiquitin-like modifier FAT10 targets it for proteasomal degradation. PLoS One 10, e0120329.

Blard, O., Feuillette, S., Bou, J., Chaumette, B., Frebourg, T., Campion, D., and Lecourtois, M. (2007). Cytoskeleton proteins are modulators of mutant tau-induced neurodegeneration in Drosophila. Hum Mol Genet 16, 555-566.

Blokhuis, A.M., Groen, E.J., Koppers, M., van den Berg, L.H., and Pasterkamp, R.J. (2013). Protein aggregation in amyotrophic lateral sclerosis. Acta Neuropathol 125, 777-794.

Blokhuis, A.M., Koppers, M., Groen, E.J., van den Heuvel, D.M., Dini Modigliani, S., Anink, J.J., Fumoto, K., van Diggelen, F., Snelting, A., Sodaar, P*., et al.* (2016). Comparative interactomics analysis of different ALS-associated proteins identifies converging molecular pathways. Acta Neuropathol 132, 175-196.

Bowerman, M., Anderson, C.L., Beauvais, A., Boyl, P.P., Witke, W., and Kothary, R. (2009). SMN, profilin IIa and plastin 3: a link between the deregulation of actin dynamics and SMA pathogenesis. Mol Cell Neurosci 42, 66-74.

Bowerman, M., Beauvais, A., Anderson, C.L., and Kothary, R. (2010). Rho-kinase inactivation prolongs survival of an intermediate SMA mouse model. Hum Mol Genet 19, 1468-1478.

Bowerman, M., Murray, L.M., Boyer, J.G., Anderson, C.L., and Kothary, R. (2012). Fasudil improves survival and promotes skeletal muscle development in a mouse model of spinal muscular atrophy. BMC Med 10, 24.

Boyd, P.J., Tu, W.Y., Shorrock, H.K., Groen, E.J.N., Carter, R.N., Powis, R.A., Thomson, S.R., Thomson, D., Graham, L.C., Motyl, A.A.L*., et al.* (2017). Bioenergetic status modulates motor neuron vulnerability and pathogenesis in a zebrafish model of spinal muscular atrophy. PLoS Genet 13, e1006744.

Boyer, J.G., Murray, L.M., Scott, K., De Repentigny, Y., Renaud, J.M., and Kothary, R. (2013). Early onset muscle weakness and disruption of muscle proteins in mouse models of spinal muscular atrophy. Skelet Muscle 3, 24.

Brzustowicz, L.M., Lehner, T., Castilla, L.H., Penchaszadeh, G.K., Wilhelmsen, K.C., Daniels, R., Davies, K.E., Leppert, M., Ziter, F., Wood, D., and et al. (1990). Genetic mapping of chronic childhood-onset spinal muscular atrophy to chromosome 5q11.2-13.3. Nature 344, 540-541.

Cao, X., Li, C., Xiao, S., Tang, Y., Huang, J., Zhao, S., Li, X., Li, J., Zhang, R., and Yu, W. (2017). Acetylation promotes TyrRS nuclear translocation to prevent oxidative damage. Proc Natl Acad Sci U S A 114, 687-692.

Carpenter, S., Karpati, G., Rothman, S., Watters, G., and Andermann, F. (1978). Pathological involvement of primary sensory neurons in Werdnig-Hoffmann disease. Acta Neuropathol 42, 91-97.

Cazzalini, O., Sommatis, S., Tillhon, M., Dutto, I., Bachi, A., Rapp, A., Nardo, T., Scovassi, A.I., Necchi, D., Cardoso, M.C*., et al.* (2014). CBP and p300 acetylate PCNA to link its degradation with nucleotide excision repair synthesis. Nucleic Acids Res 42, 8433-8448.

Chamas., L. (2017). Safety and efficacy findings in the first-in-human trial of the oral splice modulator branaplam in type 1 spinal musuclar atrophy (SMA): interim results. In 21st annual spinal muscular atrophy researcher meeting; CureSMA (Orlando, Florida).

Chang, H.C., Hung, W.C., Chuang, Y.J., and Jong, Y.J. (2004). Degradation of survival motor neuron (SMN) protein is mediated via the ubiquitin/proteasome pathway. Neurochem Int 45, 1107-1112.

Chang, T.K., Shravage, B.V., Hayes, S.D., Powers, C.M., Simin, R.T., Wade Harper, J., and Baehrecke, E.H. (2013). Uba1 functions in Atg7- and Atg3-independent autophagy. Nat Cell Biol 15, 1067-1078.

Chang, W.F., Xu, J., Chang, C.C., Yang, S.H., Li, H.Y., Hsieh-Li, H.M., Tsai, M.H., Wu, S.C., Cheng, W.T., Liu, J.L., and Sung, L.Y. (2015). SMN is required for the maintenance of embryonic stem cells and neuronal differentiation in mice. Brain Struct Funct 220, 1539-1553.

Cheever, T.R., Olson, E.A., and Ervasti, J.M. (2011). Axonal regeneration and neuronal function are preserved in motor neurons lacking ss-actin in vivo. PLoS One 6, e17768.

Chen, X., Zhao, C., Li, X., Wang, T., Li, Y., Cao, C., Ding, Y., Dong, M., Finci, L., Wang, J.H.*, et al.* (2015). Terazosin activates Pgk1 and Hsp90 to promote stress resistance. Nat Chem Biol 11, 19-25.

Chien, Y.H., Chiang, S.C., Weng, W.C., Lee, N.C., Lin, C.J., Hsieh, W.S., Lee, W.T., Jong, Y.J., Ko, T.M., and Hwu, W.L. (2017). Presymptomatic Diagnosis of Spinal Muscular Atrophy Through Newborn Screening. J Pediatr.

Chiriboga, C.A., Swoboda, K.J., Darras, B.T., Iannaccone, S.T., Montes, J., De Vivo, D.C., Norris, D.A., Bennett, C.F., and Bishop, K.M. (2016). Results from a phase 1 study of nusinersen (ISIS-SMN(Rx)) in children with spinal muscular atrophy. Neurology 86, 890-897.

Chou, A.P., Maidment, N., Klintenberg, R., Casida, J.E., Li, S., Fitzmaurice, A.G., Fernagut, P.O., Mortazavi, F., Chesselet, M.F., and Bronstein, J.M. (2008). Ziram causes dopaminergic cell damage by inhibiting E1 ligase of the proteasome. J Biol Chem 283, 34696-34703.

Ciechanover, A., and Brundin, P. (2003). The ubiquitin proteasome system in neurodegenerative diseases: sometimes the chicken, sometimes the egg. Neuron 40, 427-446.

Cifuentes-Diaz, C., Nicole, S., Velasco, M.E., Borra-Cebrian, C., Panozzo, C., Frugier, T., Millet, G., Roblot, N., Joshi, V., and Melki, J. (2002). Neurofilament accumulation at the motor endplate and lack of axonal sprouting in a spinal muscular atrophy mouse model. Hum Mol Genet 11, 1439-1447.

Clague, M.J., Heride, C., and Urbe, S. (2015). The demographics of the ubiquitin system. Trends Cell Biol 25, 417-426.

Clelland, A.K., Bales, A.B., and Sleeman, J.E. (2012). Changes in intranuclear mobility of mature snRNPs provide a mechanism for splicing defects in spinal muscular atrophy. J Cell Sci 125, 2626-2637.

Cook, J.C., and Chock, P.B. (1995). Phosphorylation of ubiquitin-activating enzyme in cultured cells. Proc Natl Acad Sci U S A 92, 3454-3457.

Cottenie, E., Kochanski, A., Jordanova, A., Bansagi, B., Zimon, M., Horga, A., Jaunmuktane, Z., Saveri, P., Rasic, V.M., Baets, J.*, et al.* (2014). Truncating and missense mutations in IGHMBP2 cause Charcot-Marie Tooth disease type 2. Am J Hum Genet 95, 590-601.

Cox, B., and Emili, A. (2006). Tissue subcellular fractionation and protein extraction for use in mass-spectrometry-based proteomics. Nat Protoc 1, 1872-1878.

Crawford, T.O., Paushkin, S.V., Kobayashi, D.T., Forrest, S.J., Joyce, C.L., Finkel, R.S., Kaufmann, P., Swoboda, K.J., Tiziano, D., Lomastro, R.*, et al.* (2012). Evaluation of SMN protein, transcript, and copy number in the biomarkers for spinal muscular atrophy (BforSMA) clinical study. PLoS One 7, e33572.

Deglincerti, A., Liu, Y., Colak, D., Hengst, U., Xu, G., and Jaffrey, S.R. (2015). Coupled local translation and degradation regulate growth cone collapse. Nat Commun 6, 6888.

Deguise, M.O., and Kothary, R. (2017). New insights into SMA pathogenesis: immune dysfunction and neuroinflammation. Ann Clin Transl Neurol 4, 522-530.

Delle Vedove, A., Storbeck, M., Heller, R., Holker, I., Hebbar, M., Shukla, A., Magnusson, O., Cirak, S., Girisha, K.M., O'Driscoll, M.*, et al.* (2016). Biallelic Loss of Proprioception-Related PIEZO2

Causes Muscular Atrophy with Perinatal Respiratory Distress, Arthrogryposis, and Scoliosis. Am J Hum Genet 99, 1206-1216.

Deng, H.X., Chen, W., Hong, S.T., Boycott, K.M., Gorrie, G.H., Siddique, N., Yang, Y., Fecto, F., Shi, Y., Zhai, H., *et al.* (2011). Mutations in UBQLN2 cause dominant X-linked juvenile and adult-onset ALS and ALS/dementia. Nature 477, 211-215.

Dlamini, N., Josifova, D.J., Paine, S.M., Wraige, E., Pitt, M., Murphy, A.J., King, A., Buk, S., Smith, F., Abbs, S., *et al.* (2013). Clinical and neuropathological features of X-linked spinal muscular atrophy (SMAX2) associated with a novel mutation in the UBA1 gene. Neuromuscul Disord 23, 391-398.

Doig, J., Griffiths, L.A., Peberdy, D., Dharmasaroja, P., Vera, M., Davies, F.J., Newbery, H.J., Brownstein, D., and Abbott, C.M. (2013). In vivo characterization of the role of tissue-specific translation elongation factor 1A2 in protein synthesis reveals insights into muscle atrophy. FEBS J 280, 6528-6540.

Dominguez, E., Marais, T., Chatauret, N., Benkhelifa-Ziyyat, S., Duque, S., Ravassard, P., Carcenac, R., Astord, S., Pereira de Moura, A., Voit, T., and Barkats, M. (2011). Intravenous scAAV9 delivery of a codon-optimized SMN1 sequence rescues SMA mice. Hum Mol Genet 20, 681-693.

Dormann, D., Rodde, R., Edbauer, D., Bentmann, E., Fischer, I., Hruscha, A., Than, M.E., Mackenzie, I.R., Capell, A., Schmid, B., *et al.* (2010). ALS-associated fused in sarcoma (FUS) mutations disrupt Transportin-mediated nuclear import. EMBO J 29, 2841-2857.

Dubowitz, V. (1964). Infantile Muscular Atrophy. A Prospective Study with Particular Reference to a Slowly Progressive Variety. Brain 87, 707-718.

Dubowitz, V. (2009). Ramblings in the history of spinal muscular atrophy. Neuromuscul Disord 19, 69-73.

Duman, O., Uysal, H., Skjei, K.L., Kizilay, F., Karauzum, S., and Haspolat, S. (2013). Sensorimotor polyneuropathy in patients with SMA type-1: electroneuromyographic findings. Muscle Nerve 48, 117-121.

Duque, S.I., Arnold, W.D., Odermatt, P., Li, X., Porensky, P.N., Schmelzer, L., Meyer, K., Kolb, S.J., Schumperli, D., Kaspar, B.K., and Burghes, A.H. (2015). A large animal model of spinal muscular atrophy and correction of phenotype. Ann Neurol 77, 399-414.

Ehrnhoefer, D.E., Wong, B.K., and Hayden, M.R. (2011). Convergent pathogenic pathways in Alzheimer's and Huntington's diseases: shared targets for drug development. Nat Rev Drug Discov 10, 853-867.

El-Abassi, R., England, J.D., and Carter, G.T. (2014). Charcot-Marie-Tooth disease: an overview of genotypes, phenotypes, and clinical management strategies. PM R 6, 342-355.

Enright, A.J., Van Dongen, S., and Ouzounis, C.A. (2002). An efficient algorithm for large-scale detection of protein families. Nucleic Acids Res 30, 1575-1584.

Eskuri, J.M., Stanley, C.M., Moore, S.A., and Mathews, K.D. (2012). Infantile onset CMT2D/dSMA V in monozygotic twins due to a mutation in the anticodon-binding domain of GARS. J Peripher Nerv Syst 17, 132-134.

Fallini, C., Bassell, G.J., and Rossoll, W. (2012). Spinal muscular atrophy: the role of SMN in axonal mRNA regulation. Brain Res 1462, 81-92.

Falsone, S.F., Gesslbauer, B., Tirk, F., Piccinini, A.M., and Kungl, A.J. (2005). A proteomic snapshot of the human heat shock protein 90 interactome. FEBS Lett 579, 6350-6354.

Faravelli, I., Nizzardo, M., Comi, G.P., and Corti, S. (2015). Spinal muscular atrophy--recent therapeutic advances for an old challenge. Nat Rev Neurol 11, 351-359.

Feather-Schussler, D.N., and Ferguson, T.S. (2016). A Battery of Motor Tests in a Neonatal Mouse Model of Cerebral Palsy. J Vis Exp.

Fernandez, R.M., Pecina, A., Munoz-Cabello, B., Antinolo, G., and Borrego, S. (2016). Co-segregation of a homozygous SMN1 deletion and a heterozygous PMP22 duplication in a patient. Clin Case Rep 4, 879-884.

Finkel, R.S., Chiriboga, C.A., Vajsar, J., Day, J.W., Montes, J., De Vivo, D.C., Yamashita, M., Rigo, F., Hung, G., Schneider, E.*, et al.* (2016). Treatment of infantile-onset spinal muscular atrophy with nusinersen: a phase 2, open-label, dose-escalation study. Lancet 388, 3017-3026.

Fischer, U., Liu, Q., and Dreyfuss, G. (1997). The SMN-SIP1 complex has an essential role in spliceosomal snRNP biogenesis. Cell 90, 1023-1029.

Fletcher, E.V., Simon, C.M., Pagiazitis, J.G., Chalif, J.I., Vukojicic, A., Drobac, E., Wang, X., and Mentis, G.Z. (2017). Reduced sensory synaptic excitation impairs motor neuron function via Kv2.1 in spinal muscular atrophy. Nat Neurosci 20, 905-916.

Foust, K.D., Wang, X., McGovern, V.L., Braun, L., Bevan, A.K., Haidet, A.M., Le, T.T., Morales, P.R., Rich, M.M., Burghes, A.H., and Kaspar, B.K. (2010). Rescue of the spinal muscular atrophy phenotype in a mouse model by early postnatal delivery of SMN. Nat Biotechnol 28, 271-274.

Freibaum, B.D., Lu, Y., Lopez-Gonzalez, R., Kim, N.C., Almeida, S., Lee, K.H., Badders, N., Valentine, M., Miller, B.L., Wong, P.C.*, et al.* (2015). GGGGCC repeat expansion in C9orf72 compromises nucleocytoplasmic transport. Nature 525, 129-133.

Fuller, H.R., Mandefro, B., Shirran, S.L., Gross, A.R., Kaus, A.S., Botting, C.H., Morris, G.E., and Sareen, D. (2015). Spinal Muscular Atrophy Patient iPSC-Derived Motor Neurons Have Reduced Expression of Proteins Important in Neuronal Development. Front Cell Neurosci 9, 506.

Gabanella, F., Butchbach, M.E., Saieva, L., Carissimi, C., Burghes, A.H., and Pellizzoni, L. (2007). Ribonucleoprotein assembly defects correlate with spinal muscular atrophy severity and preferentially affect a subset of spliceosomal snRNPs. PLoS One 2, e921.

Ghaboosi, N., and Deshaies, R.J. (2007). A conditional yeast E1 mutant blocks the ubiquitin-proteasome pathway and reveals a role for ubiquitin conjugates in targeting Rad23 to the proteasome. Mol Biol Cell 18, 1953-1963.

Giavazzi, A., Setola, V., Simonati, A., and Battaglia, G. (2006). Neuronal-specific roles of the survival motor neuron protein: evidence from survival motor neuron expression patterns in the developing human central nervous system. J Neuropathol Exp Neurol 65, 267-277.

Gogliotti, R.G., Quinlan, K.A., Barlow, C.B., Heier, C.R., Heckman, C.J., and Didonato, C.J. (2012). Motor neuron rescue in spinal muscular atrophy mice demonstrates that sensory-motor defects are a consequence, not a cause, of motor neuron dysfunction. J Neurosci 32, 3818-3829.

Gonzalez, M., McLaughlin, H., Houlden, H., Guo, M., Yo-Tsen, L., Hadjivassilious, M., Speziani, F., Yang, X.L., Antonellis, A., Reilly, M.M.*, et al.* (2013). Exome sequencing identifies a significant variant in methionyl-tRNA synthetase (MARS) in a family with late-onset CMT2. J Neurol Neurosurg Psychiatry 84, 1247-1249.

Grenfell, S.J., Trausch-Azar, J.S., Handley-Gearhart, P.M., Ciechanover, A., and Schwartz, A.L. (1994). Nuclear localization of the ubiquitin-activating enzyme, E1, is cell-cycle-dependent. Biochem J 300 (Pt 3), 701-708.

Griffin, L.B., Sakaguchi, R., McGuigan, D., Gonzalez, M.A., Searby, C., Zuchner, S., Hou, Y.M., and Antonellis, A. (2014). Impaired function is a common feature of neuropathy-associated glycyl-tRNA synthetase mutations. Hum Mutat 35, 1363-1371.

Groen, E.J., Fumoto, K., Blokhuis, A.M., Engelen-Lee, J., Zhou, Y., van den Heuvel, D.M., Koppers, M., van Diggelen, F., van Heest, J., Demmers, J.A.*, et al.* (2013). ALS-associated mutations in FUS disrupt the axonal distribution and function of SMN. Hum Mol Genet 22, 3690-3704.

Groen, E.J., and Gillingwater, T.H. (2015). UBA1: At the Crossroads of Ubiquitin Homeostasis and Neurodegeneration. Trends Mol Med 21, 622-632.

Groen, E.J., Talbot, K., and Gillingwater, T.H. (*in preparation*). Spinal muscular atrophy: Pathways from gene to treatment.

Gstaiger, M., and Aebersold, R. (2009). Applying mass spectrometry-based proteomics to genetics, genomics and network biology. Nat Rev Genet 10, 617-627.

Haas, A.L., Warms, J.V., Hershko, A., and Rose, I.A. (1982). Ubiquitin-activating enzyme. Mechanism and role in protein-ubiquitin conjugation. J Biol Chem 257, 2543-2548.

Hamilton, G., and Gillingwater, T.H. (2013). Spinal muscular atrophy: going beyond the motor neuron. Trends Mol Med 19, 40-50.

Hammond, S.M., Hazell, G., Shabanpoor, F., Saleh, A.F., Bowerman, M., Sleigh, J.N., Meijboom, K.E., Zhou, H., Muntoni, F., Talbot, K.*, et al.* (2016). Systemic peptide-mediated oligonucleotide therapy improves long-term survival in spinal muscular atrophy. Proc Natl Acad Sci U S A 113, 10962-10967.

Han, K.J., Foster, D.G., Zhang, N.Y., Kanisha, K., Dzieciatkowska, M., Sclafani, R.A., Hansen, K.C., Peng, J., and Liu, C.W. (2012). Ubiquitin-specific protease 9x deubiquitinates and stabilizes the spinal muscular atrophy protein-survival motor neuron. J Biol Chem 287, 43741-43752.

Handley-Gearhart, P.M., Stephen, A.G., Trausch-Azar, J.S., Ciechanover, A., and Schwartz, A.L. (1994). Human ubiquitin-activating enzyme, E1. Indication of potential nuclear and cytoplasmic subpopulations using epitope-tagged cDNA constructs. J Biol Chem 269, 33171-33178.

Hao le, T., Duy, P.Q., Jontes, J.D., and Beattie, C.E. (2015). Motoneuron development influences dorsal root ganglia survival and Schwann cell development in a vertebrate model of spinal muscular atrophy. Hum Mol Genet 24, 346-360.

Harding, B.N., Kariya, S., Monani, U.R., Chung, W.K., Benton, M., Yum, S.W., Tennekoon, G., and Finkel, R.S. (2015). Spectrum of neuropathophysiology in spinal muscular atrophy type I. J Neuropathol Exp Neurol 74, 15-24.

He, W., Bai, G., Zhou, H., Wei, N., White, N.M., Lauer, J., Liu, H., Shi, Y., Dumitru, C.D., Lettieri, K.*, et al.* (2015). CMT2D neuropathy is linked to the neomorphic binding activity of glycyl-tRNA synthetase. Nature 526, 710-714.

Hoffmann, J. (1893). Über chronische spinale Muskelatrophie im Kindesalter auf familiärer Basis. Deut Zeitsch Nervenheilkd 3, 427-470.

Hoffmann, J. (1897). Weiterer Beiträge zur Lehre von der hereditären progressiven spinalen Muskelatrophie im Kindesalter. Deut Zeitsch Nervenheilkd 10, 292-320.

Hoffmann, J. (1900). Dritter Eitrag zur Lehre von der hereditären progressiven spinalen Muskelatrophie im Kindesalter. Deut Zeitsch Nervenheilkd 18, 217-224.

Hosseinibarkooie, S., Peters, M., Torres-Benito, L., Rastetter, R.H., Hupperich, K., Hoffmann, A., Mendoza-Ferreira, N., Kaczmarek, A., Janzen, E., Milbradt, J.*, et al.* (2016). The Power of Human

Protective Modifiers: PLS3 and CORO1C Unravel Impaired Endocytosis in Spinal Muscular Atrophy and Rescue SMA Phenotype. Am J Hum Genet 99, 647-665.

Hosseinibarkooie, S., Schneider, S., and Wirth, B. (2017). Advances in understanding the role of disease-associated proteins in spinal muscular atrophy. Expert Rev Proteomics 14, 581-592.

Hsieh-Li, H.M., Chang, J.G., Jong, Y.J., Wu, M.H., Wang, N.M., Tsai, C.H., and Li, H. (2000). A mouse model for spinal muscular atrophy. Nat Genet 24, 66-70.

Hua, Y., Liu, Y.H., Sahashi, K., Rigo, F., Bennett, C.F., and Krainer, A.R. (2015). Motor neuron cell-nonautonomous rescue of spinal muscular atrophy phenotypes in mild and severe transgenic mouse models. Genes Dev 29, 288-297.

Hua, Y., Sahashi, K., Rigo, F., Hung, G., Horev, G., Bennett, C.F., and Krainer, A.R. (2011). Peripheral SMN restoration is essential for long-term rescue of a severe spinal muscular atrophy mouse model. Nature 478, 123-126.

Huang da, W., Sherman, B.T., and Lempicki, R.A. (2009a). Bioinformatics enrichment tools: paths toward the comprehensive functional analysis of large gene lists. Nucleic Acids Res 37, 1-13.

Huang da, W., Sherman, B.T., and Lempicki, R.A. (2009b). Systematic and integrative analysis of large gene lists using DAVID bioinformatics resources. Nat Protoc 4, 44-57.

Hunter, G., Aghamaleky Sarvestany, A., Roche, S.L., Symes, R.C., and Gillingwater, T.H. (2014). SMN-dependent intrinsic defects in Schwann cells in mouse models of spinal muscular atrophy. Hum Mol Genet 23, 2235-2250.

Hunter, G., Powis, R.A., Jones, R.A., Groen, E.J., Shorrock, H.K., Lane, F.M., Zheng, Y., Sherman, D.L., Brophy, P.J., and Gillingwater, T.H. (2016). Restoration of SMN in Schwann cells reverses myelination defects and improves neuromuscular function in spinal muscular atrophy. Hum Mol Genet.

Huo, Q., Kayikci, M., Odermatt, P., Meyer, K., Michels, O., Saxena, S., Ule, J., and Schumperli, D. (2014). Splicing changes in SMA mouse motoneurons and SMN-depleted neuroblastoma cells: evidence for involvement of splicing regulatory proteins. RNA Biol 11, 1430-1446.

Hwee, D.T., Kennedy, A.R., Hartman, J.J., Ryans, J., Durham, N., Malik, F.I., and Jasper, J.R. (2015). The small-molecule fast skeletal troponin activator, CK-2127107, improves exercise tolerance in a rat model of heart failure. J Pharmacol Exp Ther 353, 159-168.

Ibba, M., and Soll, D. (2000). Aminoacyl-tRNA synthesis. Annu Rev Biochem 69, 617-650.

Ittner, L.M., and Gotz, J. (2011). Amyloid-beta and tau--a toxic pas de deux in Alzheimer's disease. Nat Rev Neurosci 12, 65-72.

Iyer, C.C., McGovern, V.L., Murray, J.D., Gombash, S.E., Zaworski, P.G., Foust, K.D., Janssen, P.M., and Burghes, A.H. (2015). Low levels of Survival Motor Neuron protein are sufficient for normal muscle function in the SMNDelta7 mouse model of SMA. Hum Mol Genet 24, 6160-6173.

Jablonka, S., Karle, K., Sandner, B., Andreassi, C., von Au, K., and Sendtner, M. (2006). Distinct and overlapping alterations in motor and sensory neurons in a mouse model of spinal muscular atrophy. Hum Mol Genet 15, 511-518.

Jablonka, S., and Sendtner, M. (2017). Developmental regulation of SMN expression: pathophysiological implications and perspectives for therapy development in spinal muscular atrophy. Gene Ther.

Jady, B.E., Darzacq, X., Tucker, K.E., Matera, A.G., Bertrand, E., and Kiss, T. (2003). Modification of Sm small nuclear RNAs occurs in the nucleoplasmic Cajal body following import from the cytoplasm. EMBO J 22, 1878-1888.

James, P.A., Cader, M.Z., Muntoni, F., Childs, A.M., Crow, Y.J., and Talbot, K. (2006). Severe childhood SMA and axonal CMT due to anticodon binding domain mutations in the GARS gene. Neurology 67, 1710-1712.

Jedrzejowska, M., Jakubowska-Pietkiewicz, E., and Kostera-Pruszczyk, A. (2015). X-linked spinal muscular atrophy (SMAX2) caused by de novo c.1731C>T substitution in the UBA1 gene. Neuromuscul Disord 25, 661-666.

Jedrzejowska, M., Madej-Pilarczyk, A., Fidzianska, A., Mierzewska, H., Pronicka, E., Obersztyn, E., Gos, M., Pronicki, M., Kmiec, T., Migdal, M*., et al.* (2014). Severe phenotypes of SMARD1 associated with novel mutations of the IGHMBP2 gene and nuclear degeneration of muscle and Schwann cells. Eur J Paediatr Neurol 18, 183-192.

Jedrzejowska, M., Ryniewicz, B., Kabzinska, D., Drac, H., Hausmanowa-Petrusewicz, I., and Kochanski, A. (2008). A patient with both Charcot-Marie-Tooth disease (CMT 1A) and mild spinal muscular atrophy (SMA 3). Neuromuscul Disord 18, 339-341.

Jiang, X., Litkowski, P.E., Taylor, A.A., Lin, Y., Snider, B.J., and Moulder, K.L. (2010). A role for the ubiquitin-proteasome system in activity-dependent presynaptic silencing. J Neurosci 30, 1798-1809.

Joo, H.Y., Zhai, L., Yang, C., Nie, S., Erdjument-Bromage, H., Tempst, P., Chang, C., and Wang, H. (2007). Regulation of cell cycle progression and gene expression by H2A deubiquitination. Nature 449, 1068-1072.

Jordanova, A., Irobi, J., Thomas, F.P., Van Dijck, P., Meerschaert, K., Dewil, M., Dierick, I., Jacobs, A., De Vriendt, E., Guergueltcheva, V*., et al.* (2006). Disrupted function and axonal distribution of mutant tyrosyl-tRNA synthetase in dominant intermediate Charcot-Marie-Tooth neuropathy. Nat Genet 38, 197-202.

Jovicic, A., Mertens, J., Boeynaems, S., Bogaert, E., Chai, N., Yamada, S.B., Paul, J.W., 3rd, Sun, S., Herdy, J.R., Bieri, G*., et al.* (2015). Modifiers of C9orf72 dipeptide repeat toxicity connect nucleocytoplasmic transport defects to FTD/ALS. Nat Neurosci 18, 1226-1229.

Kaifer, K.A., Villalon, E., Osman, E.Y., Glascock, J.J., Arnold, L.L., Cornelison, D.D., and Lorson, C.L. (2017). Plastin-3 extends survival and reduces severity in mouse models of spinal muscular atrophy. JCI Insight 2, e89970.

Kamitani, T., Kito, K., Nguyen, H.P., and Yeh, E.T. (1997). Characterization of NEDD8, a developmentally down-regulated ubiquitin-like protein. J Biol Chem 272, 28557-28562.

Kariya, S., Obis, T., Garone, C., Akay, T., Sera, F., Iwata, S., Homma, S., and Monani, U.R. (2014). Requirement of enhanced Survival Motoneuron protein imposed during neuromuscular junction maturation. J Clin Invest 124, 785-800.

Keil, J.M., Seo, J., Howell, M.D., Hsu, W.H., Singh, R.N., and DiDonato, C.J. (2014). A short antisense oligonucleotide ameliorates symptoms of severe mouse models of spinal muscular atrophy. Mol Ther Nucleic Acids 3, e174.

Kissel, J.T., Elsheikh, B., King, W.M., Freimer, M., Scott, C.B., Kolb, S.J., Reyna, S.P., Crawford, T.O., Simard, L.R., Krosschell, K.J*., et al.* (2014). SMA valiant trial: a prospective, double-blind, placebo-controlled trial of valproic acid in ambulatory adults with spinal muscular atrophy. Muscle Nerve 49, 187-192.

Kitagaki, J., Yang, Y., Saavedra, J.E., Colburn, N.H., Keefer, L.K., and Perantoni, A.O. (2009). Nitric oxide prodrug JS-K inhibits ubiquitin E1 and kills tumor cells retaining wild-type p53. Oncogene 28, 619-624.

Ko, H.S., von Coelln, R., Sriram, S.R., Kim, S.W., Chung, K.K., Pletnikova, O., Troncoso, J., Johnson, B., Saffary, R., Goh, E.L*., et al.* (2005). Accumulation of the authentic parkin substrate

aminoacyl-tRNA synthetase cofactor, p38/JTV-1, leads to catecholaminergic cell death. J Neurosci 25, 7968-7978.

Kolb, S.J., and Kissel, J.T. (2011). Spinal muscular atrophy: a timely review. Arch Neurol 68, 979-984.

Krosschell, K.J., Kissel, J.T., Townsend, E.L., Simeone, S.D., Zhang, R.Z., Reyna, S.P., Thomas, O.C., Schroth, M.K., Acsadi, G., Kishnani, P.S., *et al.* (2017). Clinical Trial of L-Carnitine and Valproic Acid in Spinal Muscular Atrophy Type I. Muscle Nerve.

Kubben, N., and Misteli, T. (2017). Shared molecular and cellular mechanisms of premature ageing and ageing-associated diseases. Nat Rev Mol Cell Biol.

Kugelberg, E., and Welander, L. (1956). Heredofamilial juvenile muscular atrophy simulating muscular dystrophy. Arch Neurol Psychiatry 75, 500-509.

Kulathu, Y., and Komander, D. (2012). Atypical ubiquitylation - the unexplored world of polyubiquitin beyond Lys48 and Lys63 linkages. Nat Rev Mol Cell Biol 13, 508-523.

Kunst, C.B., Mezey, E., Brownstein, M.J., and Patterson, D. (1997). Mutations in SOD1 associated with amyotrophic lateral sclerosis cause novel protein interactions. Nat Genet 15, 91-94.

Kwon, D.Y., Dimitriadi, M., Terzic, B., Cable, C., Hart, A.C., Chitnis, A., Fischbeck, K.H., and Burnett, B.G. (2013). The E3 ubiquitin ligase mind bomb 1 ubiquitinates and promotes the degradation of survival of motor neuron protein. Mol Biol Cell 24, 1863-1871.

Kwon, D.Y., Motley, W.W., Fischbeck, K.H., and Burnett, B.G. (2011). Increasing expression and decreasing degradation of SMN ameliorate the spinal muscular atrophy phenotype in mice. Hum Mol Genet 20, 3667-3677.

Ladak, A., Tubbs, R.S., and Spinner, R.J. (2014). Mapping sensory nerve communications between peripheral nerve territories. Clin Anat 27, 681-690.

Lallemend, F., and Ernfors, P. (2012). Molecular interactions underlying the specification of sensory neurons. Trends Neurosci 35, 373-381.

Lao, T., Chen, S., and Sang, N. (2012). Two mutations impair the stability and function of ubiquitin-activating enzyme (E1). J Cell Physiol 227, 1561-1568.

Lashuel, H.A., Overk, C.R., Oueslati, A., and Masliah, E. (2013). The many faces of alpha-synuclein: from structure and toxicity to therapeutic target. Nat Rev Neurosci 14, 38-48.

Le Pichon, C.E., and Chesler, A.T. (2014). The functional and anatomical dissection of somatosensory subpopulations using mouse genetics. Front Neuroanat 8, 21.

Lee, I., and Schindelin, H. (2008). Structural insights into E1-catalyzed ubiquitin activation and transfer to conjugating enzymes. Cell 134, 268-278.

Lee, J.W., Beebe, K., Nangle, L.A., Jang, J., Longo-Guess, C.M., Cook, S.A., Davisson, M.T., Sundberg, J.P., Schimmel, P., and Ackerman, S.L. (2006). Editing-defective tRNA synthetase causes protein misfolding and neurodegeneration. Nature 443, 50-55.

Lee, T.V., Ding, T., Chen, Z., Rajendran, V., Scherr, H., Lackey, M., Bolduc, C., and Bergmann, A. (2008). The E1 ubiquitin-activating enzyme Uba1 in Drosophila controls apoptosis autonomously and tissue growth non-autonomously. Development 135, 43-52.

Lee, Y., Karuppagounder, S.S., Shin, J.H., Lee, Y.I., Ko, H.S., Swing, D., Jiang, H., Kang, S.U., Lee, B.D., Kang, H.C., *et al.* (2013). Parthanatos mediates AIMP2-activated age-dependent dopaminergic neuronal loss. Nat Neurosci 16, 1392-1400.

Lefebvre, S., Burglen, L., Reboullet, S., Clermont, O., Burlet, P., Viollet, L., Benichou, B., Cruaud, C., Millasseau, P., Zeviani, M., and et al. (1995). Identification and characterization of a spinal muscular atrophy-determining gene. Cell 80, 155-165.

Lefebvre, S., Burlet, P., Liu, Q., Bertrandy, S., Clermont, O., Munnich, A., Dreyfuss, G., and Melki, J. (1997). Correlation between severity and SMN protein level in spinal muscular atrophy. Nat Genet 16, 265-269.

Leroy, E., Boyer, R., Auburger, G., Leube, B., Ulm, G., Mezey, E., Harta, G., Brownstein, M.J., Jonnalagada, S., Chernova, T.*, et al.* (1998). The ubiquitin pathway in Parkinson's disease. Nature 395, 451-452.

Liao, Y.C., Liu, Y.T., Tsai, P.C., Chang, C.C., Huang, Y.H., Soong, B.W., and Lee, Y.C. (2015). Two Novel De Novo GARS Mutations Cause Early-Onset Axonal Charcot-Marie-Tooth Disease. PLoS One 10, e0133423.

Ling, K.K., Lin, M.Y., Zingg, B., Feng, Z., and Ko, C.P. (2010). Synaptic defects in the spinal and neuromuscular circuitry in a mouse model of spinal muscular atrophy. PLoS One 5, e15457.

Liu, H.Y., and Pfleger, C.M. (2013). Mutation in E1, the ubiquitin activating enzyme, reduces Drosophila lifespan and results in motor impairment. PLoS One 8, e32835.

Liu, L., Li, X., Hu, Z., Mao, X., Zi, X., Xia, K., Tang, B., and Zhang, R. (2017a). IGHMBP2-related clinical and genetic features in a cohort of Chinese Charcot-Marie-Tooth disease type 2 patients. Neuromuscul Disord 27, 193-199.

Liu, Q., Fischer, U., Wang, F., and Dreyfuss, G. (1997). The spinal muscular atrophy disease gene product, SMN, and its associated protein SIP1 are in a complex with spliceosomal snRNP proteins. Cell 90, 1013-1021.

Liu, X., Zhao, B., Sun, L., Bhuripanyo, K., Wang, Y., Bi, Y., Davuluri, R.V., Duong, D.M., Nanavati, D., Yin, J., and Kiyokawa, H. (2017b). Orthogonal ubiquitin transfer identifies ubiquitination substrates under differential control by the two ubiquitin activating enzymes. Nat Commun 8, 14286.

Liu, Y., Satz, J.S., Vo, M.N., Nangle, L.A., Schimmel, P., and Ackerman, S.L. (2014). Deficiencies in tRNA synthetase editing activity cause cardioproteinopathy. Proc Natl Acad Sci U S A 111, 17570-17575.

Loh, P.G., Yang, H.S., Walsh, M.A., Wang, Q., Wang, X., Cheng, Z., Liu, D., and Song, H. (2009). Structural basis for translational inhibition by the tumour suppressor Pdcd4. EMBO J 28, 274-285.

Lohmann, E., Coquel, A.S., Honore, A., Gurvit, H., Hanagasi, H., Emre, M., Leutenegger, A.L., Drouet, V., Sahbatou, M., Guven, G.*, et al.* (2015). A new F-box protein 7 gene mutation causing typical Parkinson's disease. Mov Disord 30, 1130-1133.

Lopez Salon, M., Morelli, L., Castano, E.M., Soto, E.F., and Pasquini, J.M. (2000). Defective ubiquitination of cerebral proteins in Alzheimer's disease. J Neurosci Res 62, 302-310.

Lorson, C.L., Hahnen, E., Androphy, E.J., and Wirth, B. (1999). A single nucleotide in the SMN gene regulates splicing and is responsible for spinal muscular atrophy. Proc Natl Acad Sci U S A 96, 6307-6311.

Lotti, F., Imlach, W.L., Saieva, L., Beck, E.S., Hao le, T., Li, D.K., Jiao, W., Mentis, G.Z., Beattie, C.E., McCabe, B.D., and Pellizzoni, L. (2012). An SMN-dependent U12 splicing event essential for motor circuit function. Cell 151, 440-454.

Lu, C., Pribanic, S., Debonneville, A., Jiang, C., and Rotin, D. (2007). The PY motif of ENaC, mutated in Liddle syndrome, regulates channel internalization, sorting and mobilization from subapical pool. Traffic 8, 1246-1264.

Lunn, M.R., and Wang, C.H. (2008). Spinal muscular atrophy. Lancet 371, 2120-2133.

Lyapina, S., Cope, G., Shevchenko, A., Serino, G., Tsuge, T., Zhou, C., Wolf, D.A., Wei, N., Shevchenko, A., and Deshaies, R.J. (2001). Promotion of NEDD-CUL1 conjugate cleavage by COP9 signalosome. Science 292, 1382-1385.

Makarov, E.M., Owen, N., Bottrill, A., and Makarova, O.V. (2012). Functional mammalian spliceosomal complex E contains SMN complex proteins in addition to U1 and U2 snRNPs. Nucleic Acids Res 40, 2639-2652.

Malissovas, N., Griffin, L.B., Antonellis, A., and Beis, D. (2016). Dimerization is required for GARS-mediated neurotoxicity in dominant CMT disease. Hum Mol Genet 25, 1528-1542.

Marshall, A., and Duchen, L.W. (1975). Sensory system involvement in infantile spinal muscular atrophy. J Neurol Sci 26, 349-359.

Martinez-Hernandez, R., Soler-Botija, C., Also, E., Alias, L., Caselles, L., Gich, I., Bernal, S., and Tizzano, E.F. (2009). The developmental pattern of myotubes in spinal muscular atrophy indicates prenatal delay of muscle maturation. J Neuropathol Exp Neurol 68, 474-481.

Massenet, S., Pellizzoni, L., Paushkin, S., Mattaj, I.W., and Dreyfuss, G. (2002). The SMN complex is associated with snRNPs throughout their cytoplasmic assembly pathway. Mol Cell Biol 22, 6533-6541.

McGovern, V.L., Gavrilina, T.O., Beattie, C.E., and Burghes, A.H. (2008). Embryonic motor axon development in the severe SMA mouse. Hum Mol Genet 17, 2900-2909.

McGovern, V.L., Iyer, C.C., Arnold, W.D., Gombash, S.E., Zaworski, P.G., Blatnik, A.J., 3rd, Foust, K.D., and Burghes, A.H. (2015). SMN expression is required in motor neurons to rescue electrophysiological deficits in the SMNDelta7 mouse model of SMA. Hum Mol Genet 24, 5524-5541.

McLaughlin, H.M., Sakaguchi, R., Giblin, W., Program, N.C.S., Wilson, T.E., Biesecker, L., Lupski, J.R., Talbot, K., Vance, J.M., Zuchner, S.*, et al.* (2012). A recurrent loss-of-function alanyl-tRNA synthetase (AARS) mutation in patients with Charcot-Marie-Tooth disease type 2N (CMT2N). Hum Mutat 33, 244-253.

McLaughlin, H.M., Sakaguchi, R., Liu, C., Igarashi, T., Pehlivan, D., Chu, K., Iyer, R., Cruz, P., Cherukuri, P.F., Hansen, N.F.*, et al.* (2010). Compound heterozygosity for loss-of-function lysyl-tRNA synthetase mutations in a patient with peripheral neuropathy. Am J Hum Genet 87, 560-566.

McNaught, K.S., Shashidharan, P., Perl, D.P., Jenner, P., and Olanow, C.W. (2002). Aggresome-related biogenesis of Lewy bodies. Eur J Neurosci 16, 2136-2148.

McWhorter, M.L., Monani, U.R., Burghes, A.H., and Beattie, C.E. (2003). Knockdown of the survival motor neuron (Smn) protein in zebrafish causes defects in motor axon outgrowth and pathfinding. J Cell Biol 162, 919-931.

Melki, J., Abdelhak, S., Sheth, P., Bachelot, M.F., Burlet, P., Marcadet, A., Aicardi, J., Barois, A., Carriere, J.P., Fardeau, M., and et al. (1990). Gene for chronic proximal spinal muscular atrophies maps to chromosome 5q. Nature 344, 767-768.

Mendell, J. (2017). AVXS-101 phase 1 gene therapy clinical trial in SMA type 1: event free survival and achievement of developmental milestones. In 21st annual spinal muscular atrophy researcher meeting; CureSMA (Orlando, Florida).

Mentis, G.Z., Blivis, D., Liu, W., Drobac, E., Crowder, M.E., Kong, L., Alvarez, F.J., Sumner, C.J., and O'Donovan, M.J. (2011). Early functional impairment of sensory-motor connectivity in a mouse model of spinal muscular atrophy. Neuron 69, 453-467.

Mercuri, E. (2017). Clinical studies of RG7916 in patients with spinal muscular atrophy: study update. In 21st annual spinal muscular atrophy researcher meeting; CureSMA (Orlando, Florida).

Mercuri, E., Bertini, E., and Iannaccone, S.T. (2012). Childhood spinal muscular atrophy: controversies and challenges. Lancet Neurol 11, 443-452.

Mercuri, E., Finkel, R., Montes, J., Mazzone, E.S., Sormani, M.P., Main, M., Ramsey, D., Mayhew, A., Glanzman, A.M., Dunaway, S.*, et al.* (2016). Patterns of disease progression in type 2 and 3 SMA: Implications for clinical trials. Neuromuscul Disord 26, 126-131.

Miller, N., Shi, H., Zelikovich, A.S., and Ma, Y.C. (2016). Motor neuron mitochondrial dysfunction in spinal muscular atrophy. Hum Mol Genet 25, 3395-3406.

Minami, R., Hayakawa, A., Kagawa, H., Yanagi, Y., Yokosawa, H., and Kawahara, H. (2010). BAG-6 is essential for selective elimination of defective proteasomal substrates. J Cell Biol 190, 637-650.

Mo, Z., Zhang, Q., Liu, Z., Lauer, J., Shi, Y., Sun, L., Griffin, P.R., and Yang, X.L. (2016). Neddylation requires glycyl-tRNA synthetase to protect activated E2. Nat Struct Mol Biol 23, 730-737.

Monani, U.R., Lorson, C.L., Parsons, D.W., Prior, T.W., Androphy, E.J., Burghes, A.H., and McPherson, J.D. (1999). A single nucleotide difference that alters splicing patterns distinguishes the SMA gene SMN1 from the copy gene SMN2. Hum Mol Genet 8, 1177-1183.

Monani, U.R., Sendtner, M., Coovert, D.D., Parsons, D.W., Andreassi, C., Le, T.T., Jablonka, S., Schrank, B., Rossoll, W., Prior, T.W.*, et al.* (2000). The human centromeric survival motor neuron gene (SMN2) rescues embryonic lethality in Smn(-/-) mice and results in a mouse with spinal muscular atrophy. Hum Mol Genet 9, 333-339.

Mor, A., White, M.A., and Fontoura, B.M. (2014). Nuclear trafficking in health and disease. Curr Opin Cell Biol 28, 28-35.

Motley, W.W., Talbot, K., and Fischbeck, K.H. (2010). GARS axonopathy: not every neuron's cup of tRNA. Trends Neurosci 33, 59-66.

Moudry, P., Lukas, C., Macurek, L., Hanzlikova, H., Hodny, Z., Lukas, J., and Bartek, J. (2012). Ubiquitin-activating enzyme UBA1 is required for cellular response to DNA damage. Cell Cycle 11, 1573-1582.

Murayama, S., Bouldin, T.W., and Suzuki, K. (1991). Immunocytochemical and ultrastructural studies of Werdnig-Hoffmann disease. Acta Neuropathol 81, 408-417.

Murray, L.M., Beauvais, A., Gibeault, S., Courtney, N.L., and Kothary, R. (2015). Transcriptional profiling of differentially vulnerable motor neurons at pre-symptomatic stage in the Smn (2b/-) mouse model of spinal muscular atrophy. Acta Neuropathol Commun 3, 55.

Murray, L.M., Comley, L.H., Thomson, D., Parkinson, N., Talbot, K., and Gillingwater, T.H. (2008). Selective vulnerability of motor neurons and dissociation of pre- and post-synaptic pathology at the neuromuscular junction in mouse models of spinal muscular atrophy. Hum Mol Genet 17, 949-962.

Murray, L.M., Lee, S., Baumer, D., Parson, S.H., Talbot, K., and Gillingwater, T.H. (2010). Pre-symptomatic development of lower motor neuron connectivity in a mouse model of severe spinal muscular atrophy. Hum Mol Genet 19, 420-433.

Mutsaers, C.A., Wishart, T.M., Lamont, D.J., Riessland, M., Schreml, J., Comley, L.H., Murray, L.M., Parson, S.H., Lochmuller, H., Wirth, B.*, et al.* (2011). Reversible molecular pathology of skeletal muscle in spinal muscular atrophy. Hum Mol Genet 20, 4334-4344.

Nafisinia, M., Riley, L.G., Gold, W.A., Bhattacharya, K., Broderick, C.R., Thorburn, D.R., Simons, C., and Christodoulou, J. (2017). Compound heterozygous mutations in glycyl-tRNA synthetase (GARS) cause mitochondrial respiratory chain dysfunction. PLoS One 12, e0178125.

Nangle, L.A., Motta, C.M., and Schimmel, P. (2006). Global effects of mistranslation from an editing defect in mammalian cells. Chem Biol 13, 1091-1100.

Naryshkin, N.A., Weetall, M., Dakka, A., Narasimhan, J., Zhao, X., Feng, Z., Ling, K.K., Karp, G.M., Qi, H., Woll, M.G., *et al.* (2014). Motor neuron disease. SMN2 splicing modifiers improve motor function and longevity in mice with spinal muscular atrophy. Science 345, 688-693.

Newbery, H.J., Gillingwater, T.H., Dharmasaroja, P., Peters, J., Wharton, S.B., Thomson, D., Ribchester, R.R., and Abbott, C.M. (2005). Progressive loss of motor neuron function in wasted mice: effects of a spontaneous null mutation in the gene for the eEF1 A2 translation factor. J Neuropathol Exp Neurol 64, 295-303.

Niehues, S., Bussmann, J., Steffes, G., Erdmann, I., Kohrer, C., Sun, L., Wagner, M., Schafer, K., Wang, G., Koerdt, S.N., *et al.* (2015). Impaired protein translation in Drosophila models for Charcot-Marie-Tooth neuropathy caused by mutant tRNA synthetases. Nat Commun 6, 7520.

Nolle, A., Zeug, A., van Bergeijk, J., Tonges, L., Gerhard, R., Brinkmann, H., Al Rayes, S., Hensel, N., Schill, Y., Apkhazava, D., *et al.* (2011). The spinal muscular atrophy disease protein SMN is linked to the Rho-kinase pathway via profilin. Hum Mol Genet 20, 4865-4878.

Oprea, G.E., Krober, S., McWhorter, M.L., Rossoll, W., Muller, S., Krawczak, M., Bassell, G.J., Beattie, C.E., and Wirth, B. (2008). Plastin 3 is a protective modifier of autosomal recessive spinal muscular atrophy. Science 320, 524-527.

Pagliardini, S., Giavazzi, A., Setola, V., Lizier, C., Di Luca, M., DeBiasi, S., and Battaglia, G. (2000). Subcellular localization and axonal transport of the survival motor neuron (SMN) protein in the developing rat spinal cord. Hum Mol Genet 9, 47-56.

Palamarchuk, A., Efanov, A., Maximov, V., Aqeilan, R.I., Croce, C.M., and Pekarsky, Y. (2005). Akt phosphorylates and regulates Pdcd4 tumor suppressor protein. Cancer Res 65, 11282-11286.

Pane, M., Lapenta, L., Abiusi, E., de Sanctis, R., Luigetti, M., Palermo, C., Ranalli, D., Fiori, S., Tiziano, F.D., and Mercuri, E. (2017). Longitudinal assessments in discordant twins with SMA. Neuromuscul Disord.

Pang, Y.L., Poruri, K., and Martinis, S.A. (2014). tRNA synthetase: tRNA aminoacylation and beyond. Wiley Interdiscip Rev RNA 5, 461-480.

Park, M.C., Kang, T., Jin, D., Han, J.M., Kim, S.B., Park, Y.J., Cho, K., Park, Y.W., Guo, M., He, W., *et al.* (2012). Secreted human glycyl-tRNA synthetase implicated in defense against ERK-activated tumorigenesis. Proc Natl Acad Sci U S A 109, E640-647.

Park, S.G., Schimmel, P., and Kim, S. (2008). Aminoacyl tRNA synthetases and their connections to disease. Proc Natl Acad Sci U S A 105, 11043-11049.

Passini, M.A., Bu, J., Roskelley, E.M., Richards, A.M., Sardi, S.P., O'Riordan, C.R., Klinger, K.W., Shihabuddin, L.S., and Cheng, S.H. (2010). CNS-targeted gene therapy improves survival and motor function in a mouse model of spinal muscular atrophy. J Clin Invest 120, 1253-1264.

Pedurupillay, C.R., Amundsen, S.S., Baroy, T., Rasmussen, M., Blomhoff, A., Stadheim, B.F., Orstavik, K., Holmgren, A., Iqbal, T., Frengen, E., *et al.* (2016). Clinical and molecular characteristics in three families with biallelic mutations in IGHMBP2. Neuromuscul Disord 26, 570-575.

Peeters, K., Palaima, P., Pelayo-Negro, A.L., Garcia, A., Gallardo, E., Garcia-Barredo, R., Mateiu, L., Baets, J., Menten, B., De Vriendt, E., *et al.* (2016). Charcot-Marie-Tooth disease type 2G redefined by a novel mutation in LRSAM1. Ann Neurol 80, 823-833.

Pellizzoni, L., Baccon, J., Charroux, B., and Dreyfuss, G. (2001). The survival of motor neurons (SMN) protein interacts with the snoRNP proteins fibrillarin and GAR1. Curr Biol 11, 1079-1088.

Pellizzoni, L., Yong, J., and Dreyfuss, G. (2002). Essential role for the SMN complex in the specificity of snRNP assembly. Science 298, 1775-1779.

Peng, Z., Liao, Z., Matsumoto, Y., Yang, A., and Tomkinson, A.E. (2016). Human DNA Ligase I Interacts with and Is Targeted for Degradation by the DCAF7 Specificity Factor of the Cul4-DDB1 Ubiquitin Ligase Complex. J Biol Chem 291, 21893-21902.

Piazzon, N., Schlotter, F., Lefebvre, S., Dodre, M., Mereau, A., Soret, J., Besse, A., Barkats, M., Bordonne, R., Branlant, C., and Massenet, S. (2013). Implication of the SMN complex in the biogenesis and steady state level of the signal recognition particle. Nucleic Acids Res 41, 1255-1272.

Pichler, A., Gast, A., Seeler, J.S., Dejean, A., and Melchior, F. (2002). The nucleoporin RanBP2 has SUMO1 E3 ligase activity. Cell 108, 109-120.

Powis, R.A. (2016). Targeting the ubiquitin proteasome system to develop novel therapeutic approaches for spinal muscular atrophy. In Centre for Integrative physiology (University of Edinburgh).

Powis, R.A., and Gillingwater, T.H. (2015). Selective loss of alpha motor neurons with sparing of gamma motor neurons and spinal cord cholinergic neurons in a mouse model of spinal muscular atrophy. J Anat.

Powis, R.A., and Gillingwater, T.H. (2016). Selective loss of alpha motor neurons with sparing of gamma motor neurons and spinal cord cholinergic neurons in a mouse model of spinal muscular atrophy. J Anat 228, 443-451.

Powis, R.A., Karyka, E., Boyd, P., Come, J., Jones, R.A., Zheng, Y., Szunyogova, E., Groen, E.J., Hunter, G., Thomson, D.*, et al.* (2016). Systemic restoration of UBA1 ameliorates disease in spinal muscular atrophy. JCI Insight 1, e87908.

Powis, R.A., Mutsaers, C.A., Wishart, T.M., Hunter, G., Wirth, B., and Gillingwater, T.H. (2014). Increased levels of UCHL1 are a compensatory response to disrupted ubiquitin homeostasis in spinal muscular atrophy and do not represent a viable therapeutic target. Neuropathol Appl Neurobiol 40, 873-887.

Prescott, A.R., Bales, A., James, J., Trinkle-Mulcahy, L., and Sleeman, J.E. (2014). Time-resolved quantitative proteomics implicates the core snRNP protein SmB together with SMN in neural trafficking. J Cell Sci 127, 812-827.

Ramser, J., Ahearn, M.E., Lenski, C., Yariz, K.O., Hellebrand, H., von Rhein, M., Clark, R.D., Schmutzler, R.K., Lichtner, P., Hoffman, E.P.*, et al.* (2008). Rare missense and synonymous variants in UBE1 are associated with X-linked infantile spinal muscular atrophy. Am J Hum Genet 82, 188-193.

Reid, D., Zinger, Y., and Raheja, D. (2016). Sensory Neuronopathy in Spinal Muscular Atrophy: A Case Presentation. J Clin Neuromuscul Dis 18, 44-46.

Reilly, M.M., Murphy, S.M., and Laura, M. (2011). Charcot-Marie-Tooth disease. J Peripher Nerv Syst 16, 1-14.

Riessland, M., Ackermann, B., Forster, A., Jakubik, M., Hauke, J., Garbes, L., Fritzsche, I., Mende, Y., Blumcke, I., Hahnen, E., and Wirth, B. (2010). SAHA ameliorates the SMA phenotype in two mouse models for spinal muscular atrophy. Hum Mol Genet 19, 1492-1506.

Riessland, M., Kaczmarek, A., Schneider, S., Swoboda, K.J., Lohr, H., Bradler, C., Grysko, V., Dimitriadi, M., Hosseinibarkooie, S., Torres-Benito, L.*, et al.* (2017). Neurocalcin Delta Suppression

Protects against Spinal Muscular Atrophy in Humans and across Species by Restoring Impaired Endocytosis. Am J Hum Genet 100, 297-315.

Rindt, H., Feng, Z., Mazzasette, C., Glascock, J.J., Valdivia, D., Pyles, N., Crawford, T.O., Swoboda, K.J., Patitucci, T.N., Ebert, A.D.*, et al.* (2015). Astrocytes influence the severity of spinal muscular atrophy. Hum Mol Genet 24, 4094-4102.

Rinetti, G.V., and Schweizer, F.E. (2010). Ubiquitination acutely regulates presynaptic neurotransmitter release in mammalian neurons. J Neurosci 30, 3157-3166.

Ripolone, M., Ronchi, D., Violano, R., Vallejo, D., Fagiolari, G., Barca, E., Lucchini, V., Colombo, I., Villa, L., Berardinelli, A.*, et al.* (2015). Impaired Muscle Mitochondrial Biogenesis and Myogenesis in Spinal Muscular Atrophy. JAMA Neurol 72, 666-675.

Robbins, K.L., Glascock, J.J., Osman, E.Y., Miller, M.R., and Lorson, C.L. (2014). Defining the therapeutic window in a severe animal model of spinal muscular atrophy. Hum Mol Genet 23, 4559-4568.

Rona, G., Borsos, M., Ellis, J.J., Mehdi, A.M., Christie, M., Kornyei, Z., Neubrandt, M., Toth, J., Bozoky, Z., Buday, L.*, et al.* (2014). Dynamics of re-constitution of the human nuclear proteome after cell division is regulated by NLS-adjacent phosphorylation. Cell Cycle 13, 3551-3564.

Rossoll, W., Jablonka, S., Andreassi, C., Kroning, A.K., Karle, K., Monani, U.R., and Sendtner, M. (2003). Smn, the spinal muscular atrophy-determining gene product, modulates axon growth and localization of beta-actin mRNA in growth cones of motoneurons. J Cell Biol 163, 801-812.

Rubinsztein, D.C. (2006). The roles of intracellular protein-degradation pathways in neurodegeneration. Nature 443, 780-786.

Rudnik-Schoneborn, S., Goebel, H.H., Schlote, W., Molaian, S., Omran, H., Ketelsen, U., Korinthenberg, R., Wenzel, D., Lauffer, H., Kreiss-Nachtsheim, M.*, et al.* (2003). Classical infantile spinal muscular atrophy with SMN deficiency causes sensory neuronopathy. Neurology 60, 983-987.

Ryan, B.J., Hoek, S., Fon, E.A., and Wade-Martins, R. (2015). Mitochondrial dysfunction and mitophagy in Parkinson's: from familial to sporadic disease. Trends Biochem Sci 40, 200-210.

Sajish, M., and Schimmel, P. (2015). A human tRNA synthetase is a potent PARP1-activating effector target for resveratrol. Nature 519, 370-373.

Sareen, D., Ebert, A.D., Heins, B.M., McGivern, J.V., Ornelas, L., and Svendsen, C.N. (2012). Inhibition of apoptosis blocks human motor neuron cell death in a stem cell model of spinal muscular atrophy. PLoS One 7, e39113.

Savli, H., Szendroi, A., Romics, I., and Nagy, B. (2008). Gene network and canonical pathway analysis in prostate cancer: a microarray study. Exp Mol Med 40, 176-185.

Schmutz, J., Martin, J., Terry, A., Couronne, O., Grimwood, J., Lowry, S., Gordon, L.A., Scott, D., Xie, G., Huang, W.*, et al.* (2004). The DNA sequence and comparative analysis of human chromosome 5. Nature 431, 268-274.

ScholarRock (2017). SRK-015 FOR SPINAL MUSCULAR ATROPHY (SMA). (http://www.scholarrock.com/pipeline/srk-015-for-sma/intro/).

Schottmann, G., Wagner, C., Seifert, F., Stenzel, W., and Schuelke, M. (2016). MORC2 mutation causes severe spinal muscular atrophy-phenotype, cerebellar atrophy, and diaphragmatic paralysis. Brain 139, e70.

Schulman, B.A., and Harper, J.W. (2009). Ubiquitin-like protein activation by E1 enzymes: the apex for downstream signalling pathways. Nat Rev Mol Cell Biol 10, 319-331.

Schwartz, A.L., Trausch, J.S., Ciechanover, A., Slot, J.W., and Geuze, H. (1992). Immunoelectron microscopic localization of the ubiquitin-activating enzyme E1 in HepG2 cells. Proc Natl Acad Sci U S A 89, 5542-5546.

Seburn, K.L., Nangle, L.A., Cox, G.A., Schimmel, P., and Burgess, R.W. (2006). An active dominant mutation of glycyl-tRNA synthetase causes neuropathy in a Charcot-Marie-Tooth 2D mouse model. Neuron 51, 715-726.

Seufert, W., Futcher, B., and Jentsch, S. (1995). Role of a ubiquitin-conjugating enzyme in degradation of S- and M-phase cyclins. Nature 373, 78-81.

Sevilla, T., Lupo, V., Martinez-Rubio, D., Sancho, P., Sivera, R., Chumillas, M.J., Garcia-Romero, M., Pascual-Pascual, S.I., Muelas, N., Dopazo, J.*, et al.* (2016). Mutations in the MORC2 gene cause axonal Charcot-Marie-Tooth disease. Brain 139, 62-72.

Shafey, D., Cote, P.D., and Kothary, R. (2005). Hypomorphic Smn knockdown C2C12 myoblasts reveal intrinsic defects in myoblast fusion and myotube morphology. Exp Cell Res 311, 49-61.

Shen, H.M., and Mizushima, N. (2014). At the end of the autophagic road: an emerging understanding of lysosomal functions in autophagy. Trends Biochem Sci 39, 61-71.

Shorrock, H.K., and Gillingwater, T.H. (2016). Development and translation of therapies for spinal muscular atrophy. European Medical Journal 4, 64-73.

Simon, C.M., Janas, A.M., Lotti, F., Tapia, J.C., Pellizzoni, L., and Mentis, G.Z. (2016). A Stem Cell Model of the Motor Circuit Uncouples Motor Neuron Death from Hyperexcitability Induced by SMN Deficiency. Cell Rep 16, 1416-1430.

Singh, N.K., Singh, N.N., Androphy, E.J., and Singh, R.N. (2006). Splicing of a critical exon of human Survival Motor Neuron is regulated by a unique silencer element located in the last intron. Mol Cell Biol 26, 1333-1346.

Singh, N.N., Howell, M.D., Androphy, E.J., and Singh, R.N. (2017). How the discovery of ISS-N1 led to the first medical therapy for spinal muscular atrophy. Gene Ther.

Sintusek, P., Catapano, F., Angkathunkayul, N., Marrosu, E., Parson, S.H., Morgan, J.E., Muntoni, F., and Zhou, H. (2016). Histopathological Defects in Intestine in Severe Spinal Muscular Atrophy Mice Are Improved by Systemic Antisense Oligonucleotide Treatment. PLoS One 11, e0155032.

Sison, S.L., Patitucci, T.N., Seminary, E.R., Villalon, E., Lorson, C.L., and Ebert, A.D. (2017). Astrocyte-produced miR-146a as a mediator of motor neuron loss in spinal muscular atrophy. Hum Mol Genet.

Sivakumar, K., Kyriakides, T., Puls, I., Nicholson, G.A., Funalot, B., Antonellis, A., Sambuughin, N., Christodoulou, K., Beggs, J.L., Zamba-Papanicolaou, E.*, et al.* (2005). Phenotypic spectrum of disorders associated with glycyl-tRNA synthetase mutations. Brain 128, 2304-2314.

Sleeman, J.E., and Lamond, A.I. (1999). Newly assembled snRNPs associate with coiled bodies before speckles, suggesting a nuclear snRNP maturation pathway. Curr Biol 9, 1065-1074.

Sleigh, J.N., Dawes, J.M., West, S.J., Wei, N., Spaulding, E.L., Gomez-Martin, A., Zhang, Q., Burgess, R.W., Cader, M.Z., Talbot, K.*, et al.* (2017a). Trk receptor signaling and sensory neuron fate are perturbed in human neuropathy caused by Gars mutations. Proc Natl Acad Sci U S A 114, E3324-E3333.

Sleigh, J.N., Gillingwater, T.H., and Talbot, K. (2011). The contribution of mouse models to understanding the pathogenesis of spinal muscular atrophy. Dis Model Mech 4, 457-467.

Sleigh, J.N., Gomez-Martin, A., Wei, N., Bai, G., Yang, X.L., and Schiavo, G. (2017b). Neuropilin 1 sequestration by neuropathogenic mutant glycyl-tRNA synthetase is permissive to vascular homeostasis. Sci Rep 7, 9216.

Sleigh, J.N., Weir, G.A., and Schiavo, G. (2016). A simple, step-by-step dissection protocol for the rapid isolation of mouse dorsal root ganglia. BMC Res Notes 9, 82.

Somers, E., Lees, R.D., Hoban, K., Sleigh, J.N., Zhou, H., Muntoni, F., Talbot, K., Gillingwater, T.H., and Parson, S.H. (2015). Vascular defects and spinal cord hypoxia in spinal muscular atrophy. Ann Neurol.

Spector, D.L., and Lamond, A.I. (2011). Nuclear speckles. Cold Spring Harb Perspect Biol 3.

Stephen, A.G., Trausch-Azar, J.S., Handley-Gearhart, P.M., Ciechanover, A., and Schwartz, A.L. (1997). Identification of a region within the ubiquitin-activating enzyme required for nuclear targeting and phosphorylation. J Biol Chem 272, 10895-10903.

Sugarman, E.A., Nagan, N., Zhu, H., Akmaev, V.R., Zhou, Z., Rohlfs, E.M., Flynn, K., Hendrickson, B.C., Scholl, T., Sirko-Osadsa, D.A., and Allitto, B.A. (2012). Pan-ethnic carrier screening and prenatal diagnosis for spinal muscular atrophy: clinical laboratory analysis of >72,400 specimens. Eur J Hum Genet 20, 27-32.

Sugaya, K., Ishihara, Y., Inoue, S., and Tsuji, H. (2014). Characterization of ubiquitin-activating enzyme Uba1 in the nucleus by its mammalian temperature-sensitive mutant. PLoS One 9, e96666.

Sunyach, C., Michaud, M., Arnoux, T., Bernard-Marissal, N., Aebischer, J., Latyszenok, V., Gouarne, C., Raoul, C., Pruss, R.M., Bordet, T., and Pettmann, B. (2012). Olesoxime delays muscle denervation, astrogliosis, microglial activation and motoneuron death in an ALS mouse model. Neuropharmacology 62, 2346-2352.

Suzuki, C., Garces, R.G., Edmonds, K.A., Hiller, S., Hyberts, S.G., Marintchev, A., and Wagner, G. (2008). PDCD4 inhibits translation initiation by binding to eIF4A using both its MA3 domains. Proc Natl Acad Sci U S A 105, 3274-3279.

Szunyogova, E., Zhou, H., Maxwell, G.K., Powis, R.A., Francesco, M., Gillingwater, T.H., and Parson, S.H. (2016). Survival Motor Neuron (SMN) protein is required for normal mouse liver development. Sci Rep 6, 34635.

Tashiro, Y., Urushitani, M., Inoue, H., Koike, M., Uchiyama, Y., Komatsu, M., Tanaka, K., Yamazaki, M., Abe, M., Misawa, H.*, et al.* (2012). Motor neuron-specific disruption of proteasomes, but not autophagy, replicates amyotrophic lateral sclerosis. J Biol Chem 287, 42984-42994.

Teixeira, F.R., Randle, S.J., Patel, S.P., Mevissen, T.E., Zenkeviciute, G., Koide, T., Komander, D., and Laman, H. (2016). Gsk3beta and Tomm20 are substrates of the SCFFbxo7/PARK15 ubiquitin ligase associated with Parkinson's disease. Biochem J 473, 3563-3580.

Thomas, F.P., Guergueltcheva, V., Gondim, F.A., Tournev, I., Rao, C.V., Ishpekova, B., Kinsella, L.J., Pan, Y., Geller, T.J., Litvinenko, I.*, et al.* (2016). Clinical, neurophysiological and morphological study of dominant intermediate Charcot-Marie-Tooth type C neuropathy. J Neurol 263, 467-476.

Thomson, A.K., Somers, E., Powis, R.A., Shorrock, H.K., Murphy, K., Swoboda, K.J., Gillingwater, T.H., and Parson, S.H. (2017). Survival of motor neurone protein is required for normal postnatal development of the spleen. J Anat 230, 337-346.

Tisdale, S., and Pellizzoni, L. (2015). Disease mechanisms and therapeutic approaches in spinal muscular atrophy. J Neurosci 35, 8691-8700.

Tokgoz, Z., Bohnsack, R.N., and Haas, A.L. (2006). Pleiotropic effects of ATP.Mg2+ binding in the catalytic cycle of ubiquitin-activating enzyme. J Biol Chem 281, 14729-14737.

Trausch, J.S., Grenfell, S.J., Handley-Gearhart, P.M., Ciechanover, A., and Schwartz, A.L. (1993). Immunofluorescent localization of the ubiquitin-activating enzyme, E1, to the nucleus and cytoskeleton. Am J Physiol 264, C93-102.

Tsai, L.K., Chen, C.L., Ting, C.H., Lin-Chao, S., Hwu, W.L., Dodge, J.C., Passini, M.A., and Cheng, S.H. (2014). Systemic administration of a recombinant AAV1 vector encoding IGF-1 improves disease manifestations in SMA mice. Mol Ther 22, 1450-1459.

Tydlacka, S., Wang, C.E., Wang, X., Li, S., and Li, X.J. (2008). Differential activities of the ubiquitin-proteasome system in neurons versus glia may account for the preferential accumulation of misfolded proteins in neurons. J Neurosci 28, 13285-13295.

Valori, C.F., Ning, K., Wyles, M., Mead, R.J., Grierson, A.J., Shaw, P.J., and Azzouz, M. (2010). Systemic delivery of scAAV9 expressing SMN prolongs survival in a model of spinal muscular atrophy. Sci Transl Med 2, 35ra42.

Verhaart, I.E.C., Robertson, A., Wilson, I.J., Aartsma-Rus, A., Cameron, S., Jones, C.C., Cook, S.F., and Lochmuller, H. (2017). Prevalence, incidence and carrier frequency of 5q-linked spinal muscular atrophy - a literature review. Orphanet J Rare Dis 12, 124.

Vester, A., Velez-Ruiz, G., McLaughlin, H.M., Program, N.C.S., Lupski, J.R., Talbot, K., Vance, J.M., Zuchner, S., Roda, R.H., Fischbeck, K.H.*, et al.* (2013). A loss-of-function variant in the human histidyl-tRNA synthetase (HARS) gene is neurotoxic in vivo. Hum Mutat 34, 191-199.

Vingill, S., Brockelt, D., Lancelin, C., Tatenhorst, L., Dontcheva, G., Preisinger, C., Schwedhelm-Domeyer, N., Joseph, S., Mitkovski, M., Goebbels, S.*, et al.* (2016). Loss of FBXO7 (PARK15) results in reduced proteasome activity and models a parkinsonism-like phenotype in mice. EMBO J 35, 2008-2025.

Viquez, O.M., Caito, S.W., McDonald, W.H., Friedman, D.B., and Valentine, W.M. (2012). Electrophilic adduction of ubiquitin activating enzyme E1 by N,N-diethyldithiocarbamate inhibits ubiquitin activation and is accompanied by striatal injury in the rat. Chem Res Toxicol 25, 2310-2321.

Wade, B.E., Wang, C.E., Yan, S., Bhat, K., Huang, B., Li, S., and Li, X.J. (2014). Ubiquitin-activating enzyme activity contributes to differential accumulation of mutant huntingtin in brain and peripheral tissues. J Neurosci 34, 8411-8422.

Wadman, R.I., Stam, M., Gijzen, M., Lemmink, H.H., Snoeck, I.N., Wijngaarde, C.A., Braun, K.P., Schoenmakers, M.A., van den Berg, L.H., Dooijes, D., and van der Pol, W.L. (2017). Association of motor milestones, SMN2 copy and outcome in spinal muscular atrophy types 0-4. J Neurol Neurosurg Psychiatry 88, 365-367.

Wadman, R.I., Stam, M., Jansen, M.D., van der Weegen, Y., Wijngaarde, C.A., Harschnitz, O., Sodaar, P., Braun, K.P., Dooijes, D., Lemmink, H.H.*, et al.* (2016). A Comparative Study of SMN Protein and mRNA in Blood and Fibroblasts in Patients with Spinal Muscular Atrophy and Healthy Controls. PLoS One 11, e0167087.

Wadman, R.I., Vrancken, A.F., van den Berg, L.H., and van der Pol, W.L. (2012). Dysfunction of the neuromuscular junction in spinal muscular atrophy types 2 and 3. Neurology 79, 2050-2055.

Wakasugi, K., and Schimmel, P. (1999). Highly differentiated motifs responsible for two cytokine activities of a split human tRNA synthetase. J Biol Chem 274, 23155-23159.

Wang, T., Jiang, X., Chen, G., and Xu, J. (2015). Interaction of amyotrophic lateral sclerosis/frontotemporal lobar degeneration-associated fused-in-sarcoma with proteins involved in metabolic and protein degradation pathways. Neurobiol Aging 36, 527-535.

Watts, R.J., Hoopfer, E.D., and Luo, L. (2003). Axon pruning during Drosophila metamorphosis: evidence for local degeneration and requirement of the ubiquitin-proteasome system. Neuron 38, 871-885.

Werdnig, G. (1891). Zwei frühinfantile hereditäre Fälle von progressiver Muskelatrophie unter dem Bilde der Dystrophie, aber auf neurotischer Grundlage. Archiv fur Psychiatrie und Nervenkrankheiten 22, 437-481.

Wijngaarde, C.A., Blank, A.C., Stam, M., Wadman, R.I., van den Berg, L.H., and van der Pol, W.L. (2017). Cardiac pathology in spinal muscular atrophy: a systematic review. Orphanet J Rare Dis 12, 67.

Wishart, T.M., Huang, J.P., Murray, L.M., Lamont, D.J., Mutsaers, C.A., Ross, J., Geldsetzer, P., Ansorge, O., Talbot, K., Parson, S.H., and Gillingwater, T.H. (2010). SMN deficiency disrupts brain development in a mouse model of severe spinal muscular atrophy. Hum Mol Genet 19, 4216-4228.

Wishart, T.M., Mutsaers, C.A., Riessland, M., Reimer, M.M., Hunter, G., Hannam, M.L., Eaton, S.L., Fuller, H.R., Roche, S.L., Somers, E.*, et al.* (2014). Dysregulation of ubiquitin homeostasis and beta-catenin signaling promote spinal muscular atrophy. J Clin Invest 124, 1821-1834.

Wishart, T.M., Paterson, J.M., Short, D.M., Meredith, S., Robertson, K.A., Sutherland, C., Cousin, M.A., Dutia, M.B., and Gillingwater, T.H. (2007). Differential proteomics analysis of synaptic proteins identifies potential cellular targets and protein mediators of synaptic neuroprotection conferred by the slow Wallerian degeneration (Wlds) gene. Mol Cell Proteomics 6, 1318-1330.

Wishart, T.M., Pemberton, H.N., James, S.R., McCabe, C.J., and Gillingwater, T.H. (2008). Modified cell cycle status in a mouse model of altered neuronal vulnerability (slow Wallerian degeneration; Wlds). Genome Biol 9, R101.

Woerner, A.C., Frottin, F., Hornburg, D., Feng, L.R., Meissner, F., Patra, M., Tatzelt, J., Mann, M., Winklhofer, K.F., Hartl, F.U., and Hipp, M.S. (2016). Cytoplasmic protein aggregates interfere with nucleocytoplasmic transport of protein and RNA. Science 351, 173-176.

Wu, C.H., Fallini, C., Ticozzi, N., Keagle, P.J., Sapp, P.C., Piotrowska, K., Lowe, P., Koppers, M., McKenna-Yasek, D., Baron, D.M.*, et al.* (2012). Mutations in the profilin 1 gene cause familial amyotrophic lateral sclerosis. Nature 488, 499-503.

Xu, C.C., Denton, K.R., Wang, Z.B., Zhang, X., and Li, X.J. (2016). Abnormal mitochondrial transport and morphology as early pathological changes in human models of spinal muscular atrophy. Dis Model Mech 9, 39-49.

Xu, G.W., Ali, M., Wood, T.E., Wong, D., Maclean, N., Wang, X., Gronda, M., Skrtic, M., Li, X., Hurren, R.*, et al.* (2010). The ubiquitin-activating enzyme E1 as a therapeutic target for the treatment of leukemia and multiple myeloma. Blood 115, 2251-2259.

Yang, X., Brownell, J.E., Xu, Q., Zhu, F., Ma, J., Loke, H.K., Rollins, N., Soucy, T.A., Minissale, J.J., Thomas, M.P.*, et al.* (2013). Absolute quantification of E1, ubiquitin-like proteins and Nedd8-MLN4924 adduct by mass spectrometry. Cell Biochem Biophys 67, 139-147.

Yang, Y., Kitagaki, J., Dai, R.M., Tsai, Y.C., Lorick, K.L., Ludwig, R.L., Pierre, S.A., Jensen, J.P., Davydov, I.V., Oberoi, P.*, et al.* (2007). Inhibitors of ubiquitin-activating enzyme (E1), a new class of potential cancer therapeutics. Cancer Res 67, 9472-9481.

Ye, Y., and Rape, M. (2009). Building ubiquitin chains: E2 enzymes at work. Nat Rev Mol Cell Biol 10, 755-764.

Zhang, H.L., Pan, F., Hong, D., Shenoy, S.M., Singer, R.H., and Bassell, G.J. (2003). Active transport of the survival motor neuron protein and the role of exon-7 in cytoplasmic localization. J Neurosci 23, 6627-6637.

Zhang, K., Donnelly, C.J., Haeusler, A.R., Grima, J.C., Machamer, J.B., Steinwald, P., Daley, E.L., Miller, S.J., Cunningham, K.M., Vidensky, S.*, et al.* (2015). The C9orf72 repeat expansion disrupts nucleocytoplasmic transport. Nature 525, 56-61.

Zhang, Z., Lotti, F., Dittmar, K., Younis, I., Wan, L., Kasim, M., and Dreyfuss, G. (2008). SMN deficiency causes tissue-specific perturbations in the repertoire of snRNAs and widespread defects in splicing. Cell 133, 585-600.

Zhou, C., Feng, Z., and Ko, C.P. (2016). Defects in Motoneuron-Astrocyte Interactions in Spinal Muscular Atrophy. J Neurosci 36, 2543-2553.

Zhou, H., Meng, J., Marrosu, E., Janghra, N., Morgan, J., and Muntoni, F. (2015). Repeated low doses of morpholino antisense oligomer: an intermediate mouse model of spinal muscular atrophy to explore the window of therapeutic response. Hum Mol Genet 24, 6265-6277.

Appendices

Appendix 1 UBA1 distribution varies between different cell types

Cell type	UBA1		UBA1a	
	Nucleus	Cytoplasm	Nucleus	Cytoplasm
HepG2	37%	63%	-	-
HEK293	54.56%	45.44%	84.66%	15.34%
Glia - DIV4	75.05%	24.95%	88.97%	11.03%
Glia - DIV8	81.66%	18.34%	90.96%	9.043%
Glia - DIV12	78.69%	21.31%	92.31%	7.686%
MN - DIV4	63.28%	36.72%	78.44%	21.59%
MN - DIV8	57.45%	42.55%	72.23%	27.77%
MN - DIV12	56.05%	43.95%	62.28%	37.75%

Appendix 1 UBA1 distribution in different cell types

Percentage of UBA1 localised within the nucleus and cytoplasm of different cell types. HepG2 data is from (Schwartz et al., 1992); distribution analysis was performed on HEK293 cells, glial cells (Glia) and motor neurons (MN) in Chapter 3. DIV: Days *in vitro.* Heat map indicates relative expression percentages.

Appendix 2 Post-filtering proteomic dataset

Accession	Protein Name	Unique peptides	Confidence score	p-value	OE/Control	KD/Control
A0A024R1A3	UBA1	25	1992.7	2.47E-08	7.5752	-2.0289
B1AHA8	HMOX1	2	146.1	1.25E-05	2.4372	-1.2306
A0A087X2D8	SPAG9	3	141.86	4.34E-06	1.6223	-1.1416
J3KPF3	SLC3A2	4	288.19	2.76E-05	1.5087	-1.1112
C9J057	ASNS	6	418.07	2.33E-04	1.4687	-1.4855
A0A090N8G0	GARS	2	102.71	1.43E-03	1.3665	-1.2432
I4AY87	MIF	2	120.61	4.98E-03	1.3432	1.0040
Q0VGA5	SARS	2	107.24	5.83E-04	1.3004	-1.1369
B3KSC3	PHGDH	3	198.13	6.55E-04	1.2948	-1.0058
P54577	YARS	2	101.88	2.88E-03	1.2916	-1.3236
Q6FHN3	NME2	2	117.64	8.48E-03	1.2814	-1.1113
F5GXH2	LDHA	2	91.25	7.61E-03	1.2758	-1.0760
Q8WTZ9	PFKP	2	144.13	1.31E-02	1.2754	-1.0276
D9IAI1	PEBP1	2	165.73	2.50E-03	1.2753	1.0065
Q9NZL4	HSPBP1	3	136.31	3.83E-03	1.2668	-1.1535
H0YL92	IPO4	2	99.74	2.69E-03	1.2586	-1.2470
B3KRM8	TSN	2	124.82	1.97E-02	1.2567	-1.0626
A0A024R222	PSAT1	3	154.43	3.05E-03	1.2530	-1.3184
B7ZMD6	IRGQ	2	102.32	8.97E-04	1.2471	-1.2290
A0A024RD93	PAICS	4	198.65	2.98E-03	1.2416	-1.0830
Q0D2Q6	PGAM1	2	93.47	1.46E-02	1.2389	-1.0883
B9A041	MDH1	2	143.46	1.08E-02	1.2374	-1.0747
A0A024R4F1	ENO1	6	465.3	1.67E-03	1.2349	-1.1247
D3DUW5	DNM1L	2	169.82	9.51E-03	1.2328	-1.1404
A0A024R6K8	WARS	2	146.73	1.12E-02	1.2327	-1.1397
B3KTP2	NPEPPS	2	131.99	4.03E-03	1.2321	-1.0102
Q13885	TUBB2A	2	63.74	7.09E-03	1.2265	-1.0788
B2RCM3	CAPN2	2	82.93	3.96E-03	1.2261	-1.0921
A0A024RAM0	TNPO1	3	186.07	4.37E-05	1.2257	-1.0256
D3DX26	RANBP1	2	99.01	3.67E-03	1.2236	-1.1805
V9HWC7	PRDX6	2	124.05	2.46E-03	1.2219	-1.0766
B2RBR9	KPNB1	7	450.51	6.35E-04	1.2191	-1.0674
V9HWE9	GSTP1	3	154.67	6.22E-03	1.2178	-1.0854
Q5SRT3	CLIC1	3	173.11	2.32E-03	1.2157	-1.1414
V9HWC2	PARK7	2	160.44	1.11E-03	1.2149	-1.0993
A0A024R5Q7	ADSS	2	134.09	2.43E-03	1.2139	-1.1676
Q5JP53	TUBB	5	343.89	7.25E-03	1.2122	-1.1239
V9HW77	CKB	2	125.04	1.01E-02	1.2106	1.0207
E7DVW5	FABP5	3	216.32	5.23E-03	1.2105	-1.2379
A0A0A6YY92	ADSL	2	143.23	4.15E-03	1.2092	-1.1857
B4DNK4	PKM	9	711.35	3.43E-03	1.2073	-1.1012
B2R7P8	ATIC	6	326.49	4.34E-04	1.2059	-1.1440
B5BU38	ANXA1	3	177.09	5.14E-04	1.2052	-1.0346
V9HWN7	ALDOA	4	248.49	6.60E-04	1.2023	-1.2127
A0A024R382	CNDP2	2	109.51	1.18E-02	1.1942	-1.1912
P23526	AHCY	2	114.16	4.26E-03	1.1937	-1.1566
B7Z1Y2	ALDOC	2	177.48	2.64E-03	1.1936	-1.1681
A8K5I0	HEL-S-103	15	1049.85	6.25E-06	1.1922	-1.2297
B4DN60	NARS	5	312.89	5.88E-04	1.1918	-1.0608
P07900	HSP90AA1	3	194.43	1.87E-03	1.1884	-1.1237
A0A024RDT4	LCP1	5	255.09	8.90E-04	1.1876	-1.1509
Q2Q9B7	G6PD	2	115.89	2.96E-04	1.1848	-1.2234
Q3B7A7	GART	3	153.2	4.51E-03	1.1827	-1.1826
V9HWB5	PPA1	2	118.96	3.49E-04	1.1823	-1.0866
A0A024RB85	PA2G4	2	105.89	2.37E-03	1.1821	-1.0591
Q9NSD9	FARSB	2	94.41	3.97E-03	1.1808	-1.0933
E7EUT5	GAPDH	4	252.14	1.70E-03	1.1800	-1.1347
Q8IWP6	TUBB4B	3	171.36	3.07E-03	1.1795	-1.1146
B4E1E0	CTPS1	2	84.36	4.39E-03	1.1794	-1.1064
A8K4W5	ACAT2	3	175.25	2.82E-03	1.1784	-1.1801
B2RD14	UCHL1	2	108.54	8.10E-03	1.1772	-1.1611
B4DHB3	PGK1	2	129.33	6.00E-03	1.1752	-1.0266
A0A0A0MSI0	PRDX1	3	145.93	1.14E-02	1.1688	-1.1767

A0A087WVQ9	EEF1A1	3	182.89	9.15E-05	1.1657	-1.2124
F5H5D3	TUBA1C	5	337.25	2.92E-03	1.1649	-1.1155
A0A024RBB7	NAP1L1	3	232.24	1.69E-03	1.1632	-1.1503
P07737	PFN1	3	195.51	3.22E-03	1.1628	-1.1342
B4DDD8	HARS	4	259.24	1.91E-03	1.1558	-1.1951
B7Z1G4	IMPDH2	2	133.44	2.40E-03	1.1504	-1.1485
I3L397	EIF5A	2	177.28	8.48E-04	1.1493	-1.2423
A0A087X1X7	EEF1D	2	114.81	1.29E-03	1.1492	-1.0758
A0A024R3W7	EEF1B2	2	167.21	4.26E-04	1.1491	-1.2699
Q53YD7	EEF1G	3	176.86	2.19E-04	1.1463	-1.2078
Q15645	TRIP13	2	119.77	8.50E-03	1.1399	-1.2405
B2RDR4	TES	2	106.58	5.18E-03	1.1394	-1.1778
B4DM31	CSE1L	2	127	1.14E-02	1.1391	-1.1006
P16152	CBR1	2	114.26	1.77E-03	1.1383	-1.1290
B2RD79	USP14	5	267.45	9.42E-04	1.1374	-1.1537
G9K388	YWHAE/FAM22A	2	137.1	4.77E-03	1.1281	-1.2118
A0A087WYC1	HSPA4	2	115.59	3.52E-03	1.1275	-1.1404
A8K690	STIP1	4	273.27	1.87E-03	1.1274	-1.1451
K7EQA1	PDCD5	3	191.73	6.88E-03	1.1257	-1.1960
J3QRS3	MYL12A	2	128.15	6.73E-04	1.1245	-1.1122
A0A024RAN2	CAST	3	172.27	2.44E-03	1.1237	-1.1010
A0A024R1U0	RANGAP1	2	147.36	2.21E-04	1.1203	-1.1820
A0A024RDY0	IPO5	5	338.22	6.32E-04	1.1133	-1.1463
B1ANR0	PABPC4	7	402.75	2.04E-05	1.1131	-1.1076
J3QLR1	RUVBL1	2	142.03	2.34E-02	1.1061	-1.0314
A0A024RDQ0	HSPH1	11	747.06	2.15E-05	1.1034	-1.1651
Q9NZZ3	CHMP5	2	115.3	2.87E-03	1.1033	-1.2016
P13639	EEF2	6	364.92	4.59E-03	1.1029	-1.2329
A0A024R1N1	MYH9	10	798.08	1.72E-03	1.1024	-1.1733
A0A024RD80	HSP90AB1	7	539.01	1.14E-03	1.0958	-1.1731
K7ESP1	DNAJC7	4	202.05	9.81E-04	1.0943	-1.2385
A8K8U1	CAND1	5	322.41	2.33E-03	1.0935	-1.1575
R4GNH3	PSMC3	3	191.39	1.07E-03	1.0906	-1.1080
Q06210	GFPT1	3	159.16	2.04E-03	1.0871	-1.2545
A0A087WUT6	EIF5B	2	84.07	1.63E-03	1.0842	-1.1764
B4DXP9	ACTR1A	2	133.58	1.90E-03	1.0824	-1.1334
H7C3P9	COPS3	3	184.04	2.16E-06	1.0800	-1.2699
A0A024R4K3	MDH2	3	172.94	3.62E-03	1.0766	1.1721
A8K7F6	EIF4A1	8	589.74	3.53E-04	1.0752	-1.2544
A0A024R904	CACYBP	2	125.19	8.29E-03	1.0737	-1.1500
P0DME0	SETSIP	2	111.7	4.87E-04	1.0666	-1.1482
A0A024R201	PSMD13	3	159.52	2.64E-03	1.0634	-1.1469
Q6NVW7	KPNA2	9	590.84	3.87E-03	1.0624	-1.2470
F8VPD4	CAD	2	134.95	6.96E-03	1.0597	-1.2567
B4DJE7	ACADM	2	116	1.51E-03	1.0584	1.2636
A0A024RCA7	RPLP2	2	146.34	5.81E-04	1.0561	-1.1062
S4R2X2	SFXN1	2	117.33	5.40E-03	1.0523	1.2088
B4DHT9	HSP90B1	4	228.17	2.61E-04	1.0491	1.1941
A0A024RBS1	GCN1L1	2	134.26	6.24E-03	1.0455	-1.1505
D3DP78	DARS	3	142.55	8.70E-04	1.0411	-1.1432
A0A024R7B7	CDC37	2	97	3.93E-03	1.0402	-1.2160
A0A024RA75	HIBADH	2	106.87	3.60E-04	1.0358	1.3690
A2A274	ACO2	2	164.79	9.99E-04	1.0293	1.2946
Q8N9M2	PSMD3	2	118.35	1.61E-02	1.0290	-1.1701
X5D299	ALDH5A1	2	96.22	4.72E-05	1.0278	1.1590
A0A024R1T9	ACLY	10	658.57	5.45E-04	1.0269	-1.2902
P54886	ALDH18A1	2	91.62	3.27E-03	1.0253	1.1438
H0YK49	ETFA	3	165.05	1.17E-04	1.0253	1.1796
A8K4I8	NIPSNAP1	2	98.49	1.89E-03	1.0213	1.2371
O95831-3	AIFM1	3	179.26	4.60E-03	1.0141	1.2093
	A0A0A6YYK3	5	280.79	9.22E-05	1.0138	-1.4788
P07305	H1F0	4	251.17	1.15E-03	1.0131	1.5511
H0YL11	IDH2	2	108.15	4.90E-04	1.0121	1.4717
I3L1P8	SLC25A11	2	177.6	3.20E-03	1.0105	1.2151
I1VE16	SEC22B	2	102.07	1.68E-03	1.0093	1.1923

A8KAK1	UGGT1	4	207.7	3.24E-03	1.0076	1.1845
Q13308	PTK7	2	96.05	5.20E-03	-1.0038	1.2386
Q5JR04	MOV10	2	116.7	9.76E-04	-1.0057	1.1794
Q7Z759	CCT8	4	259.85	4.72E-03	-1.0065	-1.1438
A0A024R0C3	NNT	3	194.71	5.18E-05	-1.0073	1.2914
B7Z2F4	CCT4	4	254.59	8.30E-04	-1.0094	-1.1948
Q6DC98	LMNB1	4	260.56	2.84E-03	-1.0146	1.1973
A0A0A0MSE2	HADH	2	85.21	5.36E-04	-1.0147	1.2656
A0A024QZ30	SDHA	3	147.97	1.46E-03	-1.0218	1.1608
A0A024QZJ8	CDK1	2	106.01	2.22E-03	-1.0219	-1.2616
B2R984	HIST1H1E	4	331.09	1.63E-03	-1.0259	1.3035
J9JID7	LMNB2	2	140.42	1.05E-02	-1.0281	1.2447
E5KNY5	LRPPRC	3	156.12	1.64E-03	-1.0295	1.1213
Q5ST80	FLOT1	5	337.53	1.14E-03	-1.0298	1.2404
A0A087WWS1	THOC1	2	98.08	2.36E-02	-1.0329	1.2106
B4DMF5	GLUD1	3	173.76	1.21E-04	-1.0331	1.1182
P07814	EPRS	3	178.86	6.95E-04	-1.0344	-1.1390
P80723	BASP1	5	230.47	3.87E-03	-1.0414	1.2690
E5RHW4	ERLIN2	2	119.01	2.91E-03	-1.0472	1.2673
A0A024QZ62	FLOT2	4	256.44	2.69E-04	-1.0496	1.1705
H7C333	GBAS	2	121.66	6.84E-04	-1.0576	1.1072
F5GWF6	CCT2	2	149.62	4.17E-03	-1.0610	-1.2058
P78527	PRKDC	21	1376.42	1.42E-03	-1.0669	1.2558
P45954	ACADSB	3	205.48	2.41E-04	-1.0677	1.2521
Q53G72	BCAP31	2	110.36	1.46E-02	-1.0698	1.1047
H3BLZ8	DDX17	2	110.37	8.31E-03	-1.0699	1.1555
A0A024R5M9	NUMA1	3	199.24	9.24E-03	-1.0705	1.1953
B4DVE1	LGALS3BP	3	148.15	9.14E-04	-1.0753	1.3314
A0A024RCB7	CD81	2	129.05	4.29E-03	-1.0755	1.2742
Q92522	H1FX	3	192.5	1.92E-03	-1.0793	1.2606
Q5I6Y5	LMNA	6	345.73	5.07E-03	-1.0803	1.1932
A0A024RCR6	BAG6	2	96.3	4.90E-04	-1.0917	-1.2532
A0A024R0Y2	ACACA	2	85.15	6.22E-04	-1.0945	-1.2813
A0A090N8Y2	PDIA4	7	426.2	4.97E-04	-1.0978	1.1029
A0A024RD82	MUT	3	169.6	1.94E-03	-1.0998	1.1830
F5H6E2	MYO1C	2	113.26	1.86E-02	-1.1019	1.1678
Q6FHF5	PCNA	2	136.75	5.42E-04	-1.1033	-1.2444
O14654	IRS4	6	348.58	6.30E-04	-1.1034	1.2411
A0A024RA27	HNRNPA2B1	3	200.66	4.53E-03	-1.1047	1.1195
Q6IB76	NDUFV2	2	96.58	5.08E-03	-1.1094	1.1029
O43491	EPB41L2	3	197.19	8.19E-04	-1.1134	1.1260
B3KSU9	ELAC2	3	147.53	1.15E-03	-1.1184	-1.1766
A0A024R3T8	PARP1	3	216.74	4.21E-03	-1.1238	1.0820
G3V1C3	API5	2	115.39	6.75E-04	-1.1288	1.0092
A0A024R118	METTL7A	2	103.37	1.10E-04	-1.1354	1.3507
A8K6V3	SF3B3	2	99.4	7.45E-04	-1.1376	1.0009
Q02952	AKAP12	2	103.56	8.69E-03	-1.1430	-1.2203
O14929	HAT1	3	219.42	7.92E-05	-1.1540	-1.2930
B2R659	HSD17B4	2	111.14	8.40E-04	-1.1559	1.0492
P12270	TPR	2	113.55	1.41E-03	-1.1577	1.1511
P14854	COX6B1	2	100.16	1.16E-03	-1.1619	1.1569
P04181	OAT	6	302.84	2.30E-04	-1.1645	1.0273
A0A087WUZ3	SPTBN1	9	600.68	2.07E-03	-1.1691	1.0566
A0A024RB16	ESYT1	2	156.77	1.73E-03	-1.1719	1.0523
G3XAM7	CTNNA1	4	266.48	1.43E-04	-1.1814	1.0555
B4DL06	CTNNB1	3	143.91	2.81E-04	-1.1875	1.1775
Q9UG16	SPTAN1	6	355.1	3.67E-03	-1.1885	1.0986
Q6P2Q9	PRPF8	5	278.83	7.02E-03	-1.1911	1.0198
A0A024R7U6	MCM4	2	128.14	6.51E-03	-1.1945	-1.1471
A6NEM2	HCFC1	2	128.76	6.18E-06	-1.2196	1.0424
Q1WWL2	PTGFRN	2	93.06	2.04E-04	-1.2263	1.4651
A0A024RBE7	TMPO	6	336.17	8.08E-03	-1.2288	1.0590
Q4TT76	ADD1	3	191.64	1.94E-05	-1.2289	1.0873
B0AZQ4	SMC3	3	161.5	8.04E-04	-1.2294	1.0714
Q99584	S100A13	2	87.7	6.86E-03	-1.2320	-1.0186

A0A024R7P2	FKBP8	4	258.66	8.80E-05	-1.2347	1.0931
P49792	RANBP2	2	122.72	8.85E-04	-1.2391	1.1613
P23229-3	ITGA6	3	169.5	3.29E-05	-1.2405	1.2211
A4FU77	SNRNP200	3	192.72	1.02E-02	-1.2539	-1.0172
H0Y394	HDLBP	2	147.89	5.78E-04	-1.2557	-1.0243
A0A087WVV2	RRBP1	5	278.92	1.18E-03	-1.2749	1.1636
Q8IY81	FTSJ3	2	103.35	4.95E-03	-1.2770	1.0070
A0A024R0Q4	PLD3	3	144.25	4.21E-05	-1.2868	-1.3192
P11717	IGF2R	2	103.71	6.30E-03	-1.3055	1.1088
P38432	COIL	2	110.25	4.13E-03	-1.3107	1.0493
A0A024R8H6	BRD3	2	123.26	5.00E-03	-1.3202	1.2752
A0A024R1X8	JUP	7	376.72	4.85E-04	-1.3226	1.1286
P49458	SRP9	2	123.7	3.34E-04	-1.3513	-1.0306
P15924	DSP	10	588.73	1.84E-03	-1.3678	1.0061
Q9Y5J9	TIMM8B	2	130.09	2.04E-04	-1.3747	-1.0012
A0A087WTW0	UHRF1	3	215.79	9.83E-04	-1.3827	-1.0624
A0A024RC67	PRC1	2	98.1	3.27E-03	-1.4047	-1.0930
B4DH46	DCAF7	3	236.57	5.19E-06	-1.4220	1.0050
Q6ZMF1	GLG1	2	177.7	1.08E-04	-1.4581	1.3975
A0A087WWE2	POLR2A	4	279.55	2.32E-03	-1.4849	1.0879
P11388	TOP2A	2	130.97	5.95E-03	-1.4923	-1.1022
Q05DA4	P4HA2	3	173.92	3.48E-03	-1.4970	1.0883
Q5T1J5	CHCHD2P9	3	155.68	7.41E-04	-1.5524	-1.0083
B2R6E2	PDCD4	3	156.83	1.41E-04	-1.5697	1.3253
Q6IAX1	FDFT1	3	183.07	1.01E-04	-1.6541	-1.0790
A8K4B4	NUSAP1	2	123.68	5.42E-04	-1.6999	1.1715
D6RFI1	DBN1	6	369.19	5.53E-06	-1.8034	1.0158
P50402	EMD	5	290.89	2.49E-04	-1.9162	1.1069
P49454	CENPF	2	100.88	5.38E-04	-2.4006	1.0821

Appendix 2 Post-filtering proteomic dataset: proteins with expression change >10% following UBA1 overexpression or UBA1 knockdown

Fold changes are presented as fold change compared to control. Unique peptides indicates the number of peptides detected that map only to that protein; p-value is from One-way ANOVA analysis performed in Mascot; score indicates the Mascot score for each protein. Proteins are ordered from greatest upregulation to greatest downregulation following UBA1 overexpression.

Appendix 3 Proteins with fold change >1.2 or >-1.2 following both UBA1 overexpression and UBA1 knockdown

					Fold change	
Gene name	Protein name	Unique peptides	Score	p-value	OE	KD
HMOX1	Heme oxygenase 1	2	146.1	1.25E-05	2.44	-1.23
ASNS	Asparagine synthetase [glutamine-hydrolyzing]	6	418.07	2.33E-04	1.47	-1.49
GARS	Glycine--tRNA ligase	2	102.71	1.43E-03	1.37	-1.24
YARS	Tyrosine--tRNA ligase, cytoplasmic	2	101.88	2.88E-03	1.29	-1.32
IPO4	Importin-4	2	99.74	2.69E-03	1.26	-1.25
PSAT1	Phosphoserine aminotransferase	3	154.43	3.05E-03	1.25	-1.32
IRGQ	Immunity-related GTPase family Q protein	2	102.32	8.97E-04	1.25	-1.23
FABP5	Fatty acid-binding protein, epidermal	3	216.32	5.23E-03	1.21	-1.24
ALDOA	Fructose-bisphosphate aldolase A	4	248.49	6.60E-04	1.2	-1.21
PTGFRN	Prostaglandin F2 receptor negative regulator	2	93.06	2.04E-04	-1.23	1.47
ITGA6	Integrin alpha-6	3	169.5	3.29E-05	-1.24	1.22
PLD3	Phospholipase D3	3	144.25	4.21E-05	-1.29	-1.32
BRD3	Bromodomain-containing protein 3	2	123.26	5.00E-03	-1.32	1.28
GLG1	Golgi apparatus protein 1	2	177.7	1.08E-04	-1.46	1.4
PDCD4	Programmed cell death protein 4	3	156.83	1.41E-04	-1.57	1.33

Appendix 3 Proteins with fold change >1.2 or >-1.2 following both UBA1 overexpression and UBA1 knockdown

Fold changes are presented as fold change compared to control. Unique peptides indicates the number of peptides detected that map only to that protein; p-value is from One-way ANOVA analysis performed in Mascot; score indicates the Mascot score for each protein. Proteins are ordered from greatest upregulation to greatest downregulation following UBA1 overexpression.

Appendix 4 Functional annotation changes in UBA1 proteomics dataset

Appendix 4 Functional annotation changes for the UBA1 proteomics dataset identified in IPA

Functional annotation changes identified in IPA for the UBA1 proteomics dataset. Number of proteins and the proteins that belong to each annotation are included. The p-value indicates the significance of the enrichment of that functional annotation within the dataset. Note the presence of neurological disease and skeletal and muscular disorders.

Functional annotation	p-value	Number of proteins	Proteins
Cellular Growth and Proliferation	3.86E-17	111	ACACA, ACLY, AHCY, AKAP12, ALDOA, ANXA1, API5, ASNS, ATIC, BAG6, BASP1, BCAP31, CACYBP, CAPN2, CAST, CBR1, CCT2, CD81, CDC37, CDK1, CENPF, CLIC1, COPS3, CSE1L, CTNNA1, CTNNB1, CTPS1, DBN1, DDX17, DNM1L, DSP, EEF1A1, EEF1B2, EEF1D, EIF4A1, EIF5A, ELAC2, EMD, ENO1, FABP5, FDFT1, FLOT1, FLOT2, FTSJ3, G6PD, GAPDH, GSTP1, HAT1, HMOX1, HNRNPA2B1, HSP90AA1, HSP90AB1, HSP90B1, HSPA4, IDH2, IGF2R, IMPDH2, IRS4, ITGA6, JUP, KPNA2, LCP1, LDHA, LMNA, LMNB1, LMNB2, MCM4, MIF, MYH9, NAP1L1, NME2, NUMA1, P4HA2, PA2G4, PARK7, PARP1, PCNA, PDCD4, PDCD5, PEBP1, PFKP, PFN1, PGK1, PKM, PRDX1, PRKDC, PRPF8, PSMC3, RANBP1, RUVBL1, S100A13, SF3B3, SLC3A2, SMC3, SNRNP200, SPTAN1, SPTBN1, STIP1, TES, THOC1, TMPO, TOP2A, TPR, TSN, TUBB, TUBB2A, TUBB4B, UCHL1, UHRF1, WARS, YARS
Cell Death and Survival	9.17E-15	100	ACACA, ACLY, ACO2, ADD1, AIFM1, AKAP12, ALDOA, ALDOC, ANXA1, API5, ASNS, BAG6, BASP1, BCAP31, CACYBP, CAPN2, CAST, CBR1, CCT2, CCT4, CCT8, CD81, CDC37, CDK1, CENPF, CHMP5, CSE1L, CTNNA1, CTNNB1, DCAF7, DDX17, DNM1L, DSP, EEF1A1, EEF1D, EIF5A, EIF5B, EMD, ENO1, FDFT1, FKBP8, FLOT2, G6PD, GAPDH, GFPT1, GLUD1, GSTP1, HAT1, HMOX1, HSD17B4, HSP90AA1, HSP90AB1, HSP90B1, HSPA4, HSPBP1, HSPH1, IDH2, IGF2R, IMPDH2, ITGA6, JUP, KPNA2, KPNB1, LDHA, LGALS3BP, LMNA, LMNB1, MDH1, MIF, MYH9, NDUFV2, NME2, NUMA1, NUSAP1, PA2G4, PARK7, PARP1, PCNA, PDCD4, PDCD5, PEBP1, PKM, POLR2A, PRDX1, PRDX6, PRKDC, RANBP1, RANBP2, RRBP1, SDHA, SF3B3, SLC3A2, SPTBN1, STIP1, THOC1, TOP2A, TPR, TUBB, UCHL1, YARS
Neurological Disease	1.81E-12	42	ACADM, AHCY, AIFM1, ANXA1, BAG6, BASP1, CKB, CSE1L, CTNNB1, DARS, EEF1A1, FARSB, FDFT1, FLOT1, GAPDH, GFPT1, GSTP1, HADH, HMOX1, HSP90AA1, HSP90B1, IMPDH2, LDHA, MDH1, MIF, MUT, MYL12A, PARK7, PARP1, PCNA, PEBP1, PFN1, PGK1, PKM, PRDX6, PSAT1, RANBP1, SDHA, TOP2A, TSN, TUBA1C, UCHL1
Skeletal and Muscular Disorders	1.81E-12	42	ACADM, AHCY, AIFM1, ANXA1, BAG6, BASP1, CKB, CSE1L, CTNNB1, DARS, EEF1A1, FARSB, FDFT1, FLOT1, GAPDH, GFPT1, GSTP1, HADH, HMOX1, HSP90AA1, HSP90B1, IMPDH2, LDHA, MDH1, MIF, MUT, MYL12A, PARK7, PARP1, PCNA, PEBP1, PFN1, PGK1, PKM, PRDX6, PSAT1, RANBP1, SDHA, TOP2A, TSN, TUBA1C, UCHL1
Cancer	2.53E-12	11	ATIC, EIF4A1, GART, HSP90AA1, HSP90AB1, HSP90B1, TOP2A, TUBA1C, TUBB, TUBB2A, TUBB4B
Organismal Injury and Abnormalities	2.53E-12	11	ATIC, EIF4A1, GART, HSP90AA1, HSP90AB1, HSP90B1, TOP2A, TUBA1C, TUBB, TUBB2A, TUBB4B
Respiratory Disease	2.53E-12	11	ATIC, EIF4A1, GART, HSP90AA1, HSP90AB1, HSP90B1, TOP2A, TUBA1C, TUBB, TUBB2A, TUBB4B

Appendix 5 Published papers

HK Shorrock, TH Gillingwater. *Development and translation of therapies for spinal muscular atrophy.* European Medical Journal Neurology. 2016 4[1]: 64-73

HR Fuller, **HK Shorrock,** et al. *Two cases of spinal muscular atrophy type II with eosinophilic oesophagitis.* Neuromuscular Diseases. 2017 4[4]: 357-362

PJ Boyd, WY Tu, **HK Shorrock** et al. *Bioenergetic status modulates motor neuron vulnerability and pathogenesis in a zebrafish model of spinal muscular atrophy.* Plos Genetics. 2017 13[4]: e1006744

P Bernabò, T Tebaldi, EJN Groen, FM Lane, E Perenthaler, F Mattedi, H Newbery, H Zhou, P Zuccotti, V Potrich, **HK Shorrock**, et al. *In vivo translatome profiling in spinal muscular atrophy reveals a novel role for SMN protein in ribosome biology.* Cell Reports. 2017 21[4]: 953-965

AK Thomson, E Somers, RA Powis, **HK Shorrock** et al. *Survival of motor neurone protein is required for normal postnatal development of the spleen*. Journal of Anatomy. 2017 230: 337-346

G Hunter, RA Powis, RA Jones, EJN Groen, **HK Shorrock** et al. *Restoration of SMN in Schwann cells reverses myelination defects and improves neuromuscular function in spinal muscular atrophy*. Human Molecular Genetics. 2016 44: 1-9